Techniques for high-multiplicity scattering amplitudes and applications to precision collider physics

JAKUB MARCIN KRYS

Techniques for high-multiplicity scattering amplitudes and applications to precision collider physics

Jakub Kryś

A Thesis presented for the degree of
Doctor of Philosophy

Institute for Particle Physics Phenomenology
Department of Physics
Durham University
United Kingdom

January 2024

Techniques for high-multiplicity scattering amplitudes and applications to precision collider physics

Jakub Kryś

Submitted for the degree of Doctor of Philosophy
January 2024

Abstract: In this thesis, we present state-of-the-art techniques for the computation of scattering amplitudes in Quantum Field Theories. Following an introduction to the topic, we describe a robust framework that enables the calculation of multi-scale two-loop amplitudes directly relevant to modern particle physics phenomenology at the Large Hadron Collider and beyond. We discuss in detail the use of finite fields to bypass the algebraic complexity of such computations, as well as the method of integration-by-parts relations and differential equations. We apply our framework to calculate the two-loop amplitudes contributing to three process: Higgs boson production in association with a bottom-quark pair, $W^{\pm}$ boson production with a photon and a jet, as well as lepton-pair scattering with an off-shell and an on-shell photon. Finally, we draw our conclusions and discuss directions for future progress of amplitude computations.

Contents

Declaration

The work in this thesis is based on joint research carried out in the Department of Physics at Durham University (UK), as well as in the Department of Physics at the University of Turin (Italy). Chapter 3 is based on Ref. [1], Chapter 4 on Ref. [2] and Chapter 5 on Ref. [3]. No part of this thesis has been submitted elsewhere for any degree or qualification.

Acknowledgements

Most of all, I would like to thank my supervisor, Simon Badger, for his continuous guidance over the last couple of years, stretching back to our time in Durham. Without his keen help, the course of my PhD would have been much rougher.

I am indebted to my collaborators: Simone Zoia, Bayu Hartanto, Ryan Moodie and Francesco Sarandrea, for patiently answering my endless and extremely specific questions, as well as for providing occasional IT support.

Finally, I thank my fellow PhD students in Torino for making my time there enjoyable and for tirelessly explaining convoluted concepts of Italian grammar.

I wish all a fruitful and happy future (and no sign mistakes when permuting tr_5).

Each of us
A cell of awareness
Imperfect and incomplete
Genetic blends
With uncertain ends
On a fortune hunt that's far too fleet

— from *Freewill* by Rush

Chapter 1

Introduction

The understanding of elementary particles and their interactions is undoubtedly one of the most fascinating quests of the scientific endeavour. Modern particle physics has proven remarkably successful at explaining phenomena which occur at size scales orders of magnitude smaller than what our brains evolved to comprehend. The Standard Model (SM), which is a collection of Quantum Field Theories (QFTs) that describe the subatomic world, allows us to rigorously test our ideas about how the Universe functions at the most bare, fundamental level. It relies on a constant interplay between theoretical predictions and their experimental verification (or negation). From the perspective of a theoretical physicist, it is crucial to be able to derive increasingly precise predictions for physically observable quantities that can be measured in particle colliders such as the Large Hadron Collider (LHC) at CERN. This theoretical precision should match what can be achieved experimentally. The growing amount of data from Run 3 at the LHC makes this a challenge for the theoretical community, pushing us to constantly improve our computational tools in order to refine our predictions.

The subject of this thesis is precisely the story of trying to overcome the current limitations in an effort to exploit the predictive power of QFT to an even greater extent. It is a famous fact of physics that QFT computations cannot be performed exactly, apart from the most trivial cases. Instead, one follows an approximate description through the so-called perturbation theory. In this approach, the leading-order (LO) terms in the computation are low in number and complexity. They represent a crude, almost 'back-of-the-envelope' estimation of the full answer. The next-to-leading-order (NLO) terms increase in number and are harder to calculate. Nonetheless, they provide a refinement of the LO result and are absolutely necessary for precision phenomenology. Roughly speaking, the cutting edge of QFT computations is currently at the next-to-next-to-leading-order (NNLO) for $2 \to 3$ processes

and at N^{3}LO for $2 \to 2$ processes. They can involve millions of individual terms, each of which can be incredibly hard to evaluate.

In this thesis, we will focus on the description of one of the key ingredients needed for QFT computations, i.e. the scattering amplitudes. We will provide the reader with a solid understanding of why they are important in the first place, how they are calculated and the difficulties that we have to overcome in practice. Naturally, we cannot jump into full detail straightaway. We hope that this thesis will be approachable to someone who already possesses basic knowledge of QFT, but we certainly do not assume previous experience in this topic at research level. For this reason, we dedicate the rest of Chapter 1 to reviewing the rudimentary information needed further on. This content should be familiar from a thorough introductory course to QFT. Next, in Chapter 2 we introduce more advanced and specialised techniques that are used to compute scattering amplitudes. We hope that despite the breadth of the concepts covered and often heavy mathematical detail, this chapter will not be too hard to follow. Our reward will come in the following chapters, where we will use the techniques described thus far to compute scattering amplitudes necessary for the precise description of three selected processes that have been deemed of high priority by the particle physics community. The biannual Les Houches report provides a wishlist of processes whose improved theoretical description would greatly contribute to our understanding of fundamental particles [4]. Amongst others, the two-loop QCD amplitudes relevant to Higgs boson production in association with a bottom-quark pair, $pp \to b\bar{b}H$, as well as to $W^\pm$ boson production with a photon and a jet, $pp \to W^\pm\gamma j$, are highly desired. They are described in Chapters 3 and 4 and represent some of the first results for five-point processes with an external massive leg at this loop order. In Chapter 5, we switch our focus to the QED process $0 \to l\bar{l}\gamma\gamma^*$, which is required to achieve the precision goal of the MUonE experiment. For this purpose, we will construct a basis of special functions for integrals needed to describe any four-point process with an off-shell leg at the two-loop order. Finally, in Chapter 6, we draw our conclusions and discuss directions for future work. Further technical detail and supplementary material is provided in several Appendices.

1.1 QFT background

The rest of this introduction is meant to provide the reader with a bridge between elementary knowledge of QFT and state-of-the-art techniques that are used to extract predictions from it. We start by providing a brief summary of the relevant information about QFTs, and in particular QCD. Next, in Section 1.3 we describe how to connect this theory to physical observables that can be measured experi-

mentally. This introduces the notion of a scattering amplitude in Section 1.4, which will be the main focus of this thesis. Finally, in Section 1.5 we discuss the famous problem of divergences in QFT computations and show how in the process of trying to keep them under control, we discover a surprising feature of QCD interactions. At the end, we will be ready to tackle the more advanced topics in Chapter 2.

One of the central equations of QFT, which describes all spin-1/2 particles, is the Dirac equation:

$$(\mathrm{i}\partial\!\!\!/ - m)\psi(x) = 0\,. \tag{1.1.1}$$

Its solutions are given by the four-component Dirac spinors $\psi(x)$, which transform in the irreducible $\left(\frac{1}{2},0\right)\otimes\left(0,\frac{1}{2}\right)$ representation[1]. There are four plane-wave solutions, which admit both positive and negative frequencies:

$$\psi(x) = u^s(p)\mathrm{e}^{-\mathrm{i}p\cdot x} \qquad \text{and} \qquad \psi(x) = v^s(p)\mathrm{e}^{+\mathrm{i}p\cdot x}\,, \tag{1.1.2}$$

where $s \in \{1,2\}$. The momentum space spinors $u(p)$ and $v(p)$ are interpreted as describing particles and antiparticles with *positive* energies. They satisfy the momentum space Dirac equations:

$$\begin{aligned}(p\!\!\!/ - m)u(p) &= 0\,,\\ (p\!\!\!/ + m)v(p) &= 0\,,\end{aligned} \tag{1.1.3}$$

as well as the following completeness relations, which are useful when performing spin sums in QFT computations:

$$\begin{aligned}\sum_{s\in\{1,2\}} u^s(p)\bar{u}^s(p) &= p\!\!\!/ + m\,,\\ \sum_{s\in\{1,2\}} v^s(p)\bar{v}^s(p) &= p\!\!\!/ - m\,.\end{aligned} \tag{1.1.4}$$

Moreover, it is convenient to split the spinors into two separate components:

$$\psi(x) = \begin{pmatrix}\psi_L(x)\\ \psi_R(x)\end{pmatrix}\,, \tag{1.1.5}$$

where the left- and right-handed Weyl spinors $\psi_L(x)$ and $\psi_R(x)$ transform in the $\left(\frac{1}{2},0\right)$ and $\left(\frac{1}{2},0\right)$ representations, respectively. It is important to note that Eq. 1.1.1 mixes these two components, which can be appreciated by writing it explicitly in matrix notation. In the so-called Weyl (or chiral) basis, the Dirac matrices are:

$$\gamma^\mu = \begin{pmatrix}0 & \sigma^\mu\\ \bar{\sigma}^\mu & 0\end{pmatrix}\,, \tag{1.1.6}$$

[1]Not to be confused with the usual four-vectors x^μ, which transform in the $\left(\frac{1}{2},\frac{1}{2}\right)$ representation.

with $\sigma^\mu \equiv (\mathbb{1}, \sigma^i)$ and $\bar{\sigma}^\mu \equiv (\mathbb{1}, -\sigma^i)$, and σ^i for $i = 1, 2, 3$ are the Pauli matrices. Thus, the Dirac equation is:

$$\begin{pmatrix} -m & \mathrm{i}\sigma^\mu \partial_\mu \\ \mathrm{i}\bar{\sigma}^\mu \partial_\mu & -m \end{pmatrix} \begin{pmatrix} \psi_L(x) \\ \psi_R(x) \end{pmatrix} = 0\,, \tag{1.1.7}$$

where each entry is in itself understood to be a (2×2) matrix. Crucially, we can see that in the absence of mass, the two components fully decouple and can be treated separately. It is also useful to define an additional γ^5 matrix:

$$\gamma^5 \equiv \mathrm{i}\,\gamma^0\gamma^1\gamma^2\gamma^3\,, \tag{1.1.8}$$

which in the Weyl representation is just:

$$\gamma^5 = \begin{pmatrix} -\mathbb{1} & 0 \\ 0 & \mathbb{1} \end{pmatrix}. \tag{1.1.9}$$

The fifth γ-matrix plays a surprisingly important role in QFT. First, the Weyl spinors can be extracted from the Dirac spinors by applying appropriate projectors:

$$P_L = \frac{\mathbb{1} - \gamma^5}{2} = \begin{pmatrix} \mathbb{1} & 0 \\ 0 & 0 \end{pmatrix}, \qquad P_R = \frac{\mathbb{1} + \gamma^5}{2} = \begin{pmatrix} 0 & 0 \\ 0 & \mathbb{1} \end{pmatrix}, \tag{1.1.10}$$

according to $\psi_L(x) = P_L\psi(x)$ and $\psi_R(x) = P_R\psi(x)$. This allows us to associate ψ_L and ψ_R with the helicity of a particle, which is the projection of its spin onto the direction of motion. The corresponding helicity values for left- and right-handed particles are -1 and $+1$, respectively[1]. Weyl spinors will play a key role in the discussion of the spinor-helicity formalism in Section 2.4. Moreover, the P_L projector appears in the $V - A$ coupling of the charged $W^\pm$ bosons to quarks and leptons, reflecting the fact that they interact only with left-handed fermions. Finally, as we will see in Chapters 3 and 4, γ^5 allows us to introduce a pseudo-scalar invariant which is needed to capture the parity information of the kinematic phase space.

Apart from fermions, we also need to know how to deal with bosons. In particular, spin-1 bosons are described by vector fields A^μ, which transform in the $(\frac{1}{2}, \frac{1}{2})$ representation of the Lorentz group. For the massive gauge bosons, that is $W^\pm$ and Z^0, imposing their equations of motion leads to three distinct solutions labelled $\varepsilon^s_\mu(p)$ and referred to as polarisation vectors. Similarly to the completeness relations for spin-1/2 fermions, Eq. 1.1.4, the polarisation vectors of the massive gauge bosons

[1] Strictly speaking, the left- and right-handed Weyl spinors are eigenstates of the chirality operator γ^5. However, for $m = 0$, helicity and chirality eigenstates coincide.

satisfy the following property:

$$\sum_{s\in\{0,1,2\}} \varepsilon^s_\mu(p)(\varepsilon^s_\nu(p))^* = -g_{\mu\nu} + \frac{p_\mu p_\nu}{M^2}\,. \tag{1.1.11}$$

On the other hand, massless gauge bosons, i.e. photons and gluons, have only two polarisations, which can be interpreted as helicity eigenstates. Their completeness relation reads:

$$\sum_{s\in\{-,+\}} \varepsilon^s_\mu(p,q)(\varepsilon^s_\nu(p,q))^* = -g_{\mu\nu} + \frac{p_\mu q_\nu + p_\nu q_\mu}{p\cdot q}\,, \tag{1.1.12}$$

where $q^\mu \neq p^\nu$ is an arbitrary reference vector which is introduced to help decompose the four-component vectors ε^μ into two-component objects, similarly to the decomposition of the Dirac spinor into Weyl spinors. The end result of any computation is independent of q^μ, which reflects gauge invariance (we will elaborate on this fact in Section 2.4).

Finally, the Standard Model famously includes a scalar particle — the Higgs boson. This boson is responsible for electroweak symmetry breaking and, as a direct consequence, giving mass to the electroweak gauge bosons $W^\pm$ and Z^0.

1.2 Quantum Chromodynamics

In this thesis, we will concern ourselves with the study of interactions involving mainly quarks and gluons. As such, a brief refresher of the relevant information is in order. SM particles carrying colour charge interact via the strong force, which is mathematically described by QCD. Its Lagrangian can be schematically represented as a sum of three parts:

$$\mathcal{L}_{\text{QCD}} = \mathcal{L}_{\text{classical}} + \mathcal{L}_{R_\xi} + \mathcal{L}_{\text{ghosts}}\,. \tag{1.2.1}$$

We begin by discussing the classical part. It is given by:

$$\mathcal{L}_{\text{classical}} = -\frac{1}{4}G^a_{\mu\nu}G^{a\,\mu\nu} + \sum_q^{n_f} \overline{\psi}^i_q \left(\mathrm{i}\not{D}_{ij} - m_q\delta_{ij}\right)\psi^j_q\,, \tag{1.2.2}$$

where:

$$G^a_{\mu\nu} = \partial_\mu A^a_\nu + \partial_\nu A^a_\mu + g_s f^{abc} A^b_\mu A^c_\nu \tag{1.2.3}$$

is the gluon field strength, while:

$$(D_\mu)_{ij} = \delta_{ij}\partial_\mu - \mathrm{i}g_s(T^a)_{ij}A^a_\mu \tag{1.2.4}$$

is the covariant derivative introduced to ensure gauge invariance under SU(N_c) transformations[1].

The QCD Lagrangian contains three types of fields. Quarks and antiquarks, corresponding to ψ_q^i and $\overline{\psi}_q^i$, respectively, transform in the fundamental and antifundamental representations of SU(N_c). In QCD, they have $n_f = 6$ flavours. The indices $i \in \{1, \ldots, N_c\}$ denote the colour charge of the (anti)quarks. It is common to drop the colour index and write ψ_q, which is understood as $\psi_q \equiv \left(\psi_q^r, \psi_q^b, \psi_q^g\right)^T$. The fundamental fields are acted on by the $N_c^2 - 1$ fundamental generators of SU(N_c) with dimensions $(N_c \times N_c)$. For SU(3), they are given by:

$$(T^a)_{ij} = \frac{1}{2}(\tau^a)_{ij}\,, \tag{1.2.5}$$

where τ^a are the eight (3×3) Gell-Mann matrices. Similarly, the antifundamental fields are acted on by the generators in the antifundamental representation, $\overline{T}^a = -(T^a)^*$. The fundamental generators are normalised according to:

$$\mathrm{tr}(T^a T^b) = T_F \delta^{ab}\,. \tag{1.2.6}$$

Usually, in QCD we take $T_F = \frac{1}{2}$ or 1. Finally, let us list one more useful relation:

$$(T^a)_{ij}(T^a)_{kl} = T_F \left(\delta_{il}\delta_{jk} - \frac{1}{N_c}\delta_{ij}\delta_{kl}\right)\,, \tag{1.2.7}$$

which is known as the Fierz identity.

The third type of a field, the gluon field, is represented by A_μ^a. It transforms in the adjoint representation, i.e. under the action of $N_c^2 - 1$ adjoint generators with dimensions $(N_c^2 - 1 \times N_c^2 - 1)$:

$$\left(T^a_{\mathrm{adj}}\right)^{bc} = -\mathrm{i} f^{abc}\,, \tag{1.2.8}$$

where $a, b, c \in \{1, \ldots, N_c^2 - 1\}$ are the colour indices and the totally antisymmetric objects f^{abc} are known as the structure constants. Typically, the adjoint generators are normalised such that $\mathrm{tr}(T^a_{\mathrm{adj}} T^b_{\mathrm{adj}}) = N_c \delta^{ab}$.

SU(N_c) generators (in any representation) satisfy the following defining relation of the Lie algebra:

$$\left[T^a, T^b\right] = \mathrm{i} f^{abc} T^c\,. \tag{1.2.9}$$

Note that for Abelian groups, the structure constants vanish. For the non-Abelian SU(3) group of QCD, they are non-vanishing and it is useful to invert the above

[1] We will keep the degree N_c of the group SU(N_c) generic in the discussion below, but of course we are interested in the QCD case of $N_c = 3$.

relation in terms of the fundamental generators:

$$f^{abc} = -\frac{\mathrm{i}}{T_F}\,\mathrm{tr}\left(\left[T^a, T^b\right] T^c\right) . \tag{1.2.10}$$

Thus, the structure constants, which are associated with 3- and 4-gluon vertices in Feynman diagrams, can be written in terms of traces of fundamental generators. This fact, along with the Fierz identity, becomes very useful when computing scattering amplitudes in QCD, as we will see in Section 2.2.

In the process of deriving the QCD gluon propagator, the notion of gauge invariance leads to two important qualitative features. First of all, just as in the case of the photon propagator in QED, instead of explicitly fixing the gauge, we find it convenient to introduce an auxiliary (i.e. non-propagating) field ξ. We write:

$$\mathcal{L}_{R_\xi} = -\frac{1}{2\xi}\left(\partial^\mu A^a_\mu\right)^2 , \tag{1.2.11}$$

which yields the gluon propagator:

$$\Pi^{\mu\nu}(p) = \frac{-\mathrm{i}\,\delta^{ab}}{p^2 + \mathrm{i}\varepsilon}\left(g^{\mu\nu} - (1-\xi)\frac{p^\mu p^\nu}{p^2 + \mathrm{i}\varepsilon}\right) . \tag{1.2.12}$$

As an example, with the term Eq. 1.2.11 included in the full QCD Lagrangian, for small ξ we must have that $\partial^\mu A^a_\mu \to 0$ in order to prevent the exponential of $\mathcal{L}$ from blowing up, such that we can still minimise the action. Thus, the choice $\xi = 0$ is equivalent to the Lorenz gauge and spares us from having to impose the Lorenz condition throughout the entire computation. Other choices are possible, of course. In fact, the most common prescription is to set $\xi = 1$, which is known as the Feynman-'t Hooft gauge. It is also possible to keep ξ generic — gauge invariance ensures that the results of computations of physical quantities will be free of ξ at the end.

The second feature, which appears only in non-Abelian gauge theories, is that gauge fixing the Lagrangian implies that not only the physical transverse modes of A^a_μ can propagate. To cancel the unphysical degrees of freedom propagating through gluon loops in Feynman diagrams, it is necessary to include in the Lagrangian Grassmann-valued fields c and $\bar{c}$ representing Faddeev-Popov ghosts and antighosts:

$$\mathcal{L}_{\text{ghosts}} = (\partial^\mu \bar{c}^{\,a})(\delta^{ac}\partial_\mu + g_s f^{abc} A^b_\mu) c^c . \tag{1.2.13}$$

These particles are not physical states. In fact, it is possible to work in non-covariant gauges, such as the axial gauge or the lightcone gauge, where ghosts decouple from physical particles and can be neglected. However, the cost of doing so is a more complicated expression for the gluon propagator, which may lead to tougher

computations. Thus, we usually accept ghosts as a peculiarity of working with non-Abelian gauge theories and include them in our computations. They couple only to gluons (and not to quarks) and receive their own Feynman rules for the propagator and the vertex.

1.3 Particle scattering

Having introduced the QFTs that describe the most fundamental particles our nature has to offer, one might rightfully wonder about the rewards for our intellectual effort (beyond personal satisfaction). After all, amongst our non-physicist friends, it is common to think that the word 'theoretical' in 'theoretical physics' is synonymous with 'hypothetical'. Not much could be further from the truth and we dedicate this section to illustrating the immense predictive power of QFTs.

Consider a typical particle physics experiment. Two beams of particles, travelling in opposite directions, interact briefly and produce a host of new states that fly away in various directions until they are registered by some kind of a detector. Naturally, the number of such scattering events is proportional to the number of particles in the two beams, N_a and N_b, as well as to the area common to the beams, A. The ratio of these quantities is known as the scattering **cross section**:

$$\sigma \equiv \frac{\text{number of scattering events}}{N_a N_b A} \,. \tag{1.3.1}$$

Typically, apart from just counting the total number of events, we want to differentiate between the type of outgoing particles, their momentum, angle of collision, etc. However, if we specify an exact value for a continuous variable such as the momentum, the numerator of Eq. 1.3.1 becomes infinitesimal. To avoid this issue, we usually work with a *differential* cross section, e.g. $\mathrm{d}\sigma/(\mathrm{d}p_1 \ldots \mathrm{d}p_n)$, such that its integral over some small range of p_i gives the *total* cross section in that region of momentum space. While cross sections can be measured in particle colliders, it is the task of QFT to make predictions for them.

In the case of hadron collisions, there is one additional complication which needs to be taken into account. The fundamental objects of QCD are quarks and gluons, however they cannot be observed individually due to colour confinement — only their colourless combinations can be detected in a collider. The LHC, being a proton-proton collider, requires a more complicated model of the interactions than just the scattering of point particles. As we will soon see, QCD exhibits a behaviour known as asymptotic freedom. That is, the coupling constant α_s decreases with energy (i.e. at small distances) and its value determines whether we are allowed to use perturbation

theory or not. Roughly speaking, above the scale $\Lambda_{\rm QCD} \sim 200$ MeV, α_s becomes small enough so that the perturbative expansion is justified. The individual 'partons' (i.e. quarks, antiquarks and gluons) act like free particles and undergo 'hard' scattering [5]. On the other hand, physics at energies below $\Lambda_{\rm QCD}$ is necessarily non-perturbative due to large α_s values. Its effects are captured by the Parton Distribution Functions (PDFs) $f_i(x, \mu_F)$, which give the probability of finding in a hadron a given parton i with momentum fraction x of this hadron. Here, μ_F is a factorisation scale which separates the high- and low-energy physics. In fact, the PDFs run with μ_F, similarly to the running of the QCD coupling α_s, and their evolution is given by the DGLAP equations[1]. Overall, the factorisation of soft and hard physics allows us to write the cross section for the scattering of two hadrons h_1, h_2 to the final state X as [6]:

$$\mathrm{d}\sigma_{h_1 h_2 \to X} = \sum_{i,j} \int_0^1 \mathrm{d}x_1 \mathrm{d}x_2 \, f_i(x_1, \mu_F) f_j(x_2, \mu_F) \, \mathrm{d}\hat{\sigma}_{ij\to X}\left(\mu_F, \mu_R, Q^2\right) + \mathcal{O}\left(\frac{\Lambda^2_{\rm QCD}}{Q^2}\right), \tag{1.3.2}$$

where i, j are the partons of hadrons h_1 and h_2, respectively, and $\hat{\sigma}_{ij\to X}$ is the *partonic* cross section for the scattering of i, j into the final state. The higher-order terms can be neglected as long as the scale Q at which we are probing the hard scattering is significantly greater than $\Lambda_{\rm QCD}$. Since the PDFs describe effects at large α_s, they cannot be calculated using perturbative QCD. Instead, they are extracted from experimental data (see e.g. Refs. [7–11]). On a positive note, they are universal, i.e. process independent, so once they have been determined from some experiment, they can be re-used in the description of any other hadron interaction.

Contrary to the PDFs, the partonic cross sections are computed using perturbative QCD. Before turning our full attention to these objects, let us briefly remark that even after the scattering has taken place, a lot of interesting physics is still ongoing (see Fig. 1.1). The final state partons can radiate a cascade of other partons in a phenomenon referred to as parton showers. Furthermore, these coloured partons cannot be detected in a collider — as the energy scale falls below $\Lambda_{\rm QCD}$, they combine together to form colourless hadrons. Finally, unstable hadrons may decay into further products. What is actually detected in a collider is then a collimated spray of hadrons and other particles referred to as a jet. Using the so-called jet algorithms and jet definitions, one then tries to reverse engineer the collision of individual partons. We refer the reader to Refs. [12, 13] for a closer look at these topics.

[1] The origin of μ_F will be discussed in more detail in Section 1.5.2.

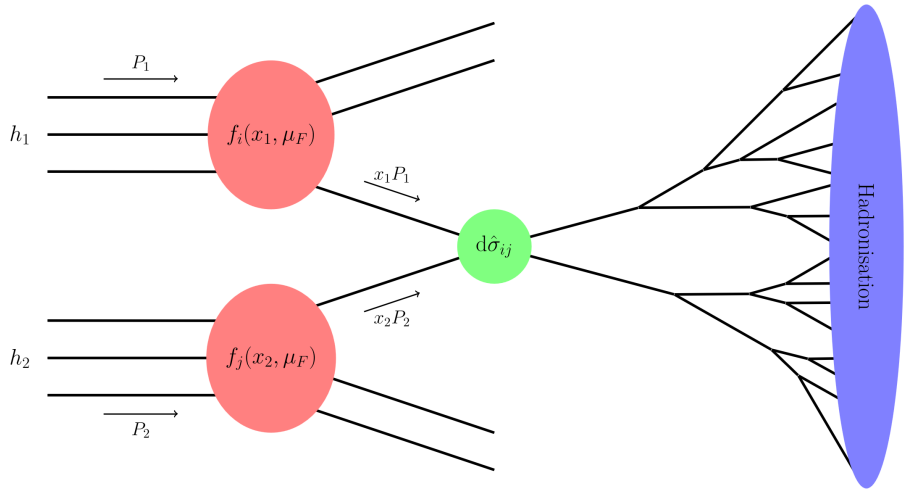

Figure 1.1: A schematic representation of a collision between two hadrons, h_1 and h_2, with total momenta P_1, P_2. A parton i carrying momentum $x_1 P_1$ undergoes hard scattering with a parton j carrying momentum $x_2 P_2$. Their factorisation from hadrons is described by the PDFs $f_i(x_1, \mu_F)$ and $f_j(x_2, \mu_F)$, while their interaction is described by the partonic cross section $\mathrm{d}\hat{\sigma}_{ij}$. The splitting lines represent subsequent parton showers, which then undergo hadronisation as the energy scale falls below Λ_{QCD}. Further decays and jets are not shown. Image courtesy of Ryan Moodie [14].

1.4 From cross sections to scattering amplitudes

Having decoupled the high- and low-energy physics within a hadron, let us now address the computation of the hard scattering between partons. The partonic cross section $\hat{\sigma}_{i\to f}$ is related to the probability of starting with some initial state i and ending up with the final state f, that is: $\mathcal{P} = |\langle f|i\rangle|^2$. These interacting states are not the free wave packets with well-defined momenta that we know how to handle using the QFT machinery. However, they do become free in the limit as $t \to -\infty$, i.e. before the interaction, as well as $t \to \infty$, i.e. after the interaction. The idea is then to view the scattering in the following way: an asymptotically free state $|i\rangle_{t=-\infty}$ evolves to a real-world state $|i\rangle$, undergoes scattering (of negligible duration) into the real-world state $|f\rangle$, which finally evolves into the free state $|f\rangle_{t=\infty}$. The evolution of the real states from and to the asymptotic states is captured by the S-matrix, which is calculated from the Hamiltonian in the 'interaction representation'. Specialising to the scattering of two partons into $n-2$ particles, we write the so-called S-matrix elements using the free multi-particle states:

$$\langle p_3, \ldots, p_n | p_1, p_2 \rangle = {}_{t=\infty}\langle p_3, \ldots, p_n | S | p_1, p_2 \rangle_{t=-\infty} \,. \tag{1.4.1}$$

Furthermore, it is customary to split the S-matrix according to:

$$S = \mathbb{1} + \mathrm{i}\,T\,. \tag{1.4.2}$$

In any scattering experiment, there is a large chance of the particles simply missing each other and nothing happening, which is expressed by the identity matrix. The interesting physics of interactions is captured by the transition matrix T:

$$_{t=\infty}\langle p_3,\ldots,p_n|\mathrm{i}\,T|p_1,p_2\rangle_{t=-\infty} = (2\pi)^4\delta^{(4)}\left(p_1+p_2-\sum_{f=3}^{n}p_f\right)\,\mathrm{i}\,\mathcal{A}(p_1,p_2\to p_3,\ldots,p_n)\,, \tag{1.4.3}$$

where we included the overall δ-function to impose 4-momentum conservation. Here, $\mathcal{A}(p_1,p_2\to p_3,\ldots,p_n)$ is the n-particle **scattering amplitude**. Finally, to relate the amplitudes to the partonic cross section, we insert Eq. 1.4.3 into Eq. 1.4.1 and integrate over a small region $\mathrm{d}^3p_3\ldots\mathrm{d}^3p_n$. This integration encodes the probability that the $n-2$ final particles will belong to that region of the momentum phase-space. Overall, the recipe reads:

$$\mathrm{d}\hat{\sigma} = \frac{1}{2E_1 2E_2|v_1-v_2|}\left(\prod_f\frac{\mathrm{d}^3p_f}{(2\pi)^3}\frac{1}{2E_f}\right)(2\pi)^4\delta^{(4)}\left(p_1+p_2-\sum_f p_f\right)|\mathcal{A}(p_1,p_2\to p_f)|^2\,. \tag{1.4.4}$$

The first term in this formula is a flux factor related to the relative velocity of the two incoming beams in the laboratory reference frame, $|v_1-v_2|$. Next, the overall δ-function imposes Lorentz invariance on the phase-space integration over $\prod_f \mathrm{d}^3p_f$. In practice, the phase-space integration is carried out using Monte Carlo event generators [15, 16]. Finally, the formula is completed by the square of the amplitude.

Scattering amplitudes represent a vital bridge between theory an experiment. On one hand, due to Eq. 1.4.4, they allow us to derive predictions for physical observables that can be measured in a collider. On the other hand, due to their connection with the S-matrix through Eq. 1.4.3, they are sensitive to our understanding of the underlying theory of interactions. As such, computing amplitudes serves as a key tool to challenge and improve our models of elementary particles. Unfortunately, in all but the simplest cases these amplitudes cannot be calculated exactly. Instead, we resort to an expansion in powers of the coupling constant:

$$\mathcal{A} = \alpha^t\left(\mathcal{A}^{(0)}+\alpha^1\mathcal{A}^{(1)}+\alpha^2\mathcal{A}^{(2)}+\ldots\right)\,. \tag{1.4.5}$$

In this formula, each term is calculated from linear combinations of expressions corresponding to Feynman diagrams. The expansion starts at the power t of the LO term $\mathcal{A}^{(0)}$. This term usually — but not always — corresponds to tree-level diagrams,

i.e. diagrams with no closed loops. Higher-order terms $\mathcal{A}^{(L)}$ gain additional powers of α due to L-loop diagrams. Therefore, at high energies where the coupling constant becomes small, we can approximate the full scattering amplitude by truncating the expansion in Eq. 1.4.5 at a desired order.

Let us stress that the computation of each element described so far, i.e. the cross sections, PDFs, the phase-space integration, amplitudes, parton showers, hadronisation and jets, is a tremendous effort undertaken by a multitude of particle physicists around the world. This thesis is a small building block of the entire enterprise and aims to shed light on just one of these aspects — the calculation of scattering amplitudes.

1.5 Divergences and dimensional regularisation

Let us now devote our attention to the study of Feynman integrals and diagrams, a fundamental tool used to compute scattering amplitudes. For a tree-level diagram, all momenta are uniquely fixed by momentum conservation at the vertices and no integration is necessary. However, each loop introduces an unconstrained 'loop momentum' which needs to be integrated over (see Fig. 1.2). We will denote them as k_l, where $1 \leq l \leq L$. It is a famous fact of QFT that many Feynman integrals contain divergences. They come in two types:

- **Ultraviolet divergences** — these appear when $k \to \infty$,
- **Infrared divergences** — these arise in processes with massless particles and are further subdivided into:
  - **Soft divergences** — when $k \to 0$,
  - **Collinear divergences** — when the loop momentum k becomes collinear to a massless external momentum.

1.5.1 UV divergence and renormalisation

The two types of divergences are handled in separate ways. Firstly, UV divergences are dealt with using renormalisation. In short, we start by realising that the masses, fields and couplings in the original Lagrangian of Eq. 1.2.2 are not 'physical', in the sense that we have been using them to define the perturbative expansion, but they do not correspond to the physical parameters that can be measured in a collider. From this perspective, the fact that our attempts at deriving predictions from QFT

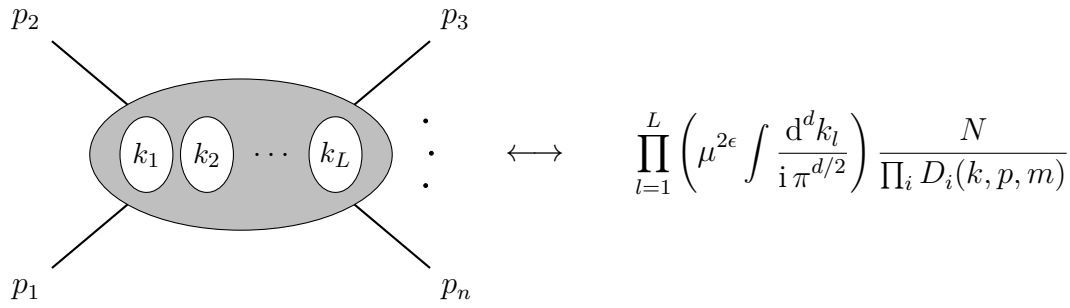

Figure 1.2: An L-loop Feynman diagram corresponds to an L-fold Feynman integral. We continue the integrals from 4 to d dimensions (see Section 1.5.3 for explanation). The numerator N is determined by the Feynman rules of the underlying theory and contains objects such as momenta, spinors and polarisation vectors. The corresponding denominators have the form $D_i = (k_i + q_i)^2 - m_i^2 + \mathrm{i}\varepsilon$, where q_i are linear combinations of external (and potentially internal) momenta and we have explicitly included the pole prescription.

result in an abundance of infinities does not shatter our dreams of having a sensible theory of real-world interactions. One simply needs to move these infinities away from the integrals and into the definitions of the naive, 'bare' couplings. It is conventional to introduce into the Lagrangian so-called counterterms (with their own Feynman rules and diagrams) designed precisely to cancel out divergences up to a given order in perturbation theory. The inclusion of counterterms (which are themselves divergent) is equivalent to shifting the couplings from their bare values to the physical ones. This means that the predictions obtained using the physical parameters will now be UV-finite. To obtain the values of the physical parameters themselves, we need to relate them to some quantity that can be measured in an experiment. This measurement can be performed at an arbitrary energy μ_R, which is known as the renormalisation scale. Then, the relationship between the bare and physical couplings allows us to write down the renormalised expression for the scattering amplitude. Even though the renormalised amplitudes are a function of the physical couplings as measured at some μ_R, the choice of this renormalisation scale is arbitrary and the predictions obtained from the renormalised amplitudes are independent of it.

The renormalisation of QCD has an immediate and astounding consequence. The physical strong coupling constant is not, in fact, a constant, but rather depends on a scale: $\alpha_s \equiv \alpha_s(\mu)$. It is then natural to wonder how the coupling evolves, or 'runs', with this scale. The answer to this question is given by the famous β-function, which in QCD takes the form [17, 18]:

$$\beta(\alpha_s) \equiv \frac{\mathrm{d}\alpha_s}{\mathrm{d}\log\mu^2} = -\sum_{i=0}^{\infty} \beta_i \left(\frac{\alpha_s}{4\pi}\right)^{i+2} . \tag{1.5.1}$$

It is currently known up to five loops [19]. Crucially, the first coefficient is:

$$\beta_0 = \frac{11}{3} C_A - \frac{4}{3} T_F n_f \,, \tag{1.5.2}$$

where n_f is the number of light quarks, i.e. quarks with masses below the scale at which we are probing the system. With $C_A = N_c = 3$ and $T_F = 1/2$, it is clear that $\beta_0 > 0$ as long as $n_f \leq 16$, which is of course the case in our world. Then, the overall minus sign in Eq. 1.5.1 means that, perhaps counterintuitively, α_s *decreases* as we move towards higher energies. This phenomenon is known as **asymptotic freedom** and motivates the factorisation of amplitudes in Eq. 1.3.2. Solving the renormalisation group equation, Eq. 1.5.1, at the lowest order gives:

$$\alpha_s(\mu) = \frac{2\pi}{\beta_0 \log\left(\frac{\mu}{\Lambda_{\text{QCD}}}\right)} \,, \tag{1.5.3}$$

where Λ_{QCD} arises as an integration constant and is the same scale we used in Section 1.3 to separate the perturbative physics of high energies from the non-perturbative PDFs of low energies.

Finally, we mention that not all theories are renormalisable, i.e. to remove all their UV divergences, we would need to add an infinite number of counterterms. Fortunately for us, QCD is indeed renormalisable (as a matter of fact, the entire Standard Model is renormalisable). As such, we can go ahead with our computation of SM scattering amplitudes and be sure that at the end of the day, we will be able to obtain UV-finite predictions. In Appendix C.1, we will demonstrate the UV renormalisation procedure explicitly for the process considered in Chapter 3. For further details of renormalisation and related topics, we refer the reader to any of the standard QFT textbooks.

1.5.2 IR divergences and the KLN theorem

The soft and collinear IR divergences arise not only from the special regimes of the loop momentum k of the virtual particles in Feynman integrals. In fact, the so-called 'real emission' of particles provides complementary singularities. From the experimental perspective, any detector is bound by a certain resolution — it is not able to detect additional particles emitted below a certain energy (soft particles) or distinguish between a group of aligned particles and a single particle carrying the same collective momentum (collinear particles). Regions of phase-space in which this happens lead to divergent phase-space integrals. However, the Kinoshita-Lee-Nauenberg (KLN) theorem guarantees the cancellation of virtual IR singularities by those stemming from real emission in amplitudes with fewer loops [20, 21]. This

happens order by order in perturbation theory, but contrary to the treatment of UV divergences with renormalisation, only at the level of the cross section. Nonetheless, as individual amplitudes are not physical observables, their IR-divergent behaviour before phase-space integration should not seem concerning. We remark that the KLN theorem leaves uncancelled the singularities arising from collinear emissions from the initial-state partons. Collinear particles with transverse momentum below a certain threshold μ_F, known as the factorisation scale, can be absorbed into the 'bare' PDFs $f_i(x)$. This leads to the 'renormalised' PDFs $f_i(x, \mu_F)$ of Eq. 1.3.2 which run with μ_F. For more details, we refer the reader to Sections 7 and 9 of Ref. [22] and to Ref. [6].

The IR pole structure of amplitudes with massless QCD partons (and an arbitrary number of particles with no colour) was originally elucidated in Ref. [23] up to the two-loop level. It was subsequently extended to cover arbitrary loop level in Refs. [24–26]. For a comprehensive review of the topic, we refer the reader to Ref. [27]. Very briefly, it turns out that IR divergences can be obtained from lower-loop amplitudes and appropriate 'pole operators'. We will use this fact in Sections 3.2 and 4.2 to subtract the IR poles from the (already renormalised) two-loop amplitudes for the processes $pp \to b\bar{b}H$ and $pp \to W^{\pm}\gamma j$, such that the leftover quantity is manifestly free of both UV and IR divergences. An explicit derivation of the IR-divergent parts will be given in Appendix C.2.

1.5.3 Dimensional regularisation

At intermediate stages of the computation, i.e. before the cancellation of divergences has taken place, it is useful to have a way of tracking and controlling these divergences. It has become standard practice to regularise both IR and UV divergences by moving away from integrals in $d = 4$ and analytically continuing the dimension to $d = 4 - 2\epsilon$ in a process known as **dimensional regularisation**[1] [30,31]. For virtual corrections, it amounts to replacing each integration measure as:

$$\int \frac{\mathrm{d}^4 k_l}{\mathrm{i}\,\pi^2} \longrightarrow \mu^{2\epsilon} \int \frac{\mathrm{d}^d k_l}{\mathrm{i}\,\pi^{d/2}}\,, \tag{1.5.4}$$

where the arbitrary regularisation scale μ is needed to keep the mass dimension of the coupling constant fixed (it is usually set to μ_R). For real corrections, dimensional regularisation instead modifies the dimensionality of the phase-space integration for the cross section to $d = 4 - 2\epsilon$. Overall, the resultant integrals are now a function of

[1] It is also common to compute integrals around e.g. $d = 6 - 2\epsilon$ or $d = 8 - 2\epsilon$ as they are often IR and/or UV finite. Then, such integrals can be related to the ones in $d = 4 - 2\epsilon$ using dimensional recurrence relations. See Refs. [28, 29] and references therein.

ϵ and the UV/IR divergences appear as poles in their Laurent expansion in ϵ. Any cancellations between terms can then be tracked through this dimensional regulator. Typically, when computing scattering amplitudes we are interested only in terms up to $\mathcal{O}\left(\epsilon^0\right)$ since the four-dimensional result is recovered by setting $\epsilon = 0$ at the end[1].

The continuation of the dimension of the loop momentum to a generic d introduces an ambiguity related to the various states and their polarisation sums. Many choices are possible for how to handle the Dirac algebra in the numerators, leading to multiple regularisation schemes (RS). For example, in the popular 't Hooft-Veltman (HV) scheme which we will use in Chapters 3–5, internal states live in d dimensions, but external states are strictly four-dimensional. It is important to remember that the meaning of 'internal' and 'external' here is not what we would expect intuitively. Fields corresponding to virtual particles (i.e. divergent loop integrals) or to real emission (i.e. soft and collinear singularities in phase-space integrals) are called internal (or singular), while all other fields are called external (or regular). Different RS choices have various advantages, e.g. preserving supersymmetric Ward identities or simplifying the expressions obtained in calculations. We refer the reader to Refs. [32, 33] for an overview of various regularisation schemes and a mathematically rigorous treatment of the spaces in which particles live.

Finally, let us remark that the dimensionally regulated Feynman integrals satisfy the following properties [34]:

- Linearity:

$$\int \mathrm{d}^d k \, [a f_1(k) + b f_2(k)] = a \int \mathrm{d}^d k \, f_1(k) + b \int \mathrm{d}^d k \, f_2(k) \,, \tag{1.5.5a}$$

  where a, b are arbitrary constants.

- Translational invariance:

$$\int \mathrm{d}^d k \, f(k+q) = \int \mathrm{d}^d k \, f(k) \,, \tag{1.5.5b}$$

  where q is an arbitrary vector that can depend on the external momenta p, as well as the loop momenta k (or both).

- Scaling:

$$\int \mathrm{d}^d k \, f(\lambda k) = \lambda^{-d} \int \mathrm{d}^d k \, f(k) \,, \tag{1.5.5c}$$

  where λ is an arbitrary positive constant.

[1] A common exception to this rule is when an $(l < L)$-loop amplitude is meant to be multiplied by the pole operator mentioned above in order to derive the pole structure of the L-loop amplitude. Then, terms beyond $\mathcal{O}(\epsilon^0)$ are required, usually up to $\mathcal{O}(\epsilon^2)$.

For now, we give these properties simply for completeness. However, as we will see in Section 2.8, they will lead to an extremely powerful method of simplifying the computation of scattering amplitudes.

A final note

Finally, we remark that the cross section itself follows a perturbative expansion similar to Eq. 1.4.5:

$$\mathrm{d}\sigma = \alpha^t \left(\mathrm{d}\sigma^{\mathrm{LO}} + \alpha^1 \mathrm{d}\sigma^{\mathrm{NLO}} + \alpha^2 \mathrm{d}\sigma^{\mathrm{NNLO}} + \dots \right) . \tag{1.5.6}$$

It is important to remember that the terms in Eq. 1.4.5 and Eq. 1.5.6 are not in one-to-one correspondence, since an n-particle, $\mathrm{N^kLO}$ cross section might receive contributions from an $(n+i)$-particle, $(k-i)$-loop amplitude, where $0 \leq i \leq k$. From the experimental perspective, real emission of extra soft or collinear particles is indistinguishable from the genuine n-point process. Thus, it needs to be included when calculating the cross section, which introduces singularities that are cancelled out by the virtual corrections coming from diagrams with loops. As an example, the two-loop, five-point amplitudes we compute in Chapter 3 are relevant not only to the process $pp \to b\bar{b}H$ at NNLO, but also to $pp \to b(\bar{b})H$ at $\mathrm{N^3LO}$ (where one b-jet is tagged) and $pp \to H$ at $\mathrm{N^4LO}$.

Overall, it is clear that precision particle phenomenology requires us to push our computational capabilities and include terms of increasingly higher order in Eq. 1.5.6. This in turn means the inclusion of scattering amplitudes with more loops and more legs, but both of these frontiers pose significant challenges. On one side, Feynman integrals with a high number of closed loops are notoriously difficult to evaluate and often lead to special functions that exhibit complicated behaviour and branch cuts. On the other hand, the inclusion of extra particles (or internal masses) means a more complicated kinematic setup, with additional scales that exacerbate algebraic complexity. A tremendous body of work has been done by the community on both fronts. The next chapter is dedicated to a detailed, yet by no means comprehensive, description of the tools used to compute scattering amplitudes. The reward for our effort will be the ability to compute high-multiplicity amplitudes at the cutting edge of knowledge, with direct relevance to precision physics at the LHC and beyond.

Chapter 2

Tools for calculating scattering amplitudes

In this chapter, we focus on various aspects of the computation of loop scattering amplitudes for high-multiplicity processes. It is important to note that there is currently no one-size-fits-all approach that would allow us to compute all the desired amplitudes at a press of a button. In practice, we use a collection of methods that are most appropriate for the task at hand. For processes at the limit of current capabilities, these tools need to be further improved or replaced with novel ideas. To this end, much work has been done by the theory community in recent years. Unfortunately, due to the overwhelming algebraic and analytic complexity, many calculations still present challenges beyond the reach of current technology. The goal of this chapter is to provide an overview of the methods we adopt in amplitude computations, as well as the problems that invariably follow. The procedure involves several highly non-trivial steps. To help the reader retain the 'big picture' of the workflow, we present its schematic outline in Fig. 2.1. Each step is discussed in more detail below.

2.1 Feynman diagrams

The starting point of our amplitude computation for a given process is the generation of all Feynman diagrams contributing to this process at the desired loop order. Feynman diagrams provide a pictorial representation of the ways in which the interaction can occur. At the same time, the corresponding Feynman integrals can be easily recovered using Feynman rules, which can be derived from the Lagrangian of the theory under consideration. As such, these diagrams are an indispensable tool of any perturbative calculation. In practice, it can be observed that usually their number

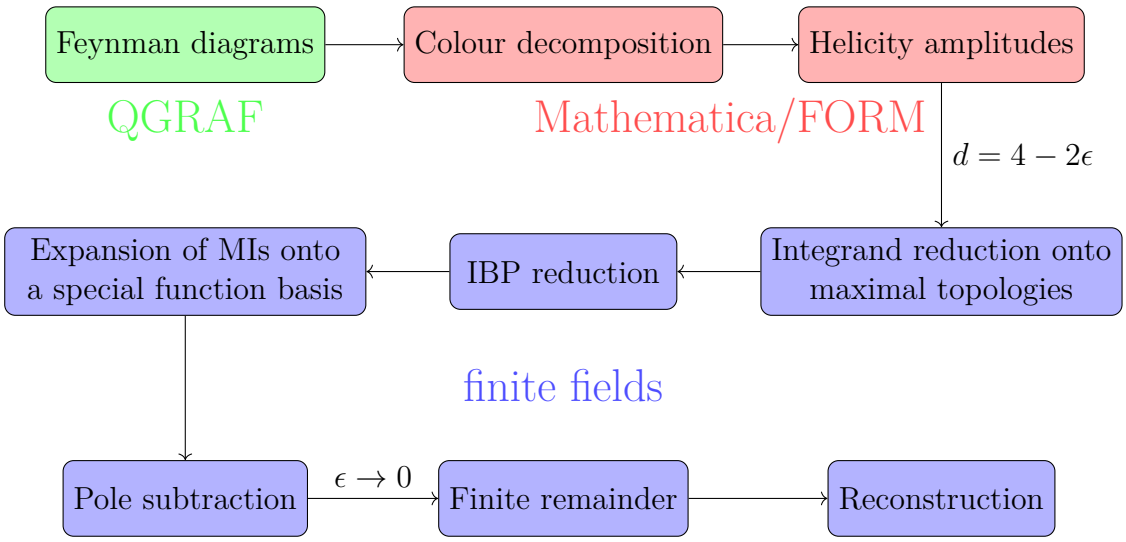

Figure 2.1: A schematic overview of the workflow we adopt to compute scattering amplitudes.

grows faster than exponentially as we increase the loop order or multiplicity (see Table 2.1 for an example). To handle the combinatorial complexity, we generate the relevant Feynman diagrams using `QGRAF` [35]. This programme has the advantage of granting the user a large degree of control over the output. For example, one can constrain it to generate diagrams without self-energy insertions or with a specified total power of the coupling constant.

2.2 Colour decomposition

Having generated the Feynman diagrams, we substitute the Feynman rules for the propagators and vertices using `Mathematica`. At this point, our QCD amplitude contains both colour and kinematic information. The idea of colour ordering is to reorganise the amplitude such that these two components separate: a purely kinematic part is multiplied by the corresponding colour factor. In other words, we perform the decomposition of the full amplitude in colour space, according to a

n	1	2	3	4	5	6	7	8
n gluons	–	–	1	4	25	220	2485	34300
$q\bar{q} + n$ gluons	1	3	16	123	1240	15495	231280	4016775

Table 2.1: Number of tree-level diagrams contributing to selected processes with n gluons.

chosen colour basis. Roughly speaking:

$$\mathcal{A}_n = \sum_i (\text{colour})_i \times A_{n\,i}\,, \tag{2.2.1}$$

where $A_{n\,i}$ are the colour-ordered amplitudes (also known as colour-stripped or partial amplitudes). The motivation behind this decomposition is that the colour-ordered amplitudes turn out to be significantly simpler to calculate.

The choice of the colour basis is not unique. We adopt the decomposition according to traces of the $SU(N_c)$ generators in the fundamental representation. As an example, let us look at 4-gluon scattering at tree-level. The s-channel diagram is:

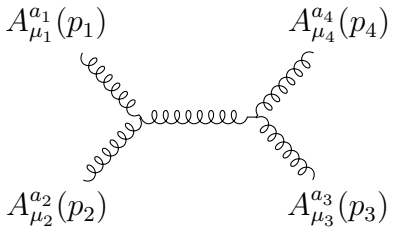

$$\xrightarrow{\text{colour}} f^{a_1 a_2 b} f^{b a_3 a_4}\,. \tag{2.2.2}$$

The colour factor of this diagram can be expressed in terms of the generators using Eqs. 1.2.7 and 1.2.10:

$$\begin{aligned} f^{a_1 a_2 b} f^{b a_3 a_4} = -\frac{1}{T_F}\Big(&\operatorname{tr}[T^{a_1} T^{a_2} T^{a_3} T^{a_4}] - \operatorname{tr}[T^{a_1} T^{a_2} T^{a_4} T^{a_3}] \\ &- \operatorname{tr}[T^{a_1} T^{a_3} T^{a_4} T^{a_2}] + \operatorname{tr}[T^{a_1} T^{a_4} T^{a_3} T^{a_3}]\Big)\,. \end{aligned} \tag{2.2.3}$$

The colour factors of the t- and u-channels can be expressed in a similar way. Combining the contributions from the three channels and using the cyclicity of the trace, we can organise the 4-gluon amplitude at tree-level as follows:

$$\mathcal{A}_4^{(0)} = g_s^2 \left(\operatorname{tr}[T^{a_1} T^{a_2} T^{a_3} T^{a_4}]\, A_4^{(0)}[1234] + \text{permutations of } (234)\right)\,, \tag{2.2.4}$$

where we have factored out $g_s^2 \equiv 4\pi\alpha_s$ for convenience. In the general case, this formula reads:

$$\mathcal{A}_n^{(0)} = g_s^{n-2} \sum_{\sigma \in S_{n-1}} \operatorname{tr}\left[T^{a_1} T^{\sigma(a_2} \dots T^{a_n)}\right] A_n^{(0)}\left[1\,\sigma(2 \dots n)\right]\,, \tag{2.2.5}$$

where the sum is over the set of all *non-cyclic* permutations of $n-1$ particles. Similar colour decompositions can be derived for amplitudes involving quarks, as well as beyond tree level [36]. At loop level, in addition to single-trace structures the colour basis contains products of traces.

The colour-ordered amplitudes A_n are calculated by adding up the kinematic parts of all Feynman diagrams contributing to a given colour factor. They are gauge

invariant and satisfy a number of important identities [37–39]:

$$A_n[123\dots n] = A_n[23\dots n\,1]\,, \qquad \text{cyclicity,} \tag{2.2.6}$$

$$A_n[123\dots n] = (-1)^n A_n[n\dots 321]\,, \qquad \text{reflection,} \tag{2.2.7}$$

$$A_n[123\dots n] + A_n[213\dots n] + A_n[231\dots n] + \dots + A_n[23\dots 1\,n] = 0\,, \quad U(1) \text{ decoupling,} \tag{2.2.8}$$

$$A_n[1,\alpha,n,\beta] = (-1)^{|\beta|} \sum_{\sigma\in OP(\{\alpha\}\cup\{\beta^T\})} A_n[1,\sigma,n]\,, \qquad \text{Kleiss-Kuiff relations.} \tag{2.2.9}$$

In the last line, the sum runs over permutations in the joint set $\{\alpha\}\cup\{\beta^T\}$ such that the order within the individual sets is preserved, and $\{\beta^T\}$ is the reversal of the set $\{\beta\}$. Crucially, these properties allow us to reduce the number of independent amplitudes that need to be computed. In fact, for n-gluon scattering, this number is just $(n-2)!$.

2.3 Helicity amplitudes

After colour decomposition, our colour-ordered amplitude contains purely kinematic information. The kinematic part of the Feynman rules for external states carries information about the spins and polarisations of particles: for massless spin-1/2 fermions, we use $\pm$ helicity states to differentiate between the two solutions to the Dirac equation, while for massless spin-1 bosons, they denote the two polarisation vectors. From the experimental perspective, we are rarely interested in differentiating between the spin states of individual particles. Usually, a beam of particles with random spins undergoes scattering and we look at the total number of products outgoing in a certain direction. Thus, to calculate the corresponding cross section, we should average over the initial spin states and sum over the final ones. This can be achieved in two different ways:

1. Perform the amplitude calculation without specifying the helicity states, then square the amplitude and do the spin sums that appear at the level of $|\mathcal{A}|^2$ using completeness relations of Eqs. 1.1.4 and 1.1.12.

2. Specify the helicity states of external particles, compute each **helicity amplitude** separately, square them and sum over all relevant helicity configurations.

In our approach, we will adopt the latter method. We denote an L-loop helicity amplitude as:

$$\mathcal{A}_n^{(L),\{h\}} \equiv \mathcal{A}_n^{(L)}(1^{h_1}2^{h_2}\dots n^{h_n})\,, \tag{2.3.1}$$

where the superscript $\{h\}$ is understood as the set of helicities h_i of the n particles, but will be usually omitted since we will exclusively compute helicity amplitudes. The full, spin-summed amplitude can then be recovered through:

$$\mathcal{A}_n^{(L)} = \sum_{\substack{\text{helicity} \\ \text{configurations}}} \mathcal{A}_n^{(L),\{h\}} \,. \tag{2.3.2}$$

At the cross section level, we get:

$$\left|\mathcal{A}_n^{(L)}\right|^2 = \sum_{\substack{\text{helicity} \\ \text{configurations}}} \left|\mathcal{A}_n^{(L),\{h\}}\right|^2 \,. \tag{2.3.3}$$

It is important to note that this sum includes only the squares of individual helicity amplitudes — there are no interferences between different helicity configurations.

There are several strong advantages to this approach. Firstly, we can see that the number of terms that need to be processed is significantly smaller than in method (1). Consider the expansion of an amplitude in the coupling constant α up to two loops:

$$\mathcal{A} = \mathcal{A}^{(0)} + \alpha\mathcal{A}^{(1)} + \alpha^2\mathcal{A}^{(2)} + \mathcal{O}\left(\alpha^3\right) \,. \tag{2.3.4}$$

Then, at the level of the cross section, we have the following contributions:

$$|\mathcal{A}|^2 = |\mathcal{A}^{(0)}|^2 \,+\, \alpha\, 2\,\mathrm{Re}\left(\mathcal{A}^{(0)*}\mathcal{A}^{(1)}\right) \,+\, \alpha^2\left(2\,\mathrm{Re}\left(\mathcal{A}^{(0)*}\mathcal{A}^{(2)}\right) + |\mathcal{A}^{(1)}|^2\right) \,+\, \mathcal{O}\left(\alpha^3\right) \,. \tag{2.3.5}$$

Let us also schematically write each L-loop amplitude as a sum of m_L Feynman diagrams: $\mathcal{A}^{(L)} = d_1^{(L)} + d_2^{(L)} + \ldots + d_{m_L}^{(L)}$. Then, at tree level:

$$\left|\mathcal{A}_n^{(0)}\right|^2 = \sum_{\substack{\text{hel.} \\ \text{confs.}}} \left|\mathcal{A}_n^{(0),\{h\}}\right|^2 = \sum_{\substack{\text{hel.} \\ \text{confs.}}} \left|d_1^{(0),\{h\}} + d_2^{(0),\{h\}} + \ldots + d_{m_0}^{(0),\{h\}}\right|^2 \,. \tag{2.3.6}$$

Each term in this sum has all helicities fixed and there are no spin sums to be performed (when evaluated at a chosen phase-space point, it is just a complex number). Thus, the number of terms we need to process at LO is $m_0 n_h$, where n_h is the number of independent helicity configurations. On the other hand, according to method (1), we have:

$$\left|\mathcal{A}_n^{(0)}\right|^2 = \left(d_1^{(0)} + d_2^{(0)} + \ldots + d_{m_0}^{(0)}\right)\left(d_1^{(0)*} + d_2^{(0)*} + \ldots + d_{m_0}^{(0)*}\right) \,, \tag{2.3.7}$$

which means we need to interfere the diagrams with each other and perform the spin sums. Thus, there are m_0^2 terms to be processed. The scaling for higher loop orders is listed in Table 2.2. For small L, the advantage of using helicity amplitudes might be minimal (or in fact, it might be detrimental to do so). For $L \geq 2$, however, the advantage becomes apparent, especially that due to the symmetries of colour-ordered

# terms	$L=0$	$L=1$	$L=2$
Method (1)	m_0^2	$m_0^2+m_0m_1$	$m_0^2+m_0m_1+m_1^2+m_0m_2$
Method (2)	m_0n_h	$(m_0+m_1)n_h$	$(m_0+m_1+m_2)n_h$

Table 2.2: Number of terms to be processed in the computation of the squared amplitude $|\mathcal{A}|^2$ *up to and including* a given loop order, assuming there are m_L diagrams at L loops. The meaning of methods (1) and (2) is explained above Eq. 2.3.1.

amplitudes, n_h is usually much smaller than 2^n. Moreover, it turns out that not all helicity amplitudes are equally challenging to compute, as we will see in the next section. In fact, a host of them vanish altogether (at least at tree level). We remark that guided by experience, it is possible to choose the reference vectors of external polarisations such that the computation of the non-zero amplitudes becomes easier. Helicity amplitudes can also provide us with more information about the scattering process, for example when working with polarised cross sections. In Chapters 4 and 5, we will see how we can use them to attach the decay current of the W boson and an off-shell photon, respectively, to an amplitude with an off-shell leg in order to obtain an amplitude for a fully on-shell process at a higher multiplicity.

When dealing with helicity amplitudes, it is conventional to introduce nomenclature encoding the number of positive/negative helicity particles involved in the process. Consider $2 \to (n-2)$ gluon scattering where the outgoing momenta all have opposite helicities to the incoming ones: $1^-2^- \to 3^+ \dots n^+$. We call such a configuration 'helicity violating'. We can cross particles 1 and 2 to the final state, which changes their helicities: $0 \to 1^+2^+ \dots n^+$. This corresponds to the 'all-plus' amplitude $A_n(1^+2^+ \dots n^+)$ with all momenta outgoing. In the next section, we will show that for gluon scattering at tree-level, this amplitude vanishes for all n. If we flip one helicity in the final state: $1^-2^- \to 3^- \dots n^+$, this corresponds to $A_n(1^+2^+3^-4^+ \dots n^+)$, which also turns out to vanish at tree-level. The first non-zero configuration is $1^-2^- \to 3^-4^- \dots n^+$, which corresponds to: $A_n(1^+2^+3^-4^-5^+ \dots n^+)$. For this reason, amplitudes with exactly two negative helicity particles are called **maximally helicity violating** (MHV). Similarly, amplitudes with exactly two positive helicities are known as anti-MHV. Furthermore, configurations with $2+k$ negative/positive helicities are referred to as N^{k}MHV/anti-N^{k}MHV. Tree-level MHV amplitudes are remarkably simple, as we will demonstrate in the next section.

2.4 Spinor helicity formalism

In Section 1.1, we saw that for massless particles, the Dirac spinor splits into two Weyl spinors that do not mix and are associated with the helicity of the particle. Therefore, we might be tempted to think that helicity amplitudes are better described using a notation specific to the two-component Weyl spinors, which are acted on by the familiar Pauli matrices. Indeed, the powerful spinor-helicity formalism provides a neat way to express helicity amplitudes based on these considerations[1].

As a first step, let us see how we can move from working with the four-component objects to two-component ones. We can write a 'slashed' momentum $\not{p}$ as:

$$\not{p} = p_\mu \gamma^\mu = p_\mu \begin{pmatrix} 0 & (\sigma^\mu)_{a\dot{b}} \\ (\bar{\sigma}^\mu)^{\dot{a}b} & 0 \end{pmatrix} \equiv \begin{pmatrix} 0 & p_{a\dot{b}} \\ p^{\dot{a}b} & 0 \end{pmatrix} , \tag{2.4.1}$$

with both dotted and un-dotted indices running over $\{1, 2\}$ and $(\sigma^\mu)_{a\dot{b}} \equiv (1,\, \sigma^i)$, $(\bar{\sigma}^\mu)^{\dot{a}b} \equiv (1,\, -\sigma^i)$, where σ^i are the three Pauli matrices. The momentum bispinors $p^{\dot{a}b}$ and $p_{a\dot{b}}$ can be thought of as (2×2) matrices and it is easy to show that:

$$\det p_{a\dot{b}} = \det p^{\dot{a}b} = m^2 \, . \tag{2.4.2}$$

For massless particles, this determinant vanishes and the matrix can be expressed as an outer product of two vectors[2]. The vectors we will choose are the momentum space Weyl spinors λ_a and $\tilde{\lambda}_{\dot{a}}$ (sometimes referred to as helicity spinors). They are the two-component, left- and right-handed equivalents of the $u(p)$ and $v(p)$ Dirac spinors with the corresponding helicities $-$ and $+$, respectively. We thus write:

$$p_{a\dot{b}} = \lambda_a \tilde{\lambda}_{\dot{b}} \, , \qquad\qquad p^{\dot{a}b} = \tilde{\lambda}^{\dot{a}} \lambda^b \, , \tag{2.4.3}$$

and the raising and lowering of indices is achieved through:

$$\lambda^a = \epsilon^{ab} \lambda_b \, , \qquad\qquad \tilde{\lambda}^{\dot{a}} = \epsilon^{\dot{a}\dot{b}} \tilde{\lambda}_{\dot{b}} \, , \tag{2.4.4}$$

with the two-dimensional Levi-Civita tensor defined as:

$$\epsilon^{ab} = \epsilon^{\dot{a}\dot{b}} = -\epsilon_{ab} = -\epsilon_{\dot{a}\dot{b}} = \begin{pmatrix} 0 & 1 \\ -1 & 0 \end{pmatrix} . \tag{2.4.5}$$

In practice, it can be rather cumbersome to keep track of the dotted and un-dotted

[1] In case the notation that follows appears daunting, we refer the reader to Ref. [40] for an in-depth discussion of the topic and useful exercises.

[2] The determinant of a matrix is 0 only if its column/row vectors are linearly dependent, which for a (2×2) matrix implies that its rank is 1. A rank-1, $(n \times m)$ matrix can always be expressed as the outer product of two non-zero vectors of length n and m.

indices, as well as their lower or upper positions at the spinors. It is more intuitive to trade this notation for spinor brackets[1]:

$$\begin{aligned} \lambda_a &\to |p]_a\,, & \tilde{\lambda}_{\dot{a}} &\to \langle p|_{\dot{a}}\,, \\ \lambda^a &\to [p|^a\,, & \tilde{\lambda}^{\dot{a}} &\to |p\rangle^{\dot{a}}\,. \end{aligned} \tag{2.4.6}$$

We can then write Eq. 2.4.1 as:

$$\not{p} = |p\rangle\,[p|\,, \qquad \not{p} = |p]\,\langle p|\,, \tag{2.4.7}$$

while the massless Dirac equation becomes the massless Weyl equation:

$$\not{p}|p\rangle = 0, \qquad \not{p}\,|p] = 0\,. \tag{2.4.8}$$

In the above, $\not{p}$ is a small abuse of the 'slashed' notation — what it really means is a contraction of p_μ with σ^μ or $\bar{\sigma}^\mu$, rather than γ^μ. The appropriate Lorentz vector can be chosen by looking at the indices of the square/angle spinors that p^μ is acting on. However, the power of spinor-helicity formalism lies in the fact that in practice, we do not ever need to perform such explicit summation over indices and instead we work with identities at the level of angle and square brackets. Introducing the shorthand notation $|i\rangle \equiv |p_i\rangle$, $|i] \equiv |p_i]$:

$$\langle ij\rangle \equiv \langle i|_{\dot{a}}|j\rangle^{\dot{a}}, \qquad [ij] \equiv [i|^a\,|j]_a\,. \tag{2.4.9}$$

It is straightforward to show that because the indices are raised and lowered using the Levi-Civita symbol, these brackets must be antisymmetric:

$$\langle ij\rangle = -\langle ji\rangle, \qquad [ij] = -[ji]\,. \tag{2.4.10}$$

We can also formulate angle-square or square-angle brackets as follows:

$$\langle ikj] \equiv \langle i|\not{k}\,|j]\,, \qquad [ikj\rangle \equiv [i|\,\not{k}|j\rangle\,. \tag{2.4.11}$$

To choose the right $\not{k}$ from Eq. 2.4.7, we just need to remember that $\langle ik] = [ik\rangle = 0$. These brackets can be extended to arbitrary lengths by inserting additional slashed momenta inside. We note some very useful identities:

$$\langle ii\rangle = [ii] = 0 \qquad \text{by antisymmetry} \tag{2.4.12a}$$

$$s_{ij} = -\langle ij\rangle[ij] \qquad \text{(for massless momenta)} \tag{2.4.12b}$$

$$[ij]^* = \langle ji\rangle \qquad \text{(for real momenta)} \tag{2.4.12c}$$

[1]The choice of assignment of dotted/undotted indices and angle/square brackets to either λ or $\tilde{\lambda}$ is arbitrary. Different conventions are seen throughout literature — the only requirement is internal consistency.

$$\sum_{i=1}^{n} |i]\,\langle i| = \sum_{i=1}^{n} |i\rangle\,[i| = 0 \qquad \text{momentum conservation} \tag{2.4.12d}$$

$$|i\rangle\langle jk\rangle + |j\rangle\langle ki\rangle + |k\rangle\langle ij\rangle = 0 \qquad \text{Schouten identity} \tag{2.4.12e}$$

$$\langle i|\gamma^\mu\,|i] = 2p_i^\mu \qquad \text{Gordon identity} \tag{2.4.12f}$$

$$\langle i|\gamma^\mu\,|j] = [j|\,\gamma^\mu|i\rangle \tag{2.4.12g}$$

$$\langle i|\gamma^\mu\,|j]^* = \langle j|\gamma^\mu\,|i] \qquad \text{(for real momenta)} \tag{2.4.12h}$$

$$\langle i|\gamma^\mu\,|j]\,\langle k|\gamma_\mu\,|l] = -2\langle ik\rangle[jl] \qquad \text{Fierz identity}\,. \tag{2.4.12i}$$

Naturally, the Schouten, Gordon and Fierz identities also hold if we exchange all angle and square brackets. Wherever γ^μ appears, it is understood as either σ^μ or $\bar{\sigma}^\mu$, as explained earlier.

In addition to massless fermions, we need to be able to write the polarisation vectors of massless spin-1 bosons in the spinor-helicity language. They have to obey the following identities:

$$p \cdot \varepsilon_\pm(p,q) = 0\,, \tag{2.4.13a}$$

$$q \cdot \varepsilon_\pm(p,q) = 0\,, \tag{2.4.13b}$$

$$\varepsilon_\pm(p,q) \cdot \varepsilon_\pm(p',q) = 0\,, \tag{2.4.13c}$$

$$\varepsilon_\pm(p,q) \cdot \varepsilon_\mp(p',p) = 0\,, \tag{2.4.13d}$$

$$\varepsilon_\pm^*(p,q) \cdot \varepsilon_\pm(p,q) = -1\,. \tag{2.4.13e}$$

To find compatible expressions for the polarisation vectors, we note that setting $p' = p$ in Eq. 2.4.13c gives $\varepsilon_\pm(p,q)\cdot\varepsilon_\pm(p,q) = 0$. This allows us to decompose ε^μ into an outer product of two vectors, in analogy to Eq. 2.4.3. To this end, we introduce a light-like reference vector q^μ and write:

$$\varepsilon_-^\mu(p,q) = \frac{\langle p|\gamma^\mu\,|q]}{\sqrt{2}[pq]}, \qquad \varepsilon_+^\mu(p,q) = \frac{\langle q|\gamma^\mu\,|p]}{\sqrt{2}\langle qp\rangle}\,. \tag{2.4.14}$$

The choice of the reference vector is arbitrary (apart from the condition $q^\mu \not\propto p^\mu$), which reflects gauge invariance. We can see this by noting that the Weyl spinors are two-component objects and can be decomposed as $|r\rangle = \frac{\langle rq\rangle}{\langle pq\rangle}|p\rangle - \frac{\langle rp\rangle}{\langle pq\rangle}|q\rangle$. Therefore, any shift in q must be of the form $q \to Aq + Bp$, where A, B are constants. Then, from Eq. 2.4.14 (and using Eq. 2.4.12f), it is easy to see that this shift will correspond to $\varepsilon^\mu \to \varepsilon^\mu + Cp^\mu$. For the amplitude to be Lorentz invariant, we need $p_\mu \mathcal{A}^\mu = 0$, where $\mathcal{A}^\mu$ is the amplitude stripped of its polarisation vectors. This is the famous Ward identity for massless gauge bosons, which can be understood as a momentum-space statement of gauge invariance. In practice, it is useful to choose q^μ such that contracting ε^μ with external momenta leads to the formation of vanishing spinor

brackets, thus greatly simplifying the algebra.

At this point, we have all the tools we need to express any amplitude of massless fermions and spin-1 bosons through the angle and square brackets. Its usefulness, however, may not be immediately clear, especially given the notation which at first appears daunting. As a quick demonstration of the power of spinor-helicity formalism, let us consider the special case of 3-particle kinematics. For any three massless momenta satisfying $p_1^\mu + p_2^\mu + p_3^\mu = 0$, we have:

$$\langle 12\rangle[21] = s_{12} = p_3^2 = 0\,. \tag{2.4.15}$$

Thus, either $\langle 12\rangle = 0$ or $[12] = 0$. If we assume $\langle 12\rangle$ is non-vanishing, then by momentum conservation and the massless Weyl equation:

$$\langle 12\rangle[23] = \langle 1|\not{2}\,|3] = -\langle 1|(\not{1} + \not{3})\,|3] = 0\,. \tag{2.4.16}$$

Thus, $[23] = 0$ and in an analogous manner, we can show that $[13] = 0$ as well. Had we assumed $[12] \neq 0$, we would have found that all angle brackets vanish instead:

$$[12] = [13] = [23] = 0 \qquad \text{or} \qquad \langle 12\rangle = \langle 13\rangle = \langle 23\rangle = 0\,. \tag{2.4.17}$$

Therefore, for 3-particle massless kinematics, the amplitude must depend on either square or angle brackets only. However, note that this result makes sense only if we work with complex momenta. Otherwise, through Eq. 2.4.12c, the angle and square brackets are complex conjugates of each other and so both types must vanish simultaneously. Amplitudes constructed from complex momenta are of course not physical, nonetheless they provide a useful building block for higher-point amplitudes in recursive techniques.

2.4.1 Little group scaling

In the previous section, we saw that the freedom in choosing the reference vector q^μ reflects gauge invariance of the amplitude. Here, we will see how another physical principle places strong constrains on the form of helicity amplitudes. We begin by observing that when trading the Weyl spinors for the bracket notation, there is some freedom in how exactly we write down Eq. 2.4.6. That is, note that both $p_{a\dot{b}} = |p]_a \langle p|_{\dot{b}}$ and $p^{\dot{a}b} = |p\rangle^{\dot{a}} [p|^b$ are invariant under the transformation:

$$|i\rangle \to z|i\rangle, \qquad\qquad |i] \to z^{-1}\,|i] \qquad \forall z \in \mathbb{C}\,. \tag{2.4.18}$$

This is known as little group scaling. Each external momentum has its own little group transformation. This implies the following relations for spin-1 massless boson

polarisations in Eq. 2.4.14:

$$\varepsilon_-^\mu(p,q) \to z^2\varepsilon_-^\mu(p,q), \qquad \varepsilon_+^\mu(p,q) \to z^{-2}\varepsilon_+^\mu(p,q)\,. \tag{2.4.19}$$

Note that the polarisation vectors are invariant under such rescalings of the reference momenta. Thus, for scattering of massless particles, the little group scaling of the corresponding amplitude is determined by the helicities of the external particles. Specifically, if we rescale the spinor brackets associated with the momentum p_i, the amplitude scales according to:

$$A_n\left(\ldots,\{p_i,h_i\},\ldots\right) \xrightarrow[|i]\to z_i^{-1}|i]}^{|i\rangle\to z_i|i\rangle} z_i^{-2h_i} A_n\left(\ldots,\{p_i,h_i\},\ldots\right), \tag{2.4.20}$$

where $h_i = \pm\frac{1}{2}$ for fermions and $h_i = \pm 1$ for massless spin-1 bosons. It turns out that this property places a strong constraint on the spinor bracket expression of the amplitude. We will consider tree-level 3-gluon scattering as a basic example. We have already seen that for 3-particle massless kinematics, the amplitude must be written in terms of angle *or* square brackets only, but we do not know the general form of the expression. Let us rescale all three momenta with separate shifts z_1, z_2, z_3 in an MHV configuration. Then:

$$A_3^{(0)}(1^-2^-3^+) \to z_1^2 z_2^2 z_3^{-2} A_3^{(0)}(1^-2^-3^+)\,. \tag{2.4.21}$$

Assuming that this amplitude depends only on angle brackets:

$$A_3^{(0)}(1^-2^-3^+) \propto \langle 12\rangle^{x_{12}}\langle 13\rangle^{x_{13}}\langle 23\rangle^{x_{23}}\,. \tag{2.4.22}$$

We can then substitute Eq. 2.4.18 into Eq. 2.4.22 and compare with the expected scaling, Eq. 2.4.21. Solving for the exponents, we get $\{x_{12}=3, x_{13}=-1, x_{23}=-1\}$. An identical exercise can be performed (assuming square brackets this type) for the anti-MHV amplitude $A_3^{(0)}(1^+2^+3^-)$, leading to an analogous result. Therefore, the 3-point gluon amplitudes are fixed (up to an overall constant) by the special 3-point kinematics and little group scaling:

$$A_3^{(0)}(1^-2^-3^+) = \kappa_1\frac{\langle 12\rangle^3}{\langle 23\rangle\langle 31\rangle}\,, \qquad A_3^{(0)}(1^+2^+3^-) = \kappa_2\frac{[12]^3}{[23][31]}\,. \tag{2.4.23}$$

We also note that flipping all helicities corresponds to exchanging $\langle ij\rangle \leftrightarrow [ji]$ [1]. With a wrong choice of the bracket type in Eq. 2.4.22, one can show by considering the mass dimension of the amplitude that the couplings κ_1 and κ_2 would have to come

[1] Note the reversed order of momenta. Upon a parity transformation, all square brackets are swapped for angle brackets and vice versa, together with their dotted/undotted indices. For example, $\langle ij\rangle = \langle i|_{\dot a}|j\rangle^{\dot a} \leftrightarrow |i]_a\,[j|^a = [j|^a\,|i]_a = [ji] = -[ij]$.

from terms in the Lagrangian that are non-local[1]. We thus reject them as unphysical. Moreover, the same argument can be used to show that the $(---)$ and $(+++)$ configurations must have vanishing amplitudes:

$$A_3^{(0)}(1^-2^-3^-) = 0, \qquad A_3^{(0)}(1^+2^+3^+) = 0\,. \tag{2.4.24}$$

In fact, the simplicity we have seen so far generalises to higher-point gluon amplitudes. With a smart choice of reference vectors, it can be shown that:

$$A_n^{(0)}(1^-2^-\ldots n^-) = 0, \qquad A_n^{(0)}(1^+2^+\ldots n^+) = 0\,, \tag{2.4.25}$$

as well as:

$$A_n^{(0)}(1^+2^-\ldots n^-) = 0, \qquad A_n^{(0)}(1^-2^+\ldots n^+) = 0\,. \tag{2.4.26}$$

The first non-vanishing amplitudes are the MHV/anti-MHV configurations:

$$A_n^{(0)}(1^+2^+\ldots i^-\ldots j^-\ldots n^+) = \frac{\langle ij\rangle^4}{\langle 12\rangle\langle 23\rangle\ldots\langle n1\rangle}\,, \tag{2.4.27}$$

$$A_n^{(0)}(1^-2^-\ldots i^+\ldots j^+\ldots n^-) = (-1)^n\frac{[ij]^4}{[12][23]\ldots[n1]}\,. \tag{2.4.28}$$

This result is known as the Parke-Taylor formula [37,41]. It can be proved inductively using the BCFW recursion relations [42, 43], with the 3-point MHV amplitudes of Eq. 2.4.23 serving as the starting point. Overall, it is now clear that the spinor-helicity formalism, together with little group scaling and locality of the Lagrangian, produce astonishingly compact results for amplitudes which are traditionally calculated as sums of hundreds or thousands of Feynman diagrams.

2.5 Momentum twistors

In the previous section, we have seen that the spinor-helicity formalism provides a convenient framework to describe helicity amplitudes. By using spinor brackets, which are intrinsically tied to helicity, we were able to exploit the properties of the amplitudes to arrive at remarkably neat expressions. Nonetheless, this formalism comes with certain drawbacks. Firstly, note that kinematic identities such as mo-

[1]The mass dimension of $\mathcal{A}_n$ in $d = 4$ is $4 - n$. From Eq. 2.4.7, we see that both $\langle\ \rangle$ and $[\ ]$ must have mass dimension 1. Thus, the constants κ_1 and κ_2 in Eq. 2.4.23 have mass dimension 0, which is consistent with the fact that they must have come from the 3-gluon interaction term in the Lagrangian of Eq. 1.2.2, $\sim A^\mu A^\nu \partial_\mu A_\nu$. Had we assumed incorrect bracket types, both constants would need to have dimension 2. Thus, the corresponding term in the Lagrangian would be $\sim A^\mu A^\nu \frac{\partial_\mu}{\Box} A_\nu$, which is non-local (it describes an interaction whose effects become more important with distance).

mentum conservation are not automatically satisfied by the spinor brackets. We can in theory use the properties listed in Eq. 2.4.12 to arrive at a minimal set of these variables. In practice, however, this proves to be cumbersome, especially for high-multiplicity processes. Moreover, the appearance of square roots complicates our computational setup, which will be made clear in the next section. We would therefore like to have a parametrisation of external kinematics which solves both these problems simultaneously.

In recent years, many amplitude computations have exploited objects known as momentum twistors (MTs) [44–46], which we will now introduce. As the first step, we define dual-space coordinates x_i^μ as:

$$p_i^\mu = x_i^\mu - x_{i+1}^\mu \,. \tag{2.5.1}$$

Using the massless Weyl equation, Eq. 2.4.8, and the 'slashed' notation in the sense of Eq. 2.4.1, it then follows that:

$$[\mu_i| \equiv \langle i|\not{x}_i = \langle i|\not{x}_{i+1} \,, \tag{2.5.2}$$

The new variables allow us to define the momentum twistors Z_i^I:

$$Z_i^I = \begin{pmatrix} |i\rangle \\ [\mu_i| \end{pmatrix} . \tag{2.5.3}$$

where the index I is understood as $I = \{\dot{a}, a\}$. We can also express $[i|$ in terms of Z_i^I. To this end, the dual twistor is defined as:

$$W_i^A = \begin{pmatrix} |\mu_i\rangle \\ [i| \end{pmatrix} = \frac{\epsilon^{ABCD} Z_{(i-1)B} Z_{iC} Z_{(i+1)D}}{\langle i-1, i\rangle\langle i, i+1\rangle} \,, \tag{2.5.4}$$

where ϵ^{ABCD} is the 4-dimensional Levi-Civita symbol. We can then expand this equation and read off the last two components:

$$[i| = \frac{\langle i, i+1\rangle\,[\mu_{i-1}| + \langle i+1, i-1\rangle\,[\mu_i| + \langle i-1, i\rangle\,[\mu_{i+1}|}{\langle i-1, i\rangle\langle i, i+1\rangle} \,. \tag{2.5.5}$$

Each Z_i^I has four components, thus the matrix of all MTs has $4n$ entries for n-particle scattering. However, not all of them are independent. Firstly, MTs are invariant under the 10-dimensional Poincaré group. Additionally, they exhibit the $U(1)$ symmetry as well, for each particle separately. We can see this from Eq. 2.5.2, which implies that under the little group scaling of $|i\rangle \to t_i|i\rangle$, with $t_i \in \mathbb{C}$, the MTs scale as: $Z_i \to t_i Z_i$. At the same time, this transformation does not affect the underlying momentum p_i^μ, thus Z_i are defined projectively. Overall, the number of independent variables needed to generate all Z_i for n-particle scattering is $4n - 10 - n \times 1 = 3n - 10$.

The momentum twistors[1] Z_i, together with their dual equivalents W_i, serve as a useful way to generate numerical phase-space points according to the following recipe:

1. Fill the twistor matrix $Z_i^I,\ i = 1, \ldots, n$ with random rational numbers.
2. Compute the dual twistor matrix W_i^I.
3. Read off spinors $|i\rangle$ and $[i|$.
4. Calculate the momenta according to the Gordon identity, $p^\mu = \frac{1}{2}\,[i|\,\gamma^\mu|i\rangle$.

Phase-space points generated in this manner are complex and rational. We can also populate the twistor matrix with rational functions instead. The corresponding phase-space parametrisation is guaranteed to automatically implement momentum conservation and the Schouten identity. However, there is no algorithmic way of choosing these functions such that the corresponding parametrisation leads to the simplest possible amplitude expressions. We will present several judicious choices in subsequent chapters.

A small drawback of using the MTs is that they lose the phase information carried by the spinor brackets $|i\rangle$ and $[i|$. This is because in reducing the number of independent variables from $4n$ to $3n - 10$, imposing the symmetries essentially fixes the frame in which we evaluate the kinematics. Thus, strictly speaking, only phase-free expressions can be obtained in terms of MTs. On the other hand, each helicity amplitude is a 'phase-full' quantity, thus we need to restore this information at the end of our computation. This can be achieved by multiplying our amplitude written using MTs by any factor with the same phase content as the amplitude, then dividing by the MT expression of this factor. In practice, we most often choose this factor to be the spinor-bracket expression of the tree-level amplitude for the corresponding helicity.

2.6 Finite fields

In the previous section, we have introduced a new, minimal set of independent variables that automatically implement constraints such as momentum conservation. Moreover, they may help us rationalise at least some of the square roots that appear in our kinematics. This was not just an elegant mathematical exercise. It turns out that MTs provide us with a powerful framework that goes hand in hand with yet another tool we employ in amplitude computations.

[1] In amplitude jargon, the term 'momentum twistors' most often refers to the $3n-10$ independent variables, rather than the Z_i's themselves. We will also adopt this terminology below.

2.6.1 Rational numbers

The problem of enormous algebraic expressions plagues almost every calculation in QFT. At the same time, sweeping cancellations often occur, leading to much more compact answers. Indeed, we have already seen how at tree level the MHV gluon amplitudes can be described by remarkably simple expressions, despite the fact that they come from hundreds, if not thousands, of Feynman diagrams. A key idea that has emerged over the past several years is to avoid this complexity at the intermediate stages of the computation by working with numerical expressions instead [47–52]. Crucially, the analytic dependence can still be recovered from the numerics at the very end of the calculation. In this section, we introduce the concept of finite fields and show how it can be used to our advantage.

A finite field is a field with a finite number of elements. We are interested in finite fields of non-negative integers:

$$\mathbb{Z}_n = \{0, \ldots, n-1\}\,, \tag{2.6.1}$$

where n is referred to as the size of the field. In particular, we will work with fields whose size is a large prime number p, as prime fields satisfy many properties which make the corresponding arithmetic especially simple. Basic operations, such as addition, subtraction and multiplication, are defined over $\mathbb{Z}_p$ through the standard modular arithmetic mod p. We can also define a multiplicative inverse $b \in \mathbb{Z}_p$ for all $a \neq 0 \in \mathbb{Z}_p$:

$$a^{-1} \equiv b \mod p \qquad \Longleftrightarrow \qquad ab \equiv 1 \mod p\,. \tag{2.6.2}$$

In fact, the existence of the inverse for all non-zero a is guaranteed only for prime fields. We can see this by considering the following set:

$$S = \{a, 2a, 3a, \ldots, (p-1)a\}\,. \tag{2.6.3}$$

Now, note that for any two integers x, x' such that: $x \not\equiv x' \mod p$, we have:

$$a(x - x') \not\equiv 0 \mod p \qquad\qquad (a \neq 0)\,. \tag{2.6.4}$$

However, this holds only because $\gcd(a, p) = 1$. It follows that the set $S \bmod n$ contains all unique, non-zero elements of $\mathbb{Z}_p$, one of which must be 1. This proves the existence of the multiplicative inverse for all $a \neq 0$ (it can be calculated using the 'extended Euclidean algorithm', see e.g. Ref. [53]). Consequently, we can conclude that rational operations over $\mathbb{Z}_p$ are well-defined. Moreover, it allows us to define a map from rational numbers to the prime field, $\mathbb{Q} \to \mathbb{Z}_p$. For $q = \frac{x}{y} \in \mathbb{Q}$:

$$q \bmod p = \left(x \times (y^{-1} \bmod p\right) \bmod p\,. \tag{2.6.5}$$

This map is not invertible, since it maps infinitely many elements of $\mathbb{Q}$ onto the finite set $\mathbb{Z}_p$. Nonetheless, the rational numbers q can be recovered from their image in $\mathbb{Z}_p$ with a very high probability using Wang's algorithm [54, 55]. This process is referred to as rational reconstruction. We remark that this algorithm is successful if $|x|, |y| < \sqrt{p/2}$. Therefore, p should be chosen sufficiently large so that it is possible to reconstruct all rational numbers appearing in the problem. However, as x, y grow in size, this defeats the purpose of using finite fields in the first place, which was to keep the size of numbers below a certain bound imposed by modular arithmetic mod p. Moreover, from the practical point of view, we want to use the efficiency of machine-size integers, which means we are usually constrained to $p < 2^{64}$. Fortunately, rational numbers exceeding such thresholds can be reconstructed without using prohibitively large prime fields. This is due to the 'Chinese remainder theorem': knowledge of the congruences of an integer x modulo $\{n_1, n_2, \ldots, n_k\}$, where all the n_i are pairwise co-prime, allows us to obtain the congruence of x modulo $n_1 n_2 \ldots n_k$. The same idea holds even for our map $\mathbb{Q} \to \mathbb{Z}_p$. Thus, by calculating several congruences:

$$\begin{aligned} q &\equiv a_{p_1} \mod p_1, \\ q &\equiv a_{p_2} \mod p_2, \\ &\vdots \\ q &\equiv a_{p_k} \mod p_k\,, \end{aligned} \tag{2.6.6}$$

we can obtain:

$$q \equiv a_{p_1 p_2 \ldots p_k} \mod (p_1 p_2 \ldots p_k)\,. \tag{2.6.7}$$

Hence, combining the images of q over several prime fields $\mathbb{Z}_{p_i}$ allows us to use Wang's algorithm on $\mathbb{Z}_{p_1 p_2 \ldots p_k}$ and successfully reconstruct $q \in \mathbb{Q}$.

2.6.2 Rational functions

So far, we have seen how we can exploit finite fields to keep the size of numerical expressions from growing throughout our computation[1]. It should not come as a surprise that this concept can be extended to allow for the reconstruction of not only rational numbers, but also rational functions in multiple variables.

Let us consider the so-called 'black box interpolation problem'. Suppose we have a set of n variables $\mathbf{x} = \{x_1, x_2, \ldots, x_n\}$. These variables will serve as the arguments of a rational function $f(\mathbf{x})$. In general, the analytic form of f is obtained by applying

[1] An alternative approach would be to use floating-point numbers instead of rational numbers, however this would quickly lead to issues with precision.

a series of rational operations on $\mathbf{x}$. We do not know f analytically at any of these steps, however we assume that we have a way of implementing them *numerically* — this is what we call the 'black box'. Specifically, the numerical operations will be done over a prime field $\mathbb{Z}_p$. We start by evaluating the variables $\mathbf{x}$ at random numerical values in $\mathbb{Z}_p$. We then apply the rational operations represented by f, all within the same prime field. After passing through this black box, the result is a number within that field, which we denote as $f(\mathbf{x}) \bmod p$. Therefore, we have obtained one sample point of the analytic result, which corresponds to the initial values we chose for $\mathbf{x}$.

The key idea of finite field methods is that it is possible to reconstruct the full analytic dependence of $f(\mathbf{x})$, with coefficients of x_i in $\mathbb{Q}$, by sampling it in this manner at multiple points. The first step of this procedure is in essence a linear fit problem. Any multivariate rational function can be written as:

$$R(\mathbf{x}) = \frac{\sum_{\boldsymbol{\alpha}} a_{\boldsymbol{\alpha}} \mathbf{x}^{\boldsymbol{\alpha}}}{\sum_{\boldsymbol{\beta}} b_{\boldsymbol{\beta}} \mathbf{x}^{\boldsymbol{\beta}}} \,. \tag{2.6.8}$$

Here, $a_{\boldsymbol{\alpha}}, b_{\boldsymbol{\beta}} \in \mathbb{Z}_p$ are coefficients of the multivariate monomials $\mathbf{x}^{\boldsymbol{\alpha}}$:

$$\mathbf{x}^{\boldsymbol{\alpha}} = \prod_{i=1}^{n} x_i^{\alpha_i} \,, \tag{2.6.9}$$

and $\boldsymbol{\alpha}$ denotes a collective set of exponents $\boldsymbol{\alpha} = \{\alpha_1, \alpha_2, \ldots, \alpha_n\}$. It is also useful to define the total degree of the monomial as the sum of all its exponents:

$$\deg(\mathbf{x}^{\boldsymbol{\alpha}}) \equiv |\boldsymbol{\alpha}| = \sum_{i=1}^{n} \alpha_i \,. \tag{2.6.10}$$

In the context of a rational function, the total degree $\deg_{\max}(f)$ is understood as the maximal total degree of any of its monomials.

With this representation of $f(\mathbf{x})$ in Eq. 2.6.8, we can try to reconstruct its analytic dependence from the numerical samples over the prime field $\mathbb{Z}_p$. In a very naive approach, we would construct the most general ansatz covering all possible monomials up to degree $\deg_{\max}(f)$. We make this explicit by writing the ansatz as:

$$R(\mathbf{x}) = \frac{\sum\limits_{\boldsymbol{\alpha}:\, |\boldsymbol{\alpha}| \leq u} a_{\boldsymbol{\alpha}} \mathbf{x}^{\boldsymbol{\alpha}}}{\sum\limits_{\boldsymbol{\beta}:\, |\boldsymbol{\beta}| \leq v} b_{\boldsymbol{\beta}} \mathbf{x}^{\boldsymbol{\beta}}} \,, \tag{2.6.11}$$

where we have abbreviated the numerator/denominator total degrees as $u = \deg_{\max}(\mathrm{num}(f))$ and $v = \deg_{\max}(\mathrm{den}(f))$. We can then formulate a system of linear equations in $a_{\boldsymbol{\alpha}}, b_{\boldsymbol{\beta}}$ by evaluating both the monomials $\mathbf{x}^{\boldsymbol{\alpha}}$ in the ansatz and the black box function $f(\mathbf{x})$

at chosen values $\mathbf{x}_j$ in $\mathbb{Z}_p$:

$$\sum_{|\boldsymbol{\alpha}|\leq u} a_{\boldsymbol{\alpha}} \mathbf{x}_j^{\boldsymbol{\alpha}} - f(\mathbf{x}_j) \sum_{|\boldsymbol{\beta}|\leq v} b_{\boldsymbol{\beta}} \mathbf{x}_j^{\boldsymbol{\beta}} = 0 \qquad j \in \{1, \ldots, |R(\mathbf{x})|\}\,. \tag{2.6.12}$$

Finding the values of these coefficients requires solving the system using linear algebra methods. In order for the system to close, we need to perform such evaluations on as many sample points as the number of ansatz terms, $|R(\mathbf{x})|$. This is far from optimal, since such a generic ansatz grows rapidly with both the degree as well as the number of variables. In fact, one can show that the number of ansatz terms is [56]:

$$|R(\mathbf{x})| = \binom{u+n}{n} + \binom{v+n}{n}\,. \tag{2.6.13}$$

Since the time complexity of the corresponding Gaussian elimination is $\mathcal{O}\left(|R(\mathbf{x})|^3\right)$, this can prove prohibitively expensive. As an example, in practice we will be dealing with cases such as six-variable functions with $u = 30, v = 10$, which gives $|R(\mathbf{x})| \approx 2 \times 10^6$. Row reducing such a system is simply not feasible. Another complication arises due to the fact that in general, even though the black box operations are implemented numerically over finite fields, obtaining each evaluation of $f(\mathbf{x})$ in the field $\mathbb{Z}_p$ might still take a long time due to the number and complexity of these operations. We refer to this as the 'evaluation time per point'.

Overall, it is clear that if we want to efficiently interpolate a rational function from its evaluations over finite fields, we need to decrease the number of needed sample points. Besides, in most applications the polynomial degrees u and v are not known *a priori*, so it is difficult to construct an ansatz in the first place. Fortunately, we can make use of more elaborate interpolation methods[1]. For univariate polynomials, the strategy is based on Newton's polynomial representation [57]. This method is particularly useful in cases where the total degree is not known, as it allows for the inclusion of higher-degree terms until their coefficients are found to be 0, at which point the iterative procedure terminates. For univariate rational functions, we distinguish between two further cases based on whether the degrees u and v are known or not. If they are known, it turns out that the naive ansatzing described above performs well enough, as for $n = 1$ the ansatz length $|R(x_1)|$ in Eq. 2.6.13 is sufficiently small to allow for efficient row reduction of the system. Finally, if the degrees are not known, the reconstruction strategy is based on a rational generalisation of Newton's polynomial formula known as Thiele's interpolation formula [57].

Multivariate reconstruction from finite fields can be achieved as well. For multivariate polynomials, it is sufficient to apply the univariate Newton's formula recursively.

[1] For a detailed description of these methods and their implementation, see Ref. [47].

That is, a multivariate polynomial $P(\mathbf{x})$ is first treated as a univariate polynomial in x_1 with coefficients that are polynomials in $x_2, x_3, \ldots, x_n$. These coefficients then become the subject of $(n-1)$-variable reconstruction and so forth. Reconstructing multivariate rational functions is significantly more complicated. The strategy is also based on a recursive use of Newton's formula, but with some important modifications. We refer the reader to Refs. [47, 58] for details.

Having completed the interpolation through one of the methods above, the only thing left to do is to recover the monomial coefficients in $\mathbb{Q}$ from their images $a_{\boldsymbol{\alpha}}, b_{\boldsymbol{\beta}} \in \mathbb{Z}_p$ using Wang's algorithm. As explained earlier, if one prime field $\mathbb{Z}_{p_1}$ is not enough, we can always perform the interpolation in another field $\mathbb{Z}_{p_2}$ and combine these results with the Chinese remainder theorem to obtain the interpolation in $\mathbb{Z}_{p_1 p_2}$. In this way, a rational function with arbitrarily large coefficients can be recovered. The reconstruction time can be estimated according to:

$$\text{Reconstruction time} \approx (\text{number of sample points}) \times (\text{evaluation time per point})\,. \tag{2.6.14}$$

It is of great practical importance to reduce both these factors as much as possible, which renders the reconstruction of complicated rational functions possible. We will elaborate on this topic in subsequent chapters.

Let us make three final remarks. Firstly, we emphasise that the reconstructed function is minimal in terms of the numerator and denominator degrees, that is $\gcd\left(\text{num}(f), \text{den}(f)\right) = 1$. Note that this is also needed for the reconstruction ansatz to be unique. Secondly, in our applications we can make the reconstruction problem easier by reducing the number of variables by one. That is, we will usually set $s_{12} = 1$ and recover its analytic dependence *a posteriori* through dimensional analysis. Finally, recall that in the computation of amplitudes, we often have to deal with the presence of square roots in the kinematics associated with the amplitude. This is a problem, because it is not always possible to take a square root of a field element $a \in \mathbb{Z}_p$. Specifically, for a field of size $p > 2$, there are only $(p+1)/2$ so-called quadratic residues, i.e. integers a such that the congruence $x^2 \equiv a \bmod p$ has a solution [59]. This fact is easy to understand as we can actually enumerate all the residues. Note that this equation admits two solutions, since it is equivalent to $(x-b)(x+b) \equiv 0 \bmod p \Longrightarrow x \equiv \pm b \bmod p$, where $b^2 = a$. Thus, the set of solutions $\{b_i\} \in \mathbb{Z}_p$ will lead to distinct quadratic residues only if no two b_i are negatives of each other in the field. This constrains us to the first half of the elements, i.e. $\{0, 1, 2, \ldots, (p-1)/2\}$. Indeed, if we try to add another solution, $(p+1)/2$, it would square to the same residue as $(p-1)/2$, because $b_i^2 \equiv (p-b_i)^2 \bmod p$ and we have

precisely $p - (p+1)/2 \equiv (p-1)/2 \bmod p$. Thus, the full set of distinct residues is:

$$\left\{0^2, 1^2, \ldots, \left(\frac{p-1}{2}\right)^2\right\}. \tag{2.6.15}$$

This fact implies that we can take the square root of a field element almost exactly 50% of the time. One approach to dealing with the other half is to simply reject the points for which the expressions under the square roots do not correspond to residues and repeat the black-box sampling procedure at another point[1]. However, in practice we find it convenient to deal with the square roots in a different manner, which will be explained in detail in Chapters 3 and 4.

Overall, we have seen that any algorithm which can be expressed as a chain of rational operations can be implemented over finite fields. This applies to both pure rational numbers, as well as analytic expressions in the form of rational functions. This turns out to be tremendously useful, since many of the steps required in amplitude computations are precisely such rational transformations. By exploiting the finite field methods, we can entirely circumvent the analytic complexity in the intermediate stages, yet still enjoy the *exact* cancellations that occur, since we are not forced to resort to floating-point numbers. The otherwise insurmountable task of computing a function analytically has been replaced by the much simpler task of providing its fast numerical evaluation over finite fields. Armed with this knowledge, we can move on to the next steps in our procedure.

2.7 Reduction onto maximal topologies

Before we begin, let us briefly summarise what we have learnt so far about our workflow for computing scattering amplitudes (see Fig. 2.1). We started by generating all Feynman diagrams that contribute to a desired loop amplitude. We then decomposed this amplitude in colour space and defined a new object, the colour-ordered amplitude, by considering only the diagrams which contribute to a particular colour factor. We then specified the helicities of external fermions and bosons in the so-called helicity amplitudes. We have learned that not all such amplitudes are equally challenging to compute (in fact, some will vanish or be free of divergences) and due to symmetries, we will not even have to compute all possible helicity configurations. We subsequently decided to employ a language which naturally captures the helicity information of the particles, that is the spinor-helicity formalism. However, we have also seen that it suffers from several drawbacks which can be remediated by one last variable change — into MTs. Not only does this parametrisation of external

[1] It is also possible to adjoin the needed square roots to the finite field, i.e. $\mathbb{Z}_p \to \mathbb{Z}_p(\sqrt{a})$.

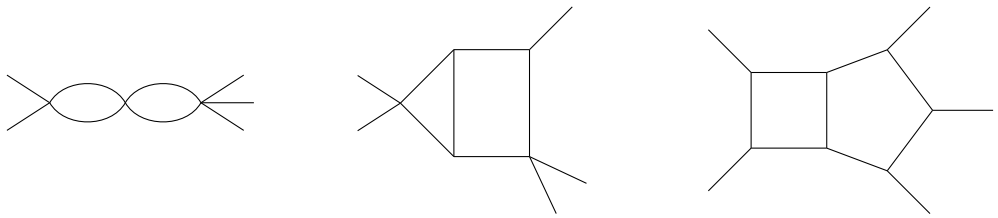

(a) (b) (c)

Figure 2.2: Examples of diagram topologies associated with five-particle Feynman diagrams. It is easy to see that topologies (a) and (b) can be obtained from the maximal topology (c) by pinching some of its propagators.

momenta automatically satisfy kinematic identities of Eq. 2.4.12, but it also allows us to rationalise some of the square roots we need to deal with. Last, but not least, we have also learnt that by performing numerical calculations over finite fields, we can bypass the analytic complexity which typically characterises QFT problems. At this point, the task of computing a colour-ordered helicity amplitude for n-particle scattering amounts to computing loop integrals of the form:

$$A_n^{(L)}\left(1^{h_1}, 2^{h_2}, \ldots, n^{h_n}\right) = \sum_{T\in\text{topologies}} \left[\prod_{l=1}^{L}\left(\mu_R^{2\epsilon}\int \frac{\mathrm{d}^d k_l}{\mathrm{i}\,\pi^{d/2}}\right)\frac{\sum_i c_i(p)\times m_i(k,p)}{\prod_{t\in T} D_t(k,p)}\right]. \tag{2.7.1}$$

The general structure of this formula can be understood simply by considering the QCD Feynman rules and all the possible Lorentz contractions that follow from them. The main sum runs over distinct integral topologies, that is sets of inverse propagators D_t associated with a given Feynman diagram (see Fig. 2.2 for a few examples). Each inverse propagator depends on external momenta p, as well as one or more loop momenta k, which act as the integration variables for the d-dimensional integrals (see Sec. 1.5). In the numerator of each topology, we have a sum of monomials m_i of both loop and external momenta, multiplied by coefficients $c_i(p)$ that depend *only* on the external momenta p. The monomials are composed of scalar products $k_i\cdot k_j$, $k_i\cdot p_j$; as well as the spinor brackets $\langle i|k_i\,|j]$, $\langle i|k_i\,p_M|j\rangle$, $[i|\,k_i\,p_M\,|j]$, where p_M denotes a massive momentum, $p_M^2 = M^2 \neq 0$. Similar objects appear in their coefficients, but because they do not contain any dependence on the loop momenta, we will usually express their external kinematics through the MTs $\mathbf{x} = \{x_1, \ldots, x_{3n-10}\}$, i.e. $c_i(p) \equiv c_i(p(\mathbf{x}))$. This ensures the coefficients are parametrised through a minimal set of variables and can be processed using the finite field framework. In fact, all the remaining steps in our workflow that deal with the computation of the coefficients will be implemented over finite fields.

We point out that not all topologies contributing to each helicity amplitude are independent, in the sense that some topologies can be written as *sub*topologies of

others. This is illustrated in Fig. 2.2. It is clear that topologies (a) and (b) can be viewed as subtopologies of topology (c) with a few propagators absent. Topologies with the maximum number of propagators allowed for L-loop, n-particle kinematics are referred to as maximal topologies. All other topologies can be obtained from them by 'pinching' appropriate propagators. Thus, the next step in our procedure is to express all topologies which contribute to Eq. 2.7.1 as subtopologies of these maximal topologies. Moreover, after this mapping we will seek to write the monomials $m_i(k,p)$ in terms of the inverse propagators of the target maximal topology. In this way, we will remove the loop momentum dependence from the numerators, so that the amplitude will be a linear combination of scalar integrals over the maximal topologies, with rational coefficients of external kinematics parametrised by the MTs.

2.7.1 Parametrising the loop momenta

Let us now discuss the aforementioned reduction of the amplitude onto scalar integrals. The key idea is to decompose the loop momenta in a D-dimensional space spanned by a carefully chosen set of basis vectors. We start by splitting each $k^{(D)}$ into the 4 and (-2ϵ)-dimensional parts:

$$k^{(D)} = k^{(4)} + k^{(-2\epsilon)} \,. \tag{2.7.2}$$

Here and below, we have suppressed the Lorentz index for readability. Let us focus on the 4-dimensional part first. We would like it to be spanned by the 4-dimensional external momenta p_i. However, due to momentum conservation, in an n-particle scattering process only $n-1$ momenta can be linearly independent. Thus, they can span at most an $(n-1)$-dimensional subspace, which we refer to as the 'physical' space (labelled using $\|$). For $n > 4$, the 4-dimensionality of p_i further restricts the number of independent momenta to exactly 4. For $n \leq 4$, the remainder of the 4-dimensional space needs to be completed by constructing $4-(n-1) = 5-n$ 'spurious' vectors (labelled using ω). Their explicit representation is not unique and we are free to choose any vectors satisfying the following orthogonality conditions[1]:

$$\omega_i \cdot p_j = 0 \,, \qquad\qquad \omega_i \cdot \omega_j = 0 \,. \tag{2.7.3}$$

The decomposition in Eq.2.7.2 then becomes:

$$k^{(D)} = k^{(4),\,\|} + k^{(4),\,\omega} + k^{(-2\epsilon)} \,. \tag{2.7.4}$$

[1]It is also common to impose a stronger condition of orthonormality between the spurious space vectors, $\omega_i \cdot \omega_j = \delta_{ij}$. However, this may require us to introduce square roots in their normalisations, leading to problems when using the finite field approach.

The spurious and (-2ϵ)-dimensional spaces taken together are often referred to as the 'transverse' space. All three subspaces appearing in Eq. 2.7.4 are orthogonal to each other, hence we can write:

$$k^{(D)} \cdot k^{(D)} = k^{(4),\,\|} \cdot k^{(4),\,\|} + k^{(4),\,\omega} \cdot k^{(4),\,\omega} + k^{(-2\epsilon)} \cdot k^{(-2\epsilon)} \,. \tag{2.7.5}$$

Overall, we parametrise each loop momentum $k_i^{(D)}$ according to:

$$k_i^{(D)} = \underbrace{\sum_{a=1}^{\min(n-1,\,4)} \alpha_{ia} p_a}_{k_i^{(4),\,\|}} + \underbrace{\sum_{b=1}^{5-n} \beta_{ib} w_b}_{k_i^{(4),\,\omega}} + k_i^{(-2\epsilon)} \,. \tag{2.7.6}$$

To find the parameters α, we take the scalar products of this equation with external momenta. On the LHS, we express the products[1] $k_i^{(D)} \cdot p_j$ in terms of the inverse propagators $D_t(k,p)$ belonging to the maximal topology we have mapped our integral onto. It turns out, however, that in certain cases not all such scalar products can be expressed through the inverse propagators. The remaining products are then referred to as the 'irreducible scalar products' (ISPs). They need to be included in order to define a full integral family. More precisely, a simple counting argument shows that ISPs are needed when [60]:

$$L \geq \max(2, 7 - 2n) \,, \tag{2.7.7}$$

where n and L are the number of legs and loops in a given Feynman diagram. Thus, for self-energy diagrams ($n = 2$), ISPs appear at $L \geq 3$, while for any process with $n \geq 3$, they appear already at $L = 2$. We point out that we will never encounter ISPs at $L = 1$, no matter the number of external legs.

Returning back to Eq. 2.7.6, taking its scalar products with p_j, but also w_j and $k_j^{(D)}$, produces a system of equations linear in α and β, which we can invert to determine these parameters. This step can also be incorporated into the finite field framework, for example using `FiniteFlow`'s linear solver [48]. The parameters α in the physical space are then functions of the inverse propagators and potentially the 'physical ISPs' introduced above, while the parameters β in the spurious space are functions of the 'spurious ISPs', $k_i^{(4),\,\omega} \cdot w_j$. We also introduce a shorthand notation for the scalar products between the (-2ϵ)-dimensional parts of the loop momenta, $\mu_{ij} \equiv -k_i^{(-2\epsilon)} \cdot k_j^{(-2\epsilon)}$. Having determined the free parameters in Eq. 2.7.6, we substitute this loop momentum decomposition into the numerator of the integral.

[1] Since we work in the HV scheme and the spurious space is orthogonal to the physical one, $k_i^{(D)} \cdot p_j = k_i^{(4)} \cdot p_j = k_i^{(4),\,\|} \cdot p_j$.

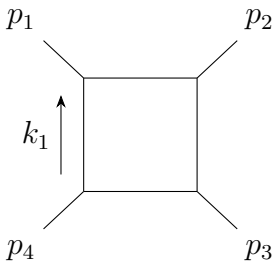

Figure 2.3: One-loop massless box Feynman diagram. The corresponding denominators are given by Eq. 2.7.8.

As an example, consider the one-loop box diagram with massless propagators and external momenta, Fig. 2.3. It has the following inverse propagators $\{D_1, D_2, D_3, D_4\}$:

$$\{k_1^2, (k_1 - p_1)^2, (k_1 - p_1 - p_2)^2, (k_1 + p_4)^2\}\,. \tag{2.7.8}$$

With $L = 1$ and $n = 4$, our parametrisation in Eq. 2.7.6 is:

$$k_1^{(D)} = \alpha_{11} p_1 + \alpha_{12} p_2 + \alpha_{13} p_3 + \beta_{11} \omega_1 + k_1^{(-2\epsilon)}\,. \tag{2.7.9}$$

Taking the scalar products of this equation with p_1, p_2, p_3 and ω_1, we find the following parameters α_{1i} and β_{11}:

$$\begin{aligned}
\alpha_{11} &= -\frac{s_{23}}{2s_{12}s_{13}} D_1 + \frac{s_{13}+s_{23}}{2s_{12}s_{13}} D_2 + \frac{s_{12}-s_{13}}{2s_{12}s_{13}} D_3 - \frac{1}{2s_{13}} D_4 + \frac{s_{23}}{2s_{13}} + 1\,,\\
\alpha_{12} &= \frac{1}{2s_{12}} D_1 - \frac{s_{13}+s_{23}}{2s_{12}s_{23}} D_2 + \frac{s_{12}+s_{13}}{2s_{12}s_{23}} D_3 - \frac{1}{2s_{23}} D_4 + \frac{1}{2}\,,\\
\alpha_{13} &= \frac{1}{2s_{13}} D_1 + \frac{s_{13}-s_{23}}{2s_{13}s_{23}} D_2 - \frac{s_{12}+s_{13}}{2s_{13}s_{23}} D_3 + \frac{s_{12}}{2s_{13}s_{23}} D_4 - \frac{s_{12}}{2s_{13}}\,,\\
\beta_{11} &= \frac{k_1^{(4),\,\omega} \cdot \omega_1}{\omega_1^2}\,.
\end{aligned} \tag{2.7.10}$$

We can then substitute the parametrisation of Eq. 2.7.9 into the numerator monomials associated with any topology that can be expressed as a subtopology of the one-loop box in Fig. 2.3. For example:

$$\begin{aligned}
\langle 1| \not{k}_1^{(D)} |2] &= \sum_{a=1}^{3} \alpha_{1a} \langle 1| \not{p}_a |2] \\
&= \alpha_{13} \langle 13 \rangle [32]\,.
\end{aligned} \tag{2.7.11}$$

The first line follows from the orthogonality properties of the loop momentum decomposition, while in the second we have imposed the massless Weyl equation, Eq. 2.4.8. We then collect the result in D_t, whose coefficients are given by rational functions of external kinematics only. As another example, the square of the loop momentum

will contain the spurious and (-2ϵ) terms:

$$k_1^{(D)} \cdot k_1^{(D)} \ni \frac{\left(k_1^{(4),\omega} \cdot \omega_1\right)^2}{\omega_1^2} - \mu_{11} \,. \tag{2.7.12}$$

Most generally, such substitutions will also lead to the appearance of the physical ISPs, provided the condition in Eq. 2.7.7 is satisfied. Typically, we want to avoid performing the substitution analytically due to the high rank of monomials in Eq. 2.7.1 and the complexity of their coefficients. Fortunately, it can also be performed numerically as an additional step in our finite field workflow.

In summary, the numerators of the Feynman integrals will contain the following four types of terms after we substitute the parametrisations of Eq. 2.7.6 into them: the inverse propagators D_t, the physical ISPs, the spurious ISPs and the extra-dimensional scalar products μ_{ij}. Let us now discuss how to eliminate the last two types. For processes where $n > 4$, the external momenta span the 4-dimensional space and there is no need to introduce the spurious space. In this case, each μ_{ij} can be traded for D_t and the physical ISPs using the orthogonality relation, Eq. 2.7.5. On the other hand, if $n \leq 4$, the spurious ISPs and μ_{ij} can still be eliminated using so-called 'transverse integration'. This can be done in two different ways: one alternative is to perform the transverse integration only in its spurious part, retaining μ_{ij} dependence which can be later removed through dimension-shifting relations [61]. In short, integrals with μ_{ij} can be expressed as integrals of the same kinematic configuration, but in higher dimensions [62]. This can improve their IR behaviour, often leading to integrals which are finite or even vanish in the limit $\epsilon \to 0$. The second alternative is to perform the integration over the full transverse space, i.e. including the spurious *and* the (-2ϵ)-dimensional space. This completely removes the scalar products μ_{ij} from the integrands, albeit at the cost of introducing an explicit dependence on ϵ. In our work, we follow this latter approach, even though it means that our finite field setup will now depend on one more variable, making the analytic reconstruction a bit more complicated. For examples of transverse integration, we refer the reader to Ref. [63], as well as to Sections 3.4 and 3.5 of Ref. [64].

Overall, we are left with only the first two types of terms in the numerators: the inverse propagators D_t associated with the given maximal topology we map our integral onto, as well as the physical ISPs needed to cover any possible scalar product $k_i \cdot p_j$ at this loop order and multiplicity. This completes the definition of an integral family. The D_t terms will of course cancel out with their counterparts in the denominators. What remains are either purely scalar integrals, i.e. with numerators equal to 1, or integrals with numerators built from (monomials of) the physical ISPs.

Any coefficients of such terms will depend on the external kinematics and ϵ only and can be factored outside of the integrals. Once again, we remark that due to our rational parametrisation of external momenta, all the steps described in this section can be seamlessly integrated into the finite field workflow.

2.8 Integration-by-parts relations

Thanks to the effort in the previous section, the helicity amplitudes we need to compute are now expressed as a sum of loop integrals in the following form:

$$A_n^{(L)}\left(1^{h_1}, 2^{h_2}, \ldots, n^{h_n}\right) = \sum_{\substack{T \in \\ \text{maximal} \\ \text{topologies}}} \sum_{\boldsymbol{\nu}} e_{T,\boldsymbol{\nu}}(p(\mathbf{x}), \epsilon) \left[\prod_{l=1}^{L} \left(\mu_R^{2\epsilon} \int \frac{\mathrm{d}^d k_l}{\mathrm{i}\,\pi^{d/2}}\right) \frac{1}{\prod_{t \in T} D_t^{\nu_t}(k,p)}\right] . \tag{2.8.1}$$

Here, we have made the dependence of D_t on the exponents ν_t explicit. As explained earlier, the index t must now run over not only the inverse propagators associated with a given maximal topology, but also the physical ISPs that were introduced to build a complete integral family. Overall, each element in the square brackets is a d-dimensional integral defined by its maximal topology T and a set of exponents $\boldsymbol{\nu}$. We write:

$$I_T^{(L)}(\nu_1, \nu_2, \ldots) = \prod_{l=1}^{L} \left(\mu_R^{2\epsilon} \int \frac{\mathrm{d}^d k_l}{\mathrm{i}\,\pi^{d/2}}\right) \frac{1}{\prod_{t \in T} D_t^{\nu_t}(k,p)} , \tag{2.8.2}$$

where $\nu_t \geq 0$ if D_t is an inverse propagator and $\nu_t \leq 0$ if D_t is an ISP. As one might expect, not all I_T are linearly independent. Within each family, it turns out we can reduce these integrals onto a basis of so-called master integrals (MIs), which we denote as MI_T. The problem of identifying such a basis and computing the reduction coefficients of each I_T onto that basis is one of the most important steps in our workflow. However, it also turns out to be extremely computationally expensive. In the next few sections, we introduce the reader to the concept of integration-by-parts reduction, as well as to the related concepts of differential equations, uniform transcendentality and symbols. These key ideas are crucial not only from the computational perspective, but also provide an insight into the analytic structure of the amplitudes.

2.8.1 A brief introduction to IBP relations

We start by making the following observation: the routing of the loop momentum k in Feynman integrals is arbitrary. It can be shifted by the external momenta or even by another loop momentum (in the case of multi-loop integrals) — the value of

the integral does not change. Surprisingly, this simple fact leads to powerful results. To see this, consider an integrand $f(k)$ and let us shift $k \to k + \lambda q$, where λ is a small constant and q is an arbitrary momentum. First, assume that $q^\mu = p^\mu$. Then, by translational invariance, Eq. 1.5.5b:

$$\int \mathrm{d}^d k\, f(k) = \int \mathrm{d}^d k\, f(k + \lambda p)\,. \tag{2.8.3}$$

Expanding the integrand for small λ, we have:

$$\int \mathrm{d}^d k\, f(k) = \int \mathrm{d}^d k\, \left[f(k) + \lambda p^\mu \frac{\partial f(k)}{\partial k^\mu} + \mathcal{O}\left(\lambda^2\right) \right]. \tag{2.8.4}$$

Thus, at $\mathcal{O}(\lambda)$:

$$\int \mathrm{d}^d k\, \frac{\partial (p^\mu f(k))}{\partial k^\mu} = 0\,, \tag{2.8.5}$$

where we deliberately moved p^μ into the derivative.

In fact, the same equation holds even if $q^\mu = k^\mu$ and the derivation is very similar. In this case, note that due to the scaling relation Eq. 1.5.5c:

$$\int \mathrm{d}^d k\, f(k) = (1+\lambda)^d \int \mathrm{d}^d k\, f(k + \lambda k)\,. \tag{2.8.6}$$

Expanding for small λ:

$$\int \mathrm{d}^d k\, f(k) = \left(1 + \lambda d + \mathcal{O}\left(\lambda^2\right)\right) \int \mathrm{d}^d k\, \left[f(k) + \lambda k^\mu \frac{\partial f(k)}{\partial k^\mu} + \mathcal{O}\left(\lambda^2\right) \right]. \tag{2.8.7}$$

Collecting terms at $\mathcal{O}(\lambda)$:

$$\int \mathrm{d}^d k\, \left[k^\mu \frac{\partial f(k)}{\partial k^\mu} + d\, f(k) \right] = \int \mathrm{d}^d k\, \frac{\partial (k^\mu f(k))}{\partial k^\mu} = 0\,, \tag{2.8.8}$$

where we have moved k^μ into the derivative by using $\partial k^\mu / \partial k^\mu = \delta^\mu_\mu = d$. Eqs. 2.8.5 and 2.8.8 also hold for any linear combination of external and loop momenta. Thus, for a generic q:

$$\int \mathrm{d}^d k\, \frac{\partial (q^\mu f(k))}{\partial k^\mu} = 0\,. \tag{2.8.9}$$

In other words, within dimensional regularisation, the boundary terms vanish. This property is the basis of the so-called integration-by-parts (IBP) relations [65]. The idea is to use Eq. 2.8.9 to generate a system of equations between d-dimensional Feynman integrals $I_T^{(L)}(\nu_1, \nu_2, \ldots)$ of Eq. 2.8.2. Each such identity leads to a relation between integrals within the same integral family T, but with different exponents $\boldsymbol{\nu}$ (for plenty of worked out examples, see Chapter 5 of Ref. [66] or Chapter 6 of Ref. [67]). Therefore, we can use these identities to lower or raise the indices until

we arrive at a simpler integral[1]. Originally, this reduction was done by hand through tedious analysis of all identities. This of course becomes infeasible, since the number of required identities grows quickly with the loop order and number of external particles. On the other hand, modern computations typically employ the Laporta algorithm, which provides an algorithmic way of reducing integrals to MIs by solving a *finite* linear system of identities using Gaussian elimination [69]. Many computer programmes based on the Laporta algorithm — often in combination with other IBP algorithms — are publicly available, e.g. `AIR` [70], `LiteRed` [29, 71], `FIRE` [72, 73], `Kira` [74, 75] and `Reduze` [76, 77].

The IBP system is under-determined, which means that the values of the MIs cannot be determined from it. However, we can express any integral included in the system as a linear combination of these MIs, with their coefficients being rational functions of the kinematics and the dimension d (usually expressed as $d = 4 - 2\epsilon$). The rationality is an important property in the context of our finite field tools in Sec. 2.6. Very often, the growth of coefficients at the intermediate stages of the IBP reduction poses a computational bottleneck. For this reason, it is extremely useful to be able to exploit numerical arithmetic over finite fields in order to bypass this complexity [48].

We remark that in practice it is common to force the algorithm to reduce the families onto a predetermined MI basis. This is because — while the choice of MIs is arbitrary — some choices turn out to be better than others, in the sense that the integrals satisfy certain properties that make them more elegant and also easier to evaluate. We will explore this idea further in Section 2.9. The definitions of such predetermined MIs can be added as additional equations to the IBP system. It is then possible to assign a lower weight to these integrals during Gaussian elimination, which means that they will be preferably chosen as the independent variables [48].

In order to decide which integrals are considered 'simpler', it is useful to define the concept of sectors. A sector $\boldsymbol{\theta} = \{\theta_1, \ldots, \theta_N\}$, where N is the total number of propagators and ISPs in the family, with $\theta_i \in \{0, 1\}$, is the set of points $\boldsymbol{\nu} = \{\nu_1, \ldots, \nu_N\}$ in the lattice $\mathbb{Z}^N$ such that:

$$H\left(\nu_i - \frac{1}{2}\right) = \theta_i \qquad i \in \{1, \ldots, N\}\,, \tag{2.8.10}$$

where $H(x)$ is the Heaviside step function. For example, an integral defined by the indices $\boldsymbol{\nu} = \{1, 0, 2, 1\}$ belongs to the sector $\boldsymbol{\theta} = \{1, 0, 1, 1\}$, while $\boldsymbol{\nu} = \{1, 0, 2, -1\}$ belongs to $\boldsymbol{\theta} = \{1, 0, 1, 0\}$. For the case $N = 2$, it is straightforward to visualise

[1] Let us remark that there exist other kinds of integral identities, such as Lorentz-invariance and homogeneity relations (for details, see Refs. [29, 60, 68]). In fact, they can be shown to be equivalent to linear combinations of the IBP relations. Nonetheless, they can still be useful in practice. They are typically appended to the 'raw' IBP system and make it less under-determined.

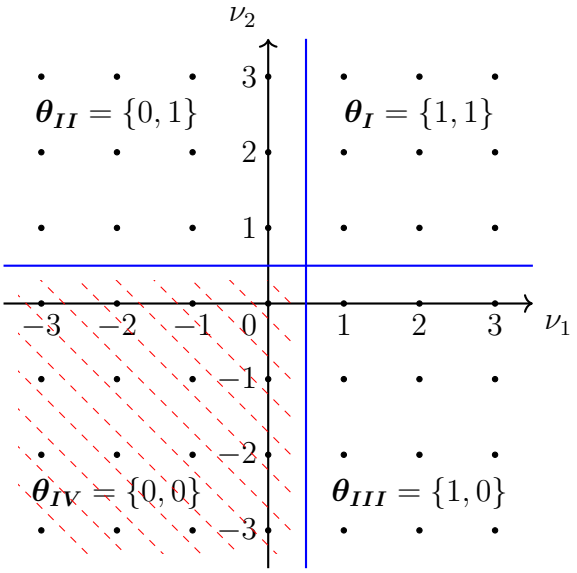

(a) Each point (ν_1, ν_2) in the lattice $\mathbb{Z}^2$ corresponds to the d-dimensional Feynman integral $I(\nu_1, \nu_2)$. The lattice is divided into sectors as defined through Eq. 2.8.10. They are ordered as $\boldsymbol{\theta}_I > \boldsymbol{\theta}_{II}, \boldsymbol{\theta}_{III} > \boldsymbol{\theta}_{IV}$. In particular, sector $\boldsymbol{\theta}_{IV}$ is trivially 0.

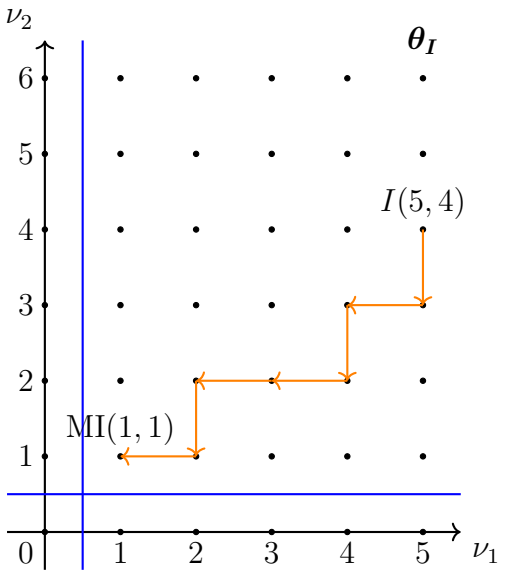

(b) A hypothetical reduction pathway within the top sector $\boldsymbol{\theta}_I$. An integral $I(5,4)$ is reduced to the master integral MI$(1,1)$ through a series of IBP relations lowering the denominator exponents.

Figure 2.4: A lattice of points visualising the integrals and sectors used in the IBP reduction ($N = 2$).

how sectors divide the lattice $\mathbb{Z}^2$ (see Fig. 2.4a). In general, the sector with the maximal number of distinct propagators, i.e. $\boldsymbol{\theta} = \{1, 1, \ldots, 1\}$, is known as the 'top sector', while sectors with progressively more $\theta_i = 0$ become 'subsectors' of the top sector and of each other[1]. The strictly non-positive sector $\boldsymbol{\theta} = \{0, 0, \ldots, 0\}$ vanishes. Furthermore, the point $\boldsymbol{\nu} = \{\theta_1, \ldots, \theta_N\}$ is called the 'corner point' of sector $\boldsymbol{\theta}$. A useful result is that if the integral at the corner point of a sector is 0, then the whole sector is also 0 [68]. It is now possible to order (albeit not uniquely) the sectors $\boldsymbol{\theta}$ with respect to each other, as well as the integrals $I_T(\boldsymbol{\nu})$ within each sector. It is natural to think of sectors with fewer unique denominators as simpler. Thus, $\sum_{i=1}^{N} \theta_i$ defines an ordering between the sectors. In the $N = 2$ example, we say that the sector $\{1, 1\}$ is higher than its subsectors $\{1, 0\}$ and $\{0, 1\}$, which are both higher than their subsector $\{0, 0\}$ (which vanishes anyway). However, sectors $\{1, 0\}$ and $\{0, 1\}$ are equal. Within such equal sectors, we can define further criteria, for example based on the total power of the denominators, followed by the total power of the ISPs, etc. With the help of an arbitrary ordering, we can replace higher $I_T(\boldsymbol{\nu})$

[1]Strictly speaking, in the case of families with ISPs, the top sector will contain a mixture of 0s and 1s, where the zeros are in the position of the ISPs.

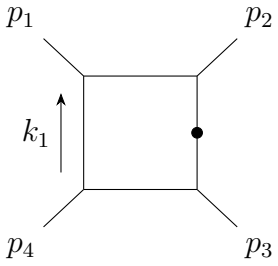

Figure 2.5: One-loop box Feynman diagram $I_{\text{box}}(1,1,2,1)$ with a 'dotted' propagator. The corresponding denominators are: $\{k_1^2, (k_1-p_1)^2, \left((k_1-p_1-p_2)^2\right)^2, (k_1+p_4)^2\}$.

by lower ones through the IBP reduction procedure, as visualised in Fig. 2.4b. It should not be surprising that the set of MIs remaining after this reduction depends on the ordering. We remark that, depending on our needs, it is possible to choose an ordering that leads to an ISP-free basis or conversely a dot-free basis, i.e without propagators raised to powers ≥ 2 (see Fig. 2.5).

Overall, IBP relations allow us to express each helicity amplitude of Eq. 2.8.1 in terms of a much smaller number of integrals:

$$A_n^{(L)}\left(1^{h_1}, 2^{h_2}, \ldots, n^{h_n}\right) = \sum_{i=1}^{|\text{MI}|} g_i(p,\epsilon) \times \text{MI}_i(p,\epsilon)\,, \tag{2.8.11}$$

where |MI| denotes the total number of linearly independent MIs in all the families. Once again, the coefficients are functions of external kinematics, as well as the dimensional regulator ϵ. We emphasise that the step of IBP reducing the integrals involved in the amplitude can also be implemented over finite fields. In particular, the IBP system generated within the Laporta algorithm can be solved using `FiniteFlow`'s linear solver (for details, see Section 5 of [48]). This is an important simplification, since analytic IBP reduction often proves to be the bottleneck of the whole computation.

Moreover, in many applications, we will be dealing with multiple permutations of the maximal topologies appearing in Eq. 2.8.1. In such cases, it is advantageous to implement an optimised strategy for obtaining the IBP solution in the permuted families, which is particularly powerful when used in conjunction with finite field techniques. It allows us to reduce the time and computational cost of the IBP reduction. We invite the reader to familiarise themselves with Appendix A, where we present this strategy in detail. We will exploit it when computing the QED amplitudes of Chapter 5.

2.9 Differential equations

Differential equations (DEs) satisfied by Feynman integrals were studied even before the invention of the IBP reduction technique (see, for example, Refs. [78, 79]). However, it was these two concepts combined together that led to the development of a powerful method for evaluating the MIs [28, 80–83]. The idea is as follows. If we differentiate an integral $I_T(\boldsymbol{\nu})$ with respect to the Mandelstam invariants, s_{ij}, or internal masses, m_i^2, we will obtain a linear combination of integrals within the same family T, but with different exponents $\boldsymbol{\nu}'$. These new integrals $I_T(\boldsymbol{\nu}')$ can then be IBP reduced onto the MIs of family T. Thus, if we apply the differentiation to the MI basis itself, we will obtain a set of first-order partial DEs (one for each kinematic variable). It is convenient to group the MIs as a vector $\overrightarrow{\mathrm{MI}}$. We then have:

$$\frac{\partial \overrightarrow{\mathrm{MI}}}{\partial \lambda} = A_\lambda(\Lambda, \epsilon)\overrightarrow{\mathrm{MI}}\,, \tag{2.9.1}$$

where $\lambda \in \Lambda \equiv \{s_{ij}, m_i^2\}$ are the independent kinematic variables and A_λ is a $(|\mathrm{MI}| \times |\mathrm{MI}|)$ matrix. Its entries are rational functions of Λ and ϵ, which is due to the nature of IBP relations. It is also common to work with the total differential rather than partial derivatives:

$$\mathrm{d}\overrightarrow{\mathrm{MI}} = \sum_\lambda \left(\frac{\partial \overrightarrow{\mathrm{MI}}}{\partial \lambda}\right) \mathrm{d}\lambda\,, \tag{2.9.2}$$

as well as to define:

$$\mathrm{d}A = \sum_\lambda A_\lambda \mathrm{d}\lambda\,. \tag{2.9.3}$$

Then, the system of DEs can be written as:

$$\mathrm{d}\overrightarrow{\mathrm{MI}} = \mathrm{d}A(\Lambda, \epsilon)\,\overrightarrow{\mathrm{MI}}\,. \tag{2.9.4}$$

Naturally, to solve this equation, we also need to provide boundary values. Sometimes, it can be convenient to use the values of MIs at a special kinematic point, for example where one of the variables in Λ vanishes or is equal to another kinematic variable. There, the MIs may become easier to evaluate.

2.9.1 The ϵ-form

In general, solving the DEs satisfied by MIs is hard. Note however, that typically we are interested in only the first few coefficients of the Laurent expansion of Eq. 2.9.4

around $\epsilon = 0$. Consider a change of basis:

$$\overrightarrow{\mathrm{MI}} \to \overrightarrow{\mathrm{MI}}' = B\,\overrightarrow{\mathrm{MI}}\,, \tag{2.9.5}$$

where B is an arbitrary matrix that can depend on Λ and ϵ. Under this transformation, the partial DEs become:

$$\frac{\partial\overrightarrow{\mathrm{MI}}'}{\partial\lambda} = \left(\frac{\partial B}{\partial\lambda}B^{-1} + BA_\lambda B^{-1}\right)\overrightarrow{\mathrm{MI}}'\,. \tag{2.9.6}$$

A key conjecture due to Ref. [84] is that it is always possible to choose B such that:

$$\left(\frac{\partial B}{\partial\lambda}B^{-1} + BA_\lambda(\Lambda,\epsilon)B^{-1}\right) = \epsilon\,\tilde{A}_\lambda(\Lambda)\,. \tag{2.9.7}$$

That is, with an appropriate transformation, the ϵ dependence factorises out of the matrices, which now contain only kinematic dependence. Note, however, that they might contain algebraic (i.e. non-rational) factors such as square roots. Overall, Eq. 2.9.1 becomes:

$$\frac{\partial\overrightarrow{\mathrm{MI}}'}{\partial\lambda} = \epsilon\,\tilde{A}_\lambda(\Lambda)\,\overrightarrow{\mathrm{MI}}'\,, \tag{2.9.8}$$

while Eq. 2.9.4:

$$\mathrm{d}\overrightarrow{\mathrm{MI}}' = \epsilon\,\mathrm{d}\tilde{A}(\Lambda)\,\overrightarrow{\mathrm{MI}}'\,. \tag{2.9.9}$$

This is known as DEs in the 'ϵ-form' [1]. We will henceforth drop the superscript $'$ on the vector of MIs as we will always be dealing with DEs in this form. In particular, Eq. 2.9.9 admits a solution in terms of the path-ordered exponential:

$$\overrightarrow{\mathrm{MI}}(\Lambda,\epsilon) = \mathbb{P}\exp\left(\epsilon\int_\gamma \mathrm{d}\tilde{A}\right)\overrightarrow{\mathrm{MI}}(\Lambda_0,\epsilon)\,, \tag{2.9.10}$$

where $\gamma : [0,1] \to \mathbb{C}^{|\Lambda|}$ is a path in the space of the kinematic invariants, with $\Lambda = \gamma(1)$ and $\Lambda_0 = \gamma(0)$. We remark that the integral is independent of the path taken as long as the two paths can be continuously deformed into each other without crossing the poles of the DEs. Because the solution is expressed through a series expansion of the matrix exponential, it is easy to see that the MIs are obtained as iterated integrals of $\tilde{A}$. Given the Laurent expansion of the MI vector:

$$\overrightarrow{\mathrm{MI}}(\Lambda,\epsilon) = \sum_{k=0}^{\infty}\epsilon^k\,\overrightarrow{\mathrm{MI}}^{(k)}(\Lambda)\,, \tag{2.9.11}$$

[1] Several packages exist for transforming the DEs into the ϵ-form. See `Fuchsia` [85], `Libra` [86], `INITIAL` [87] and `CANONICA` [88]. See also [89] for a comprehensive review of different techniques.

we can insert it into Eq. 2.9.10 and series expand both its sides in ϵ. Then, the order-by-order DE solution becomes:

$$\overrightarrow{\mathrm{MI}}^{(k)}(\Lambda) = \sum_{j=0}^{k} \int_\gamma \underbrace{\mathrm{d}\tilde{A} \cdot \ldots \cdot \mathrm{d}\tilde{A}}_{j \text{ times}} \cdot \overrightarrow{\mathrm{MI}}^{(k-j)}(\Lambda_0)\,. \tag{2.9.12}$$

The integrals:

$$\int_\gamma \mathrm{d}\Omega_1 \cdot \ldots \cdot \mathrm{d}\Omega_j = \int_0^1 \frac{\partial \Omega_j(\gamma(t_j))}{\partial t_j} \mathrm{d}t_j \int_0^{t_j} \frac{\partial \Omega_{j-1}(\gamma(t_{j-1}))}{\partial t_{j-1}} \mathrm{d}t_{j-1} \cdots \int_0^{t_2} \frac{\partial \Omega_1(\gamma(t_1))}{\partial t_1} \mathrm{d}t_1\,, \tag{2.9.13}$$

where $\mathrm{d}\Omega_i$ are exact one-forms, are known as Chen's iterated integrals (CIIs) [90]. We refer the reader to Refs. [91,92] for a thorough discussion of their properties. The empty CII, i.e. Eq. 2.9.13 for $j = 0$, is defined as 1. Finally, we point out that we can assume that the Laurent expansion in Eq. 2.9.11 starts from $\epsilon = 0$, because the DEs are insensitive to a rescaling of the integrals by a factor which does not depend on the kinematics. Thus, the MIs can be normalised to be finite, which moves any potential singularities at $\epsilon = 0$ into their coefficients.

2.9.2 The d log form and Goncharov Polylogarithms

Overall, we see that the MIs at $\mathcal{O}\left(\epsilon^k\right)$ are given by sums of up to k-fold integrals. The integration kernels are determined by the structure of the matrices $\tilde{A}$, which deserves further discussion. Let us consider the singularities of the DEs. It can be shown, for example by studying the Feynman parameter representation, that Feynman integrals cannot contain so-called essential singularities, e.g. singularities of the form $\mathrm{e}^{1/\lambda} = 1+1/\lambda+1/(2!\lambda^2)+\ldots$ at $\lambda = 0$. In particular, for each singularity λ^*, the leading behaviour of Feynman integrals is $\sim (\lambda - \lambda^*)^\alpha$ for some power α. This strongly constrains the form that the corresponding DE matrices can take [93]. Specifically, we expect them to have simple poles of the form $\sim \alpha/(\lambda - \lambda^*)$ for each λ^*. The ϵ-form DEs of Eqs. 2.9.8 and 2.9.9 satisfying this additional 'fuchsian' property are referred to as 'canonical DEs' [1].

Furthermore, in many cases of practical interest, it is possible to construct MI bases which result in DEs in the so-called 'd log form':

$$\mathrm{d}\tilde{A} = \sum_{i=1}^{|\boldsymbol{w}|} a_i \times \mathrm{d}\log w_i\,. \tag{2.9.14}$$

[1] In practice, when constructing canonical DEs, we might encounter spurious double poles or higher. For one-variable problems, they can be algorithmically removed by a suitable basis change which leaves the DEs with only simple poles in this variable. However, for multi-variable problems, it is a conjecture that this can be achieved simultaneously for all variables (see Ref. [89] for details).

Here, w_i are known as 'letters' (note that sometimes the differentials $\mathrm{d}\log w_i$ are referred to as letters instead), while their collection $\boldsymbol{w} = \{w_1, w_2, \ldots\}$ is the 'alphabet'. The matrices a_i contain rational numbers only, free of any kinematic and ϵ dependence. The letters play a central role in the analysis of DEs in the $\mathrm{d}\log$ form, since they control their singularities and determine which class of special functions the MIs are written in terms of. As mentioned before, in general the kinematic dependence of $\tilde{A}$ might no longer be rational, as the transformation Eq. 2.9.5 needed to bring DEs into canonical form might introduce non-rational functions into the definitions of the corresponding canonical MIs. In this case, the letters w_i are algebraic functions of Λ. However, if the form of Eq. 2.9.14 can be reached using rational transformations only, the letters are also rational functions. Then, it is particularly easy to write down the order-by-order solution in Eq. 2.9.12, as the iterated integrals become the well-known Goncharov Polylogarithms (GPLs)[1] [94–96]:

$$G_n(a_1, a_2, \ldots, a_n; x) = \int_0^x \frac{\mathrm{d}t}{t - a_1} G_{n-1}(a_2, \ldots, a_n; t)\,, \tag{2.9.15}$$

with the 'empty' GPL:

$$G_0(; x) = \begin{cases} 0 & \text{if } x = 0\,, \\ 1 & \text{if } x \neq 0\,. \end{cases} \tag{2.9.16}$$

Here, despite the somewhat suggestive notation, the indices a_i do not have to be numbers and are considered fully-fledged arguments of G_n, alongside x. The length of the vector $\vec{a} = (a_1, \ldots a_n)$, i.e. $|\vec{a}| = n$, is called the weight (or depth) of G_n. The GPLs are related to the usual logarithms through:

$$G_n(a, a, \ldots, a; x) = \frac{1}{n!} \log^n \left(1 - \frac{x}{a}\right) \quad \text{if } a \neq 0\,, \tag{2.9.17a}$$

$$G_n(0, 0, \ldots, 0; x) = \frac{1}{n!} \log^n x\,. \tag{2.9.17b}$$

Aside from this special case of GPLs, the complexity of the integration kernels can be estimated by studying the maximal cuts of the relevant Feynman integrals [97–99]. More generally, the letters might not be rational, or the kernels overall might not be of the $\mathrm{d}\log$ form. Then, more complicated functions appear in the solution of the DEs. For example, the presence of internal masses in the Feynman diagrams often leads to Elliptic Multiple Polylogarithms (eMPLs). We refer the reader to Refs. [100–105] for a discussion of eMPLs and also to Refs. [106–108] for a closer look at their application to Higgs+jet production with quark mass dependence.

[1] Also known as Multiple Polylogarithms (MPLs).

2.9.3 Uniform transcendentality

When talking about the canonical DEs, it is also useful to introduce the idea of 'transcendentality'. For an iterated integral f, its transcendental weight $\mathcal{T}$ is simply the number of iterated integrations needed to define f [84]. For example, $\mathcal{T}(\log x) = 1$, while $\mathcal{T}(G_n(a_1, \ldots, a_n; x)) = n$. From this definition, it follows that $\mathcal{T}(f_1 f_2) = \mathcal{T}(f_1) + \mathcal{T}(f_2)$, but note that $\mathcal{T}(f_1 + f_2)$ cannot be defined unless $\mathcal{T}(f_1) = \mathcal{T}(f_2)$. Furthermore, algebraic functions and constants have weight 0. Transcendental constants which can be obtained as values of transcendental functions at algebraic arguments have the corresponding weight, e.g. $\mathcal{T}(\pi) = 1$, since $\log(-1) = \pm \mathrm{i}\,\pi$ and $\mathcal{T}(\mathrm{i}) = \mathcal{T}(-1) = 0$, while $\mathcal{T}(\zeta(n)) = n$, since $\zeta(n) = \mathrm{Li}_n(1)$ (for $n > 1$)[1]. It is also convenient to assign $\mathcal{T}(\epsilon) = -1$. With this choice, it is clear that every term in the solution of Eq. 2.9.10 has the same transcendental weight. This property is referred to as 'uniform transcendentality' (UT). A simple example of a UT function is $f(x) = 1 + \epsilon(\log x + \pi) + \epsilon^2(\log^2 x + G_2(1, 1; x))$, with $\mathcal{T}(f) = 0$. Additionally, UT functions satisfying a more stringent condition:

$$\mathcal{T}(\mathrm{d}f) = \mathcal{T}(f) - 1\,, \tag{2.9.18}$$

are known as 'pure' function. In practice, this means that a pure function cannot contain algebraic factors that are not constant — while they do not affect the transcendental weight of a function, they affect the DE it satisfies[2]. As an example, the function $f(x) = \log(x)/x + \mathrm{i}\pi$ is UT, but not pure. It immediately follows that the iterated integral solution to the ϵ-form DEs is built out of pure functions. The reverse is also true: given a pure basis of MIs, the DEs they satisfy will be in the ϵ-form. In practice, when constructing a MI basis, we can verify the validity of the ϵ-free matrices $\tilde{A}_\lambda$ in Eq. 2.9.8 by checking the following conditions:

$$[\tilde{A}_{\lambda_i}, \tilde{A}_{\lambda_j}] = 0\,, \tag{2.9.19a}$$

$$\partial_{\lambda_i} \tilde{A}_{\lambda_j} - \partial_{\lambda_j} \tilde{A}_{\lambda_i} = 0\,, \tag{2.9.19b}$$

$$\sum_{\lambda \in \Lambda} \lambda\, \tilde{A}_\lambda = \mathrm{diag}([\mathrm{MI}_1], [\mathrm{MI}_2], \ldots)\,, \tag{2.9.19c}$$

where the sum runs over all kinematic scales and $[\mathrm{MI}_i]$ is the mass dimension of MI_i. The first two equations follow from integrability conditions, while the last one follows from Euler's homogeneous function theorem. Finally, we point out an interesting observation on the nature of dimensionally regulated amplitudes (see e.g. Ref. [109]). For a Laurent expanded L-loop amplitude in $d = 4 - 2\epsilon$, it is conjectured that the

[1] Here, $\mathrm{Li}_n(z)$ are the classical polylogarithms, which we discuss in Appendix B.

[2] Note that in literature, the term 'UT' is often implicitly taken to mean 'pure'.

External masses	Type	Topology	Publications
0	planar	penta-box	[110–114]
	non-planar	hexa-box	[113–119]
		double-pentagon	[113, 114, 120]
1	planar	penta-box	[98, 111, 121, 122]
	non-planar	hexa-box	[99, 121, 123, 124]
		double-pentagon	[125]

Table 2.3: Selected works relevant to the computation of two-loop, five-point pure MI bases. All propagators are massless.

$\mathcal{O}\left(\epsilon^k\right)$ term contains functions of transcendental weight up to $2L + k$. For example, to calculate a two-loop amplitude up to $\mathcal{O}\left(\epsilon^0\right)$, we need to supply the MI expansions up to weight 4. It is expected that in $\mathcal{N} = 4$ Super Yang-Mills theory, this bound is saturated, i.e. functions of weight *exactly* $2L + k$ are required.

Overall, pure integrals have played a central role in the derivation and evaluation of MI bases relevant to this thesis, that is bases for processes with a high number of kinematic scales. For future convenience, in Table 2.3 we collect (without claiming to be exhaustive) the publications dealing with the MI bases for two-loop, five-point processes with up to one external mass and massless propagators. Finally, before moving on, we invite the reader to familiarise themselves with the content of Appendix B, which introduces the notion of a 'symbol'. It is yet another concept related to the study of DEs satisfied by Feynman integrals and we aim to show its usefulness through several illustrative examples.

2.10 Evaluating master integrals

After a rather lengthy excursion into the world of IBPs and DEs, let us remind ourselves where we currently stand in the workflow for computing amplitudes presented in Fig. 2.1. Having written down the helicity-dependent numerators of each colour-ordered amplitude, we were faced with the task of integrating an enormous number of tensor integrals that belong to many integral topologies. Then, in Section 2.7, we mapped all these integrals onto integrals within significantly fewer *maximal* topologies. We then built a system of IBP relations for each of these maximal topologies and reduced the integrals further onto a manageable set of MIs. In principle, we can now end the amplitude computation. Our result is written in terms of rational coefficients of external kinematics and ϵ, which are trivial to evaluate over the full phase space, while the MIs that these coefficients multiply are in general functions that are extremely hard to compute analytically and that exhibit

a complicated branch cut structure. As we will see in the next section, there are good reasons why we typically extend our workflow and express the MIs in terms of appropriately chosen special functions. However, it is entirely possible to work with the amplitude at the level of MIs. Indeed, in some cases we have no other choice, since the expansion of the relevant MIs into special functions may not be known. Having phenomenological applications in mind, we list below a few methods which allow us to evaluate these MIs numerically at chosen kinematic points. In fact, we will use the last two in subsequent chapters.

- **Sector decomposition**: This method relies on the parametrisation of integrals in terms of the Feynman parameters and the $\mathcal{U}$ and $\mathcal{F}$ Symanzik polynomials. The integration phase space of the parameters is split into sectors and subsectors based on a relative ordering between the parameters. This allows us to resolve the singularities present in the integrals and place them in simple functions that can be integrated analytically. What remains to be computed are the coefficients of the ϵ poles. They receive contributions from finite integrals only and are computed numerically [126, 127]. There exist several public codes implementing this algorithm [128–131].

- **Expansion by regions**: In this method, the integration domain of the loop momenta is divided into appropriate regions where a certain kinematic quantity is small, e.g. $m_i^2/p_j^2 \ll 1$. For each such limit, the integrand is expanded in the corresponding small parameter and the expansion is truncated at a certain order, resulting in a simpler approximation. The expanded integrands are then integrated over the *full* space of loop momenta. With certain conditions [132], the original integral can be recovered by summing the individual contributions from the various regions [133–137]. For numerical implementation, see Refs. [129, 138–140].

- **Generalised series expansion**: For integrals satisfying a set of DEs, it is possible to integrate these DEs along a one-dimensional line segment[1]. If we know the value of the integrals at one point in the kinematic phase space (i.e. the boundary condition of the DEs) and want to know their value at another point, we construct a path $\gamma(t)$ between them and solve the DEs along it. Thus, the task is reduced to a one-dimensional problem in the parameter t of the path, with all the kinematic invariants set to numerical values. The solution is then obtained by using an ansatz in the form of a series expansion.

[1]We stress that this method is applicable not only to MIs, but to any set of functions satisfying DEs. We will explore this further in Chapter 3.

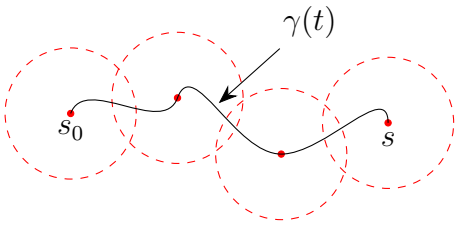

Figure 2.6: A pictorial representation of the generalised series expansion method. We connect the kinematic point $s_0 = \gamma(0)$, at which the solution to the DEs is known, to the target point $s = \gamma(1)$ with a one-parameter path $\gamma(t)$. The path is split into segments as necessitated by singularities. On each segment, we express the solution to the DEs in the form of a series expansion which has a certain radius of convergence (marked by dashed circles). Stitching together the solutions from individual segments allows us to transport the solution from s_0 to s.

Naturally, each such series has a certain radius of convergence within which it is valid. Typically, it is the distance from the centre point of the expansion to the nearest singularity. Thus, in order to obtain the full solution across the entire length of $\gamma(t)$, we split the path into multiple segments and solve the DEs on them one by one. The value of the solution from the previous segment can then serve as a boundary condition for solving the DEs in the subsequent segment [107, 108, 141]. We provide a more intuitive, graphical representation of this idea in Fig. 2.6. Recently, public implementations of this method have been presented in Refs. [142, 143].

- **Auxiliary mass flow**: This method relies on constructing the DEs not with respect to the traditional kinematic invariants, but an auxiliary mass parameter η. The original integrals can then be recovered by solving the η-DEs with $\eta = \infty$ as the boundary condition and letting η 'flow' from ∞ to $i\varepsilon^-$. Crucially, the integrals involved in the boundary condition are simpler than the ones we are aiming for. If these prove still too hard to compute, we can iterate the procedure: set up new η'-DEs for these integrals, obtain the new boundary condition in terms of even simpler integrals, and so on. Eventually, the boundary terms can be expressed in terms of scaleless integrals (which vanish in DR) or single-scale vacuum integrals (which are very simple) [144, 145]. A public implementation of this method has been made available in Ref. [146].

2.11 Special functions and finite remainders

The techniques listed above are very flexible and general. They are not in principle limited to a particular loop order or kinematic configuration, although naturally we expect a drop in performance as we move to more complicated integrals. We also point out that they do not require the MIs to be pure. Overall, following these methods, we are able to evaluate a wide class of integrals. However, the evaluation time is not fast enough for the phenomenological applications of the amplitudes presented in our work. For this reason, we usually resort to a more fine-tuned approach, which we describe below.

After reducing the amplitude onto a small set of MIs, we make use of the available results for these MIs and expand them onto a basis of special functions, which we will denote as $\{f_i(p)\}$ for now, with p indicating the collective dependence on external momenta. These functions could involve, e.g. GPLs, eMPLs or other case-specific functions better suited to a particular computation. More details on this topic will be presented in Sections 3.4, 4.3.6 and 5.4. The expansion of MIs onto $\{f_i(p)\}$ can be easily implemented over the finite fields as a multiplication of the MI coefficients $g_i(p,\epsilon)$ in Eq. 2.8.11 by a matrix encoding these MIs in terms of the special functions. Schematically, we are left with:

$$A_n^{(L)}\left(1^{h_1}, 2^{h_2}, \ldots, n^{h_n}\right) = \sum_i q_i(p,\epsilon) \times \mathrm{mon}_i\Big(\{f_i(p)\}\Big)\,, \tag{2.11.1}$$

where mon_i denote monomials formed from the special functions.

In contrast with the methods described in the previous section, special functions are not a solution that generalises easily, in the sense that their construction is difficult and has to be done case by case. Nonetheless, expanding the amplitude onto a basis of special functions has several advantages. First and foremost, all cancellations and simplifications are manifest, leading to a unique representation of the amplitude. This is an important improvement in the context of the finite field framework, as it means that we will not have to reconstruct additional, 'unphysical' coefficients. It also unveils the analytic structure that is simply hidden within the MI representation. Furthermore, having a basis of special functions grants us a more efficient numerical evaluation of a minimal number of functions. Finally, it allows us to subtract from the amplitude its UV and IR poles and define the so-called 'finite remainder':

$$F^{(L)} = \lim_{\epsilon\to 0}\left(A^{(L)} - P^{(L)}A^{(0)}\right)\,, \tag{2.11.2}$$

where the L-loop pole operator $P^{(L)}$ contains both UV and IR divergences. We stress that $P^{(L)}$ contains contributions from amplitudes at loop orders $l < L$. For a

detailed discussion, we refer the reader to subsequent chapters and Appendix C.

A few words on why we want to work with the finite remainder are in order. Since the UV poles of an amplitude are eliminated in renormalisation, while the IR poles are determined from lower-loop information [23–26], the genuinely new information we compute is contained solely in the non-singular terms. Moreover, the fact of being able to subtract these pre-determined poles from our result, such that we are left with a finite quantity in the limit $\epsilon \to 0$, is in itself already a strong check on the calculation. Finally, it has been observed that finite remainders often exhibit simpler analytic structure than the corresponding full amplitude, with certain special functions dropping out after subtracting the poles. Thus, it is the finite remainder, rather than the amplitude itself, that we take as the end point of our computational algorithm in Fig. 2.1:

$$F_n^{(L)}\left(1^{h_1}, 2^{h_2}, \ldots, n^{h_n}\right) = \sum_i r_i(p) \times \mathrm{mon}_i\Big(\{f_i(p)\}\Big)\,. \tag{2.11.3}$$

Let us make three remarks about the finite remainder. First, we emphasise that it is dependent on the renormalisation, regularisation and IR subtraction schemes. It is important to bear that in mind when cross-checking results or trying to restore the full amplitude from its remainder. Second, the pole subtraction in Eq. 2.11.2 can be straightforwardly implemented over finite fields as a subtraction on the coefficients q_i in Eq. 2.11.1. Third, due to the simplifications that occur during this subtraction, the reconstruction of the finite remainder coefficients r_i is usually easier as compared to the reconstruction of q_i.

While the special functions $\{f_i\}$ that come from the MIs are complicated functions with singularities and branch cuts, the coefficients r_i are rational functions that are computed and reconstructed from finite fields. We remind the reader that they will be usually expressed in terms of the MTs (see Section 2.5). In practical applications at the state of the art, the reconstruction processes can be enormously expensive even on modern CPU clusters. For this reason, we find it unavoidable to implement several tools which simplify the coefficients before we need to reconstruct them. They lower the polynomial degrees and will be covered in detail when discussing the reconstruction strategies in Sections 3.3 and 4.3.4.

We are now ready to take on the computation of scattering amplitudes at the cutting edge of current knowledge. In subsequent chapters, we will use the workflow developed here to tackle two-loop amplitudes for three processes directly relevant to modern particle physics phenomenology.

Chapter 3

Two-loop helicity amplitudes for $pp \to b\bar{b}H$ production

In this chapter, we present the computation of the two-loop QCD helicity amplitudes for the production of a Higgs boson in association with a bottom quark pair at a hadron collider. We take the approximation of leading colour and work in the five flavour scheme, where the bottom quarks are massless while the Yukawa coupling is non-zero. We extract analytic expressions from multiple numerical evaluations over finite fields and present the results in terms of an independent set of special functions that can be reliably evaluated over the full phase space.

The chapter is organised as follows. After providing the necessary background and context in which this work is situated, in Section 3.2 we describe the structure of the $b\bar{b}H$ amplitudes at leading colour, followed by a brief outline of the methodology used in deriving the analytic expression of the amplitudes in Section 3.3. A description of the basis of special functions is presented in Section 3.4 and a number of validations that we performed on the results derived in this work are discussed in Section 3.5. We present benchmark numerical evaluations together with evaluations on a physical phase space slice in Section 3.6. Finally, we draw our conclusions in Section 3.7.

3.1 Introduction

From the perspective of phenomenology, $pp \to b\bar{b}H$ production at the LHC has been a subject of great interest due to its potential in directly measuring the bottom-quark Yukawa coupling y_b. In the SM, the coupling strengths of the Higgs boson to the fermions and vector bosons are proportional to their mass, causing the rate of the $b\bar{b}H$ production to be suppressed with respect to, for example, Higgs production in gluon fusion ($gg \to H$) or vector boson fusion ($pp \to Hjj$), associated production

with a vector boson ($pp \to VH$), and associated production with a top-quark pair ($pp \to t\bar{t}H$). The inclusive $b\bar{b}H$ production cross section is approximately 0.5 pb at 13 TeV, however at least one b-jet needs to be tagged to distinguish this process from inclusive Higgs boson production, which lowers the detected rate by orders of magnitude [147]. Recently, the possibility of isolating the relevant signal from the background using machine learning algorithms has been studied in literature [148, 149].

In some new physics scenarios, such as the Two Higgs Doublet Models (2HDM's) and the Minimal Supersymmetric Standard Model (MSSM), y_b can be dramatically enhanced, resulting in a considerable increase of the $b\bar{b}H$ production rate [150, 151]. Thus, the study of $b\bar{b}H$ production will allow us to constrain supersymmetric models and other extensions of the SM that modify the bottom-quark Yukawa coupling. The ratio of y_b in a new physics scenario to y_b in the SM, $\kappa_b = y_b/y_b^{\text{SM}}$, is currently known to 7% and will be measured more precisely at high-luminosity LHC [152].

The theoretical approach to obtaining predictions for the $pp \to b\bar{b}H$ process has been subject of much discussion in the community. This is due to the fact that, in the presence of bottom quarks, a theoretical prediction can be computed in either the four-flavour scheme (4FS) or the five-flavour scheme (5FS). In the 4FS computation, bottom quarks are treated as massive and they do not contribute to the PDFs, hence only appearing in the final state. Large logarithms of the form $\log(m_b/Q)$ with $Q \propto m_H$ arise when the integration over the bottom-quark phase space is performed, and such contributions may spoil the convergence of the perturbative series. These large logarithms can be resummed to all orders by introducing the bottom quark PDFs. The 5FS approach stems from this prescription, where the bottom quarks are included in the PDFs, allowed to appear in the initial state, and treated as massless. We refer the reader to Ref. [153] for further discussion on the 5FS and 4FS approaches. In 5FS, the inclusive $b\bar{b}H$ production (where the tree level process is $b\bar{b} \to H$) has been computed up to N3LO QCD [154–162], while for the case where a single bottom quark is observed NLO QCD [163], weak [164] and SUSY QCD [165] corrections are available. In 4FS the $b\bar{b}H$ production has been calculated up to NLO QCD [166–171], and the supersymmetric QCD corrections [172, 173] are also known. There have also been efforts in matching the 5FS and 4FS calculations to obtain accurate predictions across the entire kinematic region [174–178]. A first step towards a massive version of the five-flavour scheme (5FMS) has been devised to naturally connect the 4FS and 5FS approaches [179, 180].

In the following, we compute the two-loop QCD corrections to the $gg \to b\bar{b}H$, $q\bar{q}/\bar{q}q \to b\bar{b}H$, $b\bar{b}/\bar{b}b \to b\bar{b}H$, $bb \to bbH$ and $\bar{b}\bar{b} \to \bar{b}\bar{b}H$ reactions in the 5FS. These two-loop amplitudes enter the computation of $pp(b\bar{b}) \to H$ at N4LO, $pp \to b(\bar{b})H$

at N3LO when one b-jet is tagged, and $pp \to b\bar{b}H$ at NNLO when two b-jets are required in the final state. We note that beyond NLO, for the computation with massless bottom quarks, a flavoured jet algorithm [181] would have to be employed when identifying the b-jets, since the use of conventional k_T or anti-k_T jet algorithms would render the fixed order computation infrared unsafe. We further remark that the two-loop amplitudes for $b\bar{b}H$ production derived here can also be used in the computation of Higgs decaying into a bottom quark pair in 5FS, by crossing initial partons to the final state. Specifically, they will contribute in the N4LO $H \to b\bar{b}$, N3LO $H \to b\bar{b}j$ and NNLO $H \to b\bar{b}jj$ computations. In addition, by crossing the $b\bar{b}$ pair to the initial state and the $gg/q\bar{q}$ pair to the final state we obtain the contribution of the bottom quark initiated channel to $H+2j$ production ($b\bar{b} \to Hjj$).

We present analytic results for the finite remainders after both UV and IR poles have been subtracted. This is possible using a basis of special functions recently identified in the context of $Wb\bar{b}$ production [182]. We obtain numerical results valid across the full phase space by applying the generalised series expansion approach [98, 142, 183] to the DEs satisfied by the special functions appearing in the finite remainders.

3.2 Structure of the $pp \to b\bar{b}H$ Amplitudes at Leading Colour

We compute the two-loop QCD corrections in the leading colour approximation for the following subprocesses:

$$0 \to \bar{b}(p_1) + b(p_2) + g(p_3) + g(p_4) + H(p_5)\,, \tag{3.2.1}$$

$$0 \to \bar{b}(p_1) + b(p_2) + \bar{q}(p_3) + q(p_4) + H(p_5)\,, \tag{3.2.2}$$

$$0 \to \bar{b}(p_1) + b(p_2) + \bar{b}(p_3) + b(p_4) + H(p_5)\,, \tag{3.2.3}$$

where all momenta are taken as outgoing:

$$\sum_{i=1}^{5} p_i = 0\,. \tag{3.2.4}$$

We work in the 5FS, where the bottom quark is taken as massless while its Yukawa coupling to the Higgs boson is kept finite, so that:

$$p_1^2 = p_2^2 = p_3^2 = p_4^2 = 0\,, \qquad p_5^2 = m_H^2\,, \tag{3.2.5}$$

where m_H is the mass of the Higgs boson. The kinematics is described by six independent scalar products, which we choose as:

$$(s_{12}, s_{23}, s_{34}, s_{45}, s_{15}, p_5^2)\,,$$

with $s_{ij} = (p_i+p_j)^2$. It is also possible to form pseudo-scalar invariants by contracting the Levi-Civita symbol $\epsilon_{\mu\nu\rho\sigma}$ with any four external momenta. The five-particle kinematics is therefore fully determined by the scalar invariants above and by one pseudo-scalar invariant, which captures all the space-time parity information of the phase space. We choose:

$$\mathrm{tr}_5 = 4i\epsilon_{\mu\nu\rho\sigma}p_1^\mu p_2^\nu p_3^\rho p_4^\sigma = [12]\langle 23\rangle[34]\langle 41\rangle - \langle 12\rangle[23]\langle 34\rangle[41]\,. \tag{3.2.6}$$

It is related to the scalar invariants through:

$$\mathrm{tr}_5^2 = \Delta_5 := \det\left(2p_i\cdot p_j\right)\Big|_{i,j=1,\ldots,4}\,, \tag{3.2.7}$$

where the right-hand side is a degree-four polynomial in the scalar invariants.

The colour decomposition of the L-loop amplitudes in the leading colour approximation is given by:

$$\begin{aligned}
\mathcal{A}^{(L)}(1_{\bar{b}},2_b,3_g,4_g,5_H) &= n^L g_s^2 y_b\left[(T^{a_3}T^{a_4})_{i_2}^{\ \bar{i}_1}\,A^{(L)}(1_{\bar{b}},2_b,3_g,4_g,5_H) + (3\leftrightarrow 4)\right],\\
\mathcal{A}^{(L)}(1_{\bar{b}},2_b,3_{\bar{q}},4_q,5_H) &= n^L g_s^2 y_b \delta_{i_4}^{\ \bar{i}_1}\delta_{i_2}^{\ \bar{i}_3}\,A^{(L)}(1_{\bar{b}},2_b,3_{\bar{q}},4_q,5_H)\,, \qquad (3.2.8)\\
\mathcal{A}^{(L)}(1_{\bar{b}},2_b,3_{\bar{b}},4_b,5_H) &= n^L g_s^2 y_b\Big[\delta_{i_4}^{\ \bar{i}_1}\delta_{i_2}^{\ \bar{i}_3}\left(A^{(L)}(1_{\bar{b}},2_b,3_{\bar{q}},4_q,5_H) + A^{(L)}(3_{\bar{b}},4_b,1_{\bar{q}},2_q,5_H)\right)\\
&\quad - \delta_{i_2}^{\ \bar{i}_1}\delta_{i_4}^{\ \bar{i}_3}\left(A^{(L)}(1_{\bar{b}},4_b,3_{\bar{q}},2_q,5_H) + A^{(L)}(3_{\bar{b}},2_b,1_{\bar{q}},4_q,5_H)\right)\Big],
\end{aligned}$$

where $n = m_\epsilon\alpha_s/(4\pi)$, $\alpha_s = g_s^2/(4\pi)$, $m_\epsilon = \mathrm{i}(4\pi)^\epsilon \mathrm{e}^{-\epsilon\gamma_E}$, T^a are the fundamental generators of $SU(N_c)$ normalised such that $\mathrm{tr}(T^aT^b) = \delta^{ab}$, while g_s and y_b are the strong coupling constant and bottom-quark Yukawa coupling, respectively. We further decompose the partial amplitudes at one and two loops based on their closed fermion loop contributions:

$$A^{(1)} = N_c A^{(1),1} + n_f A^{(1),n_f}\,, \tag{3.2.9}$$

$$A^{(2)} = N_c^2 A^{(2),1} + N_c n_f A^{(2),n_f} + n_f^2 A^{(2),n_f^2}\,, \tag{3.2.10}$$

where n_f is the number of light quarks circulating in the loop. Sample diagrams for various closed fermion loop contributions at one and two loops are presented in Figs. 3.1 and 3.2. The Feynman diagrams with the Higgs boson directly coupled to a closed bottom-quark loop vanish since, for a massless bottom-quark, they contain

Figure 3.1: Sample Feynman diagrams corresponding to the various closed fermion loop contributions at one loop as specified in Eq. 3.2.9. Black-dashed, red, black-spiralled and black lines represent Higgs bosons, bottom quarks, gluons and light quarks (bottom quarks included), respectively.

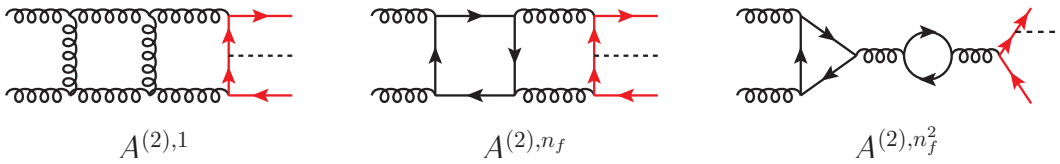

Figure 3.2: Sample Feynman diagrams corresponding to the various closed fermion loop contributions at two loops as specified in Eq. 3.2.10. Black-dashed, red, black-spiralled and black lines represent Higgs bosons, bottom quarks, gluons and light quarks (bottom quarks included), respectively.

a Dirac trace with an odd number of γ matrices. In our computation we do not consider the closed top-quark loop contribution.

The pole structure of the unrenormalised amplitudes in the HV scheme at one and two loops is given by [23–26]:

$$P^{(1)} = 2I^{(1)}(\epsilon) + \frac{\beta_0}{\epsilon} - 2s_1, \tag{3.2.11}$$

$$P^{(2)} = 2I^{(1)}(\epsilon)\left(\hat{A}^{(1)} - \frac{\beta_0}{\epsilon} + 2s_1\right) + 4I^{(2)}(\epsilon) + \left(\frac{2\beta_0}{\epsilon} - 2s_1\right)\hat{A}^{(1)} - \frac{\beta_0^2}{\epsilon^2} + \frac{\beta_1}{2\epsilon} - 4s_2 + \frac{2s_1\beta_0}{\epsilon}, \tag{3.2.12}$$

where $\hat{A}^{(1)}$ is the unrenormalised one-loop amplitude normalised to the tree-level amplitude. s_1 and s_2 are the bottom-quark Yukawa renormalisation constants, and their expressions can be found in Appendix D. We used a mixed renormalisation scheme where the strong coupling α_s and the bottom-Yukawa coupling y_b are renormalised in the $\overline{\text{MS}}$ scheme, while the bottom-quark mass and wave function are renormalised in the on-shell (OS) scheme. This allows to keep y_b finite while taking the bottom-quark mass smoothly to zero ($m_b^{\text{OS}} \to 0$) [162]. Such a mixed renormalisation scheme can be used so long as pure QCD corrections are considered. In fact, using the $\overline{\text{MS}}$ scheme to renormalise y_b allows us to better control the convergence

of the perturbative corrections by resumming the large logarithms that appear in the OS scheme by running y_b to a scale close to the Higgs mass. In the presence of electroweak (EW) corrections, however, the relationship between y_b and m_b must be imposed to guarantee the cancellation of UV singularities [147].

The $I^{(2)}(\epsilon)$ operator is defined by:

$$I^{(2)}(\epsilon) = -\frac{1}{2} I^{(1)}(\epsilon) \left[I^{(1)}(\epsilon) + \frac{\beta_0}{\epsilon} \right] + \frac{N(\epsilon)}{N(2\epsilon)} \left[\frac{\beta_0}{2\epsilon} + \frac{\gamma_1^{\text{cusp}}}{8} \right] I^{(1)}(2\epsilon) + H^{(2)}(\epsilon)\,, \tag{3.2.13}$$

while the $I^{(1)}(\epsilon)$ operators for $b\bar{b}H$ production in both the gg and the $q\bar{q}$ channels are given at leading colour by:

$$I^{(1)}_{\bar{b}bq\bar{q}H}(\epsilon) = -N_c \frac{N(\epsilon)}{2} \left(\frac{1}{\epsilon^2} + \frac{3}{2\epsilon} \right) \left[(-s_{23})^{-\epsilon} + (-s_{14})^{-\epsilon} \right], \tag{3.2.14}$$

$$I^{(1)}_{\bar{b}bggH}(\epsilon) = -N_c \frac{N(\epsilon)}{2} \left\{ \left(\frac{1}{\epsilon^2} + \frac{3}{4\epsilon} + \frac{\beta_0}{4N_c\epsilon} \right) \left[(-s_{23})^{-\epsilon} + (-s_{14})^{-\epsilon} \right] + \left(\frac{1}{\epsilon^2} + \frac{\beta_0}{2N_c\epsilon} \right) (-s_{34})^{-\epsilon} \right\}, \tag{3.2.15}$$

where $N(\epsilon) = \mathrm{e}^{\epsilon\gamma_E}/\Gamma(1-\epsilon)$, $s_{14} = s_{23} - s_{15} - s_{45} + p_5^2$ and:

$$H^{(2)}_{\bar{b}bq\bar{q}H}(\epsilon) = \frac{1}{16\epsilon} \left\{ 4\gamma_1^q - \gamma_1^{\text{cusp}} \gamma_0^q + \frac{\pi^2}{4} \beta_0 \gamma_0^{\text{cusp}} C_F \right\}, \tag{3.2.16}$$

$$H^{(2)}_{\bar{b}bggH}(\epsilon) = \frac{1}{16\epsilon} \left\{ 2\left(\gamma_1^q + \gamma_1^g\right) - \frac{1}{2}\gamma_1^{\text{cusp}} \left(\gamma_0^q + \gamma_0^g\right) + \frac{\pi^2}{8} \beta_0 \gamma_0^{\text{cusp}} \left(C_F + C_A\right) \right\}. \tag{3.2.17}$$

The β function coefficients and anomalous dimensions are given in Appendix D, while in Appendix C we provide an explicit derivation of the pole operators.

The finite remainder of the L-loop partial amplitude is obtained by subtracting the poles $P^{(L)}$ (which include both the UV and IR singularities) from the unrenormalised partial amplitude $A^{(L)}$ and setting ϵ to 0:

$$F^{(L)} = \lim_{\epsilon \to 0} \left[A^{(L)} - P^{(L)} A^{(0)} \right]. \tag{3.2.18}$$

The partial finite remainders $F^{(L)}$ inherit from the partial amplitudes the decomposition in powers of n_f:

$$F^{(1)} = N_c F^{(1),1} + n_f F^{(1),n_f}\,, \tag{3.2.19}$$

$$F^{(2)} = N_c^2 F^{(2),1} + N_c n_f F^{(2),n_f} + n_f^2 F^{(2),n_f^2}\,. \tag{3.2.20}$$

The full finite remainders $\mathcal{F}^{(L)}$ are obtained from the partial ones $F^{(L)}$ through a colour decomposition analogous to that given in Eq. 3.2.8 for the bare amplitudes:

$$\mathcal{F}^{(L)}(1_{\bar{b}}, 2_b, 3_g, 4_g, 5_H) = n^L g_s^2 y_b \left[(T^{a_3} T^{a_4})_{i_2}^{\bar{i}_1} F^{(L)}(1_{\bar{b}}, 2_b, 3_g, 4_g, 5_H) + (3 \leftrightarrow 4) \right],$$

$$\mathcal{F}^{(L)}(1_{\bar{b}},2_b,3_{\bar{q}},4_q,5_H) = n^L g_s^2 y_b \delta_{i_4}^{\bar{i}_1}\delta_{i_2}^{\bar{i}_3}\, F^{(L)}(1_{\bar{b}},2_b,3_{\bar{q}},4_q,5_H)\,, \tag{3.2.21}$$

$$\begin{aligned}\mathcal{F}^{(L)}(1_{\bar{b}},2_b,3_{\bar{b}},4_b,5_H) = n^L g_s^2 y_b \Bigg[&\delta_{i_4}^{\bar{i}_1}\delta_{i_2}^{\bar{i}_3}\left(F^{(L)}(1_{\bar{b}},2_b,3_{\bar{q}},4_q,5_H) + F^{(L)}(3_{\bar{b}},4_b,1_{\bar{q}},2_q,5_H)\right)\\ &- \delta_{i_2}^{\bar{i}_1}\delta_{i_4}^{\bar{i}_3}\left(F^{(L)}(1_{\bar{b}},4_b,3_{\bar{q}},2_q,5_H) + F^{(L)}(3_{\bar{b}},2_b,1_{\bar{q}},4_q,5_H)\right)\Bigg]\,.\end{aligned}$$

3.2.1 Tree-Level Amplitudes

The tree-level amplitudes can be obtained using the BCFW recursion relations [42,43] within the spinor helicity formalism. In the $\bar{b}bggH$ case, we choose to shift the momenta of gluons 3 and 4, while in the $\bar{b}b\bar{q}qH$ case we choose particles 1 and 4 to avoid shifting the momenta of adjacent quarks of the same flavour. Moreover, we ensure that the shifted brackets $[\hat{i}\rangle, |\hat{j}]$ do not belong to particles of helicities i^-, j^+. These choices are necessary for the validity of the recursion relations as they prevent the shifted amplitude from having poles at infinity.

For the $\bar{b}bggH$ channel we obtain the following non-vanishing tree-level amplitudes:

$$\begin{aligned}A^{(0)}(1_{\bar{b}}^+,2_b^+,3_g^+,4_g^+,5_H) &= \frac{s_5}{\langle 23\rangle\langle 34\rangle\langle 41\rangle}\,,\\ A^{(0)}(1_{\bar{b}}^+,2_b^+,3_g^-,4_g^-,5_H) &= -\frac{[12]^2}{[23][34][41]}\,,\\ A^{(0)}(1_{\bar{b}}^+,2_b^+,3_g^+,4_g^-,5_H) &= \frac{\langle 24\rangle\langle 4|5|1]^2}{s_{234}\langle 23\rangle\langle 34\rangle\langle 2|5|1]} - \frac{s_5[13]^3}{s_{134}[14][34]\langle 2|5|1]}\,.\end{aligned} \tag{3.2.22}$$

The $\bar{b}, b$ quarks need to have the same helicity as that is the only way they can couple to the Higgs boson. For the $\bar{b}b\bar{q}qH$ channel the 'all-plus' and MHV configurations vanish, and we are left with:

$$A^{(0)}(1_{\bar{b}}^+,2_b^+,3_{\bar{q}}^+,4_q^-,5_H) = \frac{\langle 4|5|1]^2}{s_{234}\langle 34\rangle\langle 2|5|1]} + \frac{s_5[31]^2}{s_{134}[34]\langle 2|5|1]}\,. \tag{3.2.23}$$

In both cases, due to the colour decomposition of the full amplitudes given by Eq. 3.2.8, the $A^{(0)}(1^+,2^+,3^-,4^+,5_H)$ partial amplitude is related to $A^{(0)}(1^+,2^+,3^+,4^-,5_H)$ by swapping the particles $1 \leftrightarrow 2, 3 \leftrightarrow 4$, and flipping the overall sign for the subprocess $\bar{b}bggH$. The remaining non-vanishing helicity configurations can be obtained by parity transformations, that is by swapping the brackets $\langle ij\rangle \leftrightarrow [ji]$.

3.3 Amplitude Reduction and Reconstruction

To obtain the analytic form of the two-loop QCD helicity amplitudes, we employ the framework thoroughly discussed in Chapter 2. Here, we provide a brief outline

of it and supply process-specific details. We start by generating a set of Feynman diagrams contributing to both the $\bar{b}bggH$ and $\bar{b}b\bar{q}qH$ processes using `QGRAF` [35], and perform diagram filtering, topology identification and colour decomposition using a collection of in-house `Mathematica` and `Form` [184,185] scripts. In the leading colour approximation, there are 749 (264) Feynman diagrams contributing to the two-loop $\bar{b}bggH$ ($\bar{b}b\bar{q}qH$) QCD amplitudes, including all closed fermion loop contributions. The numerators of the loop amplitudes are then computed for each independent helicity configuration, and the spinor-helicity manipulations are carried out using the library `Spinney` [186]. The helicity dependent loop numerators are written in terms of spinor products ($\langle ij\rangle$, $[ij]$), scalar products ($p_i \cdot p_j$, $k_i \cdot k_j$, $k_i \cdot p_j$) and spinor strings ($\langle i|k_i|j]$, $\langle i|p_5|j]$, $\langle i|k_i p_5|j\rangle$, $[i|k_i p_5|j]$), where p_i's and k_i's are the external and loop momenta, respectively. The numerators are therefore expressed as linear combinations of monomials of loop-momentum dependent objects that multiply coefficients which depend only on the external kinematics. As explained in Section 2.5, the coefficients are built from spinor products and strings (free of k_i) which not only are not independent, but also incompatible with finite field arithmetic.

Both of these problems are solved by using MTs. To obtain a configuration for the off-shell five-particle configuration, we begin with a massless configuration for six particles. While the exact parametrisation is not important, the form presented in Ref. [46] is a useful starting point. We can think of the massless process as the result of the off-shell leg decaying into a pair of massless particles. There are $3n - 10 = 8$ independent variables in the six-particle process, but we can reduce the degrees of freedom by choosing one of the decay direction to be collinear with one of the other massless legs in the five-point kinematics. Since the MTs are associated with complex momenta, we consider the angle and square bracket spinors products to be independent. We can write this explicitly as follows: the six massless momenta q_i^μ are related to the off-shell five particle momenta p_i^μ by:

$$p_1^\mu = q_1^\mu\,, \qquad p_2^\mu = q_2^\mu\,, \qquad p_3^\mu = q_3^\mu\,, \qquad p_4^\mu = q_4^\mu\,, \qquad p_5^\mu = q_5^\mu + q_6^\mu\,. \tag{3.3.1}$$

We impose the constraints $\langle q_2 q_6\rangle = 0$ and $[q_2 q_6] = 0$ to reduce the independent variables to 6. We then apply a transformation onto the following choice of variables:

$$\begin{aligned} x_1 &= s_{12}, \\ x_2 &= -\frac{\mathrm{tr}_+(1234)}{s_{12}s_{34}}, \\ x_3 &= \frac{\mathrm{tr}_+(134152)}{s_{13}\,\mathrm{tr}_+(1452)}, \\ x_4 &= \frac{s_{23}}{s_{12}}, \end{aligned} \tag{3.3.2}$$

$$x_5 = -\frac{\mathrm{tr}_-(1(2+3)(1+5)523)}{s_{23}\,\mathrm{tr}_-(1523)},$$
$$x_6 = \frac{s_{45}}{s_{12}},$$

where $\mathrm{tr}_\pm(ij\cdots kl) = \frac{1}{2}\,\mathrm{tr}((1\pm\gamma_5)\not{p}_i\not{p}_j\cdots\not{p}_k\not{p}_l)$. Some features of this parametrisation are particularly convenient. For example, the only dimensionful quantity is x_1, and tr_5 is rational. However, such a choice does break some symmetries in the problem and so different helicity configurations will have different complexities. For the process considered here, the complexity was manageable using this form. Applications to other off-shell five-particle processes may require further thought.

Having set up a rational parametrisation of the external kinematics, the helicity dependent loop numerators are constructed analytically and ready to be further processed. This is the starting point of our numerical algorithm in the finite field setup. In order to write the amplitude in terms of scalar integrals, we first define the integral families for the 15 maximal topologies, which are shown in Fig. 3.3. Each diagram topology appearing in the amplitude can be mapped onto at least one of them. After that is done, the objects which depend on the loop momenta in the numerators are written in terms of the 11 propagators and ISPs associated with the chosen maximal topology. These mapping procedures are performed numerically within the `FiniteFlow` framework [48]. We remark that since the maximal topologies have five external momenta, they completely span the 4-dimensional space and there is no need to introduce the spurious vectors. Thus, the integrand reduction technique of Section 2.7 does not lead to an explicit dependence on ϵ into the numerators. Therefore, the coefficients of these scalar integrals are functions of the external kinematics only, in the form of MTs.

At this stage, the loop amplitude is expressed as a linear combination of scalar integrals that can be reduced to a set of MIs using the IBP reduction method [65] within the finite field setup. The IBP relations are generated using `LiteRed` [29] and solved numerically over finite fields using the Laporta algorithm [69]. The IBP reduction is performed directly to a set of MIs with UT weight identified in Ref. [98]. The UT MIs are further expanded onto a basis of special functions f that is built out of the MI components, as proposed in Ref. [182]. We refer to this basis of special functions as the *master integral function basis*. Subtracting the UV and IR poles from the bare helicity amplitudes and performing Laurent expansion in the dimensional regulator ϵ, we arrive at the following expression for the finite remainders:

$$F^{(L)} = \sum_i r_i(x) m_i(f)\,, \tag{3.3.3}$$

where $m_i(f)$ are monomials of the special functions and r_i are rational functions of the

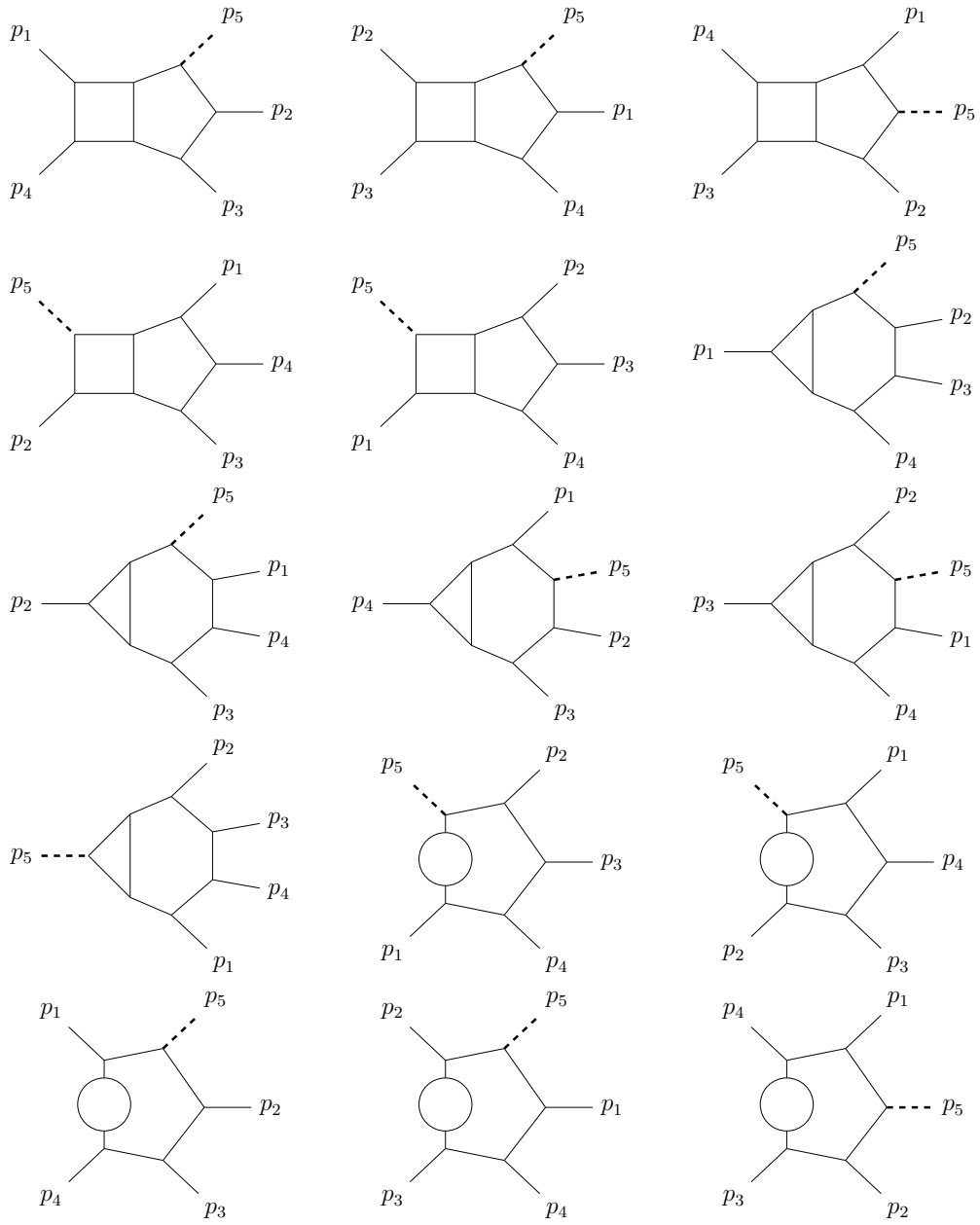

Figure 3.3: Maximal topologies present in the computation of the two-loop $pp \to b\bar{b}H$ amplitudes. They were previously also used in Ref. [182]. The massive particle is marked with a bold dashed line.

MTs x. It is important to note that the definition of the UT MIs involves three square roots. One is related to the pseudo-scalar invariant tr_5, which captures the parity-odd part of the spinor expressions and is present already in the coefficients. The other two square roots are associated with the three-mass triangle Gram determinants:

$$\Delta_3^{(1)} = 2\sqrt{(p_{23}\cdot p_5)^2 - p_5^2 s_{23}}\,, \qquad \Delta_3^{(2)} = 2\sqrt{(p_{12}\cdot p_5)^2 - p_5^2 s_{12}}\,, \tag{3.3.4}$$

where $p_{ij} = p_i + p_j$. They are not rationalised by the MT parametrisation and may therefore be problematic for the finite field setup. We overcome this issue by absorbing the three square roots into the definition of the UT MIs, which is possible because they appear only as overall normalisations of the latter. As a result, they are contained in the monomials $m_i(f)$ in Eq. 3.3.3 and do not appear in the amplitude reconstruction. We note that in our computation, while the tr_5 originating from the UT MIs is absorbed in $m_i(f)$, the tr_5 already present in the coefficients is rationalised by the MT parametrisation, Eq. 3.3.2.

At this stage, we have an algorithm which computes the coefficients of the special function monomials, $r_i(x)$ in Eq. 3.3.4, numerically over finite fields for each of the independent helicity configurations of the two processes $\bar{b}bggH$ and $\bar{b}b\bar{q}qH$. We emphasise that from the start of our numerical algorithm until reaching $r_i(x)$, the computation is done within one system of `FiniteFlow` graphs. The last step is the functional reconstruction of the rational coefficients. This task is made challenging by the high polynomial degrees, which are shown in the third column of Tables 3.1 and 3.2. We tackle the complexity of the reconstruction through the strategy already used in Refs. [182, 187]. We refer to Ref. [187] for a thorough discussion, and give here only a brief outline.

The first step of the strategy consists in fitting the linear relations among the rational coefficients. These linear relations are then used to express the rational coefficients in terms of a set of linearly independent coefficients, which are chosen to have the lowest possible degrees. The degrees of the independent rational coefficients are given in the fourth column of Tables 3.1 and 3.2.

The second step of our reconstruction strategy consists of determining the factors in the denominators of the rational coefficients. The analytic structure of the special functions is determined by the set of letters corresponding to the canonical DEs satisfied by the MIs. In other words, the singularities of the special functions and of their discontinuities are located on the hypersurfaces where any of the letters vanish (or go to infinity). It is therefore natural to expect that the rational coefficients which multiply the special functions should feature poles which are similarly linked to the letters. This motivates us to include the letters into an ansatz for the denominators of the coefficients. Since the helicity amplitudes also contain phase information, we

must include spinor structures as well. It is then simple to check, on a univariate slice of the amplitude, whether the terms in the ansatz are present in the denominators or not. For our amplitudes, we find the following list to be sufficient:

$$\begin{aligned}\Big\{&\langle ij\rangle\,,[ij]\,,\langle i|p_5|j]\,,s_{ij}\,,s_{ij}-s_{kl}\,,s_{i5}-p_5^2\,,p_5^2\,,\mathrm{tr}_5\,,\Delta_1\,,\Delta_2\,,\\&s_{15}(s_{13}+s_{34})-p_5^2 s_{34}\,,s_{25}(s_{24}+s_{34})-p_5^2 s_{34}\Big\}\,,\end{aligned} \tag{3.3.5}$$

where the indices i, j in the spinor expressions vary from 1 to 4, while the indices i, j, k, l in the Mandelstam invariants vary from 1 to 5. The various free indices in each of the factors are understood to be different from each other. Here, the ansatz of Eq. 3.3.5 allows us to determine the denominators entirely, as well as some factors in the numerators.

Having determined the denominators of the rational coefficients, we can proceed to the third and last step of our reconstruction strategy: a univariate partial fraction decomposition 'on the fly'. We find that, with the parameterisation of the external kinematics given by Eq. 3.3.2, partial fractioning with respect to x_5 is the most convenient choice. The partial fraction decomposition of multivariate functions has recently drawn a lot interest as a powerful tool to simplify the analytic expressions of scattering amplitudes. A number of new approaches have been proposed, which make use of algebraic geometry techniques to handle the multivariate case efficiently [188–192]. However, these algorithms are applied to known *analytic* expressions, i.e. after the rational reconstruction has been performed. On the contrary, our univariate partial fraction decomposition can be performed within the finite field setup itself, which consequently simplifies the reconstruction of the coefficients. The algorithm makes use of the knowledge of the denominators to construct an ansatz for the decomposition into partial fractions with respect to the chosen variable. The coefficients of this ansatz can then be solved for and reconstructed. To this end, we perform a further matching of their factors against the ansatz in Eq. 3.3.5. The matched factors are then removed, and the remaining functions are reconstructed with `FiniteFlow`'s reconstruction algorithm (see Section 2.6.2). The degrees of the rational coefficients which remain to be reconstructed are shown in the fifth column of Tables 3.1 and 3.2. Note that after partial fractioning, the denominators are not entirely determined from the ansatz in Eq. 3.3.5. The univariate partial fraction decomposition in fact introduces spurious factors in the denominators. The latter could be determined as well, but we refrain from doing so as it does not reduce the complexity of the reconstruction.

Following the strategy outlined above, we reconstructed the partial finite remainders for the independent mostly-plus helicity configurations of the subprocesses $\bar{b}bggH$

$\bar{b}bggH$	helicity configurations	$r_i(x)$	independent $r_i(x)$	partial fraction in x_5	number of points
$F^{(2),1}$	$++++$	63/57	52/46	20/6	3361
	$+++-$	135/134	119/120	28/22	24901
	$++--$	105/111	105/111	22/12	4797
$F^{(2),n_f}$	$++++$	45/41	45/41	16/6	1381
	$+++-$	94/95	94/95	17/6	1853
	$++--$	89/95	62/69	18/3	2492
$F^{(2),n_f^2}$	$++++$	12/8	9/7	0/0	3
	$+++-$	11/16	11/16	3/0	22
	$++--$	12/20	8/16	8/0	242

Table 3.1: Maximum numerator/denominator polynomial degrees of the finite remainder coefficients $r_i(x)$ in Eq. 3.3.3 at each stage of our reconstruction steps, together with the number of sample points needed for the analytic reconstruction in the $\bar{b}bggH$ subprocess, for the various closed fermion loop contributions.

$\bar{b}b\bar{q}qH$	helicity configurations	$r_i(x)$	independent $r_i(x)$	partial fraction in x_5	number of points
$F^{(2),1}$	$+++-$	82/81	69/70	24/16	10326
$F^{(2),n_f}$	$+++-$	28/30	25/24	8/6	379
$F^{(2),n_f^2}$	$+++-$	6/11	6/11	3/0	22

Table 3.2: Maximum numerator/denominator polynomial degrees of the finite remainder coefficients $r_i(x)$ in Eq. 3.3.3 at each stage of our reconstruction steps, together with the number of sample points needed for the analytic reconstruction in the $\bar{b}b\bar{q}qH$ subprocess, for the various closed fermion loop contributions.

and $\bar{b}b\bar{q}qH$. The mostly-minus helicity finite remainders can be obtained by parity conjugation. Moreover, the finite remainders for the helicity configuration $++-+$ can be obtained by swapping $1 \leftrightarrow 2$, $3 \leftrightarrow 4$ in the $+++-$ finite remainders, as discussed in Section 3.2.1 for the tree-level amplitudes. This symmetry follows from the colour structure and thus holds at any loop order. We could therefore evaluate the $++-+$ finite remainders by permuting numerically the $+++-$ ones, as we do in order to get all the other helicity configurations from the independent ones. By

permuting numerically, we mean that we obtain the values of the permuted finite remainders by evaluating the unpermuted ones at permuted points. This is possible because our approach to the evaluation of the special functions, which we discuss in Section 3.4, handles the analytic continuation to any region automatically. Each numerical permutation therefore amounts to one more evaluation for each point. The permutation that takes from $++-+$ to $++--+$ is however peculiar, as it is covered by the basis of special functions defined in Ref. [182]. We can thus reconstruct the finite remainders for both helicity configurations directly in terms of the same basis of special functions. This is much more convenient, as it reduces the number of permutations which need to be carried out numerically, this way decreasing the global evaluation time of the finite remainders. For this reason, we reconstructed the analytic expression of the $++--+$ finite remainders as well, and include the $++--+$ configuration in the independent helicity set in the following sections. The relation with the $+++-$ configuration constitutes a non-trivial check of our results, which we discuss in Section 3.5.

3.4 A Custom Basis of Special Functions for the Finite Remainders

The one and two-loop finite remainders are expressed as combinations of rational coefficients — functions of the MTs in Eq. 3.3.2 — and monomials of square roots and elements of the MI function basis $\{f_i^{(w)}\}$. The latter were classified in Ref. [182] so as to span the cyclic permutations of the planar five-particle integrals with one massive off-shell leg up to two loops. The function space of the finite remainders is however simpler than that of the integrals and of the amplitudes. This becomes particularly clear when we express the special functions in terms of CIIs [90], which we have introduced in Section 2.9.1. Here, we will write the special functions as:

$$\left[W_{i_1},\ldots,W_{i_n}\right]_{s_0}(s) = \int_0^1 dt\, \frac{d\log W_{i_n}(\gamma(t))}{dt} \left[W_{i_1},\ldots,W_{i_{n-1}}\right]_{s_0}(\gamma(t)) \,, \qquad (3.4.1)$$

where $\{d\log W_i\}$ are the logarithmic integration kernels and their arguments W_i are algebraic functions of the external kinematics. The cumulative dependence on external kinematics is denoted by s, while s_0 is an arbitrary reference point, and γ is an arbitrary contour in the phase space going from $\gamma(0) = s_0$ to $\gamma(1) = s$. The iteration starts with $[]_{s_0}(s) := 1$. The transcendental weight of the special functions is then trivially given by n in Eq. 3.4.1. At two loops up to order ϵ^0 iterated integrals with transcendental weight up to four are required. In our case, the integration kernels are given by the letters $\{W_i\}$ of the alphabet defined in Ref. [98].

Although they may look rather abstract, CIIs offer several important advantages. Most importantly, they implement automatically all the functional relations which would otherwise be hidden in a representation in terms of other types of functions, such as GPLs. This property was exploited in Ref. [182] to construct the MI function basis $\{f_i^{(w)}\}$. The expression in terms of CIIs of the MI basis functions can be obtained through their definition in terms of MI components given in Ref. [182], and the canonical DEs for the MIs given in Ref. [98] (see Ref. [182] for a thorough discussion). Another important benefit of using iterated integrals is that their analytic structure is beautifully manifest: an iterated integral may have singularities or branch points only where one of its letters vanishes or diverges. Expressing the special functions in the finite remainders in terms of CIIs therefore highlights their analytic structure. Indeed this unveils important simplifications: certain letters, which are present in the expressions of the MIs, are absent in the finite remainders. In other words, certain branch cuts of the integrals drop out of the finite remainders. We observe the same pattern noticed for the $Wb\bar{b}$ amplitudes in Ref. [182]. One letter, $W_{49} = \mathrm{tr}_5$, is present in the bare amplitudes but absent in the finite remainders. This pattern of the pseudo-scalar invariant tr_5 has already been observed explicitly in many massless two-loop five-particle finite remainders [113, 190, 193–201], and is linked to an underlying cluster algebra structure [202]. Since this letter is invariant under permutations of the external massless legs (up to a sign), we expect it to drop out from the finite remainders in general. In addition, six letters, W_i with $i = 16, 17, 27, 28, 29, 30$, are present in the two-loop integrals but drop out already at the level of the bare amplitudes (truncated at order ϵ^0 at two loops). This set of letters is not closed under all permutations of the external massless legs, and the generality of their absence is therefore less clear. It would be of great interest to uncover the physical principle underlying these simplifications.

The simplifications of the analytic structure mentioned above require the interplay among various elements of the MI function basis $\{f_i^{(w)}\}$ of Ref. [182]. In other words, the separate terms of the finite remainders may have spurious branch cuts which cancel out in the sum. It is therefore convenient to construct a new, *ad hoc* basis of special functions where the properties of the finite remainders are manifest. In addition to being more elegant from the theoretical point of view, such a basis is also much more convenient from the practical point of view. Evaluating the MI function basis $\{f_i^{(w)}\}$ in fact requires handling integration kernels — letters — which eventually cancel out in the objects we are interested in evaluating. It is desirable that these cancellations take place analytically rather than numerically, so that the spurious kernels are avoided altogether. For this reason we need a new basis of special functions where these properties are manifest, and an approach to evaluate

it which bypasses the MI function basis $\{f_i^{(w)}\}$ and its unnecessary complexity.

We thus construct a new basis of special functions, which we label by $\{h_i^{(w)}\}$, where $w = 1, 2, 3, 4$ denotes the transcendental weight. This new basis contains only those linearly independent combinations of functions $f_i^{(w)}$ which are actually present in the finite remainders, and whose iterated integral expression is free of the letters W_i with $i = 16, 17, 27, 28, 29, 30, 49$. We dub this basis *finite remainder function basis*, as opposed to the MI function basis $\{f_i^{(w)}\}$. This leads to an important simplification in the expressions of the finite remainders, which are then expressed as combinations of rational coefficients and monomials in the $h_i^{(w)}$'s and the square roots. In particular, only 23 weight-4 functions $\{h_i^{(4)}\}_{i=1}^{23}$ are required, to be compared with the 113 weight-4 functions in the MI function basis. Since the evaluation of the weight-4 functions is the most expensive step in the evaluation of the finite remainders, this reduction has a strong positive impact on the total evaluation time. Note that we have also improved the MI basis $\{f_i^{(w)}\}$ of Ref. [182] by identifying relations among the higher weight functions and products of lower weight ones which were originally missed. We achieved this following the approach of Ref. [182], but evaluating the boundary values with higher accuracy.

In order to evaluate numerically the finite remainder function basis $\{h_i^{(w)}\}$, we apply the method of the generalised power series expansion [183]. This approach has already found several successful applications to the evaluation of MIs from the DEs they satisfy [98, 99, 107, 108, 183, 203, 204]. Here, following Ref. [182], we apply it directly to the basis of special functions. This method can be applied to the finite remainder and MI function bases because they too, like the MI bases they stem from, satisfy systems of DEs in the canonical form [84]. This follows from the fact that the functions in the bases $\{h_i^{(w)}\}$ and $\{f_i^{(w)}\}$ are by construction pure (see Section 2.9.3). Thus, due to their UT weight, we can write any $h_i^{(w)}$, for $w > 0$, in terms of CIIs as:

$$h_i^{(w)}(s) = \sum_{I=(i_1,\ldots,i_w)} c_I^{(i)} \left[W_{i_1}, \ldots, W_{i_w}\right]_{s_0}(s)\,, \tag{3.4.2}$$

for some rational constant coefficients $c_I^{(i)}$ [1]. Moreover, the purity condition in Eq. 2.9.18 follows straightforwardly from the differential of CIIs:

$$d\left[W_{i_1}, \ldots, W_{i_n}\right]_{s_0}(s) = d\log W_{i_n}(s)\, \left[W_{i_1}, \ldots, W_{i_{n-1}}\right]_{s_0}(s)\,, \tag{3.4.3}$$

where we note that the derivatives of $\log W_i$ are algebraic functions and hence have transcendental weight 0. The purity of the function basis therefore implies that the vector of all weight-w functions in the finite remainder basis, $\vec{h}^{(w)} = \left(h_1^{(w)}, h_2^{(w)}, \ldots\right)^T$,

[1] In general the iterated integrals in Eq. 3.4.2 include also transcendental constants, such as π and $\zeta(3)$. We neglect them here to simplify the presentation.

satisfies a DE of the form:

$$d\vec{h}^{(w)} = \left(\sum_j b_j^{(w)}\, d\log W_j\right) \vec{h}^{(w-1)}\,, \tag{3.4.4}$$

for $w > 1$, where b_j are constant rational matrices. The matrices $b_j^{(w)}$ can be determined easily from the iterated integral expression of the functions through Eq. 3.4.3. In general, the derivatives of the weight-w functions may involve weight-$(w-1)$ functions which are not needed to express the finite remainders. These must be included in the basis as well, in order to be able to write down the DEs. So, strictly speaking, the finite remainder function basis $\{h_i^{(w)}\}$ contains all linearly independent functions which appear in the finite remainders and in the derivatives of the basis itself. The DEs Eq. 3.4.4 for all weights can be put together in one system by defining the vector of all the functions in the finite remainder basis as:

$$\vec{h} = \left(\epsilon^4\vec{h}^{(4)}\,, \epsilon^3\vec{h}^{(3)}\,, \epsilon^2\vec{h}^{(2)}\,, \epsilon\vec{h}^{(1)}\,, 1\right)^T\,, \tag{3.4.5}$$

where ϵ is an auxiliary parameter with transcendental weight -1, so that the vector $\vec{h}$ is pure with transcendental weight 0. The full basis $\vec{h}$ then satisfies a system of DEs in the canonical form [84]:

$$d\vec{h} = \epsilon \left(\sum_{i=1}^{49} a_i\, d\log W_i\right) \vec{h}\,, \tag{3.4.6}$$

where the constant matrices a_i are strictly upper block triangular, with the blocks given by the matrices $b_i^{(w)}$ in the DEs Eq. 3.4.4 for the various weights. This is in direct analogy to the canonical DEs for the MIs we saw in Eq. 2.9.14. However, this system of DEs for the vector $\vec{h}$ is much simpler than that for the MIs. First, it contains only the letters which do appear in the finite remainders, i.e. $a_i = 0$ for $i = 16, 17, 27, 28, 29, 30, 49$. Second, while the DEs for the MIs contain information about all the orders in ϵ, the system Eq. 3.4.6 encodes only those orders which are relevant for the finite remainders, i.e. up to ϵ^4. The constant matrices a_i are in fact nilpotent with degree 5, i.e. $(a_i)^5 = 0$ for any i, which follows from their strictly upper triangular form. The process-dependent basis identified for the finite remainder has a practical advantage, since we find a significant reduction in the number of weight four functions which dominate the total evaluation times. In this case, we find a reduction from 113 to 23 weight four functions, which gives a rough measure of the improvement.

The MI function basis defined in Ref. [182], and thus also the finite remainder function basis constructed here, cover the planar integral families only in those permutations of the external massless legs which preserve the cyclic ordering of the particles. The

other permutations cannot be expressed analytically in terms of functions of these bases only. Nonetheless, thanks to our numerical evaluation strategy, we can obtain the values of any permutation σ of the finite remainder basis functions by evaluating them in the standard orientation at permuted points:

$$\sigma\left[h_i^{(w)}\right](X) = h_i^{(w)}\left[\sigma(X)\right] . \tag{3.4.7}$$

This is possible because we evaluate the finite remainder function basis $\{h_i^{(w)}\}$ by solving the system of DEs Eq. 3.4.6 numerically with the method of the generalised power series expansions [183]. For this purpose, we make use of the public `Mathematica` package `DiffExp` [142]. In order to compute the boundary values, i.e. the values of the functions at some base point, we relate the finite remainder functions to MI components using the definition of the MI function basis [182], and evaluate the latter through their analytic expression in terms of GPLs [94, 95, 205] provided in Refs. [111, 122, 206]. We evaluate the GPLs numerically with the `C++` library `GiNaC` [96]. We provide in ancillary files the DEs 3.4.6 and the values of the finite remainder functions at six points, one for each $2 \to 3$ scattering region with massless incoming particles, with (at least) 200-digit accuracy. Using this information, the generalised power series expansion method allows us to evaluate the finite remainder function basis reliably anywhere in the phase space. This technique in fact handles the analytic continuation automatically, so that also the permutations required to evaluate the complete finite remainders starting from the partial ones — as shown in Eqs. 3.2.8 for the amplitudes — as well as the other helicity configurations can be performed numerically straightforwardly. We assessed the reliability of this evaluation approach by checking the convergence of the finite remainders close to the spurious poles of the rational coefficients. We discuss this and other checks in the next section.

3.5 Further Validation

The finite remainders are defined by subtracting the expected UV and IR poles from the bare amplitudes. Therefore, the fact that all the poles in ϵ cancel out, so that our expressions for the finite remainders are indeed finite, is already a strong check of the validity of our results. We have also checked that our amplitudes are correctly normalised by comparing the spin and colour averaged squared tree-level amplitudes with full colour dependence against `MadGraph` [207]. On top of that, we performed a number of additional checks, which we discuss in the next subsections.

3.5.1 Direct computation of the squared finite remainders

We checked the helicity amplitudes derived in this work against a squared matrix element computation, carried out independently following the approach used in the previous work on $u\bar{d} \to Wb\bar{b}$ [182]. In the squared matrix element computation the two-loop amplitude is interfered with the tree-level amplitude analytically. After manipulating the Dirac traces, the loop numerators contain only scalar products ($k_i \cdot k_j$, $k_i \cdot p_j$, $p_i \cdot p_j$), that can be mapped easily onto propagator denominators. This way we derive an analytic form of the two-loop squared matrix element written as a linear combination of scalar Feynman integrals. The squared matrix element is then processed further through IBP reduction to obtain the MI representation, followed by mapping of the MIs onto the basis of special functions, subtraction of UV and IR singularities, and finally Laurent expansion in ϵ. All these steps are carried out numerically over finite fields within the `FiniteFlow` framework. The squared matrix element computation uses the Conventional Dimensional Regularisation (CDR) scheme, where internal and external momenta live in $d = 4 - 2\epsilon$ dimensions. We find complete agreement with this approach and the helicity amplitudes in the HV scheme at the level of the squared finite remainders.

3.5.2 Renormalisation scale dependence

The analytic expressions of the one- and two-loop finite remainders have been derived with the renormalisation scale μ set to $\mu = 1$. The dependence of the finite remainders on the renormalisation scale can be determined by restoring the μ dependence of the strong and Yukawa couplings ($\alpha_s \to \alpha_s \mu^{2\epsilon}$, $y_b \to y_b \mu^{\epsilon}$), and by replacing $(-s_{ij})^{-\epsilon} \to (-\mu^2/s_{ij})^{\epsilon}$ in the I_1 operators defined in Eqs. 3.2.14—3.2.15, which enter the pole terms in Eqs. 3.2.11—3.2.12. In order to capture the scale dependence of the finite remainders, we define the difference:

$$\delta F^{(L),i}(\mu^2) = F^{(L),i}(\mu^2) - F^{(L),i}(\mu^2 = 1)\,, \tag{3.5.1}$$

where the dependence on the kinematic variables is understood. The difference $\delta F^{(L),i}(\mu^2)$ is entirely determined by the finite remainders evaluated at $\mu^2 = 1$ — which we reconstructed analytically — and logarithms of μ^2. For the $\bar{b}bggH$ finite remainders, it is given by:

$$\delta F^{(1),1}(\mu^2) = \frac{31}{6} A^{(0)} \log(\mu^2)\,, \tag{3.5.2}$$

$$\delta F^{(1),n_f}(\mu^2) = -\frac{2}{3} A^{(0)} \log(\mu^2)\,, \tag{3.5.3}$$

$$\delta F^{(2),1}(\mu^2) = \log(\mu^2)\left\{\left(\frac{1261}{54} - \frac{11}{72}\pi^2 + 9\zeta_3\right)A^{(0)} + \frac{53}{6}F^{(1),1}(1)\right\} + \frac{1643}{72}A^{(0)}\log^2(\mu^2)\,, \tag{3.5.4}$$

$$\delta F^{(2),n_f}(\mu^2) = \log(\mu^2)\left\{\left(-\frac{241}{27} + \frac{\pi^2}{36}\right)A^{(0)} - \frac{4}{3}F^{(1),1}(1) + \frac{53}{6}F^{(1),n_f}(1)\right\} - \frac{115}{18}A^{(0)}\log^2(\mu^2)\,, \tag{3.5.5}$$

$$\delta F^{(2),n_f^2}(\mu^2) = \log(\mu^2)\left(\frac{20}{27}A^{(0)} - \frac{4}{3}F^{(1),n_f}(1)\right) + \frac{4}{9}A^{(0)}\log^2(\mu^2)\,, \tag{3.5.6}$$

while for the $\bar{b}b\bar{q}qH$ finite remainders, it is given by:

$$\delta F^{(1),1}(\mu^2) = \frac{31}{6}A^{(0)}\log(\mu^2)\,, \tag{3.5.7}$$

$$\delta F^{(1),n_f}(\mu^2) = -\frac{2}{3}A^{(0)}\log(\mu^2)\,, \tag{3.5.8}$$

$$\delta F^{(2),1}(\mu^2) = \log(\mu^2)\left\{\left(\frac{5093}{216} - \frac{11}{12}\pi^2 + 14\zeta_3\right)A^{(0)} + \frac{53}{6}F^{(1),1}(1)\right\} + \frac{1643}{72}A^{(0)}\log^2(\mu^2)\,, \tag{3.5.9}$$

$$\delta F^{(2),n_f}(\mu^2) = \log(\mu^2)\left\{\left(-\frac{329}{54} + \frac{\pi^2}{6}\right)A^{(0)} - \frac{4}{3}F^{(1),1}(1) + \frac{53}{6}F^{(1),n_f}(1)\right\} - \frac{115}{18}A^{(0)}\log^2(\mu^2)\,, \tag{3.5.10}$$

$$\delta F^{(2),n_f^2}(\mu^2) = -\frac{4}{3}F^{(1),n_f}(1)\log(\mu^2) + \frac{4}{9}A^{(0)}\log^2(\mu^2)\,. \tag{3.5.11}$$

To check that our results for the finite remainders have the correct scale dependence, we evaluate them at two kinematic points related by a rescaling by some positive factor a:

$$\begin{aligned}\vec{s} &= (s_{12}, s_{23}, s_{34}, s_{45}, s_{15}, p_5^2)\,,\\ \vec{s}^{\,\prime} &= a\,\vec{s} = (as_{12}, as_{23}, as_{34}, as_{45}, as_{15}, ap_5^2)\,.\end{aligned} \tag{3.5.12}$$

We then verify numerically that the finite remainders satisfy the following relation:

$$\frac{F^{(L),i}(1, a\,\vec{s}) + \delta F^{(L),i}(a, a\,\vec{s})}{A^{(0)}(a\,\vec{s})} = \frac{F^{(L),i}(1, \vec{s})}{A^{(0)}(\vec{s})}\,, \tag{3.5.13}$$

where we extended the notation of the finite remainders and tree-level amplitudes to take into account their dependence on the phase space point $\vec{s}$.

3.5.3 Relation between $+++-$ and $++-+$

The partial finite remainders for the single-minus helicity configurations, $+++-$ and $++-+$, are related by a permutation of the external particles:

$$\begin{aligned} F^{(L)}(1_{\bar{b}}^{+}, 2_{b}^{+}, 3_{g}^{-}, 4_{g}^{+}, 5_{H}) &= -\, F^{(L)}(2_{\bar{b}}^{+}, 1_{b}^{+}, 4_{g}^{+}, 3_{g}^{-}, 5_{H})\,, \\ F^{(L)}(1_{\bar{b}}^{+}, 2_{b}^{+}, 3_{\bar{q}}^{-}, 4_{q}^{+}, 5_{H}) &= F^{(L)}(2_{\bar{b}}^{+}, 1_{b}^{+}, 4_{\bar{q}}^{+}, 3_{q}^{-}, 5_{H})\,. \end{aligned} \tag{3.5.14}$$

Permuting the special functions is however non-trivial, and may in general require analytic continuation. The permuted special functions are defined by:

$$\left(\sigma \circ \vec{h}\right)(\{p_i\}) = \vec{h}(\{p_{\sigma(i)}\})\,, \tag{3.5.15}$$

where σ denotes the permutation $(12345) \to (21435)$ of the external particles, and $\{p_i\}$ denotes the dependence on the external momenta. In order to check the relations Eq. 3.5.14 analytically, we need to express the permuted functions $(\sigma \circ \vec{h})$ in terms of the ones in the standard orientation, $\vec{h}$. To perform this operation in an algorithmic and robust way, we resort to the system of DEs in Eq. 3.4.6 satisfied by the finite remainder function basis. The permuted functions in fact satisfy the permuted DEs:

$$d(\sigma \circ \vec{h}) = \epsilon \left[\sum_{i=1}^{49} a_i \, d\log\left(\sigma \circ W_i\right)\right] (\sigma \circ \vec{h})\,. \tag{3.5.16}$$

Permuting the letters W_i is however trivial, as they only involve algebraic functions. Since the alphabet is closed by construction under this permutation, we obtain an explicit system of DEs for the permuted special functions:

$$d(\sigma \circ \vec{h}) = \epsilon \left(\sum_{i=1}^{49} a'_i \, d\log W_i\right) (\sigma \circ \vec{h})\,. \tag{3.5.17}$$

The latter can straightforwardly be solved in terms of CIIs (see Ref. [182] for a thorough discussion). In order to be comparable with the solution of the system Eq. 3.4.6 which defines the finite remainder function basis $\vec{h}$, we must make sure that the same boundary point is used when solving both systems of DEs in terms of iterated integrals. The boundary values can be obtained numerically with arbitrary precision using the expressions in terms of GPLs of Refs. [111, 122, 206], as discussed at the end of Section 3.4. Using the DEs Eq. 3.5.17, we can then express the permuted finite remainder special functions in terms of the ones in the original orientation through CIIs. Once that is done, the right-hand sides of Eqs. 3.5.14 are written in terms of the same special function basis as the left-hand sides. Since the rational coefficients can be permuted analytically trivially, we can immediately verify that our results for the one- and two-loop finite remainders satisfy the relations given by Eqs. 3.5.14.

3.5.4 Convergence near spurious poles

The rational coefficients in the finite remainders contain spurious poles, namely poles which are not related to the physical singularities of the amplitudes. When evaluating at a phase space point infinitesimally close to a spurious pole — but at a finite distance from all physical poles — the rational coefficients diverge, whereas the finite remainders must stay finite. This can only occur through large numerical cancellations involving both the coefficients and the special functions. Verifying this behaviour constitutes both a check on our analytic expressions for the finite remainders and a stress test of our evaluation approach for the special functions. We do it as follows. First, we use the factor matching strategy discussed in Section 3.3, with the ansatz given by Eq. 3.3.5. This allows us to determine that the spurious poles in the coefficients are associated with the following denominator factors:

$$\{P_k\} = \Big\{ \langle i|p_5|j] \,, \mathrm{tr}_5 \,, \Delta_1 \,, \Delta_2 \,, s_{15} - s_{23} \,, s_{15} - s_{24} \,, s_{13} - s_{25} \,, s_{14} - s_{25} \,, s_{15} - s_{34} \,, \\ s_{25} - s_{34} \,, s_{14} - s_{35} \,, s_{23} - s_{45} \,, s_{15}(s_{13} + s_{34}) - p_5^2 s_{34} \,, s_{25}(s_{24} + s_{34}) - p_5^2 s_{34} \Big\} \,, \tag{3.5.18}$$

where $i, j \in \{1, 2, 3, 4\}$ with $i \neq j$. Next, for each factor P_k in Eq. 3.5.18, we construct a one-dimensional slice of the phase space, parametrised by a parameter δ, such that $P_k = \delta$. As we probe the small-δ region, all the other factors in Eq. 3.5.18 and the factors associated with the physical singularities — $(p_i + p_j)^2$ and $p_i \cdot p_j$ — must stay finite, i.e. they must neither diverge nor vanish. This ensures that we target a specific spurious pole, rather than multiple at once, and that we stay away from the physical singularities. Finally, we evaluate the finite remainders on these slices for increasingly small values of δ. We evaluate the special functions with 64-digit accuracy. Our analytic expressions for the finite remainders exhibit the expected behaviour: as δ approaches zero the rational coefficients diverge, while the finite remainders converge to finite values.

3.6 Results

The analytic expressions of the independent one- and two-loop finite remainders are provided in the ancillary files of Ref [1]. We present them as combinations of linearly independent rational coefficients and monomials of the square roots and of the finite remainder basis functions. The rational coefficients are expressed in terms of the MTs defined in Eq. 3.3.2. We evaluate the finite remainder function basis numerically by integrating the DEs of Eq. 3.4.6 with the method of the generalised

series expansions. We also provide `Mathematica` scripts which illustrate how to evaluate the finite remainders interfered with the tree-level amplitudes for all the partonic channels contributing to the process $pp \to b\bar{b}H$, which we label as:

$$\begin{aligned}
\mathbf{gg}: &\quad g(-p_3) + g(-p_4) \to \bar{b}(p_1) + b(p_2) + H(p_5)\,,\\
\mathbf{q\bar{q}}: &\quad q(-p_3) + \bar{q}(-p_4) \to \bar{b}(p_1) + b(p_2) + H(p_5)\,,\\
\mathbf{\bar{q}q}: &\quad \bar{q}(-p_3) + q(-p_4) \to \bar{b}(p_1) + b(p_2) + H(p_5)\,,\\
\mathbf{b\bar{b}}: &\quad b(-p_3) + \bar{b}(-p_4) \to \bar{b}(p_1) + b(p_2) + H(p_5)\,,\\
\mathbf{\bar{b}b}: &\quad \bar{b}(-p_3) + b(-p_4) \to \bar{b}(p_1) + b(p_2) + H(p_5)\,,\\
\mathbf{bb}: &\quad b(-p_3) + b(-p_4) \to b(p_1) + b(p_2) + H(p_5)\,,\\
\mathbf{\bar{b}\bar{b}}: &\quad \bar{b}(-p_3) + \bar{b}(-p_4) \to \bar{b}(p_1) + \bar{b}(p_2) + H(p_5)\,.
\end{aligned} \tag{3.6.1}$$

The interference between the finite remainders and the tree-level amplitudes summed over colour and helicity is given at leading colour by:

$$\sum_{\text{colour}} \sum_{\text{helicity}} \mathcal{A}^{(0)*} \mathcal{F}^{(L)} =: g_s^4 y_b^2 n^L N_c^\alpha \, \mathcal{H}^{(L)}\,, \tag{3.6.2}$$

where $\alpha = 3$ for $\mathbf{gg}$ and $\alpha = 2$ for all the other channels, and the *reduced squared finite remainders*, $\mathcal{H}^{(L)}$, are given explicitly for each channel by:

$$\begin{aligned}
\mathcal{H}^{(L)}_{\mathbf{gg}} = &\sum_{\text{helicity}} \Big[A^{(0)}(1_{\bar{b}}, 2_b, 3_g, 4_g, 5_H)\Big]^* F^{(L)}(1_{\bar{b}}, 2_b, 3_g, 4_g, 5_H)\\
&+ \sum_{\text{helicity}} \Big[A^{(0)}(1_{\bar{b}}, 2_b, 4_g, 3_g, 5_H)\Big]^* F^{(L)}(1_{\bar{b}}, 2_b, 4_g, 3_g, 5_H)\,,
\end{aligned} \tag{3.6.3}$$

$$\mathcal{H}^{(L)}_{\mathbf{q\bar{q}}} = \sum_{\text{helicity}} \Big[A^{(0)}(1_{\bar{b}}, 2_b, 3_{\bar{q}}, 4_q, 5_H)\Big]^* F^{(L)}(1_{\bar{b}}, 2_b, 3_{\bar{q}}, 4_q, 5_H)\,, \tag{3.6.4}$$

$$\mathcal{H}^{(L)}_{\mathbf{\bar{q}q}} = \sum_{\text{helicity}} \Big[A^{(0)}(1_{\bar{b}}, 2_b, 4_{\bar{q}}, 3_q, 5_H)\Big]^* F^{(L)}(1_{\bar{b}}, 2_b, 4_{\bar{q}}, 3_q, 5_H)\,, \tag{3.6.5}$$

$$\begin{aligned}
\mathcal{H}^{(L)}_{\mathbf{b\bar{b}}} = &\sum_{\text{helicity}} \Big[A^{(0)}(1_{\bar{b}}, 2_b, 3_{\bar{q}}, 4_q, 5_H) + A^{(0)}(3_{\bar{b}}, 4_b, 1_{\bar{q}}, 2_q, 5_H)\Big]^*\\
&\qquad \times \Big[F^{(L)}(1_{\bar{b}}, 2_b, 3_{\bar{q}}, 4_q, 5_H) + F^{(L)}(3_{\bar{b}}, 4_b, 1_{\bar{q}}, 2_q, 5_H)\Big]\\
&+ \sum_{\text{helicity}} \Big[A^{(0)}(1_{\bar{b}}, 4_b, 3_{\bar{q}}, 2_q, 5_H) + A^{(0)}(3_{\bar{b}}, 2_b, 1_{\bar{q}}, 4_q, 5_H)\Big]^*\\
&\qquad \times \Big[F^{(L)}(1_{\bar{b}}, 4_b, 3_{\bar{q}}, 2_q, 5_H) + F^{(L)}(3_{\bar{b}}, 2_b, 1_{\bar{q}}, 4_q, 5_H)\Big]\,,
\end{aligned} \tag{3.6.6}$$

$$\begin{aligned}
\mathcal{H}^{(L)}_{\mathbf{\bar{b}b}} = &\sum_{\text{helicity}} \Big[A^{(0)}(1_{\bar{b}}, 2_b, 4_{\bar{q}}, 3_q, 5_H) + A^{(0)}(4_{\bar{b}}, 3_b, 1_{\bar{q}}, 2_q, 5_H)\Big]^*\\
&\qquad \times \Big[F^{(L)}(1_{\bar{b}}, 2_b, 4_{\bar{q}}, 3_q, 5_H) + F^{(L)}(4_{\bar{b}}, 3_b, 1_{\bar{q}}, 2_q, 5_H)\Big]\\
&+ \sum_{\text{helicity}} \Big[A^{(0)}(1_{\bar{b}}, 3_b, 4_{\bar{q}}, 2_q, 5_H) + A^{(0)}(4_{\bar{b}}, 2_b, 1_{\bar{q}}, 3_q, 5_H)\Big]^*\\
&\qquad \times \Big[F^{(L)}(1_{\bar{b}}, 3_b, 4_{\bar{q}}, 2_q, 5_H) + F^{(L)}(4_{\bar{b}}, 2_b, 1_{\bar{q}}, 3_q, 5_H)\Big]\,,
\end{aligned} \tag{3.6.7}$$

$$\begin{aligned}
\mathcal{H}^{(L)}_{\mathbf{b\bar{b}}} = &\sum_{\text{helicity}} \Big[A^{(0)}(3_{\bar{b}}, 1_b, 4_{\bar{q}}, 2_q, 5_H) + A^{(0)}(4_{\bar{b}}, 2_b, 3_{\bar{q}}, 1_q, 5_H)\Big]^* \\
&\qquad \times \Big[F^{(L)}(3_{\bar{b}}, 1_b, 4_{\bar{q}}, 2_q, 5_H) + F^{(L)}(4_{\bar{b}}, 2_b, 3_{\bar{q}}, 1_q, 5_H)\Big] \\
&+ \sum_{\text{helicity}} \Big[A^{(0)}(3_{\bar{b}}, 2_b, 4_{\bar{q}}, 1_q, 5_H) + A^{(0)}(4_{\bar{b}}, 1_b, 3_{\bar{q}}, 2_q, 5_H)\Big]^* \\
&\qquad \times \Big[F^{(L)}(3_{\bar{b}}, 2_b, 4_{\bar{q}}, 1_q, 5_H) + F^{(L)}(4_{\bar{b}}, 1_b, 3_{\bar{q}}, 2_q, 5_H)\Big]\,, \qquad (3.6.8) \\
\mathcal{H}^{(L)}_{\bar{\mathbf{b}}\mathbf{b}} = &\sum_{\text{helicity}} \Big[A^{(0)}(1_{\bar{b}}, 3_b, 2_{\bar{q}}, 4_q, 5_H) + A^{(0)}(2_{\bar{b}}, 4_b, 1_{\bar{q}}, 3_q, 5_H)\Big]^* \\
&\qquad \times \Big[F^{(L)}(1_{\bar{b}}, 3_b, 2_{\bar{q}}, 4_q, 5_H) + F^{(L)}(2_{\bar{b}}, 4_b, 1_{\bar{q}}, 3_q, 5_H)\Big] \\
&+ \sum_{\text{helicity}} \Big[A^{(0)}(1_{\bar{b}}, 4_b, 3_{\bar{q}}, 2_q, 5_H) + A^{(0)}(2_{\bar{b}}, 3_b, 1_{\bar{q}}, 4_q, 5_H)\Big]^* \\
&\qquad \times \Big[F^{(L)}(1_{\bar{b}}, 4_b, 3_{\bar{q}}, 2_q, 5_H) + F^{(L)}(2_{\bar{b}}, 3_b, 1_{\bar{q}}, 4_q, 5_H)\Big]\,. \qquad (3.6.9)
\end{aligned}$$

We evaluate the permutations of the finite remainders numerically. The analytic continuation is performed by adding a small positive imaginary part to each s_{ij} and to p_5^2, which is done automatically by `DiffExp`.

To facilitate future checks, we provide here the benchmark evaluation at a physical point corresponding to the $pp \to b\bar{b}H$ scattering process:

$$\begin{aligned}
&s_{12} = \frac{49}{576}\,, \quad s_{23} = -\frac{15337}{2048}\,, \quad s_{34} = \frac{63}{4}\,, \quad s_{45} = -\frac{288491}{38912}\,, \\
&s_{15} = \frac{455}{64}\,, \quad p_5^2 = 7\,, \quad \text{tr}_5 = \mathrm{i}\frac{49\sqrt{50998583}}{1400832}\,, \qquad (3.6.10)
\end{aligned}$$

which corresponds to the following values of the MTs:

$$\begin{aligned}
&x_1 = \frac{49}{576}\,, \quad x_2 = -\frac{77405}{76608} - \mathrm{i}\frac{\sqrt{50998583}}{76608}\,, \quad x_3 = -\frac{557251}{411874} + \mathrm{i}\frac{95\sqrt{50998583}}{411874}\,, \\
&x_4 = -\frac{2817}{32}\,, \quad x_5 = -\frac{11290}{41629} - \mathrm{i}\frac{2\sqrt{50998583}}{41629}\,, \quad x_6 = -\frac{370917}{4256}\,. \qquad (3.6.11)
\end{aligned}$$

The values of the bare two-loop amplitudes normalised by the tree-level amplitudes, $\hat{A}^{(L)} = A^{(L)}/A^{(0)}$, for the independent mostly-plus helicity configurations of the subprocesses $0 \to \bar{b}bggH$ and $0 \to \bar{b}b\bar{q}qH$ are given in Tables 3.3 and 3.4. Table 3.5 shows the values of the two-loop reduced squared finite remainders $\mathcal{H}^{(2)}$. Analogous tables for the one-loop amplitudes are given in Appendix E.

To demonstrate the suitability of our results for phenomenological applications, we present the evaluation of the finite remainders interfered with the tree-level amplitudes on a univariate slice of the phase space. For this purpose, we parametrise the momenta for the scattering processes Eq. 3.2.1 in terms of angles and energy

$\bar{b}bggH$	helicity	ϵ^{-4}	ϵ^{-3}	ϵ^{-2}	ϵ^{-1}	ϵ^{0}
$\hat{A}^{(2),1}$	$++++$	4.5	$-11.9857 + 9.42478i$	$1.38005 - 40.6951i$	$37.5629 + 74.9878i$	$-160.364 - 16.4633i$
	$+++-$	4.5	$-11.9857 + 9.42478i$	$11.3257 - 12.3672i$	$-26.8161 + 82.1522i$	$-142.327 - 160.925i$
	$++-+$	4.5	$-11.9857 + 9.42478i$	$2.69154 - 41.4561i$	$35.9446 + 68.3748i$	$-132.233 - 11.7912i$
	$++--$	4.5	$-11.9857 + 9.42478i$	$21.8803 - 71.2779i$	$85.0932 + 67.5004i$	$-293.742 + 11.2118i$
$\hat{A}^{(2),n_f}$	$++++$	0	0.5	$-0.177826 + 1.04486i$	$-0.769158 - 3.80277i$	$-5.39544 + 7.05528i$
	$+++-$	0	0.5	$-0.192856 + 1.0472i$	$1.4513 + 2.42621i$	$-3.57357 + 44.5555i$
	$++-+$	0	0.5	$-0.192856 + 1.0472i$	$-0.467396 - 4.03798i$	$-3.83854 + 2.69906i$
	$++--$	0	0.5	$0.987798 + 0.631652i$	$3.957 - 5.16329i$	$33.7155 - 38.6759i$
$\hat{A}^{(2),n_f^2}$	$++++$	0	0	0	$0.00334 - 0.000519914i$	$0.00266436 + 0.0210796i$
	$+++-$	0	0	0	0	0
	$++-+$	0	0	0	0	0
	$++--$	0	0	0	$0.262368 - 0.0923434i$	$0.532893 + 1.66516i$

Table 3.3: Numerical values of the bare $\bar{b}bggH$ partial amplitudes at two loops (normalised to the tree-level amplitude) at the kinematic point in Eq. 3.6.11 for the four independent helicity configurations and the various closed fermion loops contributions.

fractions of the final state as:

$$\begin{aligned} p_1 &= \frac{y_1\sqrt{s}}{2}\,(1\,,1\,,0\,,0)\ , \\ p_2 &= \frac{y_2\sqrt{s}}{2}\,(1\,,\cos\theta\,,-\sin\theta\sin\phi\,,-\sin\theta\cos\phi)\ , \\ p_3 &= \frac{\sqrt{s}}{2}\,(-1\,,0\,,0\,,-1)\ , \\ p_4 &= \frac{\sqrt{s}}{2}\,(-1\,,0\,,0\,,1)\ , \end{aligned} \tag{3.6.12}$$

while p_5 is fixed by momentum conservation, $p_5 = -p_1 - p_2 - p_3 - p_4$. We have chosen

$\bar{b}b\bar{q}qH$	helicity	ϵ^{-4}	ϵ^{-3}	ϵ^{-2}	ϵ^{-1}	ϵ^{0}
$\hat{A}^{(2),1}$	$++{+}-$	2	-6.81012	$25.5694 + 17.9036i$	$-60.3404 - 6.4188i$	$48.2991 - 125.381i$
	$++-+$	2	-6.81012	$22.4573 + 14.9001i$	$-60.7797 + 3.42105i$	$96.4449 - 180.941i$
$\hat{A}^{(2),n_f}$	$++{+}-$	0	1.66667	$-4.60863 + 4.18879i$	$13.2979 - 5.52188i$	$4.96804 + 95.7191i$
	$++-+$	0	1.66667	$-4.60863 + 4.18879i$	$11.2232 - 7.52422i$	$-1.06892 + 93.2862i$
$\hat{A}^{(2),n_f^2}$	$++{+}-$	0	0	0.444444	$-0.969043 + 2.79253i$	$-6.91677 - 6.08868i$
	$++-+$	0	0	0.444444	$-0.969043 + 2.79253i$	$-6.91677 - 6.08868i$

Table 3.4: Numerical values of the bare $\bar{b}b\bar{q}qH$ partial amplitudes at two loops (normalised to the tree level amplitude) at the kinematic point in Eq. 3.6.11 for the four independent helicity configurations and the various closed fermion loops contributions.

channel	Re $\mathcal{H}^{(2),1}$	Re $\mathcal{H}^{(2),n_f}$	Re $\mathcal{H}^{(2),n_f^2}$
$\mathbf{gg}$	156680.6267	-41215.80337	405.9379563
$\mathbf{q\bar{q}}$	0.09391314268	-0.02045942258	-0.004225713438
$\mathbf{\bar{q}q}$	0.3494872243	-0.08069122736	-0.004225713438
$\mathbf{b\bar{b}}$	48640.80398	-26530.01855	2458.442153
$\mathbf{\bar{b}b}$	-141130.5373	42183.03094	3711.445449
$\mathbf{bb/\bar{b}\bar{b}}$	-53679.25708	1988.662899	894.7895467

Table 3.5: Numerical values of the two-loop reduced squared finite remainders $\mathcal{H}^{(2)}$ defined in Eqs. 3.6.3—3.6.9 at the kinematic point in Eq. 3.6.11 for the various closed fermion loops contributions and the scattering channels specified in Eq. 3.6.1.

the particle with momentum p_1 to be produced at an angle of $\pi/2$ with respect to the beam axis. Requiring that the Higgs boson is on-shell, $p_5^2 = m_H^2$, constrains the angle θ as:

$$\cos\theta = 1 + \frac{2}{y_1 y_2}\left(1 - y_1 - y_2 - \frac{m_H^2}{s}\right) . \tag{3.6.13}$$

To restrict the kinematics to a one-dimensional slice, we choose:

$$s = 1\,, \qquad \phi = \frac{1}{10}\,, \qquad y_1 = \frac{3}{5}\,, \qquad m_H = \frac{1}{10}\,. \tag{3.6.14}$$

The reality of the angle θ then restricts the free parameter y_2 to the interval $y_2 \in [\frac{39}{100}, \frac{39}{40}]$. In order to evaluate the finite remainders for all the processes shown in Eq. 3.6.1, we need to compute the finite remainder special functions at 16 permutations of each phase space point, as can be seen explicitly in Eqs. 3.6.3—3.6.9. We do this by integrating the system of canonical DEs in Eq. 3.4.6 with `DiffExp` using rationalised values of the invariants. The need for rational values arises from the fact that the series expansion method, implemented in `DiffExp`, is very sensitive to the values of input parameters, as it requires high precision throughout the intermediate steps. For each permutation of each point, we compute the 'distance' (technically speaking, the number of segments into which the integration contour is divided by `DiffExp`) from the six reference points provided in the ancillary files, and choose the closest one as the initial point for the integration. In Fig. 3.4, we plot the values of the one- and two-loop reduced squared finite remainders for all the processes defined in Eq. 3.6.1 as functions of the parameter y_2.

We stress that the purpose of the plots in Fig. 3.4 is merely to demonstrate that our results for the finite remainders can be evaluated reliably in the physical scattering region. Nothing can be inferred about the convergence of the perturbative expansion at the cross section level. One interesting feature which can be appreciated from Fig. 3.4 is the appearance of a loop-induced peak in the finite remainders for the channel $\bar{\mathbf{q}}\mathbf{q}$. The peak is absent at tree level for the same channel and up to two loops for $\mathbf{q}\bar{\mathbf{q}}$. The latter channel is related to $\bar{\mathbf{q}}\mathbf{q}$ by the exchange $3 \leftrightarrow 4$ of the external particles. We observe that the peak stems from the values of the finite remainder function basis, while the rational coefficients are not enhanced in that region. In order to pinpoint more precisely the origin of this phenomenon, we construct the explicit analytic expressions for some of the special functions which exhibit the peak, starting from their iterated integral expression obtained by solving the system of canonical DEs in Eq. 3.4.6. For instance:

$$\begin{aligned} h_4^{(2)} = {} & 2\,\mathrm{Li}_2\left(1 - \frac{s_{15}}{p_5^2}\right) + 2\,\mathrm{Li}_2\left(1 - \frac{s_{23}}{s_{15}}\right) - \frac{\pi^2}{4} + \frac{1}{2}\log^2\left(p_5^2\right) + \frac{1}{2}\log^2\left(-s_{45}\right) + 2\log^2\left(s_{15}\right) \\ & - \frac{1}{2}\log^2\left(-s_{23}\right) - 2\log\left(s_{15}\right)\log\left(s_{15} - s_{23}\right) + \log^2\left(s_{15} - s_{23}\right) + \log\left(p_5^2\right)\log\left(-s_{23}\right) \\ & - 2\log\left(p_5^2\right)\log\left(s_{15}\right) - \log\left(p_5^2\right)\log\left(-s_{14}\right) + 2\log\left(s_{15}\right)\log\left(-s_{14}\right) - \log\left(-s_{23}\right)\log\left(-s_{14}\right) \\ & + i\pi\left[\log\left(p_5^2\right) - 2\log\left(s_{15}\right) + 2\log\left(s_{15} - s_{23}\right) - \log\left(-s_{23}\right) - \log\left(-s_{14}\right)\right], \end{aligned} \tag{3.6.15}$$

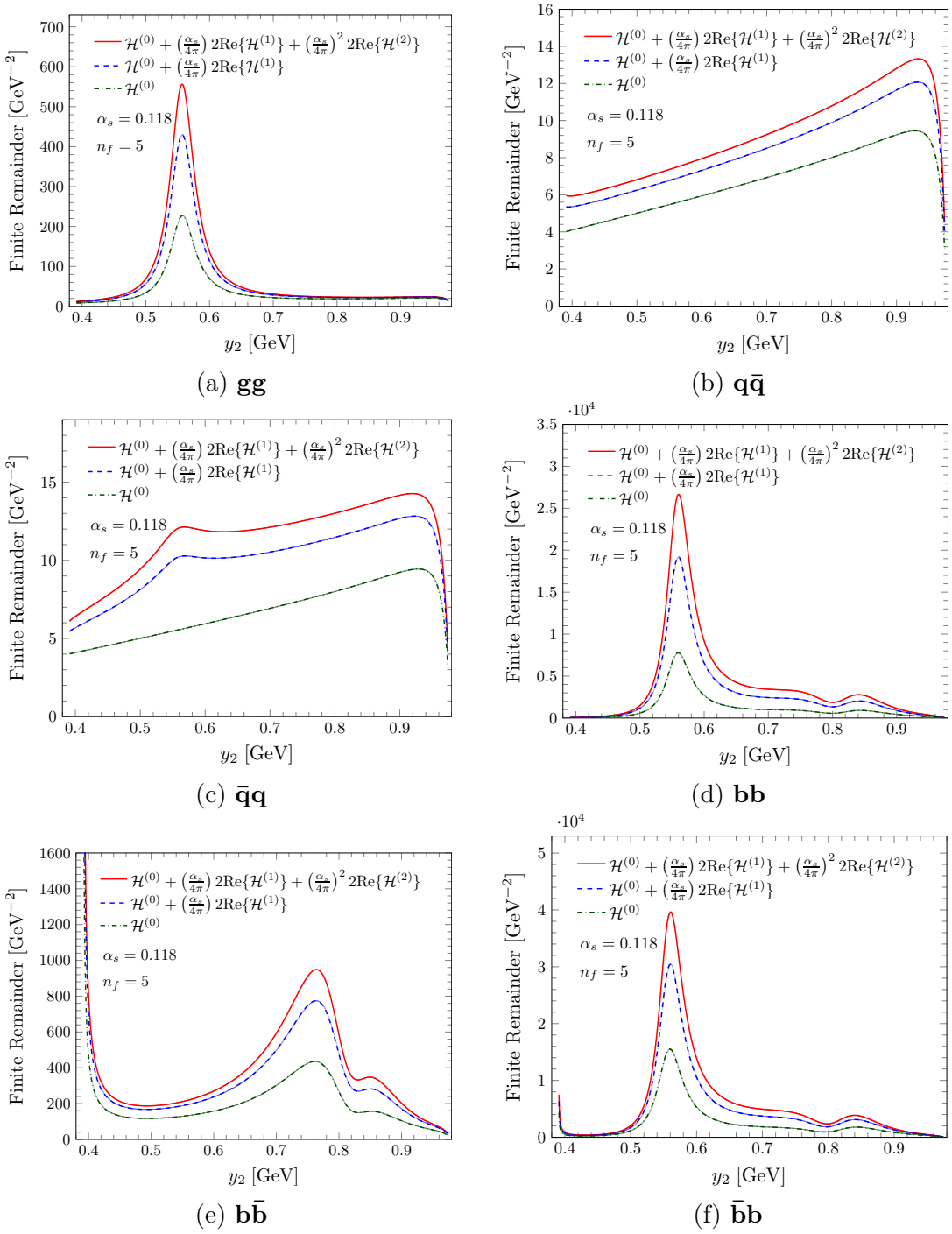

Figure 3.4: Reduced squared finite remainders $\mathcal{H}^{(L)}$ at tree level, one and two loops evaluated on the one-dimensional phase space slice defined in Eq. 3.6.12, as functions of the variable y_2, for the channels defined in Eq. 3.6.1.

which is well defined in the s_{34} physical scattering region. The analytic continuation to any other region is obtained by adding a small positive imaginary part to each s_{ij} and to p_5^2. We checked that the values of $h_4^{(2)}$ as given by Eq. 3.6.15 (and of its permutations) agree with the evaluation through the generalised series expansion.

The function $h_4^{(2)}$ exhibits no peak on the phase space sliced defined by Eqs. 3.6.12 and 3.6.14, and indeed the finite remainder for the channel $\mathbf{q\bar{q}}$ does not exhibit such feature. The permutation $3 \leftrightarrow 4$ of $h_4^{(2)}$, which contributes to $\mathbf{\bar{q}q}$, is instead peaked around $y_2 \approx 0.5566$. Thanks to the analytic expression Eq. 3.6.15, we can identify the source of the peak in the logarithms of s_{24}, which originate from the $\log(-s_{23})$'s in Eq. 3.6.15 upon swapping $3 \leftrightarrow 4$. Indeed, the tree-level amplitude for the subprocess $0 \to \bar{b}b\bar{q}qH$, given by Eq. 3.2.23, is manifestly free of $1/\langle 23\rangle$ poles. The $0 \to \bar{b}b\bar{q}qH$ diagrams with a $1/s_{23}$ pole would come with a loop and so end up scaling as $\log(-s_{23})$. While $\log(-s_{23})$ is not enhanced on the one-dimensional slice under consideration, its $3 \leftrightarrow 4$ permutation $\log(-s_{24})$, which contributes to $\mathcal{H}^{(L)}_{\mathbf{\bar{q}q}}$ for $L = 1, 2$, is peaked at $y_2 \approx 0.5566$, where s_{24} reaches its minimum absolute value on the slice. The tree-level amplitudes for the channel $\mathbf{gg}$ instead do have poles at $s_{23} = 0$, which can be seen explicitly in Eq. 3.2.22. Since $\mathcal{H}^{(L)}_{\mathbf{gg}}$ with $L = 1, 2$ receive contributions from the partial finite remainders in both the standard orientation and with the swap $3 \leftrightarrow 4$, as shown in Eq. 3.6.3, their plot in Fig. 3.4 (a) exhibits this peak already at tree level. The same holds for the $\mathbf{bb}$ and $\mathbf{\bar{b}\bar{b}}$ channels, as can be seen in Figs. 3.4 (d) and (f).

Also in Fig. 3.4, we observe divergences at $y_2 = 39/100$ for the processes $\mathbf{b\bar{b}}$ and $\mathbf{\bar{b}b}$. This divergence is associated with the propagator $1/s_{12}$, which can only appear in processes with two pairs of bottom quarks. In Eqs. 3.6.6 and 3.6.7 we can see the $q\bar{q}$ fermion pairs can appear with momenta p_1 and p_2, which is not the case for other processes. All the other features of the plots in Fig. 3.4 can be similarly understood in terms of tree-level propagators going on shell.

3.7 Summary

In this chapter, we have presented an analytic form for the two-loop QCD amplitudes to the process $pp \to b\bar{b}H$. It is the first complete set of helicity amplitudes provided for a $2 \to 3$ scattering process with an off-shell leg. In contrast to the recent $pp \to Wb\bar{b}$ computation of Ref. [182], which used the squared matrix element method (see Section 2.3) and Mandelstam invariants, we have constructed a rational parametrisation of the external kinematics in terms of momentum twistors. We have also improved on the function basis presented in Ref. [182] by identifying the missing relations between higher weight functions and products of lower weight ones. Moreover, we have used this basis to derive another one better suited to our finite remainders. The rational coefficients of the remainders were extracted from multiple evaluations over finite fields and IBP reduction. We obtained relatively compact results after determining the linear relations between the coefficients and performing

a univariate partial fraction decomposition on the fly. The final expressions were evaluated using the method of generalised series expansions as implemented in the `DiffExp` code [142].

The expressions have been validated in a number of ways and we observe that they exhibit a smooth behaviour in all scattering regions. Evaluation times appear to be suitable for phenomenological applications, especially since we have not tried to optimise the route through the phase space evaluations as has been done in other applications of the method [98, 99, 108, 203, 204].

The techniques presented here show promise for applications to other important scattering processes such as $pp \to V + 2j$ and $pp \to H + 2j$. We point out that the bases of pure MIs required for the non-planar topologies needed in these computations were made available in literature after the completion of our work [125].

Chapter 4

Two-loop helicity amplitudes for $pp \to W^{\pm}\gamma j$ production

In this chapter, we present the computation of the two-loop leading colour QCD helicity amplitudes for yet another process, $pp \to W(\to l\nu)\gamma + j$. We implement a complete reduction of the amplitudes, including the leptonic decay of the W-boson, using finite field arithmetic and extract the analytic finite remainders using a recently identified basis of special functions. Simplified analytic expressions are obtained after considering permutations of a rational kinematic parametrisation and multivariate partial fractioning. We demonstrate efficient numerical evaluation of the two-loop colour and helicity summed finite remainders for physical kinematics, and hence the suitability for phenomenological applications.

This chapter largely follows the structure of the previous one. In Section 4.2, we describe the structure of the amplitudes for $pp \to W\gamma j$ up to two loops, paying particular attention to the description of the decay of the W boson. In Section 4.3, we describe the finite field reduction setup used to extract the finite remainders, and propose an approach to simplify the analytic expressions of the latter based on a systematic search for a better parametrisation of the kinematics in terms of MTs. We describe a number of validation tests on our results in Section 4.4, and then present numerical results for the colour and helicity summed finite remainders in Section 4.5. We give our summary and outlook for the future in Section 4.6. Complete analytic expressions associated with the work in this chapter are provided in the ancillary files of Ref. [2].

4.1 Introduction

Processes with a pair of electroweak vector bosons ($W^{\pm}, Z, \gamma$) offer a wide range of observables which can test electroweak couplings and probe the Higgs sector of the SM. In particular, the production of a W boson in association with a photon ($pp \to W\gamma$) is one of the processes observed at the LHC with relatively large cross sections where clean signatures can be acquired when the W boson decays leptonically. $W\gamma$ production enables direct access to the $WW\gamma$ triple gauge boson coupling, which can be modified in certain new physics scenarios. Both ATLAS and CMS experiments have measured the $W\gamma$ process [208–213] and set the limit on the anomalous $WW\gamma$ coupling.

Predictions for $pp \to W^{\pm}\gamma$ are available through to next-to-next-to-leading order (NNLO) in QCD [214–216] and NLO in the electroweak (EW) coupling [217, 218] as well as combined NNLO in QCD and NLO in EW [219]. The colourless final state makes the process well suited for the q_T [220] and N-jettiness [221, 222] subtraction methods as implemented within the `Matrix` [223] and `MCFM` [224] Monte Carlo event generators, respectively. Resummed predictions including parton shower effects are now available [225], making this one of the most precisely known theoretical predictions. Experimental measurements are constantly improving and provide rich opportunities for precision SM tests [213, 226]. In order to suppress different types of backgrounds in the experimental analysis, it is a common practice to divide the measurement according to the jet multiplicities, i.e. $W\gamma$+0 jet, $W\gamma$+1 jet, $W\gamma$+2 jets, etc. Increasing the precision of the theoretical predictions for each of the jet bins amounts to computing higher order corrections to $W\gamma$ production in association with additional jets.

In this chapter, we present the first computation of the two-loop helicity amplitudes for the process $pp \to W^{\pm}(\to l^{\pm}\nu)\gamma + j$. The amplitude-level ingredients we provide will give useful information for future precision measurements of anomalous couplings and potentially for complete global fits of the Standard Model Effective Theory (SMEFT). A fully differential computation of $W\gamma + j$ at NNLO in QCD would also open up the possibility of N^{3}LO QCD predictions for $W\gamma$ production.

4.2 Structure of the Amplitudes

We compute the two-loop amplitudes for the production of a W^+ boson in association with a photon and a jet at hadron colliders, where the W^+ boson decays to a positron

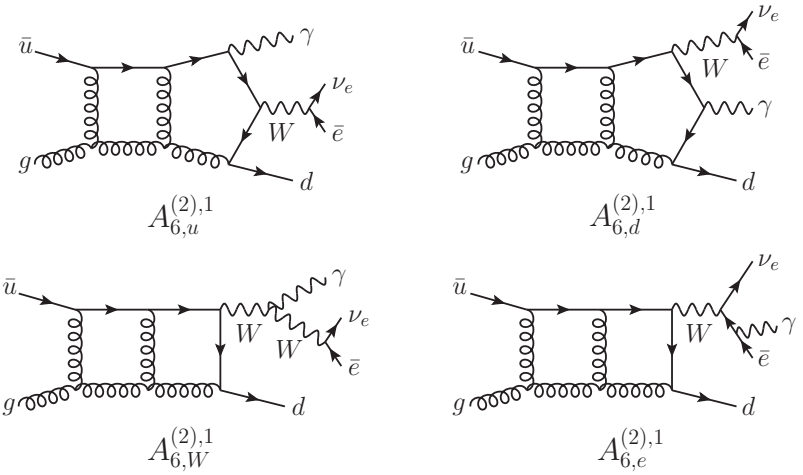

Figure 4.1: Sample two-loop Feynman diagrams for $W^+\gamma j$ production.

and an electron neutrino ($pp \to \nu_e e^+ \gamma j$), in the leading colour approximation:

$$0 \to \gamma(p_1,h_1) + \bar{u}(p_2,h_2) + g(p_3,h_3) + d(p_4,h_4) + \nu_e(p_5,h_5) + e^+(p_6,h_6)\,. \quad (4.2.1)$$

For simplicity, we henceforth denote this process as $W^+\gamma j$ production. Sample two-loop Feynman diagrams contributing at leading colour are shown in Figs. 4.1 and 4.2. The colour decomposition of the $W^+\gamma j$ L-loop amplitude is given by:

$$\mathcal{A}_6^{(L)}(1_\gamma,2_{\bar{u}},3_g,4_d,5_\nu,6_{\bar{e}}) = \sqrt{2}e g_W^2 g_s\, n^L\, (T^{a_3})_{i_4}^{\bar{i}_2}\, A_6^{(L)}(1_\gamma,2_{\bar{u}},3_g,4_d,5_\nu,6_{\bar{e}})\,, \quad (4.2.2)$$

where $n = m_\epsilon \alpha_s/(4\pi)$, $\alpha_s = g_s^2/(4\pi)$, $m_\epsilon = i(4\pi)^\epsilon \mathrm{e}^{-\epsilon\gamma_E}$, $\epsilon = (4-d)/2$ is the dimensional regulator, and T^a are the generators of $SU(N_c)$ in the fundamental representation, normalised according to $\mathrm{tr}(T^aT^b) = \delta^{ab}$. We denote by e, g_W and g_s the electron charge, the weak and strong coupling constants, respectively. The $W^+\gamma j$ amplitude can be further decomposed according to the source of photon radiation:

$$\begin{aligned} A_6^{(L)} = &\left[Q_u A_{6,u}^{(L)} + Q_d A_{6,d}^{(L)} + \left(\sum_q Q_q\right) A_{6,q}^{(L)}\right] P(s_{56}) \\ &+ (Q_u - Q_d)\left[A_{6,e}^{(L)} + A_{6,W}^{(L)} P(s_{56})\right] P(s_{156})\,, \end{aligned} \quad (4.2.3)$$

where $s_{ij} = (p_i+p_j)^2$ and $s_{ijk} = (p_i+p_j+p_k)^2$, Q_u and Q_d are the up- and down-quark charges respectively, the sum runs over the quark flavours q, while:

$$P(s) = \frac{1}{s - M_W^2 + \mathrm{i}M_W\Gamma_W}\,, \quad (4.2.4)$$

is the denominator factor of the W boson propagator. M_W and Γ_W are the mass and decay width of the W boson, respectively. The sub-amplitudes $A_{6,i}^{(L)}$ in Eq. 4.2.3

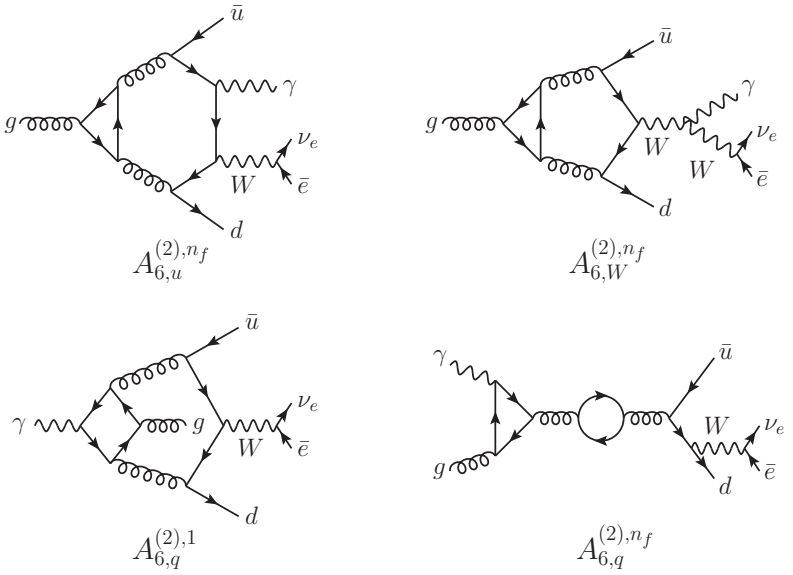

Figure 4.2: Sample two-loop Feynman diagrams for $W^+\gamma j$ production containing a closed fermion loop. $A_{6,q}^{(2),n_f}$ vanishes due to Furry's theorem.

are categorised as follows:

- $A_{6,u}^{(L)}$: the photon is radiated off the u quark;
- $A_{6,d}^{(L)}$: the photon is radiated off the d quark;
- $A_{6,W}^{(L)}$: the photon is radiated off the W boson;
- $A_{6,e}^{(L)}$: the photon is radiated off the positron;
- $A_{6,q}^{(L)}$: the photon is radiated off the internal quark loop.

We stress that the sub-amplitudes are not separately gauge invariant in the electroweak sector. Using the relation [216]:

$$P(s_{56})P(s_{156}) = \frac{1}{s_{156}-s_{56}}\Big[P(s_{56}) - P(s_{156})\Big] \tag{4.2.5}$$

we can rewrite Eq. 4.2.3 as:

$$\begin{aligned} A_6^{(L)} = {} & Q_u\left[A_{6,u}^{(L)} + \frac{1}{s_{156}-s_{56}}A_{6,W}^{(L)}\right]P(s_{56}) + Q_d\left[A_{6,d}^{(L)} - \frac{1}{s_{156}-s_{56}}A_{6,W}^{(L)}\right]P(s_{56}) \\ & + (Q_u - Q_d)\left[A_{6,e}^{(L)} - \frac{1}{s_{156}-s_{56}}A_{6,W}^{(L)}\right]P(s_{156}) + \left(\sum_q Q_q\right)A_{6,q}^{(L)}P(s_{56})\,, \end{aligned} \tag{4.2.6}$$

such that the combinations of sub-amplitudes in the square brackets and $A^{(L)}_{6,q}$ are the gauge invariant pieces. We further decompose the sub-amplitudes according to their closed fermion loop contributions. At leading colour, we have:

$$\begin{aligned} A^{(1)}_{6,i} &= N_c A^{(1),1}_{6,i}\,, \\ A^{(2)}_{6,i} &= N_c^2 A^{(2),1}_{6,i} + N_c n_f A^{(2),n_f}_{6,i}\,, \\ A^{(2)}_{6,q} &= N_c A^{(2),1}_{6,q}\,, \end{aligned} \tag{4.2.7}$$

where $i = u, d, W, e$, and n_f is the number of massless quark flavours running in the loop. We note that $A^{(L)}_{6,q}$ vanishes at tree level and one loop, while at two loops it includes non-planar contributions, and thus will not be considered in this work.

The coupling of the W boson to fermions involves vector and axial-vector $(V-A)$ vertices in the form of $\gamma^\mu(1-\gamma_5)/2$. The massless fermion pairs that are coupled to the W boson are connected to the external states and the $V-A$ coupling fixes the helicity of the fermion pairs. Therefore, we only need to take into account the vector coupling of the W boson to fermions when computing the helicity amplitudes. The contributing helicity configurations are:

$$A^{(L)}_6(1^{\pm}_\gamma, 2^+_{\bar{u}}, 3^{\pm}_g, 4^-_d, 5^-_\nu, 6^+_{\bar{e}})\,.$$

We choose $+{+}{+}{-}{-}{+}$ and $-{+}{+}{-}{-}{+}$ as the independent helicity configurations and focus on them. We obtain the amplitudes in the other helicity configurations from the independent ones by suitably permuting the external momenta and conjugating space-time parity.

The sub-amplitudes $A^{(L)}_{6,u}$ and $A^{(L)}_{6,d}$ are related by:

$$A^{(L)}_{6,u}(1^{h_1}_\gamma, 2^+_{\bar{u}}, 3^{h_3}_g, 4^-_d, 5^{h_5}_\nu, 6^{h_6}_{\bar{e}}) = A^{(L)}_{6,d}(1^{h_1}_\gamma, 4^-_{\bar{u}}, 3^{h_3}_g, 2^+_d, 5^{h_5}_\nu, 6^{h_6}_{\bar{e}})\,. \tag{4.2.8}$$

As a result, we can limit ourselves to computing the $A^{(L)}_{6,d}$ sub-amplitudes with the following helicity configurations:

$$A^{(L)}_{6,d}(1^{\pm}_\gamma, 2^{\pm}_{\bar{u}}, 3^{\pm}_g, 4^{\mp}_d, 5^-_\nu, 6^+_{\bar{e}})\,.$$

The independent helicity amplitudes for $A^{(L)}_{6,u}$ are then obtained through:

$$A^{(L)}_{6,u}(1^{\pm}_\gamma, 2^+_{\bar{u}}, 3^+_g, 4^-_d, 5^-_\nu, 6^+_{\bar{e}}) = A^{(L)}_{6,d}(1^{\pm}_\gamma, 4^-_{\bar{u}}, 3^+_g, 2^+_d, 5^-_\nu, 6^+_{\bar{e}})\,. \tag{4.2.9}$$

The pole structure of the unrenormalised $W^+\gamma j$ amplitudes in the HV scheme at one and two loops is given by [23–26]:

$$P^{(1)}_6 = 2I_1(\epsilon) + \frac{\beta_0}{2\epsilon}, \tag{4.2.10}$$

$$P_6^{(2)} = 2I_1(\epsilon)\left(\hat{A}_6^{(1)} - \frac{\beta_0}{2\epsilon}\right) + 4I_2(\epsilon) + \frac{3\beta_0}{2\epsilon}\hat{A}_6^{(1)} - \frac{3\beta_0^2}{8\epsilon^2} + \frac{\beta_1}{4\epsilon}\,, \tag{4.2.11}$$

where $\hat{A}_6^{(1)}$ is the unrenormalised one-loop amplitude divided by the tree-level amplitude. The $I_2(\epsilon)$ operator is given by:

$$I_2(\epsilon) = -\frac{1}{2}I_1(\epsilon)\left[I_1(\epsilon) + \frac{\beta_0}{\epsilon}\right] + \frac{N(\epsilon)}{N(2\epsilon)}\left[\frac{\beta_0}{2\epsilon} + \frac{\gamma_1^{\rm cusp}}{8}\right] I_1(2\epsilon) + H^{(2)}(\epsilon)\,, \tag{4.2.12}$$

while the $I_1(\epsilon)$ operator is given at leading colour by:

$$I_1(\epsilon) = -N_c\frac{N(\epsilon)}{2}\left(\frac{1}{\epsilon^2} + \frac{3}{4\epsilon} + \frac{\beta_0}{4N_c\epsilon}\right)\left[\,(-s_{23})^{-\epsilon} + (-s_{34})^{-\epsilon}\,\right], \tag{4.2.13}$$

where $N(\epsilon) = \mathrm{e}^{\epsilon\gamma_E}/\Gamma(1-\epsilon)$ and:

$$H^{(2)}(\epsilon) = \frac{1}{16\epsilon}\left\{\left(2\gamma_1^q + \gamma_1^g\right) - \gamma_1^{\rm cusp}\left(\frac{\gamma_0^q}{2} + \frac{\gamma_0^g}{4}\right) + \frac{\pi^2}{8}\beta_0\gamma_0^{\rm cusp}\left(C_F + \frac{C_A}{2}\right)\right\}. \tag{4.2.14}$$

The β-function coefficients and anomalous dimensions are tabulated in Appendix D. We stress that the pole terms in Eqs. 4.2.10 and 4.2.11 include both the UV and IR singularities. We then extract the L-loop partial finite remainder by subtracting the poles $P_6^{(L)}$ from the unrenormalised partial amplitude $A_6^{(L)}$ and sending ϵ to 0:

$$F_6^{(L)} = \lim_{\epsilon\to 0}\left[A_6^{(L)} - P_6^{(L)}A_6^{(0)}\right]. \tag{4.2.15}$$

The finite remainder $F_6^{(L)}$ follows the same decomposition as the unrenormalised partial amplitude $A_6^{(L)}$ (see Eqs. 4.2.3 and 4.2.7):

$$F_6^{(L)} = \left[Q_u F_{6,u}^{(L)} + Q_d F_{6,d}^{(L)}\right] P(s_{56}) + (Q_u - Q_d)\left[F_{6,e}^{(L)} + F_{6,W}^{(L)}P(s_{56})\right] P(s_{156})\,, \tag{4.2.16}$$

with:

$$\begin{aligned} F_{6,i}^{(1)} &= N_c F_{6,i}^{(1),1} + n_f F_{6,i}^{(1),n_f}\,, \\ F_{6,i}^{(2)} &= N_c^2 F_{6,i}^{(2),1} + N_c n_f F_{6,i}^{(2),n_f} + n_f^2 F_{6,i}^{(2),n_f^2}\,, \end{aligned} \tag{4.2.17}$$

where $i = u, d, W, e$. We note that, although the bare sub-amplitudes $A_{6,i}^{(1),n_f}$ and $A_{6,i}^{(2),n_f^2}$ vanish, there are finite contributions to the finite remainders $F_{6,i}^{(1),n_f}$ and $F_{6,i}^{(2),n_f^2}$ from the UV renormalisation and IR subtraction terms specified in Eqs. 4.2.10 and 4.2.11. As discussed below Eqs. 4.2.7, we defer the computation of $F_{6,q}^{(2)}$, as it involves the non-planar integrals.

For the charge-conjugated process, i.e. $pp \to \bar{\nu}_e e^- \gamma j$, we consider the amplitudes for:

$$0 \to \gamma(p_1,h_1) + \bar{d}(p_2,h_2) + g(p_3,h_3) + u(p_4,h_4) + e^-(p_5,h_5) + \bar{\nu}_e(p_6,h_6)\,,$$

which we denote by $W^-\gamma j$ production. The amplitudes for $W^-\gamma j$ production can be obtained from the $W^+\gamma j$ results through the following relation:

$$A_6^{(L)}(1_\gamma^{-h_1}, 2_{\bar{d}}^+, 3_g^{-h_3}, 4_u^-, 5_e^-, 6_{\bar{\nu}}^+) = \left[A_6^{(L)}(1_\gamma^{h_1}, 4_{\bar{u}}^+, 3_g^{h_3}, 2_d^-, 6_\nu^-, 5_{\bar{e}}^+)\right]_{\langle ij\rangle\leftrightarrow[ij]} . \quad (4.2.18)$$

4.3 Amplitude Computation

In this section, we describe the computation of the two-loop $W^+\gamma j$ amplitudes in the leading colour approximation. To derive their analytic form, we closely (albeit with certain departures) follow the framework adopted throughout Chapter 3 and described extensively in Chapter 2. Crucially, apart from the techniques presented so far, in this work we also make use of the the four-dimensional projector method [227, 228], which we will introduce soon.

Instead of computing the loop amplitudes using the full six-particle kinematics, we detach the leptonic decay of the W boson from the amplitude and only compute the W-production amplitudes. For the $A_{6,u}^{(L)}$ and $A_{6,d}^{(L)}$ sub-amplitudes, the W-production amplitude is a five-point amplitude with an off-shell leg (denoted by $A_{5,u/d}^{(L)\mu}$), while for the $A_{6,W}^{(L)}$ and $A_{6,e}^{(L)}$ sub-amplitudes, the W-production amplitude is a four-point amplitude with an off-shell leg (denoted by $A_4^{(L)\mu}$):

$$A_{6,u/d}^{(L)}(p_1,p_2,p_3,p_4,p_5,p_6) = A_{5,u/d}^{(L)\mu}(p_1,p_2,p_3,p_4,p_W)\; L_{A,\mu}(p_5,p_6)\,, \quad (4.3.1)$$

$$A_{6,e/W}^{(L)}(p_1,p_2,p_3,p_4,p_5,p_6) = A_4^{(L)\mu}(p_2,p_3,p_4,\tilde{p}_W)\; L_{B,\mu}^{e/W}(p_1,p_5,p_6)\,, \quad (4.3.2)$$

where $p_W = p_5 + p_6$ and $\tilde{p}_W = p_1 + p_5 + p_6$; $L_{B,\mu}^e$ ($L_{B,\mu}^W$) is the decay current with the photon emitted from the positron (W boson), and $L_{A,\mu}$ is simply the $W^+ \to \nu e^+$ decay current. The QCD corrections affect only the W-production amplitudes $A_{5,u/d}^{(L)\mu}$ and $A_4^{(L)\mu}$. We adopt the same decomposition for the finite remainders:

$$F_{6,u/d}^{(L)}(p_1,p_2,p_3,p_4,p_5,p_6) = F_{5,u/d}^{(L)\mu}(p_1,p_2,p_3,p_4,p_W)\; L_{A,\mu}(p_5,p_6)\,, \quad (4.3.3)$$

$$F_{6,e/W}^{(L)}(p_1,p_2,p_3,p_4,p_5,p_6) = F_4^{(L)\mu}(p_2,p_3,p_4,\tilde{p}_W)\; L_{B,\mu}^{e/W}(p_1,p_5,p_6)\,. \quad (4.3.4)$$

In the next subsections, we discuss the computation of $F_{5,d}^{(L)\mu}$ and $F_4^{(L)\mu}$. We recall that $F_{6,u}^{(L)}$ can be obtained from $F_{6,d}^{(L)}$ through the amplitude-level relation given in Eq. 4.2.8, which we rewrite here for the finite remainders:

$$F_{6,u}^{(L)}(1_\gamma^{h_1}, 2_{\bar{u}}^+, 3_g^{h_3}, 4_d^-, 5_\nu^{h_5}, 6_{\bar{e}}^{h_6}) = F_{6,d}^{(L)}(1_\gamma^{h_1}, 4_{\bar{u}}^-, 3_g^{h_3}, 2_d^+, 5_\nu^{h_5}, 6_{\bar{e}}^{h_6})\,. \quad (4.3.5)$$

We begin by describing how we parameterise the kinematics. Next, we discuss how we decompose the W-production five- and four-particle amplitudes, in Sections 4.3.2

and 4.3.3 respectively, using the projector method. Section 4.3.4 is devoted to the finite-field setup which we use to reconstruct the analytic expressions of the finite remainders as linear combinations of rational coefficients and monomials of independent special functions. In Section 4.3.5, we present a strategy which allows us to simplify dramatically the expressions of the coefficients. Finally, in Section 4.3.6 we discuss how our analytic results for the minimal set of independent finite remainders can be used efficiently to evaluate numerically all the contributions to the squared finite remainder summed over helicity and colour.

4.3.1 Kinematics

In this section, we describe the kinematics of the process $W^+\gamma j$ in Eq. 4.2.1. All the external momenta p_i^μ are massless:

$$p_i^2 = 0 \quad \forall\, i = 1, \ldots, 6\,, \tag{4.3.6}$$

and taken to be outgoing, so that momentum conservation is:

$$\sum_{i=1}^{6} p_i = 0\,. \tag{4.3.7}$$

We consider the external momenta p_i^μ to live in a four-dimensional Minkowski space. As a result, there are eight independent scalar invariants, which we choose as:

$$\vec{s}_6 = \{s_{12}, s_{23}, s_{34}, s_{45}, s_{56}, s_{16}, s_{123}, s_{234}\}\ . \tag{4.3.8}$$

We also use the pseudo-scalar invariant tr_5, defined in Eq. 3.2.6, which captures the parity information of the phase space.

Only a subset of these invariants are relevant for the computation of $A_{5,d}^{(L)\mu}$, which has five-point kinematics with an external massive particle. We choose the following independent five-point scalar invariants for computing $A_{5,d}^{(L)\mu}$:

$$\vec{s}_5 = \{s_{12}, s_{23}, s_{34}, s_{123}, s_{234}, s_{56}\}\ , \tag{4.3.9}$$

together with tr_5. Even fewer variables are relevant for $A_4^{(L)\mu}$. Since the latter has four-point kinematics with an external massive particle, no pseudo-scalar invariant can be formed and it is thus independent of tr_5. Moreover, it depends only on three of the scalar invariants in $\vec{s}_5$. Nonetheless, we view it as a function of $\vec{s}_5$ in order to have a homogeneous setup.

When attaching the W-boson decay currents ($L_{A,\mu}$ and $L_{B,\mu}^{e/W}$) to $A_{5,d}^{(L)\mu}$ and $A_4^{(L)\mu}$ (see Eqs. 4.3.1 and 4.3.2), we find it convenient to describe the massless six-point kinemat-

ics using a parametrisation based on MTs. We adopt the following parametrisation (see the discussion in Section 2.5):

$$Z = \begin{pmatrix} 1 & 0 & y_1 & y_2 & y_3 & y_4 \\ 0 & 1 & 1 & 1 & 1 & 1 \\ 0 & 0 & 0 & \frac{x_5}{x_2} & x_6 & 1 \\ 0 & 0 & 1 & 1 & x_7 & 1 - \frac{x_8}{x_5} \end{pmatrix}, \tag{4.3.10}$$

where we used the short-hand notation $y_i = \sum_{j=1}^{i} \prod_{k=1}^{j} \frac{1}{x_k}$. The eight MTs x_i are related to the external momenta through:

$$\begin{aligned} &x_1 = s_{12}\,, \quad x_2 = -\frac{\mathrm{tr}_+(1234)}{s_{12}s_{34}}\,, \qquad x_3 = -\frac{\mathrm{tr}_+(1345)}{s_{45}s_{13}}\,, \qquad x_4 = -\frac{\mathrm{tr}_+(1456)}{s_{14}s_{56}}\,, \\ &x_5 = \frac{s_{23}}{s_{12}}\,, \quad x_6 = -\frac{\mathrm{tr}_+(15(3+4)2)}{s_{12}s_{15}}\,, \quad x_7 = \frac{\mathrm{tr}_+(51(2+3)(2+3+4))}{s_{15}s_{23}}\,, \quad x_8 = \frac{s_{123}}{s_{12}}\,, \end{aligned} \tag{4.3.11}$$

with $\mathrm{tr}_\pm(ij\cdots kl) = \mathrm{tr}((1 \pm \gamma_5)\not{p}_i\not{p}_j\cdots\not{p}_k\not{p}_l)/2$. Note that the MTs x_i in general transform in a non-trivial way under space-time parity. We implement the action of parity on MT expressions as a change of MTs which leave unchanged the scalar invariants and flips the sign of tr_5. The definition of the parity-flipped MTs can be obtained by trading tr_+ for tr_- in Eqs. 4.3.11.

4.3.2 Structure of the five-particle W-production amplitudes

We decompose the five-point W-production amplitude $A_{5,d}^{(L)\mu}$ using the external momenta (p_1, p_2, p_3, p_4) as the spanning basis:

$$A_{5,d}^{(L)\mu} = p_1^\mu a_1^{(L)} + p_2^\mu a_2^{(L)} + p_3^\mu a_3^{(L)} + p_4^\mu a_4^{(L)}\,. \tag{4.3.12}$$

The coefficients $a_i^{(L)}$ can be obtained by inverting the system of equations:

$$a_i^{(L)} = \sum_{j=1}^{4} \left(\Delta^{-1}\right)_{ij} \tilde{A}_{5,j}^{(L)}\,, \tag{4.3.13}$$

where:

$$\Delta_{ij} = p_i \cdot p_j\,, \tag{4.3.14}$$

$$\tilde{A}_{5,i}^{(L)} = p_i \cdot A_{5,d}^{(L)}\,. \tag{4.3.15}$$

The *contracted amplitudes* $\tilde{A}_{5,i}^{(L)}$ are computed by first generating the five-point process with an on-shell W boson, followed by replacing the W-boson polarisation

vector by the four external momenta in the spanning basis, (p_1, p_2, p_3, p_4). We then apply tensor decomposition, taking into account the four-dimensional nature of the external states as proposed in Refs. [227, 228], to express each contracted amplitude $\tilde{A}^{(L)}_{5,i}$ as a linear combination of 8 independent tensor structures $\{T_j\}_{j=1}^{8}$:

$$\tilde{A}^{(L)}_{5,i} = \sum_{j=1}^{8} T_j \alpha^{(L)}_{i,j} \,, \tag{4.3.16}$$

where:

$$\begin{aligned}
T_1 &= \bar{u}(p_4)\not{p}_1 v(p_2)\; p_2\cdot\varepsilon(p_1,q_1)\; p_2\cdot\varepsilon(p_3,q_3)\,,\\
T_2 &= \bar{u}(p_4)\not{p}_1 v(p_2)\; p_2\cdot\varepsilon(p_1,q_1)\; p_4\cdot\varepsilon(p_3,q_3)\,,\\
T_3 &= \bar{u}(p_4)\not{p}_1 v(p_2)\; p_4\cdot\varepsilon(p_1,q_1)\; p_2\cdot\varepsilon(p_3,q_3)\,,\\
T_4 &= \bar{u}(p_4)\not{p}_1 v(p_2)\; p_4\cdot\varepsilon(p_1,q_1)\; p_4\cdot\varepsilon(p_3,q_3)\,,\\
T_5 &= \bar{u}(p_4)\not{p}_3 v(p_2)\; p_2\cdot\varepsilon(p_1,q_1)\; p_2\cdot\varepsilon(p_3,q_3)\,,\\
T_6 &= \bar{u}(p_4)\not{p}_3 v(p_2)\; p_2\cdot\varepsilon(p_1,q_1)\; p_4\cdot\varepsilon(p_3,q_3)\,,\\
T_7 &= \bar{u}(p_4)\not{p}_3 v(p_2)\; p_4\cdot\varepsilon(p_1,q_1)\; p_2\cdot\varepsilon(p_3,q_3)\,,\\
T_8 &= \bar{u}(p_4)\not{p}_3 v(p_2)\; p_4\cdot\varepsilon(p_1,q_1)\; p_4\cdot\varepsilon(p_3,q_3)\,.
\end{aligned} \tag{4.3.17}$$

Here, q_1 and q_3 are arbitrary reference vectors for the photon and the gluon polarisation states, respectively. We set $q_1 = p_3$ and $q_3 = p_1$ throughout our computation. The tensor coefficients $\alpha^{(L)}_{i,j}$ can be obtained by:

$$\alpha^{(L)}_{i,j} = \sum_{k=1}^{8} \left(\Theta^{-1}\right)_{jk} \sum_{\text{pol}} T_k^{\dagger} \tilde{A}^{(L)}_{5,i} \,, \tag{4.3.18}$$

where:

$$\Theta_{ij} = \sum_{\text{pol}} T_i^{\dagger} T_j \,. \tag{4.3.19}$$

The gluon and photon polarisation sums follow from Eq. 1.1.12. We also specify the helicity states of the spinors and polarisation vectors in the tensor structures $\{T_j\}_{j=1}^{8}$:

$$\begin{aligned}
T_1^{h_1h_2h_3h_4} &= \bar{u}(p_4,h_4)\not{p}_1 v(p_2,h_2)\; p_2\cdot\varepsilon(p_1,q_1,h_1)\; p_2\cdot\varepsilon(p_3,q_3,h_3)\,,\\
T_2^{h_1h_2h_3h_4} &= \bar{u}(p_4,h_4)\not{p}_1 v(p_2,h_2)\; p_2\cdot\varepsilon(p_1,q_1,h_1)\; p_4\cdot\varepsilon(p_3,q_3,h_3)\,,\\
T_3^{h_1h_2h_3h_4} &= \bar{u}(p_4,h_4)\not{p}_1 v(p_2,h_2)\; p_4\cdot\varepsilon(p_1,q_1,h_1)\; p_2\cdot\varepsilon(p_3,q_3,h_3)\,,\\
T_4^{h_1h_2h_3h_4} &= \bar{u}(p_4,h_4)\not{p}_1 v(p_2,h_2)\; p_4\cdot\varepsilon(p_1,q_1,h_1)\; p_4\cdot\varepsilon(p_3,q_3,h_3)\,,\\
T_5^{h_1h_2h_3h_4} &= \bar{u}(p_4,h_4)\not{p}_3 v(p_2,h_2)\; p_2\cdot\varepsilon(p_1,q_1,h_1)\; p_2\cdot\varepsilon(p_3,q_3,h_3)\,,\\
T_6^{h_1h_2h_3h_4} &= \bar{u}(p_4,h_4)\not{p}_3 v(p_2,h_2)\; p_2\cdot\varepsilon(p_1,q_1,h_1)\; p_4\cdot\varepsilon(p_3,q_3,h_3)\,,
\end{aligned} \tag{4.3.20}$$

$$T_7^{h_1h_2h_3h_4} = \bar{u}(p_4,h_4)\not{p}_3 v(p_2,h_2)\; p_4\cdot\varepsilon(p_1,q_1,h_1)\; p_2\cdot\varepsilon(p_3,q_3,h_3)\,,$$
$$T_8^{h_1h_2h_3h_4} = \bar{u}(p_4,h_4)\not{p}_3 v(p_2,h_2)\; p_4\cdot\varepsilon(p_1,q_1,h_1)\; p_4\cdot\varepsilon(p_3,q_3,h_3)\,,$$

from which we obtain the contracted helicity amplitudes:

$$\tilde{A}_{5,i}^{(L),h_1h_2h_3h_4} = \sum_{j,k=1}^{8} T_j^{h_1h_2h_3h_4} \left(\Theta^{-1}\right)_{jk} \tilde{\mathcal{A}}_{5,k\,i}^{(L)}\,, \tag{4.3.21}$$

with:

$$\tilde{\mathcal{A}}_{5,k\,i}^{(L)} = \sum_{\text{pol}} T_k^\dagger \tilde{A}_{5,i}^{(L)}\,. \tag{4.3.22}$$

We carry out the same decomposition for the five-particle finite remainder $F_{5,d}^{(L)\mu}$, arriving at the following formula for the contracted helicity finite remainders:

$$\tilde{F}_{5,i}^{(L),h_1h_2h_3h_4} = \sum_{j,k=1}^{8} T_j^{h_1h_2h_3h_4} \left(\Theta^{-1}\right)_{jk} \tilde{\mathcal{F}}_{5,k\,i}^{(L)}\,, \tag{4.3.23}$$

where:

$$\tilde{\mathcal{F}}_{5,k\,i}^{(L)} = \sum_{\text{pol}} T_k^\dagger\, p_{i\,\mu}\, F_{5,d}^{(L)\mu}\,. \tag{4.3.24}$$

As discussed in Section 4.2, the independent helicity configurations which we need to compute are:

$$\left\{\tilde{F}_{5,i}^{(L),+++-}, \tilde{F}_{5,i}^{(L),-++-}, \tilde{F}_{5,i}^{(L),+-++}, \tilde{F}_{5,i}^{(L),--++}\right\}\,. \tag{4.3.25}$$

We note that it is possible to compute directly the contracted finite remainders $\tilde{F}_{5,i}^{(L)}$ without specifying the helicity states. In our setup, however, such a computation would lead to more complicated analytic expressions as compared to the results obtained for the contracted helicity amplitudes.

4.3.3 Structure of the four-particle W-production amplitudes

The four-particle W-production amplitude $A_4^{(L)\mu}$ has been computed in the context of $W+1j$ production at the LHC ($q\bar{q}\to Wg$) [214], which is a crossing of the $e^+e^-\to q\bar{q}g$ amplitude [229]. In our case, it is convenient to express $A_4^{(L)\mu}$ in terms of the same special function basis as $A_{5,d}^{(L)\mu}$. This guarantees a uniform combination of the different contributions to the full amplitude. We therefore re-derive the $A_4^{(L)\mu}$ amplitude using our computational framework. We decompose the $A_4^{(L)\mu}$ amplitude

using the following tensor structures [229]:

$$A_4^{(L)\mu}(p_2,p_3,p_4) = \sum_{i=1}^{7} b_i^{(L)} Y_i^{\mu}\,, \tag{4.3.26}$$

where:

$$\begin{aligned}
Y_1^{\mu} &= \bar{u}(p_4)\not{p}_3 v(p_2)\,\varepsilon_3\cdot p_4\, p_4^{\mu} - p_3\cdot p_4\,\bar{u}(p_4)\not{\varepsilon}_3 v(p_2)\, p_4^{\mu} \\
&\quad - (p_2\cdot p_4 + p_3\cdot p_4)\left[\bar{u}(p_4)\not{p}_3 v(p_2)\,\varepsilon_3^{\mu} - \bar{u}(p_4)\not{\varepsilon}_3 v(p_2)\, p_3^{\mu}\right]\,, \\
Y_2^{\mu} &= \bar{u}(p_4)\not{p}_3 v(p_2)\,\varepsilon_3\cdot p_4\, p_3^{\mu} - p_3\cdot p_4\,\bar{u}(p_4)\not{\varepsilon}_3 v(p_2)\, p_3^{\mu} \\
&\quad - (p_2\cdot p_3 + p_3\cdot p_4)\left[\bar{u}(p_4)\not{p}_3 v(p_2)\,\varepsilon_3^{\mu} - \bar{u}(p_4)\not{\varepsilon}_3 v(p_2)\, p_3^{\mu}\right]\,, \\
Y_3^{\mu} &= \bar{u}(p_4)\not{p}_3 v(p_2)\,\varepsilon_3\cdot p_4\, p_2^{\mu} - p_3\cdot p_4\,\bar{u}(p_4)\not{\varepsilon}_3 v(p_2)\, p_2^{\mu} \\
&\quad - (p_2\cdot p_3 + p_2\cdot p_4)\left[\bar{u}(p_4)\not{p}_3 v(p_2)\,\varepsilon_3^{\mu} - \bar{u}(p_4)\not{\varepsilon}_3 v(p_2)\, p_3^{\mu}\right]\,, \\
Y_4^{\mu} &= \bar{u}(p_4)\not{p}_3 v(p_2)\,\varepsilon_3\cdot p_2\, p_4^{\mu} - p_2\cdot p_3\,\bar{u}(p_4)\not{\varepsilon}_3 v(p_2)\, p_4^{\mu}\,, \\
Y_5^{\mu} &= \bar{u}(p_4)\not{p}_3 v(p_2)\,\varepsilon_3\cdot p_2\, p_3^{\mu} - p_2\cdot p_3\,\bar{u}(p_4)\not{\varepsilon}_3 v(p_2)\, p_3^{\mu}\,, \\
Y_6^{\mu} &= \bar{u}(p_4)\not{p}_3 v(p_2)\,\varepsilon_3\cdot p_2\, p_2^{\mu} - p_2\cdot p_3\,\bar{u}(p_4)\not{\varepsilon}_3 v(p_2)\, p_2^{\mu}\,, \\
Y_7^{\mu} &= p_3\cdot p_4\,\bar{u}(p_4)\gamma^{\mu} v(p_2)\,\varepsilon_3\cdot p_2 - p_2\cdot p_3\,\bar{u}(p_4)\gamma^{\mu} v(p_2)\,\varepsilon_3\cdot p_4 \\
&\quad - (p_2\cdot p_3)\left[\bar{u}(p_4)\not{p}_3 v(p_2)\,\varepsilon_3^{\mu} - \bar{u}(p_4)\not{\varepsilon}_3 v(p_2)\, p_3^{\mu}\right]\,.
\end{aligned} \tag{4.3.27}$$

The coefficients $b_i^{(L)}$ can be determined through:

$$b_i^{(L)} = \sum_j \left(\Omega^{-1}\right)_{ij} \tilde{A}_{4,j}^{(L)}\,, \tag{4.3.28}$$

where:

$$\Omega_{ij} = \sum_{\text{pol}} Y_i^{\mu\dagger} Y_{j\mu}\,, \tag{4.3.29}$$

$$\tilde{A}_{4,i}^{(L)} = \sum_{\text{pol}} Y_i^{\mu\dagger} A_{4\,\mu}^{(L)}\,. \tag{4.3.30}$$

The gluon polarisation sum follows from Eq. 1.1.12. We note that the tensor structures in Eq. 4.3.27 are different from the ones employed in Ref. [229]. Here, we start from 12 tensor structures that are linearly independent in 4 dimensions [227,228] and reduce them to 7 by imposing Ward identities. Since $A_4^{(L)\mu}$ is a four-point amplitude, it does not depend on tr_5. For the sake of uniformity, we express it in terms of the five-point Mandelstam invariants $\vec{s}_5$, Eq. 4.3.9. In contrast to the computation of $A_{5,d}^{(L)\mu}$, here we derive the contracted amplitudes $\tilde{A}_{4,i}^{(L)}$ directly without specifying the helicity states, since the four-point computation is relatively simple. The helicity states for the tensor structures Y_μ^i are specified when the decay currents are attached, following Eq. 4.3.2. Once again, we perform the same decomposition on

the corresponding four-particle finite remainder $F_4^{(L)\mu}$. The resulting formula for the contracted finite remainders is:

$$\tilde{F}_{4,i}^{(L)} = \sum_{\text{pol}} Y_i^{\mu\dagger} F_{4\,\mu}^{(L)} \,. \tag{4.3.31}$$

4.3.4 Amplitude reduction and analytic reconstruction

In this section, we present the analytic computation of the contracted five- and four-particle finite remainders, $\tilde{F}_{5,i}^{(L),h_1h_2h_3h_4}$ Eq. 4.3.23 and $\tilde{F}_{4,i}^{(L)}$ Eq. 4.3.31 respectively, at one and two loops. We adopt the framework used in Chapter 3 based on Feynman diagrams and functional reconstruction from numerical sampling over finite fields.

In order to use the finite field technique, we need to have a rational parametrisation of the kinematics. However, just as in Chapter 3, the pseudo-scalar invariant tr_5 in the five-particle kinematics leads (through Eq. 3.2.7) to the appearance of the square root $\sqrt{\Delta_5}$. This issue may be dealt with in two ways: either parameterise the kinematics to explicitly rationalise $\sqrt{\Delta_5}$, or parameterise the finite remainders such that the dependence on tr_5 is analytic and so it never enters the computations within finite fields. In the previous chapter, we followed a mixed approach. On one hand, tr_5 which captures the parity information of the coefficients in the finite remainders was explicitly rationalised using MTs. On the other hand, tr_5 which appears in the overall prefactors of the canonical MIs was normalised away and restored at the end of the computation.

Here, we do not rationalise tr_5 using MTs. Instead, we organise our workflow such that the dependence on tr_5 is fully analytic. Note that tr_5 can enter the computation in three distinct ways. First, it can originate from the γ_5 in the axial coupling of the W boson. As discussed in Section 4.2, we set up the computation so that only the vector coupling of W is used. Second, while it is still true that we need tr_5 to capture the parity-odd part of the spinor-helicity expressions, it enters the contracted helicity finite remainder in Eq. 4.3.23 only through the spanning basis elements $T_j^{h_1h_2h_3h_4}$, which are known analytically and do not need to be reconstructed over finite fields. Finally, tr_5 present in the definitions of the canonical MIs is normalised away just as in Chapter 3[1]. With this setup, the only parts of the contracted finite remainders which need to be reconstructed are rational functions of the scalar invariants $\vec{s}_5$ only, and can thus be sampled numerically over finite fields.

[1] In addition to $\sqrt{\Delta_5}$, the overall prefactors of the canonical MIs contain other square roots, $\sqrt{\Delta_3^{(i)}}$ for $i = 1, 2, 3$, which we also normalise away and restore afterwards [98,121]. We have already seen two of them in Eq. 3.3.4. Here, the third one is needed: $\sqrt{\Delta_3^{(3)}} = 2\sqrt{(p_{13}\cdot p_5)^2 - p_5^2 s_{13}}$.

The starting point of our computation is the expression of the W-production five- and four-particle amplitudes, $A_{5,d}^{(L)\mu}$ and $A_4^{(L)\mu}$, in terms of Feynman diagrams. Using `QGRAF` [35], we find 20 diagrams for $A_{5,d}^{(1),1\mu}$, 231 diagrams for $A_{5,d}^{(2),1\mu}$, 32 diagrams for $A_{5,d}^{(2),n_f\mu}$, 7 diagrams for $A_4^{(1),1\mu}$, 74 diagrams for $A_4^{(2),1\mu}$, and 13 diagrams for $A_4^{(2),n_f\mu}$. We want to obtain analytic, IBP-compatible expressions for the contracted amplitudes, $\tilde{A}_{5,i}^{(L),h_1h_2h_3h_4}$ and $\tilde{A}_{4,i}^{(L)}$. For the four-point amplitude $A_4^{(L)\mu}$, we apply the projectors and sum over all polarisation states as in Eq. 4.3.30. For the five-point amplitude $A_{5,d}^{(L)\mu}$, we contract by the external momenta and apply the projectors, as in Eqs. 4.3.15 and 4.3.22, respectively. We then rewrite the resulting expressions in terms of scalar Feynman integrals belonging to the 15 maximal topologies shown in Fig. 3.3. We carry out all these operations analytically using `Mathematica` and `FORM` [184, 185] scripts. As a result, we obtain analytic expressions for $\tilde{\mathcal{A}}_{5,i\,k}^{(L)}$, Eq. 4.3.22, and $\tilde{A}_{4,i}^{(L)}$, Eq. 4.3.30, as linear combinations of scalar Feynman integrals with rational coefficients functions of $\vec{s}_5$. In order to obtain the contracted helicity-amplitudes $\tilde{A}_{5,i}^{(L),h_1h_2h_3h_4}$ from the $\tilde{\mathcal{A}}_{5,i\,k}^{(L)}$'s, we further need to multiply by the spanning basis elements $T_j^{h_1h_2h_3h_4}$ and by the inverse of Θ, as shown in Eq. 4.3.21. We do these operations (including the inversion of Θ) numerically within the finite field framework.

We reduce the scalar integrals to the canonical MIs identified in Ref. [98], which we modified so as to re-absorb the square roots. We generate the IBP relations [65] using `LiteRed` [29] in `Mathematica`, and solve them numerically over finite fields using the Laporta algorithm [230] through `FiniteFlow`'s linear solver. We then perform a Laurent expansion of the rational coefficients around $\epsilon = 0$, and map the canonical MIs onto square roots and the special function basis of Ref. [182] up to the required order in ϵ. We label the special function basis by $\{f_k\}$. We truncate the ϵ expansion at order ϵ^2 at one loop and at order ϵ^0 at two loops. Finally, we subtract the UV/IR poles as in Eq. 4.2.15 and define the contracted finite remainders:

$$\begin{aligned}
\tilde{F}_{5,i}^{(L),h_1h_2h_3h_4} &= \Phi_5^{h_1h_2h_3h_4} \sum_j \left[q_{i,j}^{h_1h_2h_3h_4}(\vec{s}_5) + \mathrm{tr}_5\; r_{i,j}^{h_1h_2h_3h_4}(\vec{s}_5) \right] \mathrm{mon}_j\left(\mathrm{tr}_5, \sqrt{\Delta_3^{(l)}}, \{f_k\}\right) , \\
\tilde{F}_{4,i}^{(L)} &= \sum_j t_{i,j}(\vec{s}_5)\, \mathrm{mon}_j\left(\mathrm{tr}_5, \sqrt{\Delta_3^{(l)}}, \{f_k\}\right) ,
\end{aligned} \tag{4.3.32}$$

where $\mathrm{mon}_j(x, y, \ldots)$ denotes monomials in $x, y, \ldots$, while $q_{i,j}^{h_1h_2h_3h_4}$, $r_{i,j}^{h_1h_2h_3h_4}$ and $t_{i,j}$ are rational functions of $\vec{s}_5$. Note that we pull out from the five-particle finite remainders an arbitrary phase factor $\Phi_5^{h_1h_2h_3h_4}$ carrying all the helicity weights, so that the coefficients $q_{i,j}^{h_1h_2h_3h_4}$ and $r_{i,j}^{h_1h_2h_3h_4}$ are scalar and hence functions of $\vec{s}_5$ only. We recall that the helicity configuration is assigned to the four-particle finite remainders when attaching the decay current, as discussed in Section 4.3.3. The cancellation of the poles at this stage provides a robust check of the result prior to

the rational reconstruction. Furthermore, it typically leads to simplifications which make the finite remainders easier to reconstruct than the bare amplitudes. This chain of operations is implemented in `FiniteFlow`.

Finally, we need to reconstruct the rational coefficients of the contracted finite remainders from their numerical values. Following Refs. [1,182,187,194], we perform a number of optimisations to reduce the number of required sample points. We follow the strategy outlined in Ref. [187]. First of all, we set $s_{12} = 1$. We recover the analytic dependence on s_{12} *a posteriori* through dimensional analysis. Then, similarly to the workflow outlined in Section 3.3, we fit the $\mathbb{Q}$-linear relations among the rational coefficients, and solve them so as to express the most complicated coefficients in terms of the simplest ones. Third, we perform the matching of remaining coefficients with an ansatz of factors on a random univariate phase space slice modulo a large prime number. Contrary to the ansatz presented in Eq. 3.3.5, here we do not need to include phase-dependent spinor structures. For this set of amplitudes, we find the following ansatz sufficient:

$$
\begin{aligned}
\Big\{ & s_{12}\,, s_{23}\,, s_{34}\,, s_{23}+s_{34}\,, s_{23}-s_{234}\,, s_{234}-s_{34}\,, s_{123}-s_{56}\,, s_{234}-s_{56}\,, s_{12}-s_{123}+s_{23}\,, \\
& s_{12}+s_{234}-s_{34}\,, s_{23}-s_{234}+s_{34}\,, s_{12}+s_{234}-s_{56}\,, s_{12}-s_{123}-s_{34}\,, s_{123}s_{234}-s_{23}s_{56}\,, \\
& s_{12}-s_{123}+s_{23}-s_{34}\,, s_{123}-s_{23}+s_{234}-s_{56}\,, s_{12}+s_{234}-s_{34}-s_{56}\,, \\
& s_{12}s_{234}-s_{123}s_{234}+s_{23}s_{234}-s_{234}s_{34}+s_{34}s_{56}\,, \\
& s_{12}s_{234}-s_{123}s_{234}-s_{234}s_{34}+s_{23}s_{56}+s_{34}s_{56}\,, s_{12}s_{234}+s_{234}^2-s_{234}s_{34}-s_{234}s_{56}+s_{34}s_{56}\,, \\
& s_{12}s_{123}+s_{123}s_{234}-s_{123}s_{34}-s_{12}s_{56}-s_{23}s_{56}\,, s_{12}s_{123}-s_{123}^2-s_{123}s_{34}-s_{12}s_{56}+s_{123}s_{56}\,, \\
& s_{12}^2-s_{12}s_{123}+s_{12}s_{234}-s_{123}s_{234}-2s_{12}s_{34}+s_{123}s_{34}-s_{234}s_{34}+s_{34}^2+s_{23}s_{56}\,, \\
& s_{12}s_{23}-s_{12}s_{234}+s_{23}s_{234}-s_{234}^2-s_{23}s_{34}+s_{234}s_{34}-s_{23}s_{56}+s_{234}s_{56}-s_{34}s_{56}\,, \\
& \lambda\left(s_{12},s_{34},s_{56}\right)\,, \lambda\left(s_{23},s_{14},s_{56}\right)\,, \mathrm{tr}_5^2 \Big\}\,,
\end{aligned}
\tag{4.3.33}
$$

where λ is the Källen function:

$$
\lambda(a,b,c) = a^2+b^2+c^2-2ab-2bc-2ca\,. \tag{4.3.34}
$$

Just as in Chapter 3, we are able to determine entirely the denominators of the rational coefficients, as well as some of their numerators. In Table 4.1, we show the impact of this strategy on the highest polynomial degrees of the rational coefficients which need to be reconstructed for the five-particle contracted finite remainders. Note that we process all helicity configurations of the five-particle finite remainders simultaneously, but for the n_f^0 ones we separate the contractions by the external mo-

	$s_{12}=1$	linear relations	factor matching
$\tilde{F}^{(2),1\,h_1h_2h_3h_4}_{5,i}$ with $i=1,2$	44/44	41/40	41/0
$\tilde{F}^{(2),1\,h_1h_2h_3h_4}_{5,i}$ with $i=3,4$	48/47	42/42	42/0
$\tilde{F}^{(2),n_f\,h_1h_2h_3h_4}_{5,i}$ with $i=1,2,3,4$	39/38	26/24	26/0

Table 4.1: Maximal total polynomial degrees of the rational coefficients of the contracted two-loop five-particle finite remainders at each stage of the optimisation procedure for the finite field reconstruction, in the form: numerator/denominator. The coefficients are functions of the five scalar invariants $\{s_{23}, s_{34}, s_{123}, s_{234}, s_{56}\}$ ($s_{12}=1$). The independent helicity configurations Eq. 4.3.25 are processed simultaneously, while the contractions by the external momenta for $\tilde{F}^{(2),1\,h_1h_2h_3h_4}_{5,i}$ are separated into two subsets to reduce the memory usage.

menta into two subsets, $\{p_1,p_2\}$ and $\{p_3,p_4\}$, to reduce the memory usage. After this optimisation is done, the rational coefficients are reconstructed using the multivariate functional reconstruction algorithms implemented in `FiniteFlow` (see Section 2.6.2). Note that in contrast to Chapter 3, here we do not find it necessary to perform the univariate partial fraction decomposition prior to reconstruction.

4.3.5 Simplification of the rational coefficients

The resulting analytic expressions of the rational coefficients of the finite remainders are rather bulky. The standard approach to simplify them relies on partial fraction decomposition, either multivariate [188–192, 231, 232] or univariate with respect to a suitable variable [1, 182, 187, 233]. For the rational coefficients of the four-point finite remainders, $t_{i,j}\left(\vec{s}_5\right)$ in Eq. 4.3.32, we achieve a satisfactory simplification by performing a multivariate partial fraction decomposition with the `Mathematica` package `MultivariateApart` [192], enhanced by `Singular` [234] for the computation of the Gröbner bases.

The rational coefficients of the five-particle finite remainders are instead substantially more involved. In order to simplify them, we look for a parametrisation of the five-particle kinematics leading to more compact expressions than the scalar invariants $\vec{s}_5$ Eq. 4.3.9. We investigate how the complexity of the expressions varies when using different MT parametrisations. The pseudoscalar invariant tr_5 is given by a rational function in terms of MTs, and we can thus add up the two terms of the coefficients of the special function monomials:

$$\left(q^{h_1h_2h_3h_4}_{i,j}\left(\vec{s}_5\right)+\mathrm{tr}_5\; r^{h_1h_2h_3h_4}_{i,j}\left(\vec{s}_5\right)\right)\Big|_{\vec{s}_5=\vec{s}_5(\vec{z})}=u^{h_1h_2h_3h_4}_{i,j}\left(\vec{z}\right)\,, \tag{4.3.35}$$

where by $\vec{z} = \{z_i\}_{i=1,\ldots,6}$ we denote generally the independent MTs. In particular, we consider the parametrisation proposed in Ref. [1]:

$$\begin{aligned} z_1 &= s_{12}\,, & z_2 &= -\frac{\mathrm{tr}_+(1234)}{s_{12}s_{34}}\,, \\ z_3 &= \frac{\mathrm{tr}_+(1341(5+6)2)}{s_{13}\,\mathrm{tr}_+\,(14(5+6)2)}\,, & z_4 &= \frac{s_{23}}{s_{12}}\,, \\ z_5 &= -\frac{\mathrm{tr}_-(1(2+3)(1+5+6)(5+6)23)}{s_{23}\,\mathrm{tr}_-(1(5+6)23)}\,, & z_6 &= \frac{s_{456}}{s_{12}}\,. \end{aligned} \tag{4.3.36}$$

In previous applications, such a parametrisation has been used globally, i.e. in all amplitudes/finite remainders irrespective of their helicity configuration. We find that this approach does not perform well in this case, and does not lead to a major simplification in comparison with the expressions in terms of scalar invariants $\vec{s}_5$ and tr_5. The rational parametrisation has the effect of breaking some symmetries in the kinematic quantities, which results in some configurations being simpler than others. There is no reason for the parametrisation to be a global choice, and here we exploit this fact and consider different parametrisations for each helicity configuration.

In practice, we consider all parametrisations which are obtained by permuting the massless momenta on the right-hand side of Eqs. 4.3.36. For each helicity configuration, we determine which permutations of the parametrisation lead to the most compact expression of the finite remainder at one loop. We then use them at two loops and select the one which results in the simplest expressions. We perform the change of variables over finite fields within the `FiniteFlow` framework, and measure the 'simplicity' of the rational coefficients in terms of their numerator/denominator polynomial degrees, which can be determined without reconstructing the coefficients in terms of the new variables. Once the 'best' parametrisation $\vec{s}_5 = \vec{s}_5(\vec{z})$ is chosen for each helicity configuration, we reconstruct the analytic expression of the coefficients in terms of the new variables $\vec{z}$. For this purpose, we make use of the finite field algorithm for univariate partial fraction decomposition presented in Refs. [182, 187]. We choose the variable to partial fraction with respect to so as to minimise the polynomial degrees of the separate terms of the decomposition. Breaking down the coefficients into univariate partial fractions simplifies the subsequent multivariate partial fraction decomposition, which we perform using `MultivariateApart` [192] enhanced with `Singular` [234]. We apply it to each term of the univariate partial fraction decomposition separately, which is convenient as each term is by itself much simpler than the full coefficient. This is possible because `MultivariateApart`'s algorithm commutes with summation by design. The spurious poles introduced by the univariate partial fraction decomposition therefore cancel out after the multivariate partial fraction decomposition. In summary, our algorithm for the simplification of

the rational coefficients of the five-particle finite remainders is the following:

1. Try all permutations of a given MT parametrisation on the one-loop expressions and select a few which lead to the lowest polynomial degrees.

2. Apply the parametrisations selected at step 1 on the two-loop rational coefficients and choose the one which leads to the lowest polynomial degree.

3. Decompose the two-loop coefficients in terms of the new variables into univariate partial fractions with respect to the variable which leads to the lowest polynomial degrees in the separate terms.

4. Decompose into multivariate partial fractions the separate terms of the univariate partial fractions using the algorithm of Ref. [192], and sum them up cancelling the spurious poles.

In hindsight, the first three steps could have been implemented prior to the original reconstruction in Section 4.3.4. We did not attempt this approach, because we did not need any further optimisation to reconstruct the coefficients of the W-production five-particle finite remainders. However, we believe that this strategy may be useful in future applications.

We apply this procedure separately on each of the helicity configurations, leading to different parametrisations for each of them. The resulting expressions for the coefficients are remarkably more compact than the original ones in terms of the scalar invariants $\vec{s}_5$. For the most complicated finite remainder, we achieved a compression in the file size of more than two orders of magnitude. The evaluation time of the rational coefficients is similarly improved.

4.3.6 Numerical evaluation and permutations of the amplitudes

In order to obtain the values of all the amplitudes in all the possible scattering channels, we need to evaluate the minimal set of independent objects we reconstructed for different permutations of the external momenta (see e.g. Eq. 4.2.8 for an explicit example). In this subsection, we discuss how we implement this operation in an efficient way at the level of the numerical evaluation.

We denote a generic permutation of the external momenta by:

$$\sigma = (\sigma_1\sigma_2\sigma_3\sigma_4\sigma_5\sigma_6) \ , \tag{4.3.37}$$

where the σ_i's take distinct values in $\{1,2,3,4,5,6\}$, such that the action of σ on an external momentum is given by:

$$\sigma \circ p_i = p_{\sigma_i} \,. \tag{4.3.38}$$

Not all S_6 permutations of $\{1,2,3,4,5,6\}$ are needed for this application. The required permutations belong to the subset $S_4 \times Z_2$, i.e. they are obtained by composing an S_4 permutation of $\{p_1,p_2,p_3,p_4\}$ and a Z_2 exchange of $\{p_5,p_6\}$. In particular, p_5 and p_6 need to be exchanged in order to obtain the $W^-\gamma j$ amplitudes according to Eq. 4.2.18. Only the S_4 permutations are relevant for the W-production amplitudes (and hence for the special functions), since p_5 and p_6 enter them only in the sum p_5+p_6 (see e.g. Eqs. 4.3.1 and 4.3.2). The Z_2 exchange is relevant only for the leptonic currents ($L_{A,\mu}$ and $L^{e/W}_{B,\mu}$), which are rational functions.

Given a generic amplitude/finite remainder A, function of the external momenta $\{p_i\}$, we define its permutation σ as:

$$(\sigma \circ A)(\{p_i\}) = A(\{\sigma \circ p_i\}) \,. \tag{4.3.39}$$

In other words, we can obtain the value of the permuted amplitude by evaluating the amplitude in the original orientation of the external momenta at a permuted phase space point. While this operation is trivial for the rational functions, it is in general very subtle for the special functions. The reason is that a permutation in general maps the phase space point to a different scattering region. This would require a complicated analytic continuation, since the special functions have a very intricate branch cut structure.

One way to overcome this problem is to evaluate the special functions numerically using the generalised series expansion method [141], implemented in the public `Mathematica` package `DiffExp` [142], as done in Chapter 3. Within this method, the analytic continuation can be carried out systematically. However, this approach requires that, for each phase space point where we want to evaluate the permuted amplitudes, we evaluate the special functions at as many points as the number of needed permutations.

For phase space points in the physical scattering region, we can adopt a much more efficient evaluation strategy: we use the `C++` package `PentagonFunctions++` [121], which allows us to evaluate in the physical scattering region a larger basis of special functions, named 'one-mass pentagon functions'. We denote them by $\{g_i\}$. For this purpose we translate the MI function basis $\{f_i\}$ of Ref. [182] (see Section 3.4) to the one-mass pentagon function basis $\{g_i\}$ implemented in `PentagonFunctions++`. The

translation takes the form:

$$f_i = \sum_j w_{ij} \, \mathrm{mon}_j \left(\{g_k\} \right) , \tag{4.3.40}$$

where $w_{ij} \in \mathbb{Q}$, and the sum runs over all the required monomials of the one-mass pentagon functions $\{g_k\}$. We obtain the transformation rules Qq. 4.3.40 by matching the expressions of the MIs in terms of special functions given in Ref. [182] with that of Ref. [121]. The advantage of the one-mass pentagon functions with respect to the function basis $\{f_i\}$ or Ref. [182] is that their evaluation through the package `PentagonFunctions++` is extremely efficient, and their design allows us to generate the values of all S_4 permutations of the functions from those at the unpermuted phase space point. The one-mass pentagon function basis $\{g_i\}$ is in fact closed under S_4 permutations. This means that, for any $\sigma \in S_4$, we can express the permuted one-mass pentagon functions evaluated at a given phase space point as a combination of the unpermuted pentagon functions evaluated at the same point:

$$(\sigma \circ g_i) \left(\vec{s}_5, \mathrm{tr}_5 \right) = \sum_j \Sigma_{ij}^{(\sigma)} \mathrm{mon}_j \left[\{ g_k \left(\vec{s}_5, \mathrm{tr}_5 \right) \} \right] , \tag{4.3.41}$$

where $\Sigma_{ij}^{(\sigma)} \in \mathbb{Q}$, and we spelled out the dependence on the kinematics for the sake of clarity. These transformation rules are provided in Ref. [121].[1] This strategy is advantageous because it minimises the number of evaluations of the special functions, which is the most time-consuming step in the numerical evaluation of the colour and helicity summed squared amplitudes.

It is worth highlighting the special behaviour of the pseudoscalar invariant tr_5 in this chain of operations. In the physical scattering regions, the reality of the momenta implies that $\mathrm{tr}_5^2 < 0$. In other words, tr_5 is purely imaginary. The library `PentagonFunctions++` always assumes that $\mathrm{Im}\left[\mathrm{tr}_5\right] > 0$. The sign of tr_5, however, may change upon the action of an odd-signature permutation:

$$\sigma \circ \mathrm{tr}_5 = \mathrm{sign}(\sigma) \, \mathrm{tr}_5 \, , \tag{4.3.42}$$

or space-time parity. The values of the one-mass pentagon functions for a negative imaginary part of tr_5 can be obtained by flipping the sign of a subset of functions specified in Ref. [121]. In our setup, however, we do not need to do so. As discussed

[1] Note that Ref. [121] has a different labelling of the external momenta. Moreover, the package `PentagonFunctions++` works in a specific physical scattering region (the s_{45} channel using the notation of Ref. [121]). A relabelling and a further permutation of the momenta are required to use `PentagonFunctions++` in the scattering region relevant for our application. We implemented these operations in the `Mathematica` evaluation script provided in the ancillary files, and refer to the original work, Ref. [121], for a discussion of how to use `PentagonFunctions++` in a physical region different from the default one.

in Section 4.3.4, we reduce the amplitudes to manifestly scalar MIs, and group together the special functions and the square roots arising from the definition of the canonical MIs. As a result, the monomials of special functions and square roots in the finite remainders Eq. 4.3.32 are scalar as well. Any sign change in the pentagon functions due to permutations or space-time parity is therefore compensated by that of the accompanying factor of tr_5, and we can thus evaluate both with a value of tr_5 such that $\mathrm{Im}\,[\mathrm{tr}_5] > 0$ — as by default in `PentagonFunctions++` — regardless of the permutations or space-time parity. We must only keep track of the sign of tr_5 in the rational coefficients (see Eq. 4.3.32), which enters our final expressions for the five-particle finite remainders through the values of the MTs, and is determined by the values of the external momenta through its definition Eq. 3.2.6. The same holds for the other square roots in the problem, $\sqrt{\Delta_3^{(i)}}$, which appear only in the special function monomials. The polynomials $\Delta_3^{(i)}$ are positive in the physical scattering regions. We adopt the convention of Ref. [121] that their square roots are positive, $\sqrt{\Delta_3^{(i)}} > 0$, as done in `PentagonFunctions++`.

In conclusion, we reconstruct the analytic expressions for the minimal set of independent finite remainders, and generate the values of the remaining ones by permuting the former at the numerical evaluation stage. We do this by evaluating the rational coefficients at permuted points, whereas we obtain the values of all permutations of the special functions from the values of the functions at the original phase space point only. This allows us to minimise the amount of analytic data, whose size may otherwise become problematic, and at the same time evaluate the results efficiently.

4.4 Validation

In this section, we discuss a number of validations performed on the analytic results derived in this work. First, let us remind the reader that the quantities that we reconstructed analytically are the L-loop finite remainders, where the UV and IR poles contained in the L-loop bare amplitudes are cancelled by the pole terms according to Eq. 4.2.15. These pole cancellations already provide a strong consistency check of our calculation. In the following subsections, we present further checks.

4.4.1 Comparison against full six-point computation

In order to verify the analytic expressions obtained by detaching the leptonic decay current as described in Section 4.3, we cross-check them against the helicity amplitudes obtained by computing the six-point process directly using a framework that

has been applied to the computation of several two-loop amplitudes [1, 187, 235, 236]. We perform the full six-point computation numerically using the MT parametrisation Eq. 4.3.11 by assigning rational values to the variables $x_1, \ldots, x_8$ in the coefficients and treating the special functions symbolically. We derive numerical results for all the sub-amplitudes — $A^{(L)}_{6,u}$, $A^{(L)}_{6,d}$, $A^{(L)}_{6,W}$ and $A^{(L)}_{6,e}$ — in all four contributing helicity configurations. We find full numerical agreement between the two approaches. This provides a further robust check of our analytic computation, where we derived analytic expressions only for the independent helicity configurations and obtained the remaining ones by complex conjugation and permutation of the external momenta.

4.4.2 Gauge invariance

The gauge-invariance structure of the $W^+\gamma j$ amplitude is slightly complicated by the different sources of photon emission, as discussed in Section 4.2. The individual sub-amplitudes ($A^{(L)}_{6,i}$ with $i = u, d, W, e$) are not separately gauge invariant in the electroweak (EW) sector. Only linear combinations of them, defined in Eq. 4.2.6, are. We rewrite them here for convenience:

$$\left\{ A^{(L)}_{6,u} + \frac{1}{s_{156} - s_{56}} A^{(L)}_{6,W} \,, \quad A^{(L)}_{6,d} - \frac{1}{s_{156} - s_{56}} A^{(L)}_{6,W} \,, \quad A^{(L)}_{6,e} - \frac{1}{s_{156} - s_{56}} A^{(L)}_{6,W} \right\} . \tag{4.4.1}$$

We verify explicitly that these combinations satisfy the EW Ward identity by replacing the photon polarisation vector with its momentum ($\varepsilon(p_1) \to p_1$) and checking that the resulting expressions vanish.

The QCD Ward identity (performed by replacing the gluon polarisation vector with its momentum, $\varepsilon(p_3) \to p_3$), instead, is already satisfied by the individual sub-amplitudes. We checked this explicitly as well.

We further demonstrate the gauge invariance by evaluating the helicity amplitudes using two different sets of reference momenta for the photon and gluon polarisation vectors (q_1 and q_3), finding perfect agreement.

4.4.3 Renormalisation scale dependence

Similarly to Section 3.5.2, we restore the renormalisation scale dependence of the L-loop finite remainders by adding to them the terms:

$$\delta F^{(1),1}_6 \left(\mu^2\right) = \frac{11}{6} A^{(0)}_6 \log\left(\mu^2\right) , \tag{4.4.2}$$

$$\delta F^{(1),n_f}_6 \left(\mu^2\right) = -\frac{1}{3} A^{(0)}_6 \log\left(\mu^2\right) , \tag{4.4.3}$$

$$\delta F_6^{(2),1}\left(\mu^2\right) = \log(\mu^2)\left\{\left(\frac{1813}{216} - \frac{11}{36}\pi^2 + 8\zeta_3\right)A_6^{(0)} + \frac{11}{2}F_6^{(1),1}(1)\right\} + \frac{121}{24}A_6^{(0)}\log^2(\mu^2)\,, \tag{4.4.4}$$

$$\delta F_6^{(2),n_f}\left(\mu^2\right) = \log(\mu^2)\left\{\left(\frac{\pi^2}{18} - \frac{77}{18}\right)A_6^{(0)} - F_6^{(1),1}(1) + \frac{11}{2}F_6^{(1),n_f}(1)\right\} - \frac{11}{6}A_6^{(0)}\log^2(\mu^2)\,, \tag{4.4.5}$$

$$\delta F_6^{(2),n_f^2}\left(\mu^2\right) = \log(\mu^2)\left\{\frac{10}{27}A_6^{(0)} - F_6^{(1),n_f}(1)\right\} + \frac{1}{6}A_6^{(0)}\log^2(\mu^2)\,. \tag{4.4.6}$$

The dependence on the external momenta is understood. We then verify that the μ-dependent finite remainders satisfy the correct scaling relations by evaluating them at two phase space points and checking the relation Eq. 3.5.13.

4.4.4 Tree-level and one-loop checks

We validated the tree-level and one-loop amplitudes derived in this chapter against the results available in literature. For the tree-level amplitude, we compared our helicity amplitudes against the analytic results presented in Ref. [216] and additionally, for the full colour tree-level squared matrix elements, against `Madgraph5` [207] for both processes $W^+\gamma j$ and $W^-\gamma j$. As for the one-loop amplitudes, we compared our results against the leading colour contributions of the $W^+\gamma j$ amplitudes presented in Ref. [216]. In all cases we find perfect agreement. We would like to point out that our choice of reference vectors for the photon and the gluon is different from the one used in Ref. [216]. For this reason, we compared the gauge invariant combinations of sub-amplitudes shown in Eq. 4.4.1. This check therefore further validates the gauge invariance of our result.

4.4.5 Four-point amplitude comparison

We performed a cross check of the four-point amplitudes $A_4^{(L)\mu}$ which contribute to the sub-amplitudes $A_{6,W}^{(L)}$ and $A_{6,e}^{(L)}$ against the results provided in Ref. [214] for the scattering process $q\bar{q} \to Vg$. In Ref. [214], analytic results are presented for the helicity coefficients which are linear combinations of the form factors $b_i^{(L)}$ in Eq. 4.3.26, evaluated at $\mu^2 = s_{234}$. In order to enable a direct comparison for the one- and two-loop leading colour finite remainders, we recomputed the $A_4^{(L)\mu}$ amplitudes in Eq. 4.3.26 using the tensor structures employed in Ref. [214]. Since we compute the finite remainders with $\mu^2 = 1$, we obtain the results at $\mu^2 = s_{234}$ using the formulae to restore the dependence on μ shown in Section 4.4.3. We obtain perfect numerical agreement for the helicity coefficients. We further check that the four-particle finite

remainders $F_4^{(L)\mu}$ computed using the tensor structures of Ref. [214] match the ones we derived using the tensor structures defined in Section 4.3.3 after contracting them with the decay currents according to Eq. 4.3.4.

4.5 Results

The analytic expressions for the five- and four-point contracted amplitudes ($\tilde{A}_{5,i}^{(L)}$ and $\tilde{A}_{4,i}^{(L)}$), at one and two loops, together with the decay currents ($L_{A,\mu}$, $L_{B,\mu}^{e}$, $L_{B,\mu}^{W}$) and the relevant projection matrices (Δ, Eq. 4.3.14 and Ω, Eq. 4.3.29) are provided in the ancillary files of Ref. [2]. The amplitudes are presented as linear combinations of independent rational coefficients that multiply a monomial basis of square roots and special functions.

We confirm the observations pointed out in Section 3.4 about the cancellation of the pentagon functions involving certain letters [1,182,233]. Once again, we observe that the functions involving the letters $\{W_{16}, W_{17}, W_{27}, W_{28}, W_{29}, W_{30}\}$ (in the notation of Ref. [98]) are present in the contributing integrals but drop out from the amplitudes truncated[1] at order ϵ^0 and that the functions involving the letter $W_{49} = \mathrm{tr}_5$ are present in the amplitudes and drop out from the finite remainders. It is worth noting that these cancellations occur already at the level of the separate sub-amplitudes $A_{6,i}^{(L)}$ and sub-finite remainders $F_{6,i}^{(L)}$, and not just for their gauge-invariant combinations.

The ancillary files of Ref. [2] include a `Mathematica` script to demonstrate the assembly of both the $W^+\gamma j$ and $W^-\gamma j$ amplitudes, and to perform the numerical evaluation of the finite remainders at a given kinematic point. We evaluate the special functions in the physical scattering region using the package `PentagonFunctions++` [121], as discussed in Section 4.3.6. We use the following configuration of momenta:

$$-p_2 - p_4 \to p_1 + p_3 + p_5 + p_6\,, \tag{4.5.1}$$

to define the six scattering channels for $pp \to W^+\gamma j$ production:

$$\begin{aligned}
\mathbf{u\bar{d}}: &\quad u(-p_2) + \bar{d}(-p_4) \to \gamma(p_1) + g(p_3) + \nu_e(p_5) + e^+(p_6)\,,\\
\mathbf{\bar{d}u}: &\quad \bar{d}(-p_2) + u(-p_4) \to \gamma(p_1) + g(p_3) + \nu_e(p_5) + e^+(p_6)\,,\\
\mathbf{ug}: &\quad u(-p_2) + g(-p_4) \to \gamma(p_1) + d(p_3) + \nu_e(p_5) + e^+(p_6)\,,\\
\mathbf{gu}: &\quad g(-p_2) + u(-p_4) \to \gamma(p_1) + d(p_3) + \nu_e(p_5) + e^+(p_6)\,,
\end{aligned}$$

[1]This holds for the set of independent amplitudes we reconstructed explicitly, which receive contributions only from the cyclic permutations of the MIs. Since the set of letters $\mathcal{Z}$ is not closed under all S_4 permutations, these letters are present in some of the permuted amplitudes which contribute to the helicity and colour summed squared finite remainders.

$$
\begin{aligned}
\mathbf{\bar{d}g}: &\quad \bar{d}(-p_2) + g(-p_4) \to \gamma(p_1) + \bar{u}(p_3) + \nu_e(p_5) + e^+(p_6)\,, \\
\mathbf{g\bar{d}}: &\quad g(-p_2) + \bar{d}(-p_4) \to \gamma(p_1) + \bar{u}(p_3) + \nu_e(p_5) + e^+(p_6)\,,
\end{aligned}
\tag{4.5.2}
$$

and similarly for $pp \to W^-\gamma j$ production:

$$
\begin{aligned}
\mathbf{d\bar{u}}: &\quad d(-p_2) + \bar{u}(-p_4) \to \gamma(p_1) + g(p_3) + e^-(p_5) + \bar{\nu}_e(p_6)\,, \\
\mathbf{\bar{u}d}: &\quad \bar{u}(-p_2) + d(-p_4) \to \gamma(p_1) + g(p_3) + e^-(p_5) + \bar{\nu}_e(p_6)\,, \\
\mathbf{dg}: &\quad d(-p_2) + g(-p_4) \to \gamma(p_1) + u(p_3) + e^-(p_5) + \bar{\nu}_e(p_6)\,, \\
\mathbf{gd}: &\quad g(-p_2) + d(-p_4) \to \gamma(p_1) + u(p_3) + e^-(p_5) + \bar{\nu}_e(p_6)\,, \\
\mathbf{\bar{u}g}: &\quad \bar{u}(-p_2) + g(-p_4) \to \gamma(p_1) + \bar{d}(p_3) + e^-(p_5) + \bar{\nu}_e(p_6)\,, \\
\mathbf{g\bar{u}}: &\quad g(-p_2) + \bar{u}(-p_4) \to \gamma(p_1) + \bar{d}(p_3) + e^-(p_5) + \bar{\nu}_e(p_6)\,.
\end{aligned}
\tag{4.5.3}
$$

The interference between the L-loop finite remainders and the tree-level amplitudes summed over colour and helicity in the leading colour approximation is given by:

$$
\sum_{\text{colour}} \sum_{\text{helicity}} \mathcal{A}_6^{(0)*} \mathcal{F}_6^{(L)} =: 2e^2 g_W^4 g_s^2 n^L N_c^2\, \mathcal{H}^{(L)}\,, \tag{4.5.4}
$$

where the reduced squared finite remainder $\mathcal{H}^{(L)}$ is defined by:

$$
\mathcal{H}^{(L)} = \sum_{\text{helicity}} A_6^{(0)*} F_6^{(L)}\,, \tag{4.5.5}
$$

for all scattering channels given in Eqs. 4.5 and 4.5. The reduced squared finite remainder obeys the same decomposition according to the closed fermion loop contributions as $F_6^{(L)}$:

$$
\begin{aligned}
\mathcal{H}^{(1)} &= N_c \mathcal{H}^{(1),1} + n_f \mathcal{H}^{(1),n_f}\,, \\
\mathcal{H}^{(2)} &= N_c^2 \mathcal{H}^{(2),1} + N_c n_f \mathcal{H}^{(2),n_f} + n_f^2 \mathcal{H}^{(2),n_f^2}\,.
\end{aligned}
\tag{4.5.6}
$$

We present a benchmark evaluation at the following phase space point in the physical scattering region specified by Eq. 4.5.1 (the momenta are given in units of GeV):

$$
\begin{aligned}
p_1 &= (88.551333054, -22.100690287, 40.080353191, -75.805430956)\,, \\
p_2 &= (-500, 0, 0, -500)\,, \\
p_3 &= (328.32941922, -103.84961188, -301.93375538, 76.494921387)\,, \\
p_4 &= (-500, 0, 0, 500)\,, \\
p_5 &= (152.35810946, -105.88095966, -97.709638326, 49.548385226)\,, \\
p_6 &= (430.76113825, 231.83126183, 359.56304052, -50.237875657)\,,
\end{aligned}
\tag{4.5.7}
$$

with $\text{tr}_5 = 2.167055i \cdot 10^{10}$ GeV^4. We take the W boson mass and width to be:

$$M_W = 80.4109 \text{ GeV}\,, \qquad \Gamma_W = 2.0467 \text{ GeV}\,. \tag{4.5.8}$$

High precision values for the phase space point in Eq. 4.5.7 as well as the input parameters in Eq. 4.5.8 are provided in the ancillary files. We present in Tables 4.2 and 4.3 the values of the bare two-loop amplitudes normalised to the tree-level amplitudes in the $\mathbf{u\bar{d}}$ scattering channel for each individual sub-amplitude:

$$\hat{A}_{6,i}^{(L),j} = \frac{A_{6,i}^{(L),j}}{A_{6,i}^{(0)}}\,, \tag{4.5.9}$$

for $i = u, d, W, e$ and the two closed fermion loop contributions specified in Eq. 4.2.7, namely $j = 1, n_f$. The results are presented only for the two independent helicity configurations ($+{+}{+}{-}{-}{+}$ and $-{+}{+}{-}{-}{+}$). We note that the numerical results in Tables 4.2 and 4.3, presented separately for the sub-amplitudes A_u, A_d, A_W and A_e, are gauge dependent. We used $q_1 = p_3$ and $q_3 = p_1$, where $q_1(q_3)$ is the reference momentum for the photon (gluon) polarisation vector. Gauge invariant quantities can be obtained using Eq. 4.2.6. This enables comparisons already for the smaller building blocks of the amplitude, rather than just the full amplitude. For example, the sub-amplitudes A_W and A_e can be derived by attaching the $L_{B,\mu}^{e/W}(p_1, p_5, p_6)$ decay currents to the already available $q\bar{q} \to Wg$ amplitude [214]. Indeed, we performed this check, as described in Section 4.4.5. In Table 4.4, we show the values of the two-loop reduced squared finite remainders normalised to the reduced squared tree-level amplitudes:

$$\hat{\mathcal{H}}^{(L)} = \frac{\mathcal{H}^{(L)}}{\mathcal{H}^{(0)}}\,, \tag{4.5.10}$$

for all channels of both $pp \to W^+\gamma j$ and $pp \to W^-\gamma j$ production. We give analogous tables for the one-loop amplitudes in Appendix E. In order to show the suitability and stability of our evaluation strategy, we present in Fig. 4.3 the evaluation of the reduced squared finite remainders on a one-dimensional slice of the physical phase space for all channels of $W^+\gamma j$ production. We begin by parameterising the momenta of the one-mass five-particle process relevant for the W-production amplitudes as:

$$\begin{aligned}
p_1^\mu &= u_1 \frac{\sqrt{s}}{2}\,(1, 1, 0, 0)\,, \\
p_2^\mu &= \frac{\sqrt{s}}{2}\,(-1, 0, 0, -1)\,, \\
p_3^\mu &= u_2 \frac{\sqrt{s}}{2}\,(1, \cos\theta, -\sin\phi\sin\theta, -\cos\phi\sin\theta)\,, \\
p_4^\mu &= \frac{\sqrt{s}}{2}\,(-1, 0, 0, 1)\,.
\end{aligned} \tag{4.5.11}$$

	helicity	ϵ^{-4}	ϵ^{-3}	ϵ^{-2}	ϵ^{-1}	ϵ^{0}
$\hat{A}^{(2),1}_{6,u}$	$++{+}{-}{-}{+}$	2	-49.5288	$603.232 + 4.18740i$	$-4813.11 - 82.3401i$	$28289.7 + 713.980i$
	$-{+}{+}{-}{-}{+}$	2	-49.5288	$605.560 + 1.03233i$	$-4867.68 - 10.1740i$	$28904.1 - 84.4212i$
$\hat{A}^{(2),1}_{6,d}$	$++{+}{-}{-}{+}$	2	-49.5288	$606.017 + 4.37613i$	$-4883.27 - 87.6955i$	$29148.2 + 787.284i$
	$-{+}{+}{-}{-}{+}$	2	-49.5288	$604.589 + 4.36093i$	$-4848.83 - 90.4281i$	$28743.3 + 856.481i$
$\hat{A}^{(2),1}_{6,W}$	$++{+}{-}{-}{+}$	2	-49.5288	$605.100 + 3.07126i$	$-4859.29 - 58.7793i$	$28844.2 + 480.026i$
	$-{+}{+}{-}{-}{+}$	2	-49.5288	$605.637 + 2.40762i$	$-4871.59 - 43.1992i$	$28978.3 + 302.671i$
$\hat{A}^{(2),1}_{6,e}$	$++{+}{-}{-}{+}$	2	-49.5288	$605.140 + 2.93702i$	$-4860.19 - 55.6437i$	$28853.6 + 444.669i$
	$-{+}{+}{-}{-}{+}$	2	-49.5288	$606.606 + 2.97710i$	$-4894.35 - 56.2398i$	$29236.9 + 444.300i$

Table 4.2: Bare two-loop helicity sub-amplitudes (normalised to the tree-level amplitudes as in Eq. 4.5.9) without any closed fermion loop contribution for $W^+\gamma j$ production in the $\mathbf{u\bar{d}}$ scattering channel evaluated at the kinematic point given in Eq. 4.5.7. The results are shown for the two independent helicity configurations and obtained with $q_1 = p_3$ and $q_3 = p_1$ where q_1 (q_3) is the reference momentum for the photon (gluon) polarisation vector.

We fix the value of $\cos\theta$ by requiring that:

$$(p_5 + p_6)^2 = M_{ll}^2\,, \tag{4.5.12}$$

where M_{ll}^2 is the invariant mass of the leptonic pair. We then parameterise the momenta of the leptonic pair:

$$p_5^\mu = u_3 \frac{\sqrt{s}}{2} \left(1, \cos\theta_{ll}, -\sin\phi_{ll}\sin\theta_{ll}, -\cos\phi_{ll}\sin\theta_{ll}\right)\,, \tag{4.5.13}$$

and p_6 follows from momentum conservation. We fix u_3 by requiring that $p_6^2 = 0$. In order to define a univariate phase space slice, we choose:

$$s = 10^4\,\mathrm{GeV}^2\,, \qquad M_{ll} = 60\,\mathrm{GeV}\,, \qquad \phi = \frac{1}{10}\,, \qquad u_1 = \frac{1}{7}\,, \qquad \theta_{ll} = \frac{\pi}{2}\,, \qquad \phi_{ll} = \frac{\pi}{3}\,. \tag{4.5.14}$$

The remaining variable, u_2, is constrained to the interval $[87/175, 29/50]$. We chose these values arbitrarily so that the slice crosses a number of spurious poles, i.e. points where the rational coefficients diverge, whereas the finite remainders stay finite. We checked explicitly that, while approaching such spurious poles, the values

	helicity	ϵ^{-4}	ϵ^{-3}	ϵ^{-2}	ϵ^{-1}	ϵ^{0}
$\hat{A}^{(2),n_f}_{6,u}$	$++{+}{-}{-}{+}$	0	0.333333	-7.39369	$79.8302 + 1.39580i$	$-556.215 - 14.3791i$
	$-{+}{+}{-}{-}{+}$	0	0.333333	-7.39369	$80.6063 + 0.34411i$	$-570.821 + 1.89741i$
$\hat{A}^{(2),n_f}_{6,d}$	$++{+}{-}{-}{+}$	0	0.333333	-7.39369	$80.7586 + 1.45871i$	$-576.048 - 17.8798i$
	$-{+}{+}{-}{-}{+}$	0	0.333333	-7.39369	$80.2827 + 1.45364i$	$-566.721 - 19.4318i$
$\hat{A}^{(2),n_f}_{6,W}$	$++{+}{-}{-}{+}$	0	0.333333	-7.39369	$80.4531 + 1.02375i$	$-569.113 - 9.88866i$
	$-{+}{+}{-}{-}{+}$	0	0.333333	-7.39369	$80.6321 + 0.802539i$	$-572.278 - 6.31448i$
$\hat{A}^{(2),n_f}_{6,e}$	$++{+}{-}{-}{+}$	0	0.333333	-7.39369	$80.4664 + 0.979007i$	$-569.368 - 9.14880i$
	$-{+}{+}{-}{-}{+}$	0	0.333333	-7.39369	$80.9551 + 0.992365i$	$-577.544 - 9.72557i$

Table 4.3: Bare two-loop helicity sub-amplitudes (normalised to the tree-level amplitudes as in Eq. 4.5.9) with one closed fermion loop for $W^+\gamma j$ production in the $\mathbf{u\bar{d}}$ scattering channel evaluated at the kinematic point given in Eq. 4.5.7. The results are shown for the two independent helicity configurations and obtained with $q_1 = p_3$ and $q_3 = p_1$ where q_1 (q_3) is the reference momentum for the photon (gluon) polarisation vector.

of the rational coefficients become larger and larger, while the finite remainders converge. We evaluated the pentagon functions in quadruple precision using the `PentagonFunctions++` library, and the rational coefficients in `Mathematica` with 64-digit accuracy. This is a robust check of the stability of the evaluation, since the convergence requires large numerical cancellations among various terms of the finite remainders. Fig. 4.3 shows the plots of the reduced squared finite remainders up to the two-loop order for all channels of $W^+\gamma j$ production on the univariate phase space slice defined above.

4.6 Summary

In this chapter, we have presented the two-loop leading colour QCD helicity amplitudes for the process $W^{\pm}\gamma j$ for the first time. We have obtained relatively compact analytic expressions that can be efficiently evaluated across the full physical phase space. We constructed the colour and helicity summed finite remainders, and performed several validation tests.

$W^+\gamma j$	$\mathrm{Re}\,\hat{\mathcal{H}}^{(2),1}$	$\mathrm{Re}\,\hat{\mathcal{H}}^{(2),n_f}$	$\mathrm{Re}\,\hat{\mathcal{H}}^{(2),n_f^2}$
$\mathbf{u\bar{d}}$	483.506205134	-222.568846475	22.1747738519
$\mathbf{\bar{d}u}$	462.732386147	-219.389809502	22.1747738519
$\mathbf{ug}$	894.669569294	-309.802310098	24.2425489305
$\mathbf{gu}$	796.031872994	-288.292629199	23.3127252902
$\mathbf{\bar{d}g}$	954.097242371	-317.336400774	24.2425489305
$\mathbf{g\bar{d}}$	898.961273740	-302.856612446	23.3127252902
$W^-\gamma j$	$\mathrm{Re}\,\hat{\mathcal{H}}^{(2),1}$	$\mathrm{Re}\,\hat{\mathcal{H}}^{(2),n_f}$	$\mathrm{Re}\,\hat{\mathcal{H}}^{(2),n_f^2}$
$\mathbf{d\bar{u}}$	498.332524932	-222.702160434	22.1747738519
$\mathbf{\bar{u}d}$	732.600496818	-268.121335492	22.1747738519
$\mathbf{dg}$	1786.14253164	-305.863467669	24.2425489305
$\mathbf{gd}$	1612.34790163	-407.732735568	23.3127252902
$\mathbf{\bar{u}g}$	320.710353060	-152.382317276	24.2425489305
$\mathbf{g\bar{u}}$	1300.37372328	-375.944229843	23.3127252902

Table 4.4: Reduced squared finite remainders (normalised to the reduced squared tree level amplitudes) for all closed fermion loop contributions and scattering channels evaluated at the kinematic point given in Eq. 4.5.7 for both $pp \to W^+\gamma j$ and $pp \to W^-\gamma j$ production.

To obtain the best possible theoretical predictions, it will be necessary to improve upon the leading colour approximation taken in this chapter. While it is expected that the leading colour contribution dominates, a quantitative statement is not possible without explicit computation. Sub-leading colour corrections require non-planar topologies to be taken into account, and represent a considerable increase in analytic and algebraic complexity. We point out that the bases of pure MIs required for the non-planar topologies have been recently made available in literature after the completion of our work [125].

We hope that our approach to the simplification of the reconstructed amplitudes will be of use in subsequent amplitude computations. An improved understanding of how a rational parametrisation can be tuned to simplify a particular rational coefficient would certainly be of great value. We expect this to be of particular importance when dealing with sub-leading colour and non-planar configurations, in which many different orderings appear simultaneously. It would also be interesting to study the effect of this method on the reconstruction of the amplitude, i.e. whether the reconstruction is performed in terms of s_{ij}, tr_5 variables or a rational parametrisation.

Our work opens the path for precision predictions for $pp \to W^\pm\gamma j$ production at NNLO accuracy in the strong coupling. Naturally, a detailed phenomenological study should also include EW corrections, which are known to dominate the QCD ones in some phase space regions of vector boson production. For example, for the process

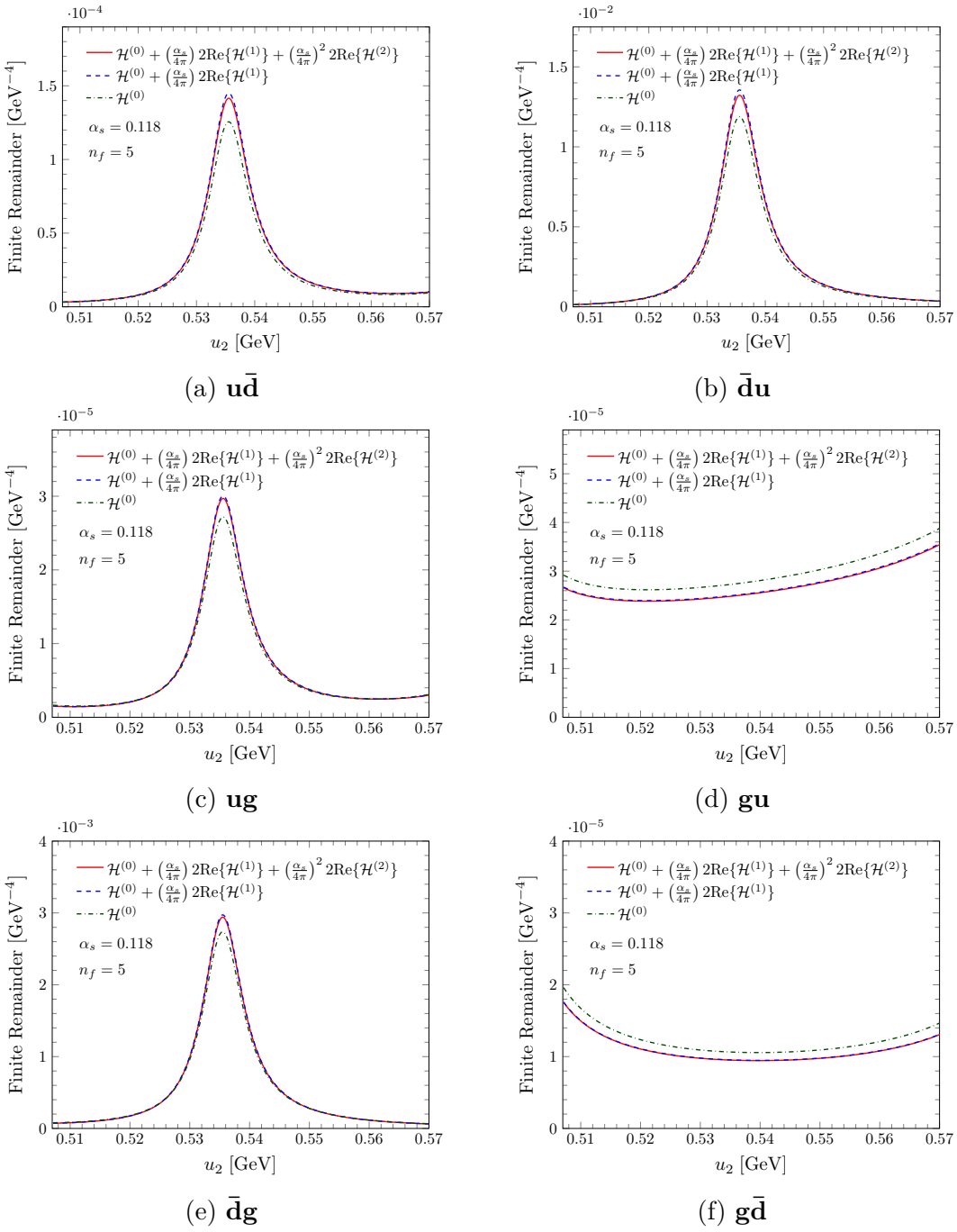

Figure 4.3: Reduced squared finite remainders $\mathcal{H}^{(L)}$ at tree level, one and two loops, evaluated on the univariate phase space slice defined by Eqs. 4.5.11, 4.5.12 and 4.5.13, with the parameters given in Eq. 4.5.14, for all channels of $W^+\gamma j$ production defined in Eq. 4.5.

$pp \to W^{\pm}j$, the NLO EW corrections can reach up to 50% of the LO, as compared to 10% for the NNLO QCD ones [237–241]. Although less pronounced, NLO EW effects are also significant for $pp \to W^{\pm}\gamma$ production [215–218, 225]. Therefore, it will be of great importance to study such corrections to the $pp \to W^{\pm}\gamma j$ process as well in order to achieve more reliable predictions across the full phase space.

Chapter 5

Two-loop QED helicity amplitudes for $0 \to \ell\bar{\ell}\gamma\gamma^*$ scattering

In this chapter, we present the computation of the two-loop QED helicity amplitudes for the scattering of a lepton pair with an off-shell and an on-shell photon, $0 \to \ell\bar{\ell}\gamma\gamma^*$, using the approximation of massless leptons. We express all MIs relevant for the scattering of four massless particles with a single external off-shell leg up to two loops in a basis of algebraically independent GPLs, which guarantees an efficient numerical evaluation and compact analytic representations of the amplitudes. Analytic forms of the amplitudes are reconstructed from numerical evaluations over finite fields. Our results complete the amplitude-level ingredients contributing to the $\mathrm{N^3LO}$ predictions of electron-muon scattering, $e\mu \to e\mu$, which are required to meet the precision goal of the future MUonE experiment.

The chapter is organised as follows. After an introduction to the topic in Section 5.1, we describe our decomposition of the helicity amplitudes and detail how we express the off-shell currents in Section 5.2. Then, in Section 5.3 we discuss our computation of analytic amplitudes by numerical evaluations over finite fields. In Section 5.4, we present the computation of the Feynman integrals in terms of a basis of special functions. We provide useful technical details in the appendices. In Appendix A, we discuss how we handle permutations of the integral families in the IBP reduction. The relevant families of Feynman integrals are defined in Appendix F. Appendix G is devoted to the analytic continuation of the special functions to the physical kinematic regions. Finally, details of the UV renormalisation and IR factorisation which determine the pole structure of the amplitudes can be found in Appendix C.3.

5.1 Introduction

The MUonE experiment [242–245] will measure the hadronic running of the electromagnetic coupling α using low-energy elastic electron-muon scattering, $e\mu \to e\mu$. This will enable a new and precise determination of the hadronic vacuum polarisation (HVP) contribution a_μ^{HVP} [246, 247] to the muon anomalous magnetic moment a_μ. This is required in light of the recent tensions between experimental [248], SM data-driven [249], and lattice QCD [250] results for a_μ. Increasing the precision of the theoretical predictions for $e\mu \to e\mu$ scattering is a high priority for the planned MUonE experiment [251, 252] and has seen good progress in the last few years [253–257]. The recent completion of full NNLO QED corrections [258] indicates that N^{3}LO corrections in differential distributions are required to meet MUonE's precision goal of 10 parts per million. Electron-line corrections, meaning corrections to the subprocess with the muon line stripped off ($e \to e\gamma^*$), are the dominant corrections [258], and a collaborative project was started to perform their fixed-order calculation at N^{3}LO [259]. With the triple-virtual corrections now available [260–262], the main missing ingredient is the real-double-virtual (RVV) matrix element ($e \to e\gamma\gamma^*$) at two loops. While these contributions could be extracted from amplitudes in the literature [214, 229, 263], our direct computation provides the massless RVV contribution in a complete and compact form.

Another application of the $0 \to \ell\bar{\ell}\gamma\gamma^*$ amplitudes is in electron-positron annihilation experiments [264]. They are required for initial-state corrections in predictions of the ratio of hadron-to-muon production in e^+e^- collisions, which is an important input for existing SM predictions of a_μ^{HVP} [265]. The two-loop amplitudes contribute to RVV corrections to $e^+e^+ \to \gamma^*$ in direct scan measurements, while radiative return measurements concern corrections to $e^+e^- \to \gamma\gamma^*$ [249]. In the latter configuration, the e^+e^- beam has a fixed centre-of-mass energy of a few GeV and the on-shell photon originates from initial state radiation (ISR). The energy lost to the ISR photon is used to effectively scan over the energies of the decay of the off-shell photon. A differential cross section of, for example, $\gamma^* \to$ hadrons with respect to the centre-of-mass energy of the decay, $\mathrm{d}\sigma/\mathrm{d}s$, can be extracted from measurements of the differential cross section with respect to the energy of the ISR photon, $\mathrm{d}\sigma/\mathrm{d}E_\gamma$. State-of-the-art predictions for these measurements are currently at NLO [265]. We provide the two-loop $e^+e^- \to \gamma\gamma^*$ amplitudes required for the double-virtual (VV) corrections at NNLO, although the bottleneck remains in the hadronic decay.

Our amplitudes are calculated in the approximation of massless leptons. In the NNLO massive $e\mu \to e\mu$ cross section calculation [258], the authors obtain photonic corrections (those with no closed fermion loops), using a small-mass expansion [266–

268] applied to the two-loop amplitudes with massless electrons for the VV corrections. This approximation relies on the electron mass being much smaller than any other scale, which is valid in the bulk of phase space. Further splitting the photonic corrections, they take the subset of electron-line corrections and find that the relative difference to the true massive NNLO differential cross section is generally around $10^{-3}\alpha^2$, where α is the fine-structure constant, which is negligible compared to the 10^{-5} precision goal. The approximation breaks down in soft and collinear regions, where they treat the amplitudes using IR factorisation [269–271], and is not used for contributions including closed fermion loops [268, 272]. Our amplitudes can be used analogously for the RVV corrections at N^{3}LO.

A key ingredient for computing the scattering amplitudes are analytic expressions for the required Feynman integrals. Complete analytic results for four-point processes up to two loops are already available in the literature [273–275]. Expansions of these integrals up to higher orders in the dimensional regularisation parameter ϵ have also been reconsidered recently [276], in view of their usage for N^{3}LO corrections to $2 \to 2$ processes in QCD [277, 278]. The state of the art for integrals with this kinematic configuration has reached three loops [279–282]. We revisit the computation of the one- and two-loop integrals following the approach of Refs. [112, 114, 121, 125, 182] based on the construction of a basis of independent special functions, which gives a unique and uniform representation of all the required Feynman integrals up to transcendental weight four. This enables a more efficient computation of the amplitudes using the modern workflow based on finite field arithmetic, and leads to more compact expressions. We give explicit expressions for the basis functions in terms of GPLs which can be evaluated in an efficient and stable way throughout the physical phase space. We compute all crossings of all massless one- and two-loop four-particle Feynman integrals with an external off-shell leg, so that our results for the integrals may be of use for any scattering process with these kinematics.

5.2 Structure of the amplitude

We calculate the one- and two-loop QED corrections to the process:

$$0 \to \ell(p_1, h_1) + \bar{\ell}(p_2, h_2) + \gamma(p_3, h_3) + \gamma^*(p_4)\,, \tag{5.2.1}$$

which we call $0 \to \ell\bar{\ell}\gamma\gamma^*$ for short. Here, ℓ denotes an on-shell massless lepton and γ (γ^*) an on-shell (off-shell) photon, while h_i and p_i are the helicity and momentum of the i^{th} particle. We take the external momenta p_i to be all outgoing. They satisfy

the following momentum-conservation and on-shell conditions:

$$\sum_{i=1}^{4} p_i^\mu = 0\,, \qquad\qquad p_i^2 = 0 \quad \forall\, i = 1,2,3\,. \tag{5.2.2}$$

The single-off-shell four-particle phase space is described by three independent scalar invariants, which we choose as:

$$\vec{s} \coloneqq \{s_{12}, s_{23}, s_4\}\,, \tag{5.2.3}$$

where $s_{i\ldots j} \coloneqq (p_i + \ldots + p_j)^2$. We use dimensional regularisation in the HV scheme [33], with $D = 4 - 2\epsilon$ spacetime dimensions and four-dimensional external momenta.

Because of the off-shell photon in the process, the helicity amplitudes $\mathcal{A}^\mu(1_\ell, 2_{\bar{\ell}}, 3_\gamma, 4_{\gamma^*})$ are actually off-shell currents carrying a free Lorentz index. We consider the perturbative QED expansion of the helicity amplitudes:

$$\mathcal{A}^\mu(1_\ell, 2_{\bar{\ell}}, 3_\gamma, 4_{\gamma^*}) = g_e^2 \sum_{L\geq 0} \left(n_\epsilon \frac{\alpha}{4\pi}\right)^L \mathcal{A}^{(L)\mu}(1_\ell, 2_{\bar{\ell}}, 3_\gamma, 4_{\gamma^*})\,, \tag{5.2.4}$$

with prefactor $n_\epsilon = \mathrm{i}\,(4\pi)^\epsilon \mathrm{e}^{-\epsilon\gamma_E}$, electromagnetic coupling g_e, and $\alpha = g_e^2/(4\pi)$. We truncate the expansion at $L = 2$ loops. We set the renormalisation scale μ_R to 1 throughout the computation and restore the dependence on it in the final analytic result by dimensional analysis. For the bare amplitudes, we have that:

$$\mathcal{A}^{(L)\mu}(\mu_R) = \left(\mu_R^{2\epsilon}\right)^L \mathcal{A}^{(L)\mu}(\mu_R = 1)\,. \tag{5.2.5}$$

There are two independent helicity configurations (h_1, h_2, h_3), which we take as:

$$\{-+-\,,\quad -++\}\,. \tag{5.2.6}$$

We derive the analytic expressions for these helicity amplitudes. We obtain the remaining helicity configurations, $\{+-+\,,\quad +--\}$, through parity transformation (see Appendix C of Ref. [283]).

We decompose the loop-level helicity amplitudes $\mathcal{A}^{(L)\mu}$ into gauge-invariant subamplitudes $\mathcal{A}_{i,j}^{(L)\mu}$, where the subscript i counts the number of closed massless fermion loops and j the number of external photons attached to closed fermion loops. The non-zero contributions are:

$$\mathcal{A}^{(1)\mu} = \mathcal{A}_{0,0}^{(1)\mu} + n_l\, \mathcal{A}_{1,1}^{(1)\mu}\,, \tag{5.2.7a}$$

$$\mathcal{A}^{(2)\mu} = \mathcal{A}_{0,0}^{(2)\mu} + n_l \left(\mathcal{A}_{1,0}^{(2)\mu} + \mathcal{A}_{1,1}^{(2)\mu} + \mathcal{A}_{1,2}^{(2)\mu}\right) + n_l^2 \mathcal{A}_{2,1}^{(2)\mu}\,, \tag{5.2.7b}$$

where n_l denotes the number of charged lepton flavours running in the loops. Representative Feynman diagrams contributing to these subamplitudes are illustrated

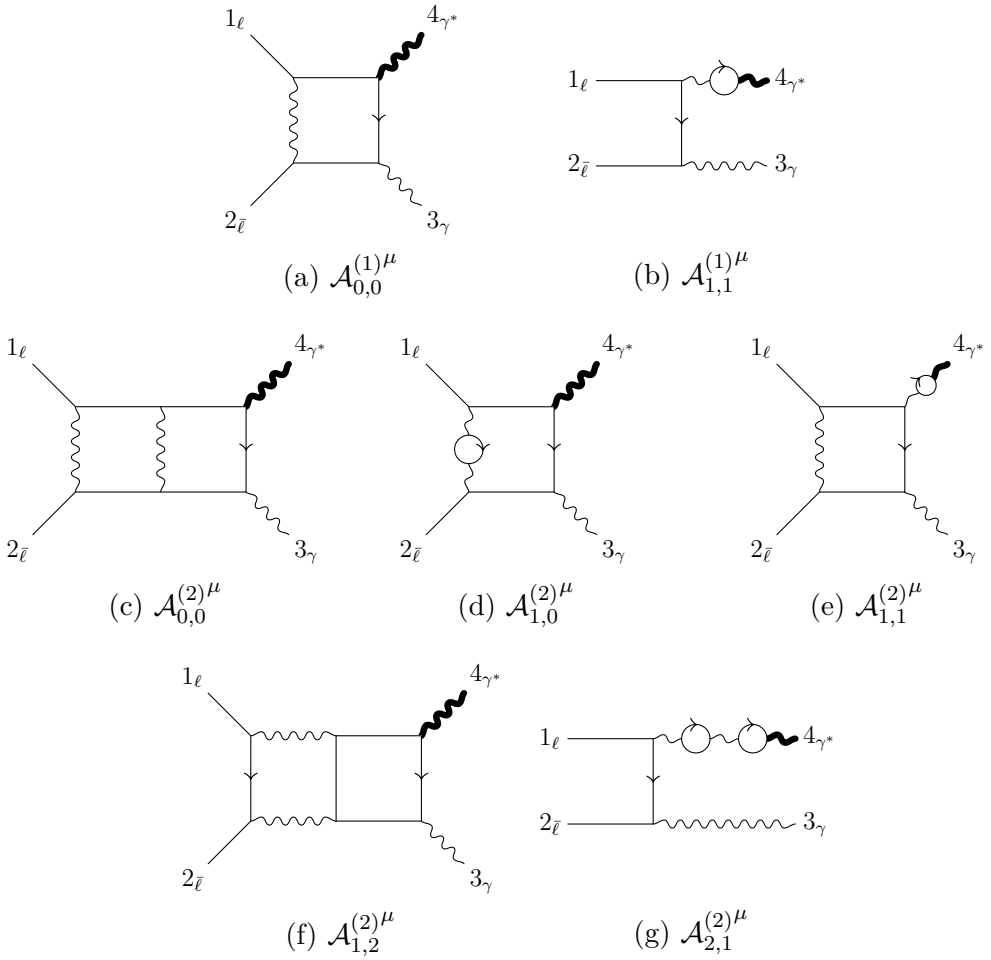

(a) $\mathcal{A}^{(1)\mu}_{0,0}$ (b) $\mathcal{A}^{(1)\mu}_{1,1}$

(c) $\mathcal{A}^{(2)\mu}_{0,0}$ (d) $\mathcal{A}^{(2)\mu}_{1,0}$ (e) $\mathcal{A}^{(2)\mu}_{1,1}$

(f) $\mathcal{A}^{(2)\mu}_{1,2}$ (g) $\mathcal{A}^{(2)\mu}_{2,1}$

Figure 5.1: Representative Feynman diagrams for the subamplitudes defined in Eq. 5.2.7. The off-shell external leg is indicated by a bold line.

in Fig. 5.1. Amplitudes with a closed fermion loop attached to an odd number of photons vanish by Furry's theorem.

We decompose the amplitude and subamplitude currents as:

$$\mathcal{A}^{(L)\mu} = \sum_{k=1}^{4} a_k^{(L)}\, q_k^\mu\,, \qquad\qquad \mathcal{A}_{i,j}^{(L)\mu} = \sum_{k=1}^{4} a_{i,j;k}^{(L)}\, q_k^\mu\,, \tag{5.2.8}$$

using the following basis written in the spinor-helicity formalism:

$$q_k^\mu = p_k^\mu \quad \forall\, k = 1,2,3\,, \qquad\qquad q_4^\mu = \frac{\langle 2|p_3 p_1 \sigma^\mu |2] - \langle 1|p_3 p_2 \sigma^\mu |1]}{2 s_{12}}\,. \tag{5.2.9}$$

Note that q_4 is orthogonal to the momenta p_i by construction; one can in fact show that $q_4^\mu \propto \varepsilon^{\mu\nu\rho\sigma} q_{1\nu} q_{2\rho} q_{3\sigma}$. The subamplitude coefficients $a_{i,j;k}^{(L)}$ can be related to the amplitude ones $a_k^{(L)}$ through Eq. 5.2.7.

The scattering amplitudes $\mathcal{M}^{(L)}$ for fully on-shell processes (for instance, for $0 \to e^- e^+ \gamma \mu^- \mu^+$) are obtained by contracting the amplitude currents $\mathcal{A}^{(L)\mu}$ (for $0 \to e^- e^+ \gamma\gamma^*$) with a suitable decay current $\mathcal{V}_\mu$ (in this example, $\gamma^* \to \mu^- \mu^+$) as:

$$\mathcal{M}^{(L)} \coloneqq \mathcal{A}^{(L)} \cdot \mathcal{V} = \sum_{k=1}^{4} a_k^{(L)}\, (q_k \cdot \mathcal{V})\,. \tag{5.2.10}$$

In this manner, the on-shell amplitudes $\mathcal{M}^{(L)}$ are given by the scalar product between the vector of coefficients $(a_1^{(L)}, \ldots, a_4^{(L)})$, and that of decay-vector contractions $(q_1 \cdot \mathcal{V}, \ldots, q_4 \cdot \mathcal{V})$. The coefficients $a_k^{(L)}$ depend on the helicities of the three on-shell particles in Eq. 5.2.1, while the decay vector $\mathcal{V}_\mu$ depends on the helicities of the particles the off-shell photon decays to. The helicity-summed interference between the L_1-loop and the L_2-loop matrix elements is then given by:

$$\mathcal{M}^{(L_1,L_2)} = \frac{1}{4} \sum_{\vec{h}} \mathcal{M}_{\vec{h}}^{(L_1)^*} \mathcal{M}_{\vec{h}}^{(L_2)}\,, \tag{5.2.11}$$

where the subscripts $\vec{h}$ indicates the helicities of all on-shell particles — that is, including the decay products of the off-shell photon — and the overall constant factor averages over the helicities of the incoming particles.

The output of the computation described in Section 5.3 is the set of four projections $\mathcal{A}_{i,j}^{(L)} \cdot q_k$ for each helicity configuration listed in Eq. 5.2.6. From these, we determine the subamplitude coefficients $a_{i,j;k}^{(L)}$ by inverting Eq. 5.2.8 as:

$$a_{i,j;k}^{(L)} = \sum_{m=1}^{4} \left(\mathrm{G}^{-1}\right)_{km} \left(\mathcal{A}_{i,j}^{(L)} \cdot q_m\right)\,, \tag{5.2.12}$$

where G is the Gram matrix of the vectors q_i, that is, the matrix of entries $\mathrm{G}_{ij} \coloneqq q_i \cdot q_j$

for $i, j = 1, \ldots, 4$. At loop level, we write the subamplitude coefficients as:

$$a^{(L)}_{i,j;k} = \sum_{w=-2L}^{4-2L} \sum_{r} c_{r,w}\, \mathrm{mon}_r(F)\, \epsilon^w, \tag{5.2.13}$$

where $\mathrm{mon}_r(F)$ are monomials of special functions F (see Section 5.4), and the coefficients $c_{r,w}$ are rational functions of the kinematics. We drop the dependence on i, j, k, and L on the right-hand side of Eq. 5.2.13 for compactness. We truncate the Laurent expansion around $\epsilon = 0$ to the orders required for computing NNLO predictions. We express the coefficients $c_{r,w}$ as $\mathbb{Q}$-linear combinations of a smaller set of linearly-independent coefficients (see Section 5.3). The analytic expressions of the latter are given explicitly in terms of MTs. We simplify these expressions through a multivariate partial fraction decomposition using `MultivariateApart` [192], and by collecting the common factors.

In the ancillary files of Ref. [284], the directory `amplitudes/` contains `Mathematica` files describing the bare helicity subamplitude currents $\mathcal{A}^{(L)\mu}_{i,j}$ by their coefficients $a^{(L)}_{i,j;k}$ in the form of Eq. 5.2.13. The `Mathematica` script `current.m` is a reference implementation of the numerical evaluation of the bare amplitude coefficients $a^{(L)}_k$ in Eq. 5.2.13, including summation of subamplitudes in Eq. 5.2.7, treatment of dependent helicities, and renormalisation scale restoration in Eq. 5.2.5. The `Mathematica` script `evaluation.wl` demonstrates the construction of the five-particle on-shell amplitudes in Eq. 5.2.10 for the process $0 \to e^- e^+ \gamma \mu^- \mu^+$, and their helicity-summation to obtain the squared matrix elements in Eq. 5.2.11. The results of the script are checked against a reference point included in `reference_point.json`.

We perform the following checks of our amplitudes:

Ward identity We verify the gauge invariance of the subamplitudes $\mathcal{A}^{(L)\mu}_{i,j}$ by checking that they vanish on replacing the on-shell photon's polarisation vector with its momentum.

One-loop crosscheck We successfully crosscheck our one-loop $n_l = 0$ helicity-summed matrix element contracted with the decay $\gamma^* \to \mu^- \mu^+$ against the QED NLO electron-line corrections for $e\mu \to e\mu\gamma$ obtained with `McMule` [285, 286].

Finite remainder We verify that the ϵ-poles of the bare amplitudes have the structure predicted by UV renormalisation and IR factorisation [23–26, 287]. We then subtract the expected poles and define finite remainders at one and two loops as:

$$\mathcal{F}^{(1)\mu} = \left[\mathcal{A}^{(1)\mu} - \frac{3}{2}\frac{\beta_0}{\epsilon}\mathcal{A}^{(0)\mu}\right] - Z^{(1)}\mathcal{A}^{(0)\mu}\,, \tag{5.2.14a}$$

$$\mathcal{F}^{(2)\mu} = \left[\mathcal{A}^{(2)\mu} - \frac{5}{2}\frac{\beta_0}{\epsilon}\mathcal{A}^{(1)\mu} - \left(-\frac{15}{8}\frac{\beta_0^2}{\epsilon^2} + \frac{3}{4}\frac{\beta_1}{\epsilon}\right)\mathcal{A}^{(0)\mu}\right] - Z^{(2)}\mathcal{A}^{(0)\mu} - Z^{(1)}\mathcal{F}^{(1)\mu}\,, \tag{5.2.14b}$$

where the square brackets separate renormalisation of UV poles from subtraction of IR poles. The derivation of these formulae follows the procedure outlined in Appendix C.3. The coefficients $Z^{(L)}$ are given in Appendix D.

5.3 Setup of the calculation

In this section, we briefly outline the workflow we use to calculate our amplitudes. For an in-depth discussion, we refer the reader to Chapter 2. Firstly, we generate all Feynman diagrams contributing to Eq. 5.2.1 using `QGRAF` [35]. Each diagram is then replaced with the corresponding Feynman rules for vertices, propagators, and external states, leading to a collection of D-dimensional Feynman integrals. Next, we filter the integrals according to Eqs. 5.2.4 and 5.2.7 using a collection of `Mathematica` and `FORM` scripts [184, 185]. Within each subamplitude $\mathcal{A}_{i,j}^{(L)\mu}$, we then collect the integrals according to their topology, by which we mean a unique set of denominators. At this point, the subamplitudes are sums of Feynman integrals over distinct integral topologies, with the numerators given by linear combinations of monomials that depend on the loop as well as the external momenta. To work with the projected helicity subamplitudes $\mathcal{A}_{i,j}^{(L)} \cdot q_k$, we specify the polarisations of external particles according to Eq. 5.2.6, as well as the projector q_k^μ of the off-shell photon from Eq. 5.2.9.

It is natural to express helicity-dependent objects using the spinor-helicity formalism. Then, the monomials of loop momenta contain the following scalar products and spinor strings:

$$\Big\{k_i \cdot k_j,\, k_i \cdot p_j,\, \langle ij\rangle,\, [ij],\, \langle i|k_i|j],\, \langle i|p_4|j],\, \langle i|k_i p_4|j\rangle,\, [i|k_i p_4|j]\Big\}\,. \tag{5.3.1}$$

Their coefficients, on the other hand, are composed of the same type of objects, but do not contain any dependence on loop momenta k_i. Similarly to our previous work, we express these coefficients using a rational parametrisation in terms of MTs. The single-off-shell four-particle phase space p is obtained from a massless five-particle parametrisation q (defined in Appendix A of Ref. [187] with $\{x_2 \leftrightarrow x_4, x_3 \leftrightarrow x_5\}$) according to:

$$p_i = q_i \qquad \forall i = 1,2,3, \qquad\qquad p_4 = q_4 + q_5\,. \tag{5.3.2}$$

The MTs x_i are then related to the scalar invariants $\vec{s}$ through:

$$s_{12} = x_1\,, \qquad s_{23} = x_1 x_2\,, \qquad s_4 = x_1 x_3\,. \tag{5.3.3}$$

The phase information for the helicity configurations of Eq. 5.2.6 is restored using the following phase factors:

$$\Phi(-++) = \frac{\langle 12\rangle}{\langle 23\rangle^2}\,, \qquad \Phi(-+-) = \frac{[12]}{[13]^2}\,, \tag{5.3.4}$$

which in our MT parametrisation are given by:

$$\Phi(-++) = x_1^2\,, \qquad \Phi(-+-) = -\frac{1}{x_1(1+x_2-x_3)^2}\,. \tag{5.3.5}$$

We refer to Appendix C of Ref. [283] for a thorough discussion of how to restore the phase information in a MT parametrisation.

This marks the start of our finite field sampling procedure [47]. Firstly, we define the set of maximal topologies, i.e. topologies with the maximum number of propagators allowed by our kinematic configuration. In Fig. 5.2, we present these maximal topologies in an arbitrary ordering of the external momenta (we give their explicit definitions in Appendix F). Several orderings of the external momenta are relevant for the amplitudes, and we treat them as distinct families. Next, we map all topologies present so far onto one of these maximal topologies. The loop momenta dependent objects of Eq. 5.3.1 are then expressed through the nine inverse propagators and ISPs associated with the chosen maximal topology. In this way, each subamplitude is now a sum of integrals compatible with IBP reduction [65, 288], while their coefficients depend on the external kinematics and ϵ. We generate the required IBP relations using `LiteRed` [29]. The resulting IBP system is then solved using the Laporta algorithm [69] with `FiniteFlow`'s linear solver to yield the reduction of all the integrals present within our maximal topologies onto a much smaller subset of MIs. We choose the MIs such that they satisfy DEs in the canonical form [84] (see Section 5.4.1).

In many amplitude applications, multiple permutations of the ordered topologies (such as the ones in Fig. 5.2) can appear. In this case, it might be beneficial to use an optimised strategy for the IBP reduction which performs the reduction in the ordered families only and then permutes the solutions onto the desired 'unordered' families. This permutation can be implemented numerically within finite fields, thus avoiding the need to work with large analytic IBP solutions. Overall, this approach allows us to reduce the time and memory consumption required for the IBP reduction stage, which often proves to be the bottleneck of the whole computation. We describe this strategy in detail in Appendix A.

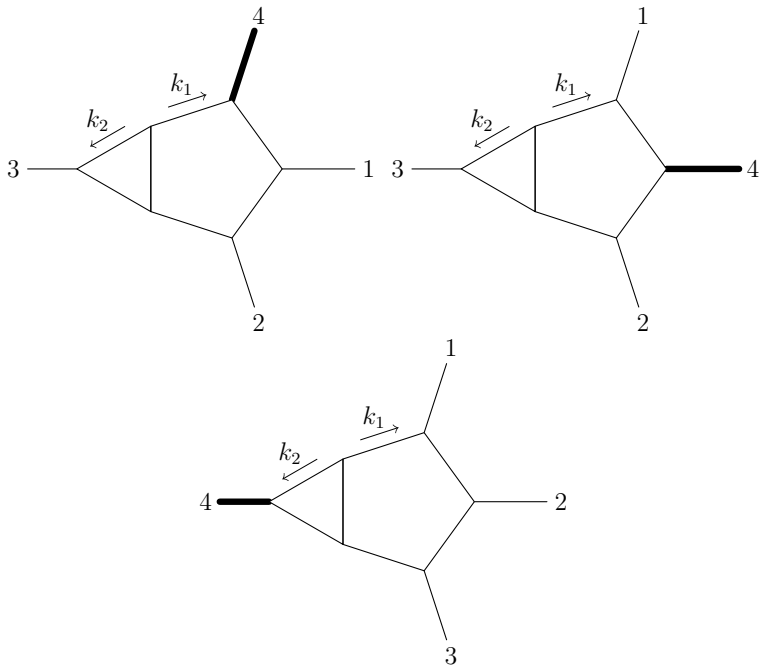

(a) Penta-triangles

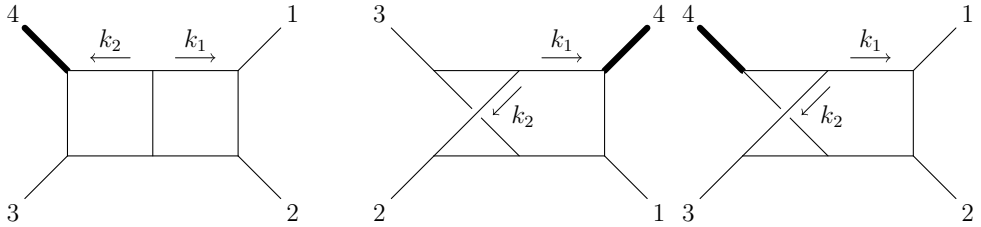

(b) Double-box (c) Crossed double-boxes

Figure 5.2: The two-loop amplitudes include six ordered integral families: three penta-triangles, a double-box, and two crossed double-boxes. All are planar except for the crossed double-boxes. The off-shell external leg is indicated by a bold line. External legs have outgoing momenta.

After IBP reduction, each projected helicity subamplitude $\mathcal{A}^{(L)}_{i,j} \cdot q_k$ is written as a linear combination of MIs multiplied by rational coefficients of ϵ and the kinematic variables. We now write the MIs in terms of a basis of special functions up to the required order in ϵ (see Section 5.4). Finally, we Laurent expand the amplitude around $\epsilon = 0$, the deepest pole being $1/\epsilon^{2L}$ at L loops. The only step left is to reconstruct the rational coefficients of the special-function monomials from their samples over finite fields. To simplify this task, we employ chosen strategies already described in Section 3.3. Specifically, we look for $\mathbb{Q}$-linear relations among the rational coefficients of each helicity subamplitude, which allows us to select those coefficients for reconstruction which have the lowest degrees. Then, we employ the technique of matching the denominators of the rational coefficients against an ansatz. Here, we use the following factors:

$$\Big\{\langle ij\rangle,\, [ij],\, \langle i|p_4|j],\, s_{ij} - s_{k4},\, s_{i4} - s_4,\, s_4\Big\}\,, \tag{5.3.6}$$

for all $i, j, k = 1, 2, 3$ such that $i \neq j \neq k$. This list includes denominator factors of the DEs satisfied by the MIs (listed in Eq. 5.4.2), as well as spinor structures aimed at capturing the phase information of helicity amplitudes. We reconstruct the analytic form of the remaining rational functions using `FiniteFlow`'s built-in multivariate functional reconstruction algorithm (see Section 2.6).

Finally, we note that further simplification strategies can be used for more computationally demanding processes. We refer the reader to Section 4.3.5 and Refs. [187, 283, 289–291].

5.4 Computation of the master integrals

The MIs for the relevant integral families were computed analytically in Refs. [273, 274, 276] (see also Ref. [275] for a thorough discussion of the analytic continuation). We revisit this computation to obtain expressions for the MIs which are better suited to the workflow discussed above. To this end, we compute the MIs for all permutations of the external legs in terms of a *basis* of special functions, following the approach of Refs. [112, 114, 121, 125, 182]. In other words, we express the relevant Feynman integrals in terms of a set of special functions which are algebraically independent. Having such a unified and unique representation for all permutations of the integral families allows for simplifications and cancellations among different permutations. This leads to a simpler expression of the amplitudes and to a more efficient functional reconstruction within the finite field setup. We emphasise that our results cover all MIs required for computing *any* two-loop four-particle amplitude with a single external off-shell leg, and not just the ones present in this work.

We discuss the construction of the basis in Section 5.4.1, and how we express it in terms of GPLs in Section 5.4.2. Finally, we give some details about the numerical evaluation and the checks we performed in Section 5.4.3.

5.4.1 Construction of the special function basis

We follow the strategy presented in Ref. [125]. The starting point are the DEs satisfied by the MIs for each family [28, 78, 83, 292, 293]. Let T label an integral family, e.g. the double-box in Fig. 5.2b for an arbitrary permutation of the external massless momenta. We choose a basis of *pure* master integrals $\overrightarrow{\mathrm{MI}}_T$, that is, a basis which satisfies DEs in the canonical form [84]:

$$\mathrm{d}\overrightarrow{\mathrm{MI}}_T(\vec{s};\epsilon) = \epsilon \left(\sum_{i=1}^{7} A_i^{(T)}\, \mathrm{d}\log w_i(\vec{s})\right) \cdot \overrightarrow{\mathrm{MI}}_T(\vec{s};\epsilon)\,. \tag{5.4.1}$$

Here, d is the total differential, $\mathrm{d}f \coloneqq \mathrm{d}s_{12}\,\partial_{s_{12}} f + \mathrm{d}s_{23}\,\partial_{s_{23}} f + \mathrm{d}s_4\,\partial_{s_4} f$, $A_i^{(T)}$ are constant $(|\mathrm{MI}_T| \times |\mathrm{MI}_T|)$ matrices, where $|\mathrm{MI}_T|$ is the number of MIs of the family T, and:

$$\begin{aligned} &w_1 = s_{12}\,, && w_2 = s_{23}\,, && w_3 = s_{12} + s_{23}\,, && w_4 = s_{12} - s_4\,, \\ &w_5 = s_{23} - s_4\,, && w_6 = s_{12} + s_{23} - s_4\,, && w_7 = s_4 \end{aligned} \tag{5.4.2}$$

are the 'letters'. We find such canonical bases by a mixture of methods: the package `DlogBasis` [294], the analysis of results in the literature for related integral families (massless two-loop five-point planar integrals [110] and two-loop four-point integrals with two massive external legs [295, 296]), and a set of heuristic rules (see e.g. Ref. [89]). We normalise the MIs such that their expansion around $\epsilon = 0$ starts from order ϵ^0:

$$\overrightarrow{\mathrm{MI}}_T(\vec{s};\epsilon) = \sum_{k\geq 0} \epsilon^k\, \overrightarrow{\mathrm{MI}}_T^{(k)}(\vec{s})\,. \tag{5.4.3}$$

For the purpose of computing two-loop scattering amplitudes up to their finite part (i.e., up to order ϵ^0), it suffices to restrict our attention to $k \leq 4$. Since the MIs satisfy canonical DEs, Eq. 5.4.1, the ϵ-order of the MI coefficients $\overrightarrow{\mathrm{MI}}_T^{(k)}(\vec{s})$ equals their transcendental weight [84]. We compute the derivatives of the MIs using `FiniteFlow` [48] and `LiteRed` [29]. We do so only for the integral families with the ordering of the external momenta shown in Fig. 5.2, and obtain those for all other orderings of the external massless legs by permutation. We provide the definition of the pure MIs and the corresponding DEs for all one- and two-loop four-point one-mass families in Fig. 5.2 in the folder `pure_mi_bases/` of the ancillary files of

Ref. [284].

In order to solve the DEs in Eq. 5.4.1, we need boundary values, i.e., values of all MIs up to order ϵ^4 at a phase-space point. Due to the simplicity — by today's standards — of the integrals under consideration, an arbitrary (non-singular) phase-space point would do. Nonetheless, we make a more refined choice following some of the criteria of Refs. [114, 121]. We choose the following point in the s_{12} channel (see Appendix G),

$$\vec{s}_0 = \left(2, -\frac{1}{2}, 1\right) , \tag{5.4.4}$$

motivated by two principles: that it is symmetric under the permutations which preserve the s_{12} channel (i.e., swapping $p_1 \leftrightarrow p_2$), and that it contains few distinct prime factors. The first condition reduces the number of permuted integral families we need to evaluate in order to obtain the boundary values. The second condition reduces the number of independent transcendental constants appearing in the boundary values, which simplifies the construction of the basis of special functions. The order-ϵ^0 boundary values $\overrightarrow{\mathrm{MI}}_T^{(0)}$ are rational constants. We obtain them up to their overall normalisation by solving the 'first-entry conditions' [297], i.e., by requiring the absence of unphysical branch cuts in the solutions. We fix the overall normalisation and the higher-order boundary values $\overrightarrow{\mathrm{MI}}_T^{(k)}(\vec{s}_0)$ (for $1 \leq k \leq 4$) by evaluating all MIs with `AMFlow` [146] (interfaced to `FiniteFlow` [48] and `LiteRed` [29]) at $\vec{s}_0$ with at least 60-digit precision. We anticipate from Section 5.4.2 that, although we use floating-point boundary values, our results in terms of GPLs are fully analytic.

The canonical DEs in Eq. 5.4.1 and the boundary values for all integral families are the input for the algorithm of Ref. [125] for constructing a basis of special functions. We refer to the original work for a thorough discussion. Out of all MI coefficients up to transcendental weight 4, the algorithm selects a subset, denoted $F \coloneqq \{F_i^{(k)}(\vec{s})\}$, which satisfy two constraints. First, they are *algebraically independent*, that is, there are no polynomial functional relations among them. Second, the MI coefficients of all families (including all permutations of the external massless legs) up to transcendental weight 4 are expressed as polynomials in the $\{F_i^{(k)}(\vec{s})\}$ and the zeta values $\zeta_2 = \pi^2/6$ and ζ_3. For example, an arbitrary weight-2 MI coefficient $\mathrm{MI}^{(2)}(\vec{s})$ has the general form

$$\mathrm{MI}^{(2)}(\vec{s}) = \sum_{i=1}^{3} c_i \, F_i^{(2)}(\vec{s}) + \sum_{i\leq j=1}^{4} d_{ij} \, F_i^{(1)}(\vec{s}) \, F_j^{(1)}(\vec{s}) + e \, \zeta_2 \, , \tag{5.4.5}$$

with $c_i, d_{ij}, e \in \mathbb{Q}$. This special subset of MI coefficients, $\{F_i^{(k)}(\vec{s})\}$, constitutes our special function basis. We give the number of functions in the basis in Table 5.1. Note that there is freedom in the choice of which MI coefficients make up the basis.

Weight	Number of basis functions
1	4
2	3
3	20
4	67

Table 5.1: Number of functions $\{F_i^{(k)}\}$ in the basis weight by weight.

We make use of this freedom to choose as many basis elements as possible from the one-loop family, then complement them with coefficients from the planar two-loop families, and finally complete them with coefficients from the non-planar two-loop families. In this way, no two-loop MI coefficients appear in the one-loop amplitudes, and no non-planar two-loop MI coefficients appear in those amplitudes where only planar diagrams contribute (as is often the case in the leading colour approximation of QCD).

The folder `mi2func/` of the ancillary files [284] contains the expression of all MI coefficients (for all one- and two-loop integral families in all permutations of the external massless legs) up to weight 4 in terms of our special function basis. This result enables the efficient amplitude computation strategy based on finite field arithmetic discussed in Section 5.3. However, at this stage the basis functions $\{F_i^{(k)}\}$ are expressed in terms of CIIs [90] and numerical boundary values $\overrightarrow{\mathrm{MI}}^{(k)}(\vec{s}_0)$. This representation is excellent for investigating the analytic properties of Feynman integrals and amplitudes, but it is not readily suitable for an efficient numerical evaluation. In the next section, we discuss how we construct a representation of the function basis in terms of GPLs and zeta values which is well suited for an efficient and stable numerical evaluation.

5.4.2 Expression in terms of GPLs

Since the letters in Eq. 5.4.2 are rational and linear in all variables, we can solve the canonical DEs in Eq. 5.4.1 algorithmically in terms of GPLs (see Section 2.9.2 for their definition). Order by order in ϵ, the solution is given by:

$$\overrightarrow{\mathrm{MI}}_T^{(k)}(\vec{s}) = \sum_{i=1}^{7} A_i^{(T)} \cdot \int_\gamma \mathrm{d}\log\Big(w_i(\vec{s}=\gamma)\Big)\, \overrightarrow{\mathrm{MI}}_T^{(k-1)}\Big(\vec{s}=\gamma\Big) + \vec{b}_T^{(k)}\,, \tag{5.4.6}$$

starting from the constant weight-0 boundary values $\overrightarrow{\mathrm{MI}}_T^{(0)}$ determined in the previous subsection. Here, γ is a path connecting an arbitrary base point $\vec{s}_{\mathrm{base}}$ to the end point $\vec{s}$. The weight-k constants $\vec{b}_T^{(k)}$ are given by the values of the integrals at the base point, $\vec{b}_T^{(k)} = \overrightarrow{\mathrm{MI}}_T^{(k)}(\vec{s}_{\mathrm{base}})$. For $\vec{s}_{\mathrm{base}}$, we may use the boundary point $\vec{s}_0$ in Eq. 5.4.4, so that the constants $\vec{b}_T^{(k)}$ coincide with the boundary values determined

numerically in the previous section. We follow a different approach, which allows us to trade all numerical constants in the expressions for zeta values.

We find it convenient to change variables from (s_{12}, s_{23}, s_4) to (z_1, z_2, s_4), with:

$$z_1 = \frac{s_{12}}{s_4}\,, \qquad\qquad z_2 = \frac{s_{23}}{s_4}\,. \tag{5.4.7}$$

In this way, there is only one dimensionful variable, s_4, the dependence on which is fixed as an overall factor by dimensional analysis. We then integrate the canonical DEs as in Eq. 5.4.6 along the following piece-wise path in the (z_1, z_2, s_4) space:

$$(0,0,0) \xrightarrow{\gamma_1} (z_1,0,0) \xrightarrow{\gamma_2} (z_1,z_2,0) \xrightarrow{\gamma_3} (z_1,z_2,s_4)\,. \tag{5.4.8}$$

Since the Feynman integrals are divergent at the chosen base point, the latter is understood in a *regularised* sense (we refer to Section 4 of Ref. [92] for a thorough discussion). Choosing $(0,0,0)$ as base point has the important benefit of removing spurious transcendental numbers that would pollute the solution were we to choose a base point where the integrals are finite. As we will see below, only zeta values appear. Roughly speaking, we define regularised, finite values $\vec{b}_T^{(k)} \coloneqq \mathrm{Reg}\,\overrightarrow{\mathrm{MI}}_T^{(k)}(\vec{s}_{\mathrm{base}})$ by introducing a regulator and formally setting to 0 the (divergent) logarithms of the regulator. Since the integrals are finite at a generic end point $\vec{s}$, the divergences at the base point must cancel out with divergences arising in the integration. We can thus drop all these divergences. Provided that we do it consistently between the integration and the base point values $\vec{b}_T^{(k)}$, this leads to a finite and unique result. In practice, we fix the finite base point values $\vec{b}_T^{(k)}$ by matching the solution $\overrightarrow{\mathrm{MI}}_T^{(k)}$ evaluated at the boundary point $\vec{s}_0$ against the boundary values discussed in the previous subsection.

We therefore keep the $\vec{b}_T^{(k)}$ as symbols and integrate the canonical DEs as in Eq. 5.4.6 along the path in Eq. 5.4.8 up to weight 4. We parameterise each piece of the path in Eq. 5.4.8 linearly. For instance, $\gamma_2(t) = (z_1, t, 0)$, with $t \in [0, z_2]$.

- The γ_1 integration leads to GPLs with indices in $\{0, 1\}$ and argument z_1.
- The γ_2 integration leads to GPLs with indices in $\{0, 1, 1 - z_1, -z_1\}$ and argument z_2.
- The γ_3 integration leads to powers of $\log(-s_4)$, fixed by dimensional analysis.

Once we have obtained expressions for all MIs in terms of GPLs and symbolic constants $\vec{b}_T^{(k)}$, we equate them to the numerical boundary values at $\vec{s}_0$, and solve for the $\vec{b}_T^{(k)}$. We use `GiNaC` [96, 298] to evaluate the GPLs numerically. Finally, we use the `PSLQ` algorithm [299] to express the ensuing values of $\vec{b}_T^{(k)}$ in terms of ζ_2 and ζ_3.

As a result, we obtain a fully analytic representation of all MIs — and thus of our special function basis $\{F_i^{(k)}\}$ — in terms of GPLs and zeta values, up to weight 4.

Contrary to the functions in the basis $\{F_i^{(k)}\}$, the GPLs in their representation satisfy functional relations. We make use of this freedom to optimise our expressions in view of their numerical evaluation by reducing the number of distinct GPLs that need to be evaluated. First, we use the shuffle algebra of GPLs to push all trailing zeros into logarithms (see Eq. 2.9.17b). Next, we employ the scaling relation:

$$G(a_1, \ldots, a_n; x) = G\left(\frac{a_1}{x}, \ldots, \frac{a_n}{x}; 1\right), \tag{5.4.9}$$

which holds for $x, a_n \neq 0$. As a result, all GPLs have argument 1 and indices:

$$l_0 = 0\,, \qquad l_1 = \frac{s_4}{s_{12}}\,, \qquad l_2 = \frac{s_4}{s_{23}}\,, \qquad l_3 = \frac{s_4 - s_{12}}{s_{23}}\,, \qquad l_4 = -\frac{s_{12}}{s_{23}}\,. \tag{5.4.10}$$

Finally, we decompose the GPLs to *Lyndon words* [300] using `PolyLogTools` [301]; we refer to the latter work for a thorough explanation, and give here only a simple example. This procedure requires that we choose a symbolic ordering of the GPL indices. We choose $l_0 \prec l_1 \prec l_2 \prec l_3 \prec l_4$, meaning that l_1 is greater than l_0, and so on. Consider the GPL $G(l_1, l_0; 1)$, whose indices are not sorted according to the ordering above, since $l_1 \succ l_0$. We can use the shuffle algebra of GPLs to rewrite it in terms of GPLs whose indices are sorted according to the chosen ordering:

$$G(l_1, l_0; 1) = G(l_0; 1)\, G(l_1; 1) - G(l_0, l_1; 1)\,. \tag{5.4.11}$$

Doing this consistently throughout all expressions reduces the number of higher-weight GPLs in favour of products of lower-weight ones, which are cheaper to evaluate numerically. To maximise the impact in this sense, we tested all possible orderings of the indices and selected the one — given above — which minimises the number of weight-4 GPLs. The resulting representation of the function basis contains 4 weight-1, 6 weight-2, 19 weight-3, and 25 weight-4 GPLs, as well as 3 logarithms:

$$\log(s_{12}/s_4)\,, \qquad \log(s_{23}/s_4)\,, \qquad \log(-s_4)\,. \tag{5.4.12}$$

We write the latter in terms of logarithms rather than GPLs as they play an important role in the factorisation of the IR divergences in the scattering amplitudes (see Appendix C.3 for the IR structure of the amplitudes we compute here). We stress that $\log(-s_4)$ is the only function of a dimensionful argument in our representation of the function basis.

We provide in the folder `mi2func/` of the ancillary files [284] the expression of the basis functions $\{F_i^{(k)}\}$ in terms of GPLs, logarithms, ζ_2 and ζ_3.

It is important to stress that the GPLs are multi-valued functions. For unit argument, there is a pole on the integration contour whenever one of the indices lies between 0 and 1. In this case, the contour must be deformed in the complex plane, either above or below the pole, leading to different branches. Our GPLs are thus well-defined only in the kinematic region where all GPL indices in Eq. 5.4.10 are either less than 0 or greater than 1, and we need $s_4 < 0$ for the argument of all logarithms in Eq. 5.4.12 to be positive. We discuss how to analytically continue the GPLs and the logarithms in Eq. 5.4.12 to the kinematic regions of interest in Appendix G.

5.4.3 Performance and validation

We validated our results for the MIs of all families by cross-checking them against values obtained with `AMFlow` [146] at several random points in all the physical kinematic regions discussed in Appendix G. Furthermore, we find agreement with the results of Ref. [276]. We employ `GiNaC` to evaluate the GPLs.

Our results allow for an efficient and stable evaluation of the MIs, and are thus ready for immediate deployment in phenomenology. Indeed, the amplitudes we computed in this work have already been implemented in `McMule` [285, 286] to provide the real-double-virtual electron-line corrections to $e\mu \to e\mu$ scattering. The evaluation is efficient, running at ≈ 130 events per second in the bulk of the phase space [302] using `handyG` [303] for the evaluation of the GPLs.

Chapter 6

Conclusions

In this thesis, we presented selected techniques needed for precision calculations of high-multiplicity loop scattering amplitudes. Such calculations constitute a crucial ingredient of the LHC precision programme, which aims to bring the theoretical uncertainties to the percent level and below. We started by discussing the general framework for computing predictions for physical observables using the machinery of QFT. Having established the key role of the scattering amplitude in this process, we described the challenges associated with their computation in practice. We dedicated Chapter 2 to a detailed discussion of a variety of tools employed to overcome these challenges. In particular, we showed how the use of finite fields helps us tackle the daunting algebraic complexity present in state-of-the-art calculations. We also noted the importance of the IBP reduction, which hugely reduces the number of integrals that need to be computed for the amplitude. This led us to the technique of differential equations, and in particular differential equations in the canonical form, which can be used to evaluate bases of pure master integrals with unexpected ease.

We applied the techniques presented in the first part of this thesis to three processes at the cutting edge of QCD and QED computations. First, we computed the two-loop helicity amplitudes for the production of the Higgs boson in association with a bottom-quark pair. This five-point process with a massive external leg is of great phenomenological interest, since an improved measurement of the bottom-quark Yukawa coupling could help constrain certain supersymmetric models which affect this coupling. In order to speed up the reconstruction of the analytic form of the rational coefficients from their numerical samples over finite fields, we implemented several optimisation tools which lower the complexity of this task. Moreover, exploiting the differential equation technique, we constructed a special function basis for the finite remainder of the amplitude which can be efficiently evaluated across the full phase space.

The second computation we tackled was the production of the W boson in association with a photon and a jet. Here, the W boson was assumed to further decay into a lepton pair, which allowed us to apply the familiar five-point kinematics with one off-shell leg to the scattering of six massless particles. Studying $W\gamma + n(\text{jet})$ production grants access to the $WW\gamma$ coupling, which can also be affected by new physics scenarios. In this work, we employed a new technique for simplifying the reconstructed functional coefficients based on a systematic search for the optimal rational parametrisation. In the future, this technique can be readily implemented also before reconstruction as an additional node of finite field operations, such that the search will not suffer from the algebraic complexity. Finally, in contrast to the previous set of amplitudes, we employed the tailored set of one-mass pentagon functions for the expansion of master integrals. These functions have the key advantage of being closed under the permutations of the massless momenta, which allows us to significantly reduce the number of kinematic points at which they have to be evaluated in order to serve a phenomenologically useful role.

Finally, we switched our focus to QED, computing the two-loop amplitudes for the scattering of a lepton pair with an off-shell and an on-shell photon. Our work completes the amplitude-level ingredients contributing to the N^{3}LO predictions of electron-muon scattering $e\mu \to e\mu$, which are required to meet the precision goal of the MUonE experiment. Here, the lower multiplicity meant that the reconstruction of analytic expressions from finite fields did not pose as serious a challenge as for the previous two processes. Instead, we focused on optimising the setup of the IBP reduction by exploiting numerical permutations of the IBP solutions obtained within a small set of families with specific orderings of external legs. This method allowed us to decrease the time and memory consumption of the IBP reduction stage, which becomes especially important in the case of processes with many integral families. Furthermore, we have constructed a basis of algebraically independent GPLs needed for the master integrals relevant to any scattering process of four massless particles with a single external off-shell leg up to two loops. This guarantees an efficient numerical evaluation and a compact analytic representation of the amplitudes.

Looking forward into the future, computations of amplitudes of higher multiplicity and loop order than the ones considered in this thesis are naturally going to present serious challenges. While we should be careful not to take the number of Feynman diagrams as a definitive measure of complexity, we can obtain its rough estimate by looking at how this number scales as we add more external legs to a given process. For example, adding an extra gluon to the $\bar{b}b\bar{q}qH$ channel of $pp \to b\bar{b}H$ production in Chapter 3 increases the number of diagrams from 720 to 10142. Similarly, for the $\bar{b}bggH$ channel, the number grows from 3690 to 57478. Six-point kinematics with

zero or one off-shell external legs means eight and nine Mandelstam invariants in the problem, respectively, which greatly increases the complexity even when using the finite field reconstruction technique. In terms of the IBP relations, while the three-loop, four-point kinematics with up to one off-shell leg has received significant attention already (see Ref. [304] and references therein), much less is known about the two-loop, six-point case even in a fully massless configuration [305, 306].

We would also like to point out the recent computation of the pure master integral bases for all two-loop integrals for five-particle kinematics with an off-shell leg [125], which appeared in literature after the completion of the work presented in this thesis. The full set of pure bases for this kinematic configuration opens the door to a new range of computations, such as $pp \to H + 2j$ and $pp \to W\gamma\gamma$ at NNLO, as well as the sub-leading colour corrections to the processes in Chapters 3 and 4. As a preliminary estimate, we observe that the inclusion of the non-planar families increases the finite field reconstruction time by as much as an order of magnitude. We remark that this problem can be alleviated by using IBP relations simplified using syzygy relations [307–313]. We refer the reader to Ref. [314] for details.

Overall, we believe that the work presented in this thesis represents a valuable contribution to the study of scattering amplitudes. We hope that the detailed introductory material serves as a useful reference for those new to the subject. With more and more data pouring in from the LHC and future colliders, it is clear that further breakthroughs in our computational techniques are needed to fully control the NNLO frontier and move towards the $\mathrm{N^3LO}$ one. The Les Houches wishlist [4] continuously calls for new theoretical results, of which the scattering amplitudes are a key ingredient. Finally, we remark that, at some point in the future, obtaining analytic results for the amplitudes might become unfeasible and one should also consider pursuing a robust method for their numerical computation instead. Such numerical results can then be used further to produce predictions for the associated cross sections. From the perspective of phenomenology, this approach might become more efficient than first computing fully analytic amplitudes and subsequently evaluating them at chosen phase space points.

Appendix A

Optimised IBP reduction for amplitudes with many permuted families

In this appendix, we discuss how we can incorporate the IBP reduction in our workflow in a more efficient way, particularly when the amplitude includes many permutations of the same integral families. We exploit this method when computing the amplitudes presented in Chapter 5. We start by pointing out a certain fact related to Eq. 2.8.11: the number of MIs for all families considered together is not the same as the sum of numbers of MIs for these families considered separately. That is:

$$|\mathrm{MI}| \equiv |\mathrm{MI}_{\bigcup_T}| \leq \sum_{\substack{T\in \\ \text{maximal} \\ \text{topologies}}} |\mathrm{MI}_T|\,, \tag{A.1}$$

where $\bigcup_T$ indicates the union of all maximal topologies T. This statement might seem somewhat surprising. Indeed, if we formulate one big system of IBP relations between integrals in all the families and perform the IBP reduction, the resultant MI basis is equal to the sum of the bases obtained by solving smaller systems of IBP relations within each family one by one. This is because IBP relations, by construction, cannot include integrals from different families. However, it turns out that integrals belonging to sectors other than the top sector can often be mapped between families (see Fig. A.1 for an easy to understand example). Therefore, an amplitude reduced using N_T separate IBP systems contains leftover MIs that can be further reduced onto each other with the help of non-IBP mappings. To avoid this redundancy, we typically build a combined system which covers all the families in the problem. It contains the pure IBP relations, as well as the additional inter-family

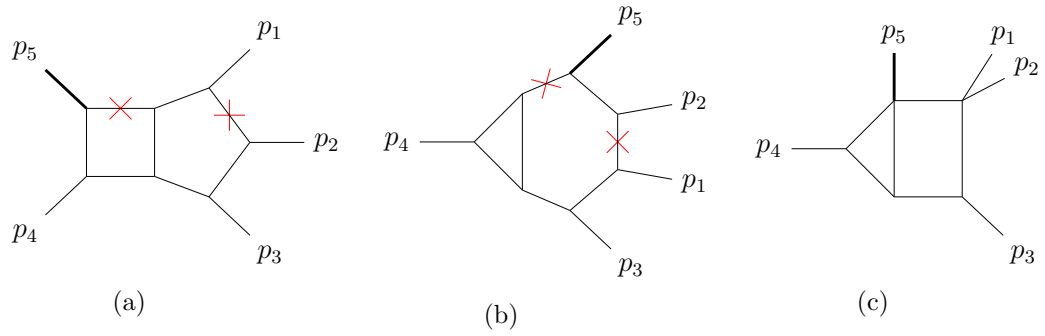

Figure A.1: A simple example of possible non-IBP relations between integrals within different (maximal) topologies. Integrals in lower sectors often map to each other. The bold line indicates the massive momentum, p_5, while red crosses denote a removed denominator, i.e. the corresponding ν_i is 0. Here, diagrams (a) and (b) both collapse onto diagram (c). Such relations are often hard to discover just from analysing the propagators of the integrals, especially if the two families use vastly different conventions for loop momentum routing. However, a visual representation often makes spotting these relations trivial.

mappings[1]. Unfortunately, for large N_T, this often leads to a prohibitively expensive computation and may even constitute the main bottleneck of the whole workflow.

There is, however, a more efficient way of performing the reduction. Recall that the integral families fed into the reduction are defined by their propagators and ISPs. Specialising to the five-particle case, each family can therefore be denoted as $T(ijklm)$, where T is the family type and $ijklm$ is an ordering of the external momenta within that type (understood as $ijklm \equiv p_i, \ldots, p_m$). Note that in the presence of an internal or external mass, we need to further distinguish between topology subtypes based on the position of this mass. For example, we refer to the topology of Fig. A.1a as 'zzz penta-box(12345)', and to that of Fig. A.1b as 'mzz hexa-triangle(52134)' (we follow the naming convention of Ref. [98]).

Consider two families which are of the same (sub)type and differ only by a permutation $\sigma \equiv (\sigma_i, \ldots, \sigma_m)$ which preserves the position of any massive legs. Then, we can write $T' = (\sigma \circ T)(ijklm) = T(\sigma_i, \ldots, \sigma_m)$ and the IBP reduction of any integral $I_{T'}(\boldsymbol{\nu})$ can be expressed by permuting the reduction of $I_T(\boldsymbol{\nu})$ according to σ:

$$
\begin{aligned}
I_{T(ijklm)}(\boldsymbol{\nu}) &= \sum_{i=1}^{|\mathrm{MI}_T|} c_i(p, \epsilon) \times \mathrm{MI}_{T(ijklm),\, i} \\
\implies I_{T'}(\boldsymbol{\nu}) &= \sum_{i=1}^{|\mathrm{MI}_T|} c_i(\sigma(p), \epsilon) \times \mathrm{MI}_{T',\, i}\,.
\end{aligned}
\tag{A.2}
$$

[1] In practice, these mappings are found by comparing integrals based on their representation in terms of the $\mathcal{U}$ and $\mathcal{F}$ Symanzik polynomials (see Section 4 of Ref. [29] and also Ref. [231]).

Here, p denotes the collective dependence on the external momenta $p_i, \ldots, p_m$, with $\sigma(p) \equiv p_{\sigma_i}, \ldots, p_{\sigma_m}$. The new reduction coefficients $c_i' = c_i(\sigma(p), \epsilon)$ are computed as a permutation of the external kinematics in the old coefficients $c_i(p, \epsilon)$, while the new master integrals $\mathrm{MI}_{T'}$ are obtained by permuting the external momenta in the propagators and ISPs of MI_T[1].

In our applications, the reduction coefficients c_i will most often be parametrised by the momentum twistors $\mathbf{x}$. Then, since they will be rational functions of $\mathbf{x}$ and ϵ, permuting the external kinematics to obtain c_i' is trivial. Moreover, the rationality means that this approach to IBP reduction is perfectly compatible with the finite field sampling procedure. From Eq. A.2, we can see that permuting the coefficients amounts to evaluating them at a permuted phase-space point. This is also equivalent to a change of the kinematic variables, which is an operation that can be easily implemented in `FiniteFlow`[2] [48]. Thus, we never have to know and permute the analytic form of the coefficients, which leads to a significant reduction in the computational cost. Overall, for an integral family with n massless particles, we do not need to explicitly perform the IBP reduction in up to $n!$ permutations of it. In fact, we only need to do it once — in an arbitrarily chosen permutation of this family, which we label $T(\sigma_{\mathrm{id}})$. Then, the reduction of any permutation of this family is obtained by considering σ such that $\sigma \circ \sigma_{\mathrm{id}}$ brings us onto the target family, that is $T' = (\sigma \circ T)(\sigma_{\mathrm{id}})$, and applying the steps above.

Let us now discuss a small issue with this new strategy. As pointed out in the beginning of this section, the total number of MIs after the reduction is smaller than the sum of MIs in the individual families. This redundancy is not taken care of in the approach we have described above, since the reduction is performed only within the main families $T(\sigma_{\mathrm{id}})$ and then permuted to cover all needed permutations. Thus, the inter-family mappings between the MIs are not found and the reduced amplitude will contain MIs which are in fact not fully linearly independent. Strictly speaking, there is no requirement for the amplitude to be expressed in terms of independent objects. However, it is desirable to do so, as this ensures that any cancellations happen analytically and prevents instabilities or issues with precision during the numerical evaluation of the amplitude. Moreover, it is more computationally efficient, as it reduces the number of independent coefficients that have to be processed when expanding the amplitude into special functions (see Section 2.11).

In practice, we obtain these missing relations between MIs by performing *their*

[1] In the case of pure MIs, which are often defined as combinations of integrals I_T, we also need to permute any potential kinematic prefactor of these integrals according to σ.

[2] When working with the s_{ij} variables, the permutation $s_{\sigma(ij)}$ will in general take us outside of their minimal set, but we can always express the new Mandelstam variables through the same minimal set using momentum conservation and on-shell conditions.

reduction in the 'traditional' approach (i.e. all families included together in one system) in `LiteRed`. This expresses the MIs from all families in terms of the truly independent ones:

$$\mathrm{MI}_i = \sum_j^{|\mathrm{MI}|} f_{ij}(p,\epsilon) \times \mathrm{MI}_j \qquad i \in \left\{1, \ldots, \sum_T |\mathrm{MI}_T|\right\} . \tag{A.3}$$

Here, i runs over the 'naive' MIs of all maximal topologies and $|\mathrm{MI}|$ is the number of truly independent MIs in the sense of Eq. A.1. We stress that this additional reduction of the naive MIs does not present such a high complexity as the reduction needed for the amplitude itself. Firstly, the identities generated through the Laporta algorithm only need to cover the rank and number of dotted propagators present in the MI bases, rather than the full amplitude. Secondly, an extremely useful property of UT integrals[1] is that any linear relation between them cannot contain a dependence on the kinematic variables, i.e. $f(p,\epsilon) \to f(\epsilon)$ in Eq. A.3. This is simply because adding such kinematic factors would break the canonical form of the DEs and would imply that at least one of these integrals was not in fact UT. Thus, when using UT bases, which has become the standard in modern amplitude computations, this additional reduction can be performed with the kinematic variables set to random numeric values (subject to momentum conservation). Finally, all the missing relations between MIs can be worked out once and for all — they will be applicable to any process at the same loop order and number of particles (and masses), since the IBP reduction is specific only to the kinematic setup.

Having obtained the missing relations between the naive MIs, we apply them to our amplitude and collect the coefficients of the true, linearly independent MIs. Overall, we find that this alternative approach performs much better than the previously employed strategy of considering all integral families together in one shared system. The benefit grows with the number of permutations of the maximal topologies, since including additional families in the IBP system is expensive, but numerically permuting the solution from one family onto another is cheap.

[1] We discuss the UT property of integrals in Section 2.9.3.

Appendix B

Symbols

B.1 Introduction

In this appendix, we introduce another useful concept related to DEs and iterated integrals. We begin by noting that the representation of the solution to the ϵ-form DEs in Eq. 2.9.9 is not unique. Most generally, the answer is written using Chen's iterated integrals (CIIs) [90]. However, as pointed out above Eq. 2.9.15, if the 'letters' are rational in at least one variable, CIIs can be expressed in terms of GPLs [93]. This has the advantage that robust and stable numerical evaluation of GPLs is available (see Refs. [96, 298, 315]). On the downside, contrary to CIIs, GPLs contain a large degree of redundancy in the sense that they satisfy extra functional relations, obscuring possible simplifications and cancellations. Other representations apart from CIIs and GPLs are also possible. Due to the conjecture pointed out in Section 2.9.3, typically we will be interested in computing the DE solution up to transcendental weight 4. Another remarkable conjecture exists: any transcendental function of weight $k < 4$ can be expressed in terms of the usual logarithms and polylogarithms Li_k only [316,317], while at weight $k = 4$ all functions can be expressed in terms of $\mathrm{Li}_4(x), \mathrm{Li}_{2,2}(x, y)$ and weight-4 products of lower-weight functions[1] [93]. Here, the classical polylogarithms $\mathrm{Li}_n(z)$ are defined as:

$$\mathrm{Li}_n(z) = \sum_{k=1}^{\infty} \frac{z^k}{k^n}\,, \qquad |z| < 1,\ n \in \mathbb{N}\,, \tag{B.1.1}$$

[1] See Section 6 of Ref. [318], which considers this problem for the spanning set of functions with $k \leq 4$ in the special case of Harmonic Polylogarithms (GPLs with all indices $a_i \in \{0, \pm 1\}$).

while the multiple polylogarithms (GPLs) $\mathrm{Li}_{m_1,\ldots,m_k}$ are their multi-index, multi-variable generalisations [95, 301]:

$$\mathrm{Li}_{m_1,\ldots,m_n}(z_1,\ldots,z_n) = \sum_{0<k_1<\ldots<k_n} \frac{z_1^{k_1}\ldots z_n^{k_n}}{k_1^{m_1}\ldots k_n^{m_n}} \tag{B.1.2a}$$

$$= \sum_{k_n=1}^{\infty} \frac{z_n^{k_n}}{k_n^{m_n}} \sum_{k_{n-1}=1}^{k_n-1} \frac{z_{n-1}^{k_{n-1}}}{k_{n-1}^{m_{n-1}}} \ldots \sum_{k_1=1}^{k_2-1} \frac{z_1^{k_1}}{k_1^{m_1}}\,, \qquad |z_i|<1,\ m_i\in\mathbb{N}\,. \tag{B.1.2b}$$

Note that in these two definitions, $|z_i| < 1$, but the functions can be analytically continued to cover regions where $|z_i| \geq 1$. The $\mathrm{Li}_{m_1,\ldots,m_k}$ GPLs can be viewed as the series representation of the GPLs defined in Eq. 2.9.15. They are related through the following equation [318]:

$$\mathrm{Li}_{m_1,\ldots,m_n}(z_1,\ldots,z_n) = (-1)^n\, G\left(\vec{0}_{m_n-1}, \frac{1}{z_n}, \ldots, \vec{0}_{m_1-1}, \frac{1}{z_1\ldots z_n}; 1\right)\,, \tag{B.1.3}$$

where $\vec{0}_m$ denotes a vector of zeros of length m. For example, the aforementioned $\mathrm{Li}_{2,2}(x,y)$ can be written as:

$$\mathrm{Li}_{2,2}(x,y) = G\left(0, \frac{1}{y}, 0, \frac{1}{xy}; 1\right)\,. \tag{B.1.4}$$

Overall, the solution to the canonical DEs written in terms of special functions rather than CIIs is likely to contain a large degree of redundancy. Moreover, due to the abundance of representations, it is not easy to choose the most appropriate set of functions or even verify if two expressions are equivalent. We would like to have a tool which can find relations between transcendental functions and be representation independent. To this end, we introduce the notion of a 'symbol' [317, 318]. After giving its definition and properties, we will demonstrate its power based on several illustrative examples. To motivate our effort, we remark that the main result of Ref. [317] was the application of the symbol to re-write a 17-page expression for a quantity known as the two-loop, six-point remainder function (related to Wilson loops) in $\mathcal{N}=4$ SYM [319, 320] as a remarkably compact combination of classical polylogarithms that fits on just a handful of lines.

B.2 Definition and properties

The symbol of a CII with $\mathrm{d}\log$ kernels is defined as:

$$\mathcal{S}\left(\int_\gamma \mathrm{d}\log w_1 \cdot \ldots \cdot \mathrm{d}\log w_n\right) \equiv w_1 \otimes \ldots \otimes w_n\,. \tag{B.2.1}$$

We can think of it as an elementary n-fold tensor where each entry w_i is implicitly understood as its corresponding $\mathrm{d}\log$. It satisfies certain properties that we would expect from the behaviour of logarithms[1]:

$$A \otimes (ab) \otimes B = A \otimes a \otimes B + A \otimes b \otimes B\,, \tag{B.2.2a}$$

$$A \otimes \left(\frac{a}{b}\right) \otimes B = A \otimes a \otimes B - A \otimes b \otimes B\,, \tag{B.2.2b}$$

$$A \otimes a^n \otimes B = n(A \otimes a \otimes B)\,, \tag{B.2.2c}$$

where A, B are elementary tensors and a, b are algebraic functions. Note that in the last line, n becomes a coefficient in front of the symbol, rather than a part of it. Moreover, a symbol which contains a constant (not only rational) vanishes:

$$A \otimes c \otimes B = 0\,, \tag{B.2.3}$$

which can be understood as a consequence of $\mathrm{d}\log c = 0$. This means that, when working with the symbol, we are insensitive to constants, including transcendental ones like π.

Since CIIs are defined as repeated integrations over some kernels (see Eq. 2.9.13), the total differential acts on the symbol defined through Eq. B.2.1 as:

$$\mathrm{d}(w_1 \otimes \ldots \otimes w_n) = \mathrm{d}\log w_n\,(w_1 \otimes \ldots \otimes w_{n-1})\,. \tag{B.2.4}$$

This property goes hand in hand with the definition of pure functions in Eq. 2.9.18. Crucially, it can be reversed and allows us to define the symbol recursively [317]. For a transcendental function F with $\mathcal{T}(F) = k$ whose total differential can be written as:

$$\mathrm{d}F = \sum_i f_i\,\mathrm{d}\log w_i\,, \tag{B.2.5}$$

where f_i are functions with $\mathcal{T}(f_i) = k - 1$, we have:

$$\mathcal{S}(F) = \sum_i \mathcal{S}(f_i) \otimes w_i\,. \tag{B.2.6}$$

The starting point of the recursion is the 'empty' symbol: $\mathcal{S}(1)$. Let us see how to use this definition. For now, we will focus on the classical polylogarithms $\mathrm{Li}_n(z)$. In this case, we will need the symbol of a single weight-1 function — the logarithm: $\mathcal{S}(\log w) = w$, which can itself be obtained using Eqs. B.2.5 and B.2.6. Here, the w on the RHS is understood as an elementary tensor in the sense of Eq. B.2.1. This immediately allows us to obtain the symbol of any Li_n. Note that the weight-1

[1] For a detailed discussion of symbol properties, see Ref. [318].

polylogarithm is just the normal logarithm:

$$\mathrm{Li}_1(z) = -\log(1-z)\,. \tag{B.2.7}$$

Moreover, the following iterative definition holds:

$$\mathrm{Li}_n(z) = \int_0^z \frac{\mathrm{d}t}{t}\mathrm{Li}_{n-1}(t)\,, \qquad n>1\,, \tag{B.2.8}$$

which is equivalent to the differential relation:

$$\mathrm{dLi}_n(z) = (\mathrm{d}\log z)\mathrm{Li}_{n-1}(z)\,, \qquad n>1\,. \tag{B.2.9}$$

Thus, Eqs. B.2.6 and B.2.7 give:

$$\begin{aligned}
\mathcal{S}(\mathrm{Li}_1(z)) &= -(1-z)\,,\\
\mathcal{S}(\mathrm{Li}_2(z)) &= -(1-z)\otimes z\,,\\
&\vdots\\
\mathcal{S}(\mathrm{Li}_n(z)) &= -(1-z)\otimes \underbrace{z\otimes\ldots\otimes z}_{n-1 \text{ times}}\,.
\end{aligned} \tag{B.2.10}$$

Note that in deriving the first line, we used $\mathcal{S}(-f) = -\mathcal{S}(f)$ and this minus sign cannot be dropped or absorbed, i.e. $\mathcal{S}(\mathrm{Li}_1(z)) \neq (z-1)$. Moreover, it should not be confused with the symbol expression $-1\otimes(1-z)$, which vanishes due to Eq. B.2.3. To avoid confusion, the symbol is often written using square brackets, e.g. $\mathcal{S}(\mathrm{Li}_2(z)) = -[1-z,z]$.

The symbol of the GPLs can be obtained recursively in a similar manner. We will need the differential equivalent of the integral definition in Eq. 2.9.15 [94]:

$$\mathrm{d}G(a_{n-1},\ldots,a_1;a_n) = \sum_{i=1}^{n-1} G(a_{n-1},\ldots,\hat{a}_i,\ldots,a_1;a_n)\,\mathrm{d}\log\left(\frac{a_i-a_{i+1}}{a_i-a_{i-1}}\right)\,, \tag{B.2.11}$$

where $a_1,\ldots,a_n$ are unique non-zero indices, a_0 is understood as 0 and $\hat{a}_i$ denotes the index that should be removed in a particular GPL. The starting point of the recursion is the symbol of the 'empty' GPL, defined as the empty symbol:

$$\mathcal{S}(G(;z)) = [\,]\,. \tag{B.2.12}$$

Clearly, the reader will now understand why we mentioned the alternative notation for the symbol. We can now move up on the recursion ladder by one step:

$$\mathrm{d}G(a;z) = G(;z)\,\mathrm{d}\log\left(\frac{a-z}{a}\right)\,. \tag{B.2.13}$$

Then, the weight-1 GPL has the symbol:

$$\mathcal{S}(G(a;z)) = \left[\frac{a-z}{a}\right] = [a-z] - [a]\,. \tag{B.2.14}$$

Proceeding in this manner, we can then calculate the symbols of all GPLs with higher weights.

We also need to know how to obtain the symbol of a product of functions, e.g. $\mathcal{S}(\log(z)\mathrm{Li}_2(z))$. To this end, we point out that the CIIs satisfy so-called shuffle relations[1]. Specialising to the case of GPLs, we have:

$$G(\vec{a};z)G(\vec{b};z) = \sum_{\vec{c}=\vec{a}\sqcup\vec{b}} G(\vec{c};z)\,. \tag{B.2.15}$$

The shuffle product $\vec{a}\sqcup\vec{b}$ denotes all possible ways of permuting the union of indices $\vec{a}$ and $\vec{b}$ such that the ordering of indices within each set is preserved. Perhaps a simple example illustrates this definition better:

$$\begin{aligned} G(a_1,a_2;z)G(b_1,b_2;z) = {} & G(a_1,a_2,b_1,b_2;z) + G(a_1,b_1,a_2,b_2;z) + G(a_1,b_1,b_2,a_2;z) \\ & + G(b_1,a_1,a_2,b_2;z) + G(b_1,a_1,b_2,a_2;z) + G(b_1,b_2,a_1,a_2;z)\,. \end{aligned} \tag{B.2.16}$$

Therefore, the shuffle relations allow us to write a product of GPLs of weight $|\vec{a}|$ and $|\vec{b}|$ as a linear combination of GPLs of weight $|\vec{a}| + |\vec{b}|$. Thus, we can now calculate the symbol of the product $\mathcal{S}(\log(z)\mathrm{Li}_2(z))$ by expressing the two functions as special instances of GPLs, taking the shuffle product of these GPLs according to Eq. B.2.15 and finally mapping the symbol over the resultant sum of higher-weight GPLs. However, it is often easier to follow an alternative route, which arises due to the fact that:

$$\mathcal{S}(f_1 f_2) = \mathcal{S}(f_1) \times \mathcal{S}(f_2)\,, \tag{B.2.17}$$

where the RHS is understood as the shuffle product of the individual symbols. Indeed, the symbol itself inherits the shuffle algebra:

$$(w_1 \otimes \ldots \otimes w_n) \times (v_1 \otimes \ldots \otimes v_m) = \sum_{\vec{z}=\vec{w}\sqcup\vec{v}} (z_1 \otimes \ldots \otimes z_{n+m})\,. \tag{B.2.18}$$

Therefore, in our example we may simply write:

$$\begin{aligned} \mathcal{S}(\log(z)\mathrm{Li}_2(z)) &= (z) \times (-(1-z)\otimes z) \\ &= -z\otimes(1-z)\otimes z - 2(1-z)\otimes z\otimes z \end{aligned} \tag{B.2.19}$$

[1]For this simple weight-3 function, its symbol can be obtained more directly by taking the differential and using Eq B.2.6. Nonetheless, we find it illustrative to introduce the shuffle product, as it becomes useful in more complicated cases.

$$= -[z, 1-z, z] - 2[1-z, z, z]\,.$$

In the last line, we have again used the alternative notation in order to make the position of the minus sign and a constant absolutely clear.

B.3 Examples

Overall, we see that thanks to symbols of the classical polylogarithms, Eq. B.2.10, and GPLs, Eq. B.2.14, as well as the symbol shuffling, Eq. B.2.18, and finally the relation in Eq. B.1.3, we can now compute the symbol of any function that may appear in the weight-4 function basis. Thinking ahead to our amplitude applications, it is clear that the symbol will allow us to find relations between linearly dependent objects such as GPLs and express our results in a much more compact form. Having expended the effort of understanding the last few pages, let us enjoy the fruits of our labour sprouting in the form of several illustrative examples.

Example 1
Given a functional relation, we can check its validity — but only up to constants. More precisely, while we can never prove with full certainty that an identity is valid by looking at its symbols, we can definitely show that an identity is not correct by proving that the symbols do not match up. The symbols allow us to fix the most complicated part of the identities. What is left is essentially boundary values, which can be determined for example by evaluating both sides of the relation at a numerical point. Consider the well-known dilogarithm reflection identity:

$$\mathrm{Li}_2(1-z) = -\mathrm{Li}_2(z) - \log(z)\log(1-z) + \frac{\pi^2}{6}\,, \tag{B.3.1}$$

valid in the domain $z \in \mathbb{C} \setminus \{(-\infty, 0] \cup [1, \infty)\}$. For the two dilogarithms, we can straightforwardly use Eq. B.2.10, while for the product of ordinary logs we need to use the shuffle algebra. At the symbol level, the identity reads:

$$-[z, 1-z] = +[1-z, z] - [z] \sqcup\!\sqcup [1-z]\,. \tag{B.3.2}$$

Taking the shuffle product leaves the two sides equal. Thus, we managed to verify that the identity holds — up the factor of $\pi^2/6$, which we can easily find by evaluating the rest of the identity at e.g. $z = 1$.

Example 2
If we're trying to construct a functional relation, the symbol can also help us to fix

the coefficients of the functions. Let us conjecture another identity:

$$\mathrm{Li}_2\left(\frac{1}{z}\right) = a\,\mathrm{Li}_2(z) + b\log^2(-z) + c\,, \tag{B.3.3}$$

where a, b, c are rational constants. Then, at the symbol level:

$$\begin{aligned} -\left[1-\frac{1}{z},\frac{1}{z}\right] &= -a[1-z,z] + b[-z] \sqcup [-z] \\ [z-1,z] - [z,z] &= -a[z-1,z] + 2b[z]\,, \end{aligned} \tag{B.3.4}$$

To get to the second line, we have expanded the LHS using the symbol properties in Eqs. B.2.2 and B.2.3, while on the RHS we used $[-x] = [x]$, which is a direct consequence of these properties. Thus, $a = -1$, $b = -1/2$. We still need to fix the so-called 'beyond the symbol terms'. These include not only the weight-2 constants such as π^2, but also products of weight-1 constants with a log. The latter type can be often fixed by differentiating both sides of the identity, thus producing a relation at a lower weight. In this case, differentiating Eq. B.3.3 with the known values of a and b shows that no log $\times$constant terms are missing. Hence, only weight-2 constants are allowed in c and we can fix it by evaluating the identity at a chosen value of z. In this way, we find:

$$\mathrm{Li}_2\left(\frac{1}{z}\right) = -\mathrm{Li}_2(z) - \frac{1}{2}\log^2(-z) - \frac{\pi^2}{6}\,, \qquad z \in \mathbb{C}\setminus[0,\,\infty)\,, \tag{B.3.5}$$

which is indeed a well-known dilogarithm relation. Finally, the reader might wonder why we have conjectured $\log(-z)$ instead of $\log(z)$. After all, as pointed out above, both these functions have the same symbol — $[z]$. The reason is simple: swapping the sign of the argument in the log would mean that there is no domain in which all the functions in this relation are well-defined and they would consequently have to be analytically continued.

Example 3

For more complicated identities, calculating the symbol by hand becomes unfeasible. Consider the following weight-3 relation:

$$\begin{aligned} \mathrm{Li}_3(z) = &-\mathrm{Li}_3\left(\frac{z}{z-1}\right) - \mathrm{Li}_3(1-z) \\ &+ \frac{1}{6}\log^3(1-z) - \frac{1}{2}\log(z)\log^2(1-z) + \frac{1}{6}\pi^2\log(1-z) + \zeta(3)\,, \end{aligned} \tag{B.3.6}$$

which holds for $z \in \mathbb{C}\setminus\{(-\infty,0]\cup[1,\infty)\}$. The symbol of the LHS is trivial thanks to Eq. B.2.10:

$$\mathcal{S}(\mathrm{Li}_3(z)) = -[1-z,z,z]\,. \tag{B.3.7}$$

The RHS requires much more work, namely repeated application of shuffle products

and symbol properties in Eq. B.2.2. These operations can be easily automated, however. In particular, we make use of the `Mathematica` package `PolyLogTools` [301], which enables the computation of symbols of arbitrary combinations of GPLs. Indeed, with the help of this package, it is trivial to verify that the sum of symbols of the terms on the RHS is equal to Eq. B.3.7.

The `PolyLogTools` package introduces several powerful tools related to the symbol. In particular, we point out its functionality related to the so-called 'fibration basis'. Given a GPL expression F whose letters (i.e. the arguments) satisfy certain conditions, it is possible to write it in the following form:

$$F = \sum_i c_i \, G(\vec{a}_i;\, x)\,, \tag{B.3.8}$$

for some variable x, where $\vec{a}_i$ are independent of x and the coefficients c_i include only those GPLs that are independent of x (see Ref. [301] and references therein). The GPLs appearing on the RHS of this formula are known as the fibration basis. Moreover, it is also possible to 'integrate' a symbol: given a symbol tensor S, it is possible to find a fibration basis such that $\mathcal{S}(F) = S$. This means that we can determine the functional form corresponding to a symbol expression (up to beyond-the-symbol terms).

B.4 Relation to canonical DEs and discontinuities

Let us now take a step back and make a connection between the symbols and the differential equations satisfied by master integrals. In Section 2.9, we saw that by making a suitable change of basis, it is possible to construct MIs such that the corresponding DEs are in the canonical form of Eq. 2.9.9. Then, their solution is given by a path-ordered exponential of the ϵ-free DE matrix $\tilde{A}$. This exponential is understood through its series expansion, leading to repeated integrations over kernels dictated by $\tilde{A}$. Further, we introduced the notion of uniform transcendentality and an even stronger condition on 'pure' functions, Eq. 2.9.18, which says that the transcendental weight of pure functions is lowered by 1 upon differentiation. Moreover, we learned that the solution of any canonical DEs is pure and vice versa — a given basis of pure functions will satisfy the canonical DEs. We should therefore be able to write down these DEs in a way which makes the purity property manifest. Indeed, notice that the differential equivalent of Eq. 2.9.12 is:

$$\mathrm{d}\overrightarrow{\mathrm{MI}}^{(k)} = \mathrm{d}\tilde{A}\,\overrightarrow{\mathrm{MI}}^{(k-1)} \quad \forall k > 0, \qquad \mathrm{d}\overrightarrow{\mathrm{MI}}^{(0)} = 0\,. \tag{B.4.1}$$

If we specialise to the cases where the DE matrix can be written in the d log form of Eq. 2.9.14, then (for $k > 0$) this becomes:

$$\mathrm{d}\overrightarrow{\mathrm{MI}}^{(k)} = \left(\sum_i a_i \,\mathrm{d}\log w_i\right) \overrightarrow{\mathrm{MI}}^{(k-1)} \,. \tag{B.4.2}$$

Note that $\overrightarrow{\mathrm{MI}}^{(0)}$ must be a vector of constants due to its vanishing derivative. This means that the leading term in the Laurent expansion of pure MIs does not contain any kinematic dependence.

We can use Eq. B.4.2 to express the solution of the canonical DEs up to and including weight n in the following form:

$$\overrightarrow{\mathrm{MI}}^{(n)} = \sum_{\alpha_1,\ldots,\alpha_n} \vec{c}_{\alpha_1,\ldots,\alpha_n} \int \mathrm{d}\log w_{\alpha_1} \ldots \mathrm{d}\log w_{\alpha_n} \,, \qquad n > 0 \,. \tag{B.4.3}$$

Note that each coefficient $\vec{c}_{\alpha_1,\ldots,\alpha_n}$ is a vector of rational numbers — they are calculated from the products of matrices a_i, which are dotted into the weight-0 vector $\overrightarrow{\mathrm{MI}}^{(0)}$. Naturally, to obtain explicit values for $\overrightarrow{\mathrm{MI}}^{(n)}$, we need to supply the integration contour. Nonetheless, the symbol, which discards this information, can still tell us a lot about the analytic structure of the solution. It can be trivially read off from the above equation:

$$\mathcal{S}\left(\overrightarrow{\mathrm{MI}}^{(n)}\right) = \sum_{\alpha_1,\ldots,\alpha_n} \vec{c}_{\alpha_1,\ldots,\alpha_n} [w_{\alpha_1}, \ldots, w_{\alpha_n}] \,. \tag{B.4.4}$$

It turns out that the first entry of the symbol encodes its branch cut structure. In particular, a Feynman integral with the symbol $[w_{\alpha_1}, \ldots, w_{\alpha_n}]$ has a discontinuity if $w_{\alpha_1} = 0$ or ∞. Of course, singular points of Feynman integrals are not random and we expect them to be connected to special values of the Mandelstam variables. Indeed, there exists a so-called first-entry condition which states that $\vec{c}_{\alpha_1,\ldots,\alpha_n} = 0$ if $w_{\alpha_1} \neq s_{ij}$, i.e. a symbol cannot appear in the solution of the DEs if its first letter is not a Mandelstam variable with a physical discontinuity[1] [297]. This turns out to be a very strong condition which in many cases fixes the values of $\overrightarrow{\mathrm{MI}}^{(0)}$ up to an overall normalisation factor. Beyond the first entry, the structure of the symbols is further constrained by the so-called Steinmann relations, which state that there is no double continuity associated with overlapping channels [322–325]. Overall, such conditions created by physical principles constrain the structure of the symbols and canonical DEs. This is evident when studying the pure MI bases relevant to this thesis (see Refs. [98, 99]).

[1] Strictly speaking, it is the absence of discontinuities at certain points that implies the first-entry condition, but this statement should not be inverted. In fact, it is possible to write an amplitude using a function which satisfies the first-entry condition, yet has the forbidden singularity. See Section 3 of Ref. [321] for an explicit example.

Appendix C

Derivation of the pole structure

In this appendix, we provide a detailed derivation of the full pole structure of the $pp \to b\bar{b}H$ amplitudes presented in Eqs. 3.2.11 to 3.2.17. We do this for completeness, but also in the hope of illuminating the procedure, which can be far from obvious. The pole structure of the $pp \to W^{\pm}\gamma j$ amplitudes can be derived similarly. We also outline the related calculation for the $0 \to \ell\bar{\ell}\gamma\gamma^*$ QED amplitudes of Chapter 5.

C.1 UV singularities

Let us start with the UV singularities. Renormalising the amplitude amounts to replacing the bare couplings x_B in the Lagrangian with the physical ones:

$$x_B = Z_x x_R \,. \tag{C.1.1}$$

The renormalisation factors are expanded as $Z_x = 1 + \delta_x$, where δ_x are the counterterms added to the bare Lagrangian and which are designed precisely to cancel out the divergences. Thus, we can think of renormalisation as absorbing the infinities from x_B into Z_x. Then, working with the renormalised parameters x_R in the Lagrangian is known as 'renormalised perturbation theory'. Let us now see how to achieve that. Specialising to the $pp \to b\bar{b}H$ process of Chapter 3, the bare amplitude admits the following expansion (similar to that of Eq. 1.4.5):

$$A_B = a_B y_{b,B} \left(A_B^{(0)} + a_B A_B^{(1)} + a_B^2 A_B^{(2)} + \ldots \right) , \tag{C.1.2}$$

where $a_B = \alpha_{s,B}/(4\pi)$ and $\alpha_{s,B}$, $y_{b,B}$ are the bare strong coupling constant and the bare Yukawa coupling of the b quark[1]. We will work in the $\overline{\text{MS}}$ scheme and make

[1] See Refs. [326, 327] for details, but note the difference of $\alpha_{s,B}^{1/2}$ as the leading power due to one fewer jet and, in the second reference, the expansion in powers of $\alpha_{s,B}/(2\pi)$, which introduces relative factors of 2 with respect to our convention.

the following replacements for the two couplings[1]:

$$\alpha_{s,B} = S_\epsilon \, Z_{\alpha_s} \, \alpha_{s,R}(\mu_R), \tag{C.1.3}$$

$$y_{b,B} = Z_y \, y_{b,R}(\mu_R) \,, \tag{C.1.4}$$

where μ_R is the renormalisation scale. The factor $S_\epsilon = \mathrm{e}^{\epsilon\gamma_E}(4\pi)^{-\epsilon}$ cancels out with the m_ϵ factor extracted from the colour-ordered amplitudes in Eq. 3.2.8 and so will be dropped in the following discussion. The renormalisation factors themselves admit a perturbative expansion in the renormalised strong coupling constant:

$$Z_{\alpha_s} = 1 + a_R r_1 + a_R^2 r_2 + \mathcal{O}\left(a_R^3\right), \tag{C.1.5}$$

$$Z_y = 1 + a_R s_1 + a_R^2 s_2 + \mathcal{O}\left(a_R^3\right) \,, \tag{C.1.6}$$

where $a_R = \alpha_{s,R}/(4\pi)$. Substituting Eqs. C.1.3 through C.1.6 into Eq. C.1.2, we obtain the amplitude expansion in terms of the renormalised parameters:

$$A_R = a_R y_{b,R} \left(A_R^{(0)} + a_R A_R^{(1)} + a_B^2 A_R^{(2)} + \ldots \right) \,, \tag{C.1.7}$$

with the individual amplitudes given by:

$$\begin{aligned} A_R^{(0)} &= A_B^{(0)} \,, \\ A_R^{(1)} &= A_B^{(1)} + 2A_B^{(0)}(r_1 + s_1) \,, \\ A_R^{(2)} &= A_B^{(2)} + 2A_B^{(1)}(2r_1 + s_1) + 4A_B^{(0)}(r_2 + r_1 s_1 + s_2) \,. \end{aligned} \tag{C.1.8}$$

The coefficients r_1, r_2, s_1, s_2 are listed in Appendix D. Note that we use their values as given in Ref. [327] for the sake of consistency, but in Eq. C.1.8 we have rescaled them by powers of 2 to make them compatible with our expansion. Overall, we see that each UV-finite amplitude $A_R^{(L)}$ is defined by adding to the bare amplitude $A_B^{(L)}$ terms related to the β-function whose ϵ poles cancel out the UV divergences. This completes the renormalisation of the $pp \to b\bar{b}H$ amplitudes in Chapter 3.

C.2 IR singularities

The renormalised amplitudes $A_R^{(L)}$ are only UV-finite — the IR divergences remain. The IR pole structure of two-loop amplitudes in massless gauge theories was originally derived in Ref. [23] and later extended in Refs. [24–26]. Here, we provide a brief summary of these results, followed by their application to the process $pp \to b\bar{b}H$.

[1]We treat all quarks as massless, while the wave function counterterm in the massless on-shell scheme is 0 (see Section 3.2 for an explanation as to why we use a mixed renormalisation scheme). Therefore, we only renormalise the strong coupling constant and the b quark Yukawa coupling.

C.2.1 Overview of IR singularities

The $\overline{\text{MS}}$-renormalised amplitudes $A_R^{(L)}$ admit the following structure[1]:

$$A_R^{(1)} = 2\boldsymbol{I}^{(1)}(\epsilon)A_R^{(0)} + F^{(1)}\,, \tag{C.2.1}$$

$$A_R^{(2)} = 2\boldsymbol{I}^{(1)}(\epsilon)A_R^{(1)} + 4\boldsymbol{I}^{(2)}(\epsilon)A_R^{(0)} + F^{(2)}\,. \tag{C.2.2}$$

The IR-divergent part is determined by amplitudes at lower loop order, while the full amplitude also receives a finite part $F^{(L)}$, which is the genuinely new contribution that needs to be computed. The pole operators $\boldsymbol{I}^{(L)}(\epsilon)$ are given by [23]:

$$\boldsymbol{I}^{(1)}(\epsilon) = \frac{1}{2}\frac{\mathrm{e}^{\epsilon\gamma_E}}{\Gamma(1-\epsilon)}\sum_i\left(\frac{1}{\epsilon^2} - \frac{\gamma_0^i}{2\epsilon}\frac{1}{\boldsymbol{T}_i^2}\right)\sum_{j\neq i}\boldsymbol{T}_j\cdot\boldsymbol{T}_j\left(\frac{\mu_R^2}{-s_{ij}}\right)^{\epsilon}\,, \tag{C.2.3}$$

$$\boldsymbol{I}^{(2)}(\epsilon) = \frac{\mathrm{e}^{-\epsilon\gamma_E}\Gamma(1-2\epsilon)}{\Gamma(1-\epsilon)}\left(\frac{\gamma_1^{\text{cusp}}}{8} + \frac{\beta_0}{2\epsilon}\right)\boldsymbol{I}^{(1)}(2\epsilon) - \frac{1}{2}\boldsymbol{I}^{(1)}(\epsilon)\left(\boldsymbol{I}^{(1)}(\epsilon) + \frac{\beta_0}{\epsilon}\right) + \boldsymbol{H}_{\text{RS}}^{(2)}(\epsilon)\,, \tag{C.2.4}$$

where $s_{ij} = 2\sigma_{ij}\,p_i\cdot p_j$ with $\sigma_{ij} = +1$ if both momenta are incoming or outgoing and $\sigma_{ij} = -1$ otherwise. The values of the β-function coefficients and the anomalous dimensions are given in Appendix D. We remark that the one-loop pole operator $\boldsymbol{I}^{(1)}(\epsilon)$ is independent of the regularisation scheme, while the two-loop operator $\boldsymbol{I}^{(2)}(\epsilon)$ is not. Its dependence enters through the quantity $\boldsymbol{H}_{\text{RS}}^{(2)}(\epsilon)$, which contains $\mathcal{O}\left(1/\epsilon\right)$ poles only:

$$\begin{aligned}\boldsymbol{H}_{\text{RS}}^{(2)}(\epsilon) = {}& \frac{1}{16\epsilon}\sum_i\left(\gamma_1^i - \frac{1}{4}\gamma_1^{\text{cusp}}\gamma_0^i + \frac{\pi^2}{16}\beta_0\gamma_0^{\text{cusp}}C_i\right)\\ &+ \frac{\mathrm{i}f^{abc}}{24\epsilon}\sum_{(i,j,k)}\boldsymbol{T}_i^a\boldsymbol{T}_j^b\boldsymbol{T}_k^c\ln\left(\frac{-s_{ij}}{-s_{jk}}\right)\ln\left(\frac{-s_{jk}}{-s_{ki}}\right)\ln\left(\frac{-s_{ki}}{-s_{ij}}\right)\\ &- \frac{\mathrm{i}f^{abc}}{128\epsilon}\gamma_0^{\text{cusp}}\sum_{(i,j,k)}\boldsymbol{T}_i^a\boldsymbol{T}_j^b\boldsymbol{T}_k^c\left(\frac{\gamma_0^i}{C_i} - \frac{\gamma_0^j}{C_j}\right)\ln\left(\frac{-s_{ij}}{-s_{jk}}\right)\ln\left(\frac{-s_{ki}}{-s_{ij}}\right)\,,\end{aligned} \tag{C.2.5}$$

where the sum runs over unordered tuples (i,j,k) of distinct parton indices. As pointed out in Ref. [24], the last two lines appear only because the pole operators $\boldsymbol{I}^{(L)}(\epsilon)$ in Ref. [23] were not defined in a minimal scheme, but also include terms finite in ϵ. Due to colour conservation, they contribute only if the amplitude contains at least four partons. Additionally, the last line appears only for *more* than 4 partons due to momentum conservation. More importantly, these last two lines produce terms subleading in N_c. Thus, in the leading-colour approximation, we will neglect them and use the first line only.

[1]Note that similarly to the previous section, we rescale $\boldsymbol{I}^{(1)}(\epsilon)$ and $\boldsymbol{I}^{(2)}(\epsilon)$ by 2 and 2^2, respectively, to account for the different expansion parameter a_R in Ref. [23].

Overall, despite the intimidating appearance of the formulas above, it can be appreciated that the only non-trivial piece of deriving the IR pole structure of the two-loop amplitudes is due to the operators $\boldsymbol{T}_i^a$, which we will refer to as 'colour insertion operators'. Each $\boldsymbol{T}_i^a$ acts on the colour structure of the amplitude by inserting a gluon with the adjoint index a onto the parton i. The rules are as follows:

- $\boldsymbol{T}_c^a : \delta^{bc} = -\mathrm{i}f^{abc}$ if c is a gluon,
- $\boldsymbol{T}_i^a : \delta_{ij} = +(T^a)_{ij}$ if i is an outgoing quark,
- $\boldsymbol{T}_i^a : \delta_{ji} = -(T^a)_{ji}$ if i is an outgoing antiquark,
- $\boldsymbol{T}_i^a : \delta_{ji} = -(T^a)_{ji}$ if i is an incoming quark,
- $\boldsymbol{T}_i^a : \delta_{ij} = +(T^a)_{ij}$ if i is an incoming antiquark.

We find it very helpful to use pictures akin to Feynman diagrams to better understand these rules (see Fig. C.1). Before applying them to our process of interest, it is useful to note that the product of two colour insertion operators, $\boldsymbol{T}_i \cdot \boldsymbol{T}_j \equiv \boldsymbol{T}_i^a \boldsymbol{T}_j^a$, trivially commutes:

$$\boldsymbol{T}_i \cdot \boldsymbol{T}_j = \boldsymbol{T}_j \cdot \boldsymbol{T}_i \,, \tag{C.2.6}$$

while for $i = j$ the action of the product gives the quadratic Casimir of the appropriate representation of $SU(N_c)$:

$$\boldsymbol{T}_i^2 = C_i \,, \tag{C.2.7}$$

with $C_q = C_{\bar{q}} = C_F$ and $C_g = C_A$. Moreover, due to colour conservation:

$$\sum_{i=1}^{n} \boldsymbol{T}_i^a |A_n\rangle = 0 \,, \tag{C.2.8}$$

$$\sum_{(i,j)} \boldsymbol{T}_i \cdot \boldsymbol{T}_j = -\sum_i \boldsymbol{T}_i^2 = -\sum_i C_i \,, \tag{C.2.9}$$

where $|A_n\rangle$ denotes a vector in the n-dimensional colour space, with A_n being the UV-renormalised amplitude of n coloured partons[1]. These equations can be used to check whether we have applied the colour insertion operators to our amplitude correctly.

C.2.2 Application to $pp \to b\bar{b}H$ amplitudes

We now have all the tools to derive the IR pole structure of the $pp \to b\bar{b}H$ amplitudes in Chapter 3. First of all, we note that by applying the first line of Eq. C.2.5 to the

[1] For a description of the colour-space formalism, see Ref. [328].

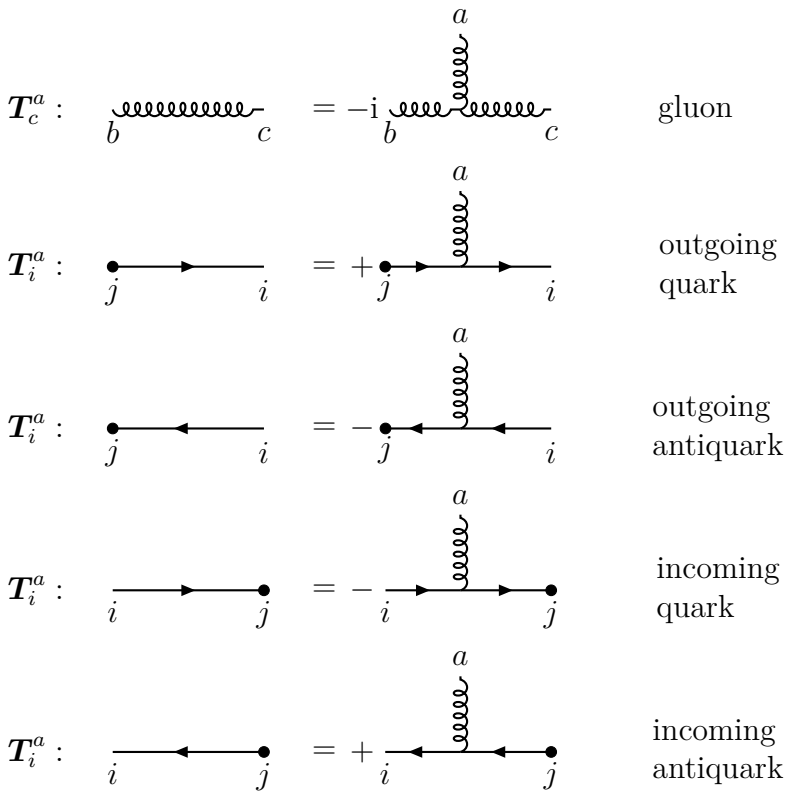

Figure C.1: Graphical representation of the action of the colour insertion operators on partons. The dot • indicates a Feynman diagram vertex and allows us to distinguish between incoming and outgoing quarks and antiquarks. The fundamental and antifundamental indices should be read in the direction opposite to fermion flow, while the adjoint indices in the three-point gluon vertex should be read anticlockwise.

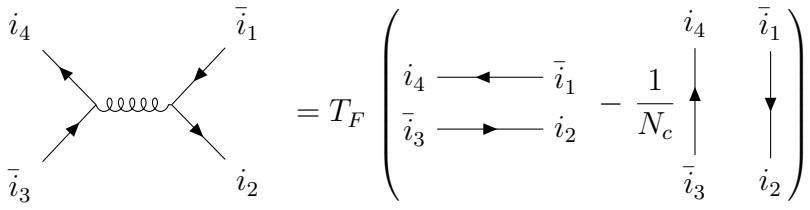

Figure C.2: The colour structure of a sample diagram contributing to the $\bar{b}b\bar{q}qH$ channel at tree level. We employ the Fierz identity to write $(T^a)_{i_4}^{\ \bar{i}_3}(T^a)_{i_2}^{\ \bar{i}_1} = T_F\left(\delta_{i_4}^{\ \bar{i}_1}\delta_{i_2}^{\ \bar{i}_3} - \frac{1}{N_c}\delta_{i_2}^{\ \bar{i}_1}\delta_{i_4}^{\ \bar{i}_3}\right)$. Note that particles 3 and 4 have to be crossed into the final state to correspond to the process definition in Eq. 3.2.2, where all particles are outgoing. Thus, we should treat them as an outgoing antiquark and an outgoing quark, respectively, when applying the rules from Fig. C.1.

$\bar{b}b\bar{q}qH$ and $\bar{b}bggH$ channels, Eqs. 3.2.16 and 3.2.17 follow trivially. Then, to derive the two-loop pole operator $\boldsymbol{I}^{(2)}(\epsilon)$, we only need to concern ourselves with the action of the colour insertion operators $\boldsymbol{T}_i^a$ within $\boldsymbol{I}^{(1)}(\epsilon)$.

The $\bar{b}b\bar{q}qH$ channel

As the first step, we write down all the colour structures that appear in the relevant Feynman diagrams. Note that factors such as N_c, T_F, C_A or C_F are not considered a part of these structures — we only include δ-functions, fundamental generators $(T^a)_i^{\ \bar{j}}$ and the structure constants f^{abc}. For this channel, we find two colour structures (see Fig. C.2):

$$\boldsymbol{c} = \left(\delta_{i_4}^{\ \bar{i}_1}\delta_{i_2}^{\ \bar{i}_3} \qquad \delta_{i_2}^{\ \bar{i}_1}\delta_{i_4}^{\ \bar{i}_3}\right)^T . \tag{C.2.10}$$

Then, the action of the products $\boldsymbol{T}_i \cdot \boldsymbol{T}_j$ produces linear combinations of these structures, which we encode in the matrices $\mathcal{C}_{ij}$ defined as follows:

$$\boldsymbol{T}_i \cdot \boldsymbol{T}_j : \boldsymbol{c} = \mathcal{C}_{ij}\boldsymbol{c} . \tag{C.2.11}$$

Note that we do not have to compute $\mathcal{C}_{ij}$ for all possible combinations of partons i and j. Due to Eq. C.2.7, all $\mathcal{C}_{ii}$ are diagonal and their entries are given by the quadratic Casimirs C_i in the relevant representation. Moreover, the commutativity property Eq. C.2.6 further reduces the number of necessary computations. Overall, for n coloured partons, we only need to compute $n(n+1)/2$ matrices.

As an example, let us see how the operator product $\boldsymbol{T}_1 \cdot \boldsymbol{T}_4$ acts on the two colour structures in this channel. Applying the rules listed in Fig. C.1 (remember that particle 3 is treated as an outgoing antiquark, while particle 4 as an outgoing quark),

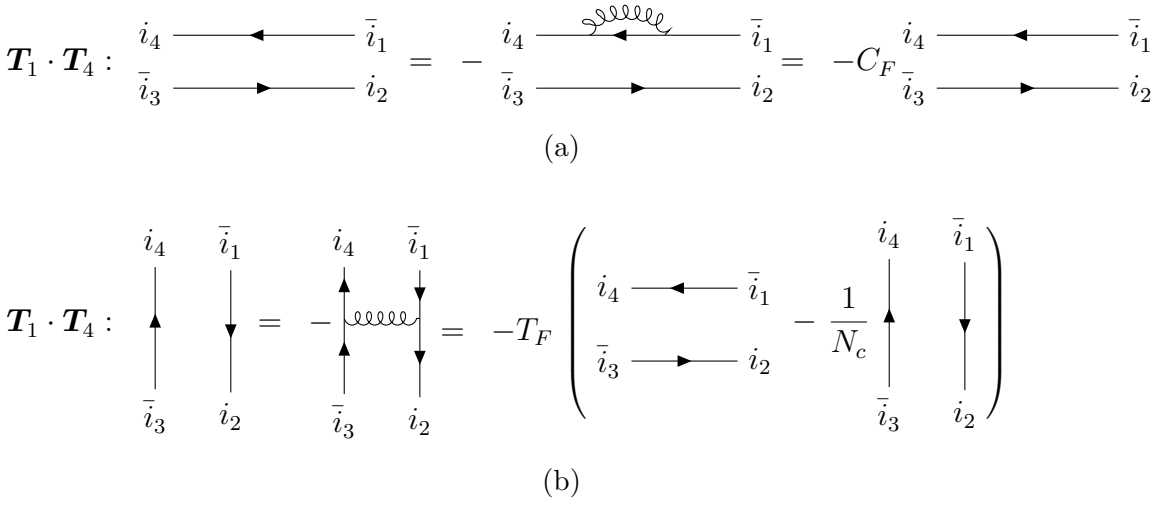

Figure C.3: A pictorial representation of the action of the colour insertion operators $\boldsymbol{T}_1 \cdot \boldsymbol{T}_4$ on the colour factors (a): $\delta_{i_4}^{\ \bar{i}_1}\delta_{i_2}^{\ \bar{i}_3}$ and (b): $\delta_{i_2}^{\ \bar{i}_1}\delta_{i_4}^{\ \bar{i}_3}$.

we obtain:

$$\boldsymbol{T}_1 \cdot \boldsymbol{T}_4 : \delta_{i_4}^{\ \bar{i}_1}\delta_{i_2}^{\ \bar{i}_3} = -(T^a T^a)_{i_4}^{\ \bar{i}_1}\delta_{i_2}^{\ \bar{i}_3} = -C_F \delta_{i_4}^{\ \bar{i}_1}\delta_{i_2}^{\ \bar{i}_3}\,, \tag{C.2.12}$$

$$\boldsymbol{T}_1 \cdot \boldsymbol{T}_4 : \delta_{i_2}^{\ \bar{i}_1}\delta_{i_4}^{\ \bar{i}_3} = -(T^a)_{i_2}^{\ \bar{i}_1}(T^a)_{i_4}^{\ \bar{i}_3} = -T_F\left(\delta_{i_4}^{\ \bar{i}_1}\delta_{i_2}^{\ \bar{i}_3} - \frac{1}{N_c}\delta_{i_2}^{\ \bar{i}_1}\delta_{i_4}^{\ \bar{i}_3}\right)\,, \tag{C.2.13}$$

where in both lines we have used the Fierz identity in the last equality. Perhaps a graphical representation of these operations in Fig. C.3 is once again more illustrative. We can now read off the matrix $\mathcal{C}_{14}$:

$$\mathcal{C}_{14} = \begin{pmatrix} -C_F & 0 \\ -T_F & \frac{T_F}{N_c} \end{pmatrix}\,. \tag{C.2.14}$$

In the same manner, we need to obtain the remaining matrices $\mathcal{C}_{ij}$. Needless to say, performing these operations by hand (or even using their diagrammatical equivalents) becomes tedious and extremely prone to errors. We therefore automate this task in `Mathematica` and make use of the package `ColorMath` [329] to achieve the simplifications of the various colour structures that arise as a result of applying the colour insertion operators. We make sure to verify that Eq. C.2.9 holds as a check on our calculations.

Once all the matrices $\mathcal{C}_{ij}$ have been computed, we have all the information needed to act with the pole operators $\boldsymbol{I}^{(L)}$ on the renormalised amplitudes $A_R^{(L)}$ and subtract the IR singularities. Note that if we want to retain full colour dependence, for each colour-ordered amplitude the subtraction will involve multiple lower-loop amplitudes with different colour factors. However, within the leading-colour approximation the

situation is much simpler as the pole operators become diagonal. Indeed, replacing each $\boldsymbol{T}_i \cdot \boldsymbol{T}_j$ with the corresponding $\mathcal{C}_{ij}$ (and each $\boldsymbol{T}_i^2$ with the corresponding quadratic Casimir C_i), we retain only the highest power of N_c to find:

$$\boldsymbol{I}^{(1)}_{\bar{b}bg\bar{q}qH} = -N_c \frac{N(\epsilon)}{2}\left(\frac{1}{\epsilon^2}+\frac{3}{2\epsilon}\right)\left((-s_{23})^{-\epsilon}+(-s_{14})^{-\epsilon}\right)\begin{pmatrix}1 & 0\\ 0 & 1\end{pmatrix}, \tag{C.2.15}$$

where $N(\epsilon) = \mathrm{e}^{\epsilon\gamma_E}/\Gamma(1-\epsilon)$. Moreover, it turns out that the second colour factor $\delta_{i_2}^{\ \bar{i}_1}\delta_{i_4}^{\ \bar{i}_3}$ always appears suppressed by $1/N_c$ with respect to the first factor $\delta_{i_4}^{\ \bar{i}_1}\delta_{i_2}^{\ \bar{i}_3}$, as can be appreciated from our simple example in Fig. C.2. Thus, in the leading-colour approximation, we simply drop it. This justifies the decomposition in Eq. 3.2.8 and completes the derivation of the pole operator $I^{(1)}_{\bar{b}bg\bar{q}qH}$ in Eq. 3.2.14, which now acts solely on the amplitude associated with the colour factor $\delta_{i_4}^{\ \bar{i}_1}\delta_{i_2}^{\ \bar{i}_3}$.

Finally, we combine the UV and IR poles in a single operator $P^{(L)}$ which we can use to subtract both types of divergences from the amplitude. Substituting Eq. C.1.8 into Eqs. C.2.1 and C.2.2, we obtain the finite part:

$$\begin{aligned}
F^{(1)} &= A_R^{(1)} - 2I^{(1)}(\epsilon)A_R^{(0)} \\
&= A_B^{(1)} + 2A_B^{(0)}(r_1+s_1) - 2I^{(1)}(\epsilon)A_B^{(0)} \\
&= A_B^{(1)} - \underbrace{2\left(I^{(1)}(\epsilon) - r_1 - s_1\right)}_{P^{(1)}} A_B^{(0)}\,,
\end{aligned} \tag{C.2.16}$$

$$\begin{aligned}
F^{(2)} &= A_R^{(2)} - 2I^{(1)}(\epsilon)A_R^{(1)} - 4I^{(2)}(\epsilon)A_R^{(0)} \\
&= A_B^{(2)} + 2A_B^{(1)}(2r_1+s_1) + 4A_B^{(0)}(r_2+r_1s_1+s_2) \\
&\quad - 2I^{(1)}(\epsilon)\left(A_B^{(1)} + 2A_B^{(0)}(r_1+s_1)\right) - 4I^{(2)}(\epsilon)A_B^{(0)} \\
&= A_B^{(2)} - \underbrace{\left(2I^{(1)}(\epsilon)\left(\hat{A}_B^{(1)} + 2r_1 + 2s_1\right) + 4I^{(2)}(\epsilon) - 2(2r_1+s_1)\hat{A}_B^{(1)} - 4(r_2+r_1s_1+s_2)\right)}_{P^{(2)}} A_B^{(0)}\,,
\end{aligned} \tag{C.2.17}$$

where $\hat{A}_B^{(1)}$ is the one-loop bare amplitude divided by the tree-level amplitude. Thus, to obtain the finite remainders, we simply subtract the operators $P^{(1)}$ and $P^{(2)}$ (multiplied by the tree-level amplitude) from the *bare* amplitudes $A_B^{(1)}$ and $A_B^{(2)}$.

The $\bar{b}bggH$ channel

The derivation of the pole structure in the $\bar{b}bggH$ channel follows exactly the same steps as described in the previous section. However, we believe it is still useful to outline it, since there are a few subtleties that we did not have to take care of in the

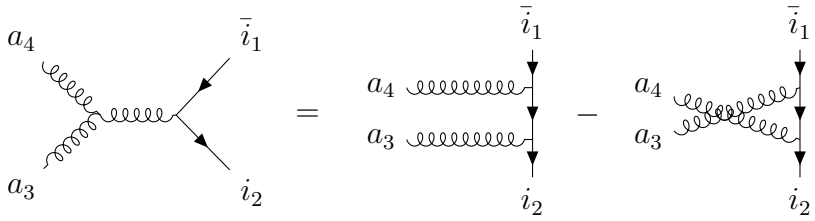

Figure C.4: The colour structure of a sample diagram contributing to the $\bar{b}bggH$ channel at tree level. It is also a graphical representation of the relation which defines the structure constants, $\mathrm{i}f^{abc}(T^c)_{i_2}^{\ \bar{i}_1} = (T^aT^b)_{i_2}^{\ \bar{i}_1} - (T^bT^a)_{i_2}^{\ \bar{i}_1}$.

case of the $\bar{b}bggH$ channel. First of all, here we find three colour structures:

$$\boldsymbol{c} = \left((T^{a_3}T^{a_4})_{i_2}^{\ \bar{i}_1} \qquad (T^{a_4}T^{a_3})_{i_2}^{\ \bar{i}_1} \qquad \delta_{i_2}^{\ \bar{i}_1}\delta^{ab}\right)^T . \tag{C.2.18}$$

While the first two factors can be spotted in a naive analysis of tree-level diagrams such as Fig. C.4, the third factor appears only at loop level. Thus, from a practical point of view, it is useful to have an automated routine which is able to extract the colour structure of all diagrams up to the desired loop order.

Just as before, we apply all the needed combinations of the $\boldsymbol{T}_i \cdot \boldsymbol{T}_j$ operators on the colour structures in $\boldsymbol{c}$ and extract the matrices $\mathcal{C}_{ij}$. We then know how to act with the pole operator $\boldsymbol{I}^{(1)}_{\bar{b}bggH}$ on the renormalised amplitude $A_R^{(L)}$ in this channel. Again, in the leading-colour approximation, the pole operator is diagonal, i.e. there is no mixing of different colour structures. However, contrary to $\boldsymbol{I}^{(1)}_{\bar{b}b\bar{q}qH}$, it is not proportional to the identity matrix. We find:

$$\boldsymbol{I}^{(1)}_{\bar{b}bggH} = -N_c\frac{N(\epsilon)}{2}\begin{pmatrix} \mathrm{I}_1 & 0 & 0 \\ 0 & \mathrm{I}_2 & 0 \\ 0 & 0 & \mathrm{I}_3 \end{pmatrix} ,$$

where:

$$\begin{aligned} \mathrm{I}_1 = \mathrm{I}_2 &= \left(\frac{1}{\epsilon^2} + \frac{3}{4\epsilon} + \frac{\beta_0}{4N_c\epsilon}\right)\left((-s_{23})^{-\epsilon} + (-s_{14})^{-\epsilon}\right) + \left(\frac{1}{\epsilon^2} + \frac{\beta_0}{2N_c\epsilon}\right)(-s_{34})^{-\epsilon} , \\ \mathrm{I}_3 &= \left(\frac{1}{\epsilon^2} + \frac{3}{2\epsilon}\right)(-s_{12})^{-\epsilon} + \left(\frac{2}{\epsilon^2} + \frac{\beta_0}{2N_c\epsilon}\right)(-s_{34})^{-\epsilon} . \end{aligned} \tag{C.2.19}$$

As in the previous section, the last colour factor is always suppressed by $1/N_c$ with respect to the first two and we simply drop it. This completes the derivation of the $\bar{b}bggH$ leading-colour decomposition, Eq. 3.2.8, and its pole operators, Eq. 3.2.15.

A careful reader might be alarmed by the presence of the β_0/N_c term at leading colour. Indeed, since $\beta_0 = \frac{11}{3}C_A - \frac{4}{3}T_F n_f$ and $C_A = N_c$, we would expect only the $11/3$ contribution to survive. However, in most applications the number of light

fermions circulating in closed loops is $n_f = 4$ or 5, thus $n_f/N_c \approx \mathcal{O}(1)$. It is therefore reasonable to retain the n_f term as well and the whole contribution is written in terms of the first β function coefficient as β_0/N_c. This also provides the motivation for the decomposition in Eqs. 3.2.9 and 3.2.10.

C.3 Pole structure of the QED process $0 \to \ell\bar{\ell}\gamma\gamma^*$

To derive the pole structure of the process $0 \to \ell\bar{\ell}\gamma\gamma^*$ in Chapter 5, we depart from the procedure described above. In particular, in QED there is no colour structure, therefore applying the colour insertion operators would not make sense here. Instead, we follow the approach found in Refs. [24–26, 287] and provide a brief outline below.

We renormalise the QED coupling constant by trading the bare coupling, α_B, for the renormalised one, α_R, through:

$$\alpha_B = \alpha_R(\mu_R)\, Z_\alpha\Big(\alpha_R(\mu_R)\Big)\, \mu_R^{2\epsilon}\, S_\epsilon\,, \tag{C.3.1}$$

with $S_\epsilon = \mathrm{e}^{\epsilon\gamma_E}(4\pi)^{-\epsilon}$. The renormalisation factor Z_α in the $\overline{\text{MS}}$ scheme is [330, 331]:

$$Z_\alpha(\alpha) = 1 - \frac{\alpha}{4\pi}\frac{\beta_0}{\epsilon} - \left(\frac{\alpha}{4\pi}\right)^2\left(-\frac{\beta_0^2}{\epsilon^2} + \frac{1}{2}\frac{\beta_1}{\epsilon}\right) + \mathcal{O}\Big(\alpha^3\Big)\,. \tag{C.3.2}$$

The QED β-function is defined from the renormalised coupling as:

$$\frac{\mathrm{d}\alpha_{\mathrm{R}}(\mu_R)}{\mathrm{d}\ln\mu_R} = \Big[-2\,\epsilon + \beta\Big(\alpha_{\mathrm{R}}(\mu_R)\Big)\Big]\,\alpha_{\mathrm{R}}(\mu_R)\,, \tag{C.3.3}$$

and expanded as:

$$\beta(\alpha) = -2\,\frac{\alpha}{4\pi}\sum_{k\geq 0}\beta_k\left(\frac{\alpha}{4\pi}\right)^k\,, \tag{C.3.4}$$

with:

$$\beta_0 = -\frac{4}{3}n_l\,, \qquad\qquad \beta_1 = -4\,n_l\,. \tag{C.3.5}$$

The photon wave function renormalisation factor is $Z_A = Z_\alpha$, which we include due to the external off-shell photon. The complete renormalisation procedure is then:

$$\mathcal{A}_R^\mu(\alpha_R) = Z_A^{\frac{1}{2}}(\alpha_R)\,\mathcal{A}_B^\mu(\alpha_B)\,, \tag{C.3.6}$$

where α_B is expressed in terms of α_R through Eq. C.3.1.

The IR poles of the renormalised amplitude factorise as [23–26, 287]:

$$\mathcal{A}_R^\mu(\alpha_R) = Z(\alpha_R)\,\mathcal{F}^\mu(\alpha_R)\,, \tag{C.3.7}$$

so that $Z(\alpha_R)$ captures all IR poles and $\mathcal{F}^\mu$ is a finite remainder. We obtain the explicit two-loop expression of the IR factor $Z(\alpha_R)$ by choosing QED parameters ($C_A = 0$, $C_F = 1$, and $T_F = 1$) in the non-abelian gauge-theory expressions of Ref. [25]. We expand it as:

$$Z(\alpha) = \sum_{k\geq 0} Z^{(L)} \left(\frac{\alpha}{4\pi}\right)^L. \tag{C.3.8}$$

The coefficients $Z^{(L)}$ up to two loops are given by:

$$Z^{(0)} = 1\,, \quad Z^{(1)} = \frac{\Gamma_0'}{4\epsilon^2} + \frac{\Gamma_0}{2\epsilon}\,, \quad Z^{(2)} = \frac{{Z^{(1)}}^2}{2} - \frac{3\beta_0\Gamma_0'}{16\epsilon^3} + \frac{\Gamma_1' - 4\beta_0\Gamma_0}{16\epsilon^2} + \frac{\Gamma_1}{4\epsilon}\,. \tag{C.3.9}$$

They are expressed in terms of the anomalous dimension Γ:

$$\Gamma = \gamma^{\text{cusp}} \ln\left(\frac{-s_{12}}{\mu^2}\right) + 2\gamma^l + \gamma^A, \tag{C.3.10}$$

and its derivative:

$$\Gamma' \equiv \frac{\partial\Gamma}{\partial \ln\mu} = -2\gamma^{\text{cusp}}\,. \tag{C.3.11}$$

Here, γ^{cusp} is the cusp anomalous dimension, while γ^l and γ^A are the lepton's and the photon's collinear anomalous dimensions, respectively. We expand all anomalous dimensions $y \in \{\Gamma, \gamma^i\}$ as:

$$y = \frac{\alpha}{4\pi} \sum_{k\geq 0} y_k \left(\frac{\alpha}{4\pi}\right)^k. \tag{C.3.12}$$

Their zeroth- and first-order coefficients are listed in Appendix D.

Putting together the subtraction of UV and IR poles and expanding the resulting finite remainder $\mathcal{F}^\mu(\alpha_R)$ in α_R leads to the definitions in Eq. 5.2.14.

Appendix D

Renormalisation Constants

The bottom-quark Yukawa renormalisation constants are [162, 326]:

$$r_1 = -\frac{\beta_0}{2\epsilon}\,, \tag{D.1}$$

$$r_2 = \frac{\beta_0^2}{4\epsilon^2} - \frac{\beta_1}{8\epsilon}\,, \tag{D.2}$$

$$s_1 = -\frac{3C_F}{2\epsilon}\,, \tag{D.3}$$

$$s_2 = \frac{3}{8\epsilon^2}\Big(3C_F^2 + \beta_0 C_F\Big) - \frac{1}{8\epsilon}\left(\frac{3C_F^2}{2} + \frac{97}{6}C_F C_A - \frac{10}{3}C_F T_F n_f\right), \tag{D.4}$$

where the first two β function coefficients are:

$$\beta_0 = \frac{11}{3}C_A - \frac{4}{3}T_F n_f\,, \tag{D.5}$$

$$\beta_1 = \frac{34}{3}C_A^2 - \frac{20}{3}C_A T_F n_f - 4C_F T_F n_f\,, \tag{D.6}$$

with $C_A = N_c$, $C_F = T_F(N_c^2 - 1)/N_c$.

The zeroth and first-order coefficients of the anomalous dimensions are given by [25]:

$$\gamma_0^g = -\frac{11}{3}C_A + \frac{4}{3}T_F n_f\,, \tag{D.7}$$

$$\gamma_1^g = C_A^2\left(-\frac{692}{27} + \frac{11\pi^2}{18} + 2\zeta_3\right) + 4C_F T_F n_f + C_A T_F n_f\left(\frac{256}{27} - \frac{2\pi^2}{9}\right), \tag{D.8}$$

$$\gamma_0^q = -3C_F\,, \tag{D.9}$$

$$\gamma_1^q = C_F^2\left(-\frac{3}{2} + 2\pi^2 - 24\zeta_3\right) + C_F C_A\left(-\frac{961}{54} - \frac{11\pi^2}{6} + 26\zeta_3\right) + C_F T_F n_f\left(\frac{130}{27} + \frac{2\pi^2}{3}\right), \tag{D.10}$$

$$\gamma_0^l = -3\,, \tag{D.11}$$

$$\gamma_1^l = -\frac{3}{2} + 2\pi^2 - 24\,\zeta_3 + n_f\left(\frac{130}{27} + \frac{2}{3}\pi^2\right), \tag{D.12}$$

$$\gamma_0^A = -\beta_0\,, \tag{D.13}$$

$$\gamma_1^A = -\beta_1\,, \tag{D.14}$$

$$\gamma_0^{\rm cusp} = 4\,, \tag{D.15}$$

$$\gamma_1^{\rm cusp} = \left(\frac{268}{9} - \frac{4\pi^2}{3}\right) C_A - \frac{80}{9} T_F n_f\,. \tag{D.16}$$

We emphasise that while in QCD we have $N_c = 3$ and usually set $T_F = 1/2$ or 1, when working in QED one needs to set $C_A = 0$, $C_F = 1$ and $T_F = 1$ in the expressions listed above.

Appendix E

One-Loop Results

In this appendix, we collect the numerical results relevant to the amplitudes presented in Chapters 3 and 4. Tables E.1 and E.3 show the bare one-loop amplitudes for the two processes $pp \to b\bar{b}H$ and $pp \to W^{\pm}\gamma j$, respectively. Tables E.2 and E.4 show the corresponding reduced squared tree-level amplitudes $\mathcal{H}^{(0)}$ and the reduced squared one-loop finite remainders.

$\bar{b}bggH$	helicity	ϵ^{-2}	ϵ^{-1}	ϵ^{0}	ϵ^{1}	ϵ^{2}
$\hat{A}^{(1),1}$	$++++$	-3	$3.07857 - 3.14159i$	$0.317351 + 8.42128i$	$-1.25257 - 8.56907i$	$25.8294 - 4.35648i$
	$+++-$	-3	$3.07857 - 3.14159i$	$-2.99786 - 1.02133i$	$2.86487 - 28.7164i$	$30.3093 - 26.3373i$
	$++-+$	-3	$3.07857 - 3.14159i$	$-0.119814 + 8.67497i$	$-1.43041 - 5.33656i$	$19.6373 - 0.110475i$
	$++--$	-3	$3.07857 - 3.14159i$	$-6.51606 + 18.6156i$	$-21.7849 + 24.0036i$	$-24.6605 + 55.6878i$
$\hat{A}^{(1),n_f}$	$++++$	0	0	$-0.005010 + 0.000779871i$	$-0.00700827 - 0.0150298i$	$0.0109029 - 0.0163643i$
	$+++-$	0	0	0	0	0
	$++-+$	0	0	0	0	0
	$++--$	0	0	$-0.393552 + 0.138515i$	$-0.793221 - 1.11035i$	$0.635641 - 1.48796i$
$\bar{b}b\bar{q}qH$	helicity	ϵ^{-2}	ϵ^{-1}	ϵ^{0}	ϵ^{1}	ϵ^{2}
$\hat{A}^{(1),1}$	$+++-$	-2	2.48840	$-9.99430 - 8.95182i$	$2.20899 - 24.3401i$	$4.76962 - 27.6604i$
	$++-+$	-2	2.48840	$-8.43825 - 7.45006i$	$7.21741 - 24.6383i$	$13.6369 - 20.4876i$
$\hat{A}^{(1),n_f}$	$+++-$	0	-0.666667	$0.726782 - 2.09440i$	$2.29387 + 2.28325i$	$-2.54017 + 0.316127i$
	$++-+$	0	-0.666667	$0.726782 - 2.09440i$	$2.29387 + 2.28325i$	$-2.54017 + 0.316127i$

Table E.1: Numerical values of the bare $\bar{b}bggH$ and $\bar{b}b\bar{q}qH$ partial amplitudes at one loop (normalised to the tree-level amplitude) at the kinematic point in Eq. 3.6.11 for the four independent helicity configurations and the various closed fermion loops contributions.

channel	$\mathcal{H}^{(0)}$	Re $\mathcal{H}^{(1),1}$	Re $\mathcal{H}^{(1),n_f}$
$\mathbf{gg}$	1121.375369	4905.689964	204.1069797
$\mathbf{q\bar{q}}$	0.001095232986	-0.008958148524	0.0007959961305
$\mathbf{\bar{q}q}$	0.001095232986	0.01182947634	0.0007959961305
$\mathbf{b\bar{b}}$	738.4111805	5948.275150	-2005.976183
$\mathbf{\bar{b}b}$	774.9861507	-8346.007933	-2253.325645
$\mathbf{bb/\bar{b}\bar{b}}$	71.81424881	-678.1382010	-243.5040325

Table E.2: Numerical values of the tree-level reduced squared amplitudes $\mathcal{H}^{(0)}$ and one-loop reduced squared finite remainders $\mathcal{H}^{(1)}$ defined in Eqs. 3.6.3-3.6.9 at the kinematic point in Eq. 3.6.11 for the closed fermion loops contributions and the scattering channels specified in Eq. 3.6.1.

	helicity	ϵ^{-2}	ϵ^{-1}	ϵ^0	ϵ^1	ϵ^2
$\hat{A}_u^{(1),1}$	$+++--+$	-2	23.8477	$-138.615-2.09370i$	$523.949+12.3666i$	$-1448.23-21.7701i$
	$-++--+$	-2	23.8477	$-139.779-0.516164i$	$535.218-2.01397i$	$-1503.32+46.1044i$
$\hat{A}_d^{(1),1}$	$+++--+$	-2	23.8477	$-140.008-2.18806i$	$539.871+13.7461i$	$-1538.48-30.4669i$
	$-++--+$	-2	23.8477	$-139.294-2.18046i$	$532.471+15.2170i$	$-1499.51-44.3866i$
$\hat{A}_W^{(1),1}$	$+++--+$	-2	23.8477	$-139.550-1.53563i$	$534.185+8.26368i$	$-1503.99-6.62167i$
	$-++--+$	-2	23.8477	$-139.818-1.20381i$	$536.639+5.03856i$	$-1515.10+9.39205i$
$\hat{A}_e^{(1),1}$	$+++--+$	-2	23.8477	$-139.570-1.46851i$	$534.360+7.61926i$	$-1504.71-3.48177i$
	$-++--+$	-2	23.8477	$-140.303-1.48855i$	$541.353+7.64165i$	$-1538.44-2.31498i$

Table E.3: Bare one-loop helicity sub-amplitudes (normalised to the tree-level amplitudes as in Eq. 4.5.9) without any closed fermion loop contribution for $W^+\gamma j$ production in the $\mathbf{u\bar{d}}$ scattering channel evaluated at the kinematic point given in Eq. 4.5.7. The results are shown for the two independent helicity configurations and obtained with $q_1 = p_3$ and $q_3 = p_1$ where q_1 (q_3) is the reference momentum for the photon (gluon) polarisation vector.

$W^+\gamma j$	$\mathcal{H}^{(0)}$ $[\times 10^{-10}\,\mathrm{GeV}^{-4}]$	Re $\hat{\mathcal{H}}^{(1),1}$	Re $\hat{\mathcal{H}}^{(1),n_f}$
$\mathbf{u\bar{d}}$	32.9224527109	-20.4269208141	4.22462265354
$\mathbf{\bar{d}u}$	35.8863373066	-20.0350027848	4.22462265354
$\mathbf{ug}$	4.84655650134	-26.9389515414	4.45445318051
$\mathbf{gu}$	15.2151742999	-25.3235043118	4.37533965902
$\mathbf{\bar{d}g}$	9.18270882925	-28.3542876136	4.45445318051
$\mathbf{g\bar{d}}$	26.4333120479	-27.3120879601	4.37533965902
$W^-\gamma j$	$\mathcal{H}^{(0)}$ $[\times 10^{-10}\,\mathrm{GeV}^{-4}]$	Re $\hat{\mathcal{H}}^{(1),1}$	Re $\hat{\mathcal{H}}^{(1),n_f}$
$\mathbf{d\bar{u}}$	48.5521763841	-20.5759435967	4.22462265354
$\mathbf{\bar{u}d}$	5.60724308955	-25.0921274652	4.22462265354
$\mathbf{dg}$	0.161819754065	-53.2745933316	4.45445318051
$\mathbf{gd}$	2.59919214772	-35.7387232774	4.37533965902
$\mathbf{\bar{u}g}$	0.471356750696	-25.5067063821	4.45445318051
$\mathbf{g\bar{u}}$	27.6357549618	-32.8902240077	4.37533965902

Table E.4: Reduced squared tree-level amplitude (absolute) and reduced squared one-loop finite remainders (normalised to the reduced squared tree amplitudes) for the various closed fermion loop contributions and scattering channels of both $pp \to W^+\gamma j$ and $pp \to W^-\gamma j$ production, evaluated at the kinematic point given in Eq. 4.5.7.

Appendix F

Definition of the four-point integral families

For each two-loop integral family T corresponding to one of the maximal topologies shown in Fig. 5.2, the Feynman integrals have the form:

$$j^T(a_1,\ldots,a_9) = \mathrm{e}^{2\epsilon\gamma_E} \int \frac{\mathrm{d}^{4-2\epsilon}k_1}{\mathrm{i}\pi^{2-\epsilon}} \frac{\mathrm{d}^{4-2\epsilon}k_2}{\mathrm{i}\pi^{2-\epsilon}} \frac{1}{D_{T,1}^{a_1}\ldots D_{T,9}^{a_9}}\,. \tag{F.1}$$

The sets $\{D_{T,1},\ldots,D_{T,9}\}$ contain seven (inverse) propagators and two ISPs ($a_8, a_9 \leq 0$). For the maximal topologies under consideration, they are given by[1]:

- penta-triangle, **mzz** configuration:

$$\begin{aligned}\Big\{&k_1^2, (k_1+p_1+p_2+p_3)^2, (k_1+p_2+p_3)^2, (k_1+p_3)^2, k_2^2, (k_2-p_3)^2,\\ &(k_1+k_2)^2, (k_2-p_1-p_2-p_3)^2, (k_2-p_2-p_3)^2\Big\}\,,\end{aligned} \tag{F.2}$$

- penta-triangle, **zmz** configuration:

$$\begin{aligned}\Big\{&k_1^2, (k_1-p_1)^2, (k_1+p_2+p_3)^2, (k_1+p_3)^2, k_2^2, (k_2-p_3)^2, (k_1+k_2)^2,\\ &(k_2+p_1)^2, (k_2-p_2-p_3)^2\Big\}\,,\end{aligned} \tag{F.3}$$

- penta-triangle, **zzz** configuration:

$$\begin{aligned}\Big\{&k_1^2, (k_1-p_1)^2, (k_1-p_1-p_2)^2, (k_1-p_1-p_2-p_3)^2, k_2^2, (k_2+p_1+p_2+p_3)^2,\\ &(k_1+k_2)^2, (k_2+p_1)^2, (k_2+p_1+p_2)^2\Big\}\,,\end{aligned} \tag{F.4}$$

[1] We use a naming convention analogous to that of Ref. [98].

- planar double-box:

$$\Big\{k_1^2, (k_1-p_1)^2, (k_1-p_1-p_2)^2, k_2^2, (k_2+p_1+p_2+p_3)^2, (k_2+p_1+p_2)^2, \\ (k_1+k_2)^2, (k_1-p_1-p_2-p_3)^2, (k_2+p_1)^2\Big\}, \tag{F.5}$$

- crossed double-box, **mz** configuration:

$$\Big\{k_1^2, (k_1+p_1+p_2+p_3)^2, (k_1+p_2+p_3)^2, k_2^2, (k_2-p_2)^2, (k_1+k_2)^2, \\ (k_1+k_2+p_3)^2, (k_1+p_3)^2, (k_2-p_1-p_2-p_3)^2\Big\}, \tag{F.6}$$

- crossed double-box, **zz** configuration:

$$\Big\{k_1^2, (k_1-p_1)^2, (k_1-p_1-p_2)^2, k_2^2, (k_2-p_3)^2, (k_1+k_2)^2, \\ (k_1+k_2-p_1-p_2-p_3)^2, (k_1-p_1-p_2-p_3)^2, (k_2+p_1)^2\Big\}. \tag{F.7}$$

We also use the one-loop (one-mass) box family, made of the following integrals:

$$j^{\text{box}}(a_1,a_2,a_3,a_4) = \mathrm{e}^{\epsilon\gamma_E} \int \frac{\mathrm{d}^{4-2\epsilon}k}{\mathrm{i}\pi^{2-\epsilon}} \frac{1}{D_{\text{box},1}^{a_1} D_{\text{box},2}^{a_2} D_{\text{box},3}^{a_3} D_{\text{box},4}^{a_4}}, \tag{F.8}$$

with the four inverse propagators $D_{\text{box},i}$:

$$\Big\{k_1^2, (k_1-p_1)^2, (k_1-p_1-p_2)^2, (k_1-p_1-p_2-p_3)^2\Big\}. \tag{F.9}$$

Feynman's prescription for the imaginary parts of all propagators is implicit.

These family definitions (strictly with the ordering of inverse propagators and ISPs shown above) correspond to the integrals `j[family,`a_1`,...]` that build the canonical MI bases provided in the `pure_mi_bases/` directory of the ancillary files [284]. In this notation, each `j[...]` represents a Feynman integral within a given integral family, while the numbers a_i refer to the powers of its propagators and ISPs.

Appendix G

Analytic continuation

In Chapter 5, we analytically continue the GPLs by adding a small positive (or negative) imaginary part to the GPL indices l_i in Eq. 5.4.10 whenever they fall between 0 and 1. The imaginary part of each index prescribes how to deform the integration contour around the pole associated with it. We do similarly for the logarithms in Eq. 5.4.12. To this end, following Ref. [275], we change variables from (s_{12}, s_{23}, s_4) to (s_{12}, s_{23}, s_{13}), with $s_4 = s_{12} + s_{23} + s_{13}$. We then add a small positive imaginary part to the new variables:

$$s_{12} \longrightarrow s_{12} + \mathrm{i}\, c_1\, \delta\,, \qquad s_{23} \longrightarrow s_{23} + \mathrm{i}\, c_2\, \delta\,, \qquad s_{13} \longrightarrow s_{13} + \mathrm{i}\, c_3\, \delta\,, \tag{G.1}$$

where c_1, c_2 and c_3 are arbitrary positive constants, and δ is a positive infinitesimal. Finally, we check whether this substitution gives a positive or negative imaginary part to each GPL index l_i. This depends on the domain of the kinematic variables. We focus on three kinematic regions which are of phenomenological interest. The analytic continuation for any other region may be obtained similarly.

Electron-line corrections to $e^-\mu^- \to e^-\mu^-\gamma$. To define the domain of the kinematic variables relevant for this application, we embed the four-particle off-shell process of Eq. 5.2.1 in the five-particle process $e^-\mu^- \to e^-\mu^-\gamma$. We then determine the kinematic constraints for the five-particle process (see e.g. Appendix A of Ref. [121]), and from them derive the constraints on the four-point off-shell kinematics. The result is:

$$\mathcal{P}_{e\mu\to e\mu\gamma} \coloneqq \{\vec{s}\colon\, s_{12} < 0 \,\wedge\, s_{23} < 0 \,\wedge\, 0 < s_{13} < -s_{12} - s_{23}\}\,. \tag{G.2}$$

The GPL index $l_4 = -s_{12}/s_{23}$ is always negative in $\mathcal{P}_{e\mu\to e\mu\gamma}$, hence no analytic continuation is required. The other three indices may instead fall between 0 and 1.

Index	$\mathcal{P}_{e\mu\to e\mu\gamma}$	$\mathcal{P}_{e\bar{e}\to\gamma\gamma^*}$	$\mathcal{P}_{\gamma^*\to e\bar{e}\gamma}$
l_1	$-$	$+$	0
l_2	$-$	0	0
l_3	$-$	0	0
l_4	0	0	0

Table G.1: Imaginary parts of the GPL indices defined by Eq. 5.4.10 in the three kinematic regions discussed in Appendix G. The symbol $+$ ($-$) denotes a positive (negative) imaginary part, while 0 means no analytic continuation is needed.

Let us study l_1. Changing variables from s_4 to s_{13} and adding imaginary parts as in Eq. G.1 gives:

$$l_1 = \frac{s_{12}+s_{13}+s_{23}}{s_{12}} + \frac{\mathrm{i}\delta}{s_{12}^2}\left[(c_2+c_3)s_{12} - c_1(s_{13}+s_{23})\right] + \mathcal{O}\left(\delta^2\right). \tag{G.3}$$

The imaginary part of l_1 may be either negative or positive in $\mathcal{P}_{e\mu\to e\mu\gamma}$. However, it is strictly negative in the subregion of $\mathcal{P}_{e\mu\to e\mu\gamma}$ where $0 < l_1 < 1$. We therefore assign a negative imaginary part to l_1 whenever $0 < l_1 < 1$ in $\mathcal{P}_{e\mu\to e\mu\gamma}$. The analysis of the other indices follows similarly, and is summarised in Table G.1. The arguments of the three logarithms in Eq. 5.4.12 are positive in $\mathcal{P}_{e\mu\to e\mu\gamma}$.

Corrections to $e^-e^+ \to \gamma\gamma^*$. The relevant domain of the kinematic variables in this case can be derived directly for the four-point kinematics, and is typically named the s_{12} channel. It is given by:

$$\mathcal{P}_{e\bar{e}\to\gamma\gamma^*} \coloneqq \{\vec{s}\colon s_{23} < 0 \,\wedge\, s_{13} < 0 \,\wedge\, s_{12} > -s_{23} - s_{13}\}. \tag{G.4}$$

The GPL indices l_2, l_3 and l_4 can never fall between 0 and 1 in $\mathcal{P}_{e\bar{e}\to\gamma\gamma^*}$, and hence require no analytic continuation. We instead need to add a positive imaginary part to l_1. In this region, also the logarithms in Eq. 5.4.12 need to be analytically continued. The argument of $\log(s_{12}/s_4)$ is positive in $\mathcal{P}_{e\bar{e}\to\gamma\gamma^*}$. By adding imaginary parts to the arguments of the other logarithms and studying them where the arguments are negative in $\mathcal{P}_{e\bar{e}\to\gamma\gamma^*}$, we determine that the analytic continuation is achieved through the following replacements:

$$\log(s_{23}/s_4) \longrightarrow \log(-s_{23}/s_4) + \mathrm{i}\pi\,, \qquad \log(-s_4) \longrightarrow \log(s_4) - \mathrm{i}\pi\,. \tag{G.5}$$

Corrections to the decay $\gamma^* \to e^-e^+\gamma$. The relevant domain of the kinematic variables is:

$$\mathcal{P}_{\gamma^*\to e\bar{e}\gamma} \coloneqq \{\vec{s}\colon s_{12} > 0 \,\wedge\, s_{23} > 0 \,\wedge\, s_{13} > 0\}. \tag{G.6}$$

All GPL indices l_i in Eq. 5.4.10 are either $l_i < 0$ or $l_i > 1$, hence no analytic continuation is required. The same holds for the first two logarithms in Eq. 5.4.12, whose arguments are positive. The only function which needs to be analytically continued is $\log(-s_4)$. We achieve this by replacing:

$$\log(-s_4) \longrightarrow \log(s_4) - \mathrm{i}\pi\,. \tag{G.7}$$

The information about the imaginary parts of the GPL indices can be fed into the publicly available libraries for evaluating these functions numerically, such as `FastGPL` [332], `GiNaC` [96, 298], and `handyG` [303]. This typically leads to longer evaluation times with respect to GPLs which do not need analytic continuation. We find that this is not an issue for the planned applications of our results (see Section 5.4.3). Nonetheless, we note that a more performant evaluation may be achieved by tailoring the GPL representation to the kinematic region of interest in such a way that no GPLs require analytic continuation. We refer the reader to Refs. [275, 276] for a detailed discussion.

Bibliography

[1] S. Badger, H. B. Hartanto, J. Kryś and S. Zoia, *Two-loop leading-colour QCD helicity amplitudes for Higgs boson production in association with a bottom-quark pair at the LHC*, *JHEP* **11** (2021) 012, [2107.14733].

[2] S. Badger, H. B. Hartanto, J. Kryś and S. Zoia, *Two-loop leading colour helicity amplitudes for $W^{\pm}\gamma + j$ production at the LHC*, 2201.04075.

[3] S. Badger, J. Kryś, R. Moodie and S. Zoia, *Lepton-pair scattering with an off-shell and an on-shell photon at two loops in massless QED*, 2307.03098.

[4] A. Huss, J. Huston, S. Jones and M. Pellen, *Les Houches 2021—physics at TeV colliders: report on the standard model precision wishlist*, *J. Phys. G* **50** (2023) 043001, [2207.02122].

[5] R. P. Feynman, *Very high-energy collisions of hadrons*, *Phys. Rev. Lett.* **23** (Dec, 1969) 1415–1417.

[6] J. C. Collins, D. E. Soper and G. F. Sterman, *Factorization of Hard Processes in QCD*, *Adv. Ser. Direct. High Energy Phys.* **5** (1989) 1–91, [hep-ph/0409313].

[7] H1, ZEUS collaboration, H. Abramowicz et al., *Combination of measurements of inclusive deep inelastic $e^{\pm}p$ scattering cross sections and QCD analysis of HERA data*, *Eur. Phys. J. C* **75** (2015) 580, [1506.06042].

[8] S. Alekhin, J. Blümlein, S. Moch and R. Placakyte, *Parton distribution functions, α_s, and heavy-quark masses for LHC Run II*, *Phys. Rev. D* **96** (2017) 014011, [1701.05838].

[9] T.-J. Hou et al., *New CTEQ global analysis of quantum chromodynamics with high-precision data from the LHC*, *Phys. Rev. D* **103** (2021) 014013, [1912.10053].

[10] NNPDF collaboration, R. D. Ball et al., *An open-source machine learning framework for global analyses of parton distributions*, *Eur. Phys. J. C* **81** (2021) 958, [2109.02671].

[11] A. Buckley, J. Ferrando, S. Lloyd, K. Nordström, B. Page, M. Rüfenacht et al., *LHAPDF6: parton density access in the LHC precision era*, *Eur. Phys. J. C* **75** (2015) 132, [1412.7420].

[12] T. Plehn, *Lectures on LHC Physics*, *Lect. Notes Phys.* **844** (2012) 1–193, [0910.4182].

[13] S. Höche, *Introduction to parton-shower event generators*, in *Theoretical Advanced Study Institute in Elementary Particle Physics: Journeys Through the Precision Frontier: Amplitudes for Colliders*, pp. 235–295, 2015, 1411.4085, DOI.

[14] R. I. Moodie, *Precision QCD corrections to gluon-initiated diphoton-plus-jet production at the LHC*, Ph.D. thesis, Durham U., 2022. 2210.07115.

[15] C. Reuschle, *Event simulation for colliders — A basic overview*, *J. Phys. Conf. Ser.* **608** (2015) 012072, [1411.7321].

[16] J. M. Campbell et al., *Event Generators for High-Energy Physics Experiments*, in *Snowmass 2021*, 3, 2022, 2203.11110.

[17] C. G. Callan, *Broken scale invariance in scalar field theory*, *Phys. Rev. D* **2** (Oct, 1970) 1541–1547.

[18] K. Symanzik, *Small distance behavior in field theory and power counting*, *Commun. Math. Phys.* **18** (1970) 227–246.

[19] P. A. Baikov, K. G. Chetyrkin and J. H. Kühn, *Five-Loop Running of the QCD coupling constant*, *Phys. Rev. Lett.* **118** (2017) 082002, [1606.08659].

[20] T. Kinoshita, *Mass Singularities of Feynman Amplitudes*, *Journal of Mathematical Physics* **3** (12, 2004) 650–677, [https://pubs.aip.org/aip/jmp/article-pdf/3/4/650/11042382/650_1_online.pdf].

[21] T. D. Lee and M. Nauenberg, *Degenerate systems and mass singularities*, *Phys. Rev.* **133** (Mar, 1964) B1549–B1562.

[22] R. Ellis, W. Stirling and B. Webber, *QCD and Collider Physics*. Cambridge Monographs on Particle Physics, Nuclear Physics and Cosmology. Cambridge University Press, 2003.

[23] S. Catani, *The Singular behavior of QCD amplitudes at two loop order*, *Phys. Lett.* **B427** (1998) 161–171, [hep-ph/9802439].

[24] T. Becher and M. Neubert, *Infrared singularities of scattering amplitudes in perturbative QCD*, *Phys. Rev. Lett.* **102** (2009) 162001, [0901.0722].

[25] T. Becher and M. Neubert, *On the Structure of Infrared Singularities of Gauge-Theory Amplitudes*, *JHEP* **06** (2009) 081, [0903.1126].

[26] E. Gardi and L. Magnea, *Factorization constraints for soft anomalous dimensions in QCD scattering amplitudes*, *JHEP* **03** (2009) 079, [0901.1091].

[27] N. Agarwal, L. Magnea, C. Signorile-Signorile and A. Tripathi, *The infrared structure of perturbative gauge theories*, *Phys. Rept.* **994** (2023) 1–120, [2112.07099].

[28] Z. Bern, L. J. Dixon and D. A. Kosower, *Dimensionally regulated pentagon integrals*, *Nucl. Phys. B* **412** (1994) 751–816, [hep-ph/9306240].

[29] R. N. Lee, *Presenting LiteRed: a tool for the Loop InTEgrals REDuction*, 1212.2685.

[30] C. G. Bollini, J. J. Giambiagi and A. G. Dominguez, *Analytic regularization and the divergences of quantum field theories*, *Il Nuovo Cimento (1955-1965)* **31** (1964) 550–561.

[31] G. 't Hooft and M. Veltman, *Regularization and renormalization of gauge fields*, *Nuclear Physics B* **44** (1972) 189–213.

[32] A. Signer and D. Stockinger, *Using Dimensional Reduction for Hadronic Collisions*, *Nucl. Phys. B* **808** (2009) 88–120, [0807.4424].

[33] C. Gnendiger et al., *To d, or not to d: recent developments and comparisons of regularization schemes*, *Eur. Phys. J. C* **77** (2017) 471, [1705.01827].

[34] K. G. Wilson, *Quantum field - theory models in less than 4 dimensions*, *Phys. Rev. D* **7** (May, 1973) 2911–2926.

[35] P. Nogueira, *Automatic Feynman graph generation*, *J. Comput. Phys.* **105** (1993) 279–289.

[36] L. J. Dixon, *Calculating scattering amplitudes efficiently*, in *Theoretical Advanced Study Institute in Elementary Particle Physics (TASI 95): QCD and Beyond*, pp. 539–584, 1, 1996, hep-ph/9601359.

[37] M. L. Mangano and S. J. Parke, *Multiparton amplitudes in gauge theories*, *Phys. Rept.* **200** (1991) 301–367, [hep-th/0509223].

[38] R. Kleiss and H. Kuijf, *Multigluon cross sections and 5-jet production at hadron colliders*, *Nuclear Physics B* **312** (1989) 616–644.

[39] Z. Bern, J. J. M. Carrasco and H. Johansson, *New Relations for Gauge-Theory Amplitudes*, *Phys. Rev. D* **78** (2008) 085011, [0805.3993].

[40] H. Elvang and Y.-t. Huang, *Scattering Amplitudes in Gauge Theory and Gravity*. Cambridge University Press, 2015.

[41] S. J. Parke and T. R. Taylor, *Amplitude for n-gluon scattering*, *Phys. Rev. Lett.* **56** (Jun, 1986) 2459–2460.

[42] R. Britto, F. Cachazo and B. Feng, *New recursion relations for tree amplitudes of gluons*, *Nucl. Phys. B* **715** (2005) 499–522, [hep-th/0412308].

[43] R. Britto, F. Cachazo, B. Feng and E. Witten, *Direct proof of tree-level recursion relation in Yang-Mills theory*, *Phys. Rev. Lett.* **94** (2005) 181602, [hep-th/0501052].

[44] A. Hodges, *Eliminating spurious poles from gauge-theoretic amplitudes*, *JHEP* **05** (2013) 135, [0905.1473].

[45] S. Badger, H. Frellesvig and Y. Zhang, *A Two-Loop Five-Gluon Helicity Amplitude in QCD*, *JHEP* **12** (2013) 045, [1310.1051].

[46] S. Badger, *Automating QCD amplitudes with on-shell methods*, *J. Phys. Conf. Ser.* **762** (2016) 012057, [1605.02172].

[47] T. Peraro, *Scattering amplitudes over finite fields and multivariate functional reconstruction*, *JHEP* **12** (2016) 030, [1608.01902].

[48] T. Peraro, *FiniteFlow: multivariate functional reconstruction using finite fields and dataflow graphs*, *JHEP* **07** (2019) 031, [1905.08019].

[49] J. Klappert and F. Lange, *Reconstructing rational functions with FireFly*, *Comput. Phys. Commun.* **247** (2020) 106951, [1904.00009].

[50] J. Klappert, S. Y. Klein and F. Lange, *Interpolation of dense and sparse rational functions and other improvements in FireFly*, *Comput. Phys. Commun.* **264** (2021) 107968, [2004.01463].

[51] A. von Manteuffel and R. M. Schabinger, *A novel approach to integration by parts reduction*, *Phys. Lett. B* **744** (2015) 101–104, [1406.4513].

[52] S. Abreu, J. Dormans, F. Febres Cordero, H. Ita, M. Kraus, B. Page et al., *Caravel: A C++ Framework for the Computation of Multi-Loop Amplitudes with Numerical Unitarity*, 2009.11957.

[53] D. Knuth, *Art of Computer Programming, Volume 2: Seminumerical Algorithms*. Pearson Education, 2014.

[54] P. S. Wang, *A p-adic algorithm for univariate partial fractions*, in *Proceedings of the Fourth ACM Symposium on Symbolic and Algebraic Computation*, SYMSAC '81, (New York, NY, USA), p. 212217, Association for Computing Machinery, 1981, DOI.

[55] P. S. Wang, M. J. T. Guy and J. H. Davenport, *P-adic reconstruction of rational numbers*, *SIGSAM Bull.* **16** (May, 1982) 23.

[56] Page, Ben, *Large ansätze and finite-field methods*, 2021 SAGEX Mathematica and Maple School. Available at: https://youtu.be/XmVDq7HD1Cs.

[57] M. Abramowitz, I. A. Stegun and D. M. Miller, *Handbook of mathematical functions with formulas, graphs and mathematical tables (national bureau of standards applied mathematics series no. 55)*, *Journal of Applied Mechanics* **32** (1965) 239–239.

[58] A. Cuyt and W. shin Lee, *Sparse interpolation of multivariate rational functions*, *Theoretical Computer Science* **412** (2011) 1445–1456.

[59] G. Hardy, E. Wright, D. Heath-Brown and J. Silverman, *An Introduction to the Theory of Numbers*. Oxford mathematics. OUP Oxford, 2008.

[60] A. G. Grozin, *Integration by parts: An Introduction*, *Int. J. Mod. Phys. A* **26** (2011) 2807–2854, [1104.3993].

[61] S. Badger, C. Brønnum-Hansen, H. B. Hartanto and T. Peraro, *First look at two-loop five-gluon scattering in QCD*, *Phys. Rev. Lett.* **120** (2018) 092001, [1712.02229].

[62] Z. Bern and A. G. Morgan, *Massive loop amplitudes from unitarity*, *Nucl. Phys. B* **467** (1996) 479–509, [hep-ph/9511336].

[63] P. Mastrolia, T. Peraro and A. Primo, *Adaptive Integrand Decomposition in parallel and orthogonal space*, *JHEP* **08** (2016) 164, [1605.03157].

[64] S. Badger, J. Henn, J. Plefka and S. Zoia, *Scattering Amplitudes in Quantum Field Theory*, 2306.05976.

[65] K. G. Chetyrkin and F. V. Tkachov, *Integration by Parts: The Algorithm to Calculate beta Functions in 4 Loops*, *Nucl. Phys.* **B192** (1981) 159–204.

[66] V. Smirnov, *Feynman Integral Calculus*. Springer, 2006, 10.1007/3540306110.

[67] S. Weinzierl, *Feynman Integrals*. 1, 2022, 10.1007/978-3-030-99558-4.

[68] R. N. Lee, *Group structure of the integration-by-part identities and its application to the reduction of multiloop integrals*, *JHEP* **07** (2008) 031, [0804.3008].

[69] S. Laporta, *High precision calculation of multiloop Feynman integrals by difference equations*, *Int. J. Mod. Phys.* **A15** (2000) 5087–5159, [hep-ph/0102033].

[70] C. Anastasiou and A. Lazopoulos, *Automatic integral reduction for higher order perturbative calculations*, *JHEP* **07** (2004) 046, [hep-ph/0404258].

[71] R. N. Lee, *LiteRed 1.4: a powerful tool for reduction of multiloop integrals*, *J. Phys. Conf. Ser.* **523** (2014) 012059, [1310.1145].

[72] A. V. Smirnov, *Algorithm FIRE – Feynman Integral REduction*, *JHEP* **10** (2008) 107, [0807.3243].

[73] A. V. Smirnov and F. S. Chuharev, *FIRE6: Feynman Integral REduction with Modular Arithmetic*, *Comput. Phys. Commun.* **247** (2020) 106877, [1901.07808].

[74] P. Maierhöfer, J. Usovitsch and P. Uwer, *Kira - A Feynman integral reduction program*, *Comput. Phys. Commun.* **230** (2018) 99–112, [1705.05610].

[75] J. Klappert, F. Lange, P. Maierhöfer and J. Usovitsch, *Integral reduction with Kira 2.0 and finite field methods*, *Comput. Phys. Commun.* **266** (2021) 108024, [2008.06494].

[76] C. Studerus, *Reduze-Feynman Integral Reduction in C++*, *Comput. Phys. Commun.* **181** (2010) 1293–1300, [0912.2546].

[77] A. von Manteuffel and C. Studerus, *Reduze 2 - Distributed Feynman Integral Reduction*, 1201.4330.

[78] G. Barucchi and G. Ponzano, *Differential equations for oneloop generalized Feynman integrals*, *Journal of Mathematical Physics* **14** (11, 2003) 396–401, [https://pubs.aip.org/aip/jmp/article-pdf/14/3/396/10964093/396_1_online.pdf].

[79] V. A. Golubeva, *Some problems in the analytic theory of feynman integrals*, *Russian Mathematical Surveys* **31** (apr, 1976) 139.

[80] A. V. Kotikov, *Differential equations method: New technique for massive Feynman diagrams calculation*, *Phys. Lett. B* **254** (1991) 158–164.

[81] A. Kotikov, *Differential equations method: the calculation of vertex-type feynman diagrams*, *Physics Letters B* **259** (1991) 314–322.

[82] E. Remiddi, *Differential equations for Feynman graph amplitudes*, *Nuovo Cim. A* **110** (1997) 1435–1452, [hep-th/9711188].

[83] T. Gehrmann and E. Remiddi, *Differential equations for two loop four point functions*, *Nucl. Phys. B* **580** (2000) 485–518, [hep-ph/9912329].

[84] J. M. Henn, *Multiloop integrals in dimensional regularization made simple*, *Phys. Rev. Lett.* **110** (2013) 251601, [1304.1806].

[85] O. Gituliar and V. Magerya, *Fuchsia: a tool for reducing differential equations for Feynman master integrals to epsilon form*, *Comput. Phys. Commun.* **219** (2017) 329–338, [1701.04269].

[86] R. N. Lee, *Libra: A package for transformation of differential systems for multiloop integrals*, *Comput. Phys. Commun.* **267** (2021) 108058, [2012.00279].

[87] C. Dlapa, J. Henn and K. Yan, *Deriving canonical differential equations for Feynman integrals from a single uniform weight integral*, *JHEP* **05** (2020) 025, [2002.02340].

[88] C. Meyer, *Algorithmic transformation of multi-loop Feynman integrals to a canonical basis*, other thesis, Humboldt U., Berlin, 1, 2018. 10.18452/18763.

[89] C. Dlapa, *Algorithms and techniques for finding canonical differential equations of Feynman integrals*, Ph.D. thesis, Munich U., 2022. 10.5282/edoc.29769.

[90] K.-T. Chen, *Iterated path integrals*, *Bull. Am. Math. Soc.* **83** (1977) 831–879.

[91] F. Brown, *Iterated integrals in quantum field theory*, in *6th Summer School on Geometric and Topological Methods for Quantum Field Theory*, 2013, DOI.

[92] S. Abreu, R. Britto and C. Duhr, *The SAGEX review on scattering amplitudes Chapter 3: Mathematical structures in Feynman integrals*, *J. Phys. A* **55** (2022) 443004, [2203.13014].

[93] J. M. Henn, *Lectures on differential equations for Feynman integrals*, *J. Phys. A* **48** (2015) 153001, [1412.2296].

[94] A. B. Goncharov, *Multiple polylogarithms and mixed Tate motives*, *arXiv Mathematics e-prints* (Mar., 2001) math/0103059, [math/0103059].

[95] A. B. Goncharov, *Multiple polylogarithms, cyclotomy and modular complexes*, *arXiv e-prints* (May, 2011) arXiv:1105.2076, [1105.2076].

[96] J. Vollinga and S. Weinzierl, *Numerical evaluation of multiple polylogarithms*, *Comput. Phys. Commun.* **167** (2005) 177, [hep-ph/0410259].

[97] A. Primo and L. Tancredi, *On the maximal cut of feynman integrals and the solution of their differential equations*, *Nuclear Physics B* **916** (Mar, 2017) 94116.

[98] S. Abreu, H. Ita, F. Moriello, B. Page, W. Tschernow and M. Zeng, *Two-Loop Integrals for Planar Five-Point One-Mass Processes*, *JHEP* **11** (2020) 117, [2005.04195].

[99] S. Abreu, H. Ita, B. Page and W. Tschernow, *Two-Loop Hexa-Box Integrals for Non-Planar Five-Point One-Mass Processes*, 2107.14180.

[100] J. Broedel, C. Duhr, F. Dulat and L. Tancredi, *Elliptic polylogarithms and iterated integrals on elliptic curves. Part I: general formalism*, *JHEP* **05** (2018) 093, [1712.07089].

[101] J. Broedel, C. Duhr, F. Dulat and L. Tancredi, *Elliptic polylogarithms and iterated integrals on elliptic curves II: an application to the sunrise integral*, *Phys. Rev. D* **97** (2018) 116009, [1712.07095].

[102] L. Adams and S. Weinzierl, *Feynman integrals and iterated integrals of modular forms*, *Commun. Num. Theor. Phys.* **12** (2018) 193–251, [1704.08895].

[103] J. Broedel, C. Duhr, F. Dulat, B. Penante and L. Tancredi, *Elliptic Feynman integrals and pure functions*, *JHEP* **01** (2019) 023, [1809.10698].

[104] L. Adams and S. Weinzierl, *The ε-form of the differential equations for Feynman integrals in the elliptic case*, *Phys. Lett. B* **781** (2018) 270–278, [1802.05020].

[105] M. Walden and S. Weinzierl, *Numerical evaluation of iterated integrals related to elliptic Feynman integrals*, *Comput. Phys. Commun.* **265** (2021) 108020, [2010.05271].

[106] R. Bonciani, V. Del Duca, H. Frellesvig, J. M. Henn, F. Moriello and V. A. Smirnov, *Two-loop planar master integrals for Higgs→ 3 partons with full heavy-quark mass dependence*, *JHEP* **12** (2016) 096, [1609.06685].

[107] R. Bonciani, V. Del Duca, H. Frellesvig, J. M. Henn, M. Hidding, L. Maestri et al., *Evaluating a family of two-loop non-planar master integrals for Higgs + jet production with full heavy-quark mass dependence*, *JHEP* **01** (2020) 132, [1907.13156].

[108] H. Frellesvig, M. Hidding, L. Maestri, F. Moriello and G. Salvatori, *The complete set of two-loop master integrals for Higgs + jet production in QCD*, *JHEP* **06** (2020) 093, [1911.06308].

[109] C. Duhr, *Mathematical aspects of scattering amplitudes*, in *Theoretical Advanced Study Institute in Elementary Particle Physics: Journeys Through the Precision Frontier: Amplitudes for Colliders*, pp. 419–476, 2015, 1411.7538, DOI.

[110] T. Gehrmann, J. Henn and N. Lo Presti, *Analytic form of the two-loop planar five-gluon all-plus-helicity amplitude in QCD*, *Phys. Rev. Lett.* **116** (2016) 062001, [1511.05409].

[111] C. G. Papadopoulos, D. Tommasini and C. Wever, *The Pentabox Master Integrals with the Simplified Differential Equations approach*, *JHEP* **04** (2016) 078, [1511.09404].

[112] T. Gehrmann, J. Henn and N. Lo Presti, *Pentagon functions for massless planar scattering amplitudes*, *JHEP* **10** (2018) 103, [1807.09812].

[113] S. Abreu, L. J. Dixon, E. Herrmann, B. Page and M. Zeng, *The two-loop five-point amplitude in $\mathcal{N} = 4$ super-Yang-Mills theory*, *Phys. Rev. Lett.* **122** (2019) 121603, [1812.08941].

[114] D. Chicherin and V. Sotnikov, *Pentagon Functions for Scattering of Five Massless Particles*, *JHEP* **12** (2020) 167, [2009.07803].

[115] D. Chicherin, T. Gehrmann, J. Henn, N. Lo Presti, V. Mitev and P. Wasser, *Analytic result for the nonplanar hexa-box integrals*, *JHEP* **03** (2019) 042, [1809.06240].

[116] D. Chicherin, J. Henn and V. Mitev, *Bootstrapping pentagon functions*, *JHEP* **05** (2018) 164, [1712.09610].

[117] D. Chicherin, J. M. Henn and E. Sokatchev, *Scattering Amplitudes from Superconformal Ward Identities*, *Phys. Rev. Lett.* **121** (2018) 021602, [1804.03571].

[118] D. Chicherin, J. M. Henn and E. Sokatchev, *Implications of nonplanar dual conformal symmetry*, *JHEP* **09** (2018) 012, [1807.06321].

[119] S. Abreu, B. Page and M. Zeng, *Differential equations from unitarity cuts: nonplanar hexa-box integrals*, *JHEP* **01** (2019) 006, [1807.11522].

[120] D. Chicherin, T. Gehrmann, J. Henn, P. Wasser, Y. Zhang and S. Zoia, *All Master Integrals for Three-Jet Production at Next-to-Next-to-Leading Order*, *Phys. Rev. Lett.* **123** (2019) 041603, [1812.11160].

[121] D. Chicherin, V. Sotnikov and S. Zoia, *Pentagon functions for one-mass planar scattering amplitudes*, *JHEP* **01** (2022) 096, [2110.10111].

[122] D. D. Canko, C. G. Papadopoulos and N. Syrrakos, *Analytic representation of all planar two-loop five-point Master Integrals with one off-shell leg*, *JHEP* **01** (2021) 199, [2009.13917].

[123] A. Kardos, C. G. Papadopoulos, A. V. Smirnov, N. Syrrakos and C. Wever, *Two-loop non-planar hexa-box integrals with one massive leg*, 2201.07509.

[124] C. G. Papadopoulos and C. Wever, *Internal Reduction method for computing Feynman Integrals*, *JHEP* **02** (2020) 112, [1910.06275].

[125] S. Abreu, D. Chicherin, H. Ita, B. Page, V. Sotnikov, W. Tschernow et al., *All Two-Loop Feynman Integrals for Five-Point One-Mass Scattering*, 2306.15431.

[126] T. Binoth and G. Heinrich, *An automatized algorithm to compute infrared divergent multiloop integrals*, *Nucl. Phys. B* **585** (2000) 741–759, [hep-ph/0004013].

[127] T. Binoth and G. Heinrich, *Numerical evaluation of multiloop integrals by sector decomposition*, *Nucl. Phys. B* **680** (2004) 375–388, [hep-ph/0305234].

[128] C. Bogner and S. Weinzierl, *Resolution of singularities for multi-loop integrals*, *Comput. Phys. Commun.* **178** (2008) 596–610, [0709.4092].

[129] A. V. Smirnov, *FIESTA4: Optimized Feynman integral calculations with GPU support*, *Comput. Phys. Commun.* **204** (2016) 189–199, [1511.03614].

[130] S. Borowka, G. Heinrich, S. P. Jones, M. Kerner, J. Schlenk and T. Zirke, *SecDec-3.0: numerical evaluation of multi-scale integrals beyond one loop*, *Comput. Phys. Commun.* **196** (2015) 470–491, [1502.06595].

[131] G. Heinrich, S. P. Jones, M. Kerner, V. Magerya, A. Olsson and J. Schlenk, *Numerical Scattering Amplitudes with pySecDec*, 2305.19768.

[132] B. Jantzen, *Foundation and generalization of the expansion by regions*, *JHEP* **12** (2011) 076, [1111.2589].

[133] M. Beneke and V. A. Smirnov, *Asymptotic expansion of Feynman integrals near threshold*, *Nucl. Phys. B* **522** (1998) 321–344, [hep-ph/9711391].

[134] V. A. Smirnov and E. R. Rakhmetov, *The Strategy of regions for asymptotic expansion of two loop vertex Feynman diagrams*, *Theor. Math. Phys.* **120** (1999) 870–875, [hep-ph/9812529].

[135] V. A. Smirnov, *Problems of the strategy of regions*, *Phys. Lett. B* **465** (1999) 226–234, [hep-ph/9907471].

[136] A. Pak and A. Smirnov, *Geometric approach to asymptotic expansion of Feynman integrals*, *Eur. Phys. J. C* **71** (2011) 1626, [1011.4863].

[137] B. Ananthanarayan, A. Pal, S. Ramanan and R. Sarkar, *Unveiling Regions in multi-scale Feynman Integrals using Singularities and Power Geometry*, *Eur. Phys. J. C* **79** (2019) 57, [1810.06270].

[138] B. Ananthanarayan, A. B. Das and R. Sarkar, *Asymptotic analysis of Feynman diagrams and their maximal cuts*, *Eur. Phys. J. C* **80** (2020) 1131, [2003.02451].

[139] B. Jantzen, A. V. Smirnov and V. A. Smirnov, *Expansion by regions: revealing potential and Glauber regions automatically*, *Eur. Phys. J. C* **72** (2012) 2139, [1206.0546].

[140] G. Heinrich, S. Jahn, S. P. Jones, M. Kerner, F. Langer, V. Magerya et al., *Expansion by regions with pySecDec*, *Comput. Phys. Commun.* **273** (2022) 108267, [2108.10807].

[141] F. Moriello, *Generalised power series expansions for the elliptic planar families of Higgs + jet production at two loops*, *JHEP* **01** (2020) 150, [1907.13234].

[142] M. Hidding, *DiffExp, a Mathematica package for computing Feynman integrals in terms of one-dimensional series expansions*, *Comput. Phys. Commun.* **269** (2021) 108125, [2006.05510].

[143] T. Armadillo, R. Bonciani, S. Devoto, N. Rana and A. Vicini, *Evaluation of Feynman integrals with arbitrary complex masses via series expansions*, *Comput. Phys. Commun.* **282** (2023) 108545, [2205.03345].

[144] X. Liu, Y.-Q. Ma and C.-Y. Wang, *A Systematic and Efficient Method to Compute Multi-loop Master Integrals*, *Phys. Lett. B* **779** (2018) 353–357, [1711.09572].

[145] X. Liu and Y.-Q. Ma, *Multiloop corrections for collider processes using auxiliary mass flow*, *Phys. Rev. D* **105** (2022) L051503, [2107.01864].

[146] X. Liu and Y.-Q. Ma, *AMFlow: A Mathematica package for Feynman integrals computation via auxiliary mass flow*, *Comput. Phys. Commun.* **283** (2023) 108565, [2201.11669].

[147] D. Pagani, H.-S. Shao and M. Zaro, *RIP $Hb\bar{b}$: how other Higgs production modes conspire to kill a rare signal at the LHC*, *JHEP* **11** (2020) 036, [2005.10277].

[148] C. Grojean, A. Paul and Z. Qian, *Resurrecting $b\bar{b}h$ with kinematic shapes*, *JHEP* **04** (2021) 139, [2011.13945].

[149] P. Konar, B. Mukhopadhyaya, R. Rahaman and R. K. Singh, *Probing non-standard $b\bar{b}h$ interaction at the LHC at $\sqrt{s} = 13$ TeV*, *Phys. Lett. B* **818** (2021) 136358, [2101.10683].

[150] C. Balazs, J. L. Diaz-Cruz, H. J. He, T. M. P. Tait and C. P. Yuan, *Probing Higgs bosons with large bottom Yukawa coupling at hadron colliders*, *Phys. Rev. D* **59** (1999) 055016, [hep-ph/9807349].

[151] S. Dawson, C. B. Jackson, L. Reina and D. Wackeroth, *Higgs production in association with bottom quarks at hadron colliders*, *Mod. Phys. Lett. A* **21** (2006) 89–110, [hep-ph/0508293].

[152] M. Cepeda et al., *Report from Working Group 2: Higgs Physics at the HL-LHC and HE-LHC*, *CERN Yellow Rep. Monogr.* **7** (2019) 221–584, [1902.00134].

[153] F. Maltoni, G. Ridolfi and M. Ubiali, *b-initiated processes at the LHC: a reappraisal*, *JHEP* **07** (2012) 022, [1203.6393].

[154] D. Dicus, T. Stelzer, Z. Sullivan and S. Willenbrock, *Higgs boson production in association with bottom quarks at next-to-leading order*, *Phys. Rev. D* **59** (1999) 094016, [hep-ph/9811492].

[155] C. Balazs, H.-J. He and C. P. Yuan, *QCD corrections to scalar production via heavy quark fusion at hadron colliders*, *Phys. Rev. D* **60** (1999) 114001, [hep-ph/9812263].

[156] F. Maltoni, Z. Sullivan and S. Willenbrock, *Higgs-Boson Production via Bottom-Quark Fusion*, *Phys. Rev. D* **67** (2003) 093005, [hep-ph/0301033].

[157] R. V. Harlander, K. J. Ozeren and M. Wiesemann, *Higgs plus jet production in bottom quark annihilation at next-to-leading order*, *Phys. Lett. B* **693** (2010) 269–273, [1007.5411].

[158] S. Bühler, F. Herzog, A. Lazopoulos and R. Müller, *The fully differential hadronic production of a Higgs boson via bottom quark fusion at NNLO*, *JHEP* **07** (2012) 115, [1204.4415].

[159] R. V. Harlander, S. Liebler and H. Mantler, *SusHi: A program for the calculation of Higgs production in gluon fusion and bottom-quark annihilation in the Standard Model and the MSSM*, *Comput. Phys. Commun.* **184** (2013) 1605–1617, [1212.3249].

[160] A. H. Ajjath, P. Banerjee, A. Chakraborty, P. K. Dhani, P. Mukherjee, N. Rana et al., *NNLO QCD⊕QED corrections to Higgs production in bottom quark annihilation*, *Phys. Rev. D* **100** (2019) 114016, [1906.09028].

[161] C. Duhr, F. Dulat and B. Mistlberger, *Higgs Boson Production in Bottom-Quark Fusion to Third Order in the Strong Coupling*, *Phys. Rev. Lett.* **125** (2020) 051804, [1904.09990].

[162] R. Mondini and C. Williams, *Bottom-induced contributions to Higgs plus jet at next-to-next-to-leading order*, *JHEP* **05** (2021) 045, [2102.05487].

[163] J. M. Campbell, R. K. Ellis, F. Maltoni and S. Willenbrock, *Higgs-Boson Production in Association with a Single Bottom Quark*, *Phys. Rev. D* **67** (2003) 095002, [hep-ph/0204093].

[164] S. Dawson and P. Jaiswal, *Weak Corrections to Associated Higgs-Bottom Quark Production*, *Phys. Rev. D* **81** (2010) 073008, [1002.2672].

[165] S. Dawson, C. B. Jackson and P. Jaiswal, *SUSY QCD Corrections to Higgs-b Production : Is the Δ_b Approximation Accurate?*, *Phys. Rev. D* **83** (2011) 115007, [1104.1631].

[166] S. Dittmaier, M. Krämer and M. Spira, *Higgs radiation off bottom quarks at the Tevatron and the CERN LHC*, *Phys. Rev. D* **70** (2004) 074010, [hep-ph/0309204].

[167] S. Dawson, C. B. Jackson, L. Reina and D. Wackeroth, *Exclusive Higgs boson production with bottom quarks at hadron colliders*, *Phys. Rev. D* **69** (2004) 074027, [hep-ph/0311067].

[168] S. Dawson, C. B. Jackson, L. Reina and D. Wackeroth, *Higgs boson production with one bottom quark jet at hadron colliders*, *Phys. Rev. Lett.* **94** (2005) 031802, [hep-ph/0408077].

[169] M. Wiesemann, R. Frederix, S. Frixione, V. Hirschi, F. Maltoni and P. Torrielli, *Higgs production in association with bottom quarks*, *JHEP* **02** (2015) 132, [1409.5301].

[170] B. Jager, L. Reina and D. Wackeroth, *Higgs boson production in association with b jets in the POWHEG BOX*, *Phys. Rev. D* **93** (2016) 014030, [1509.05843].

[171] N. Deutschmann, F. Maltoni, M. Wiesemann and M. Zaro, *Top-Yukawa contributions to bbH production at the LHC*, *JHEP* **07** (2019) 054, [1808.01660].

[172] N. Liu, L. Wu, P. Wu and J. M. Yang, *Complete one-loop effects of SUSY QCD in $b\bar{b}h$ production at the LHC under current experimental constraints*, *JHEP* **01** (2013) 161, [1208.3413].

[173] S. Dittmaier, P. Häfliger, M. Krämer, M. Spira and M. Walser, *Neutral MSSM Higgs-boson production with heavy quarks: NLO supersymmetric QCD corrections*, *Phys. Rev. D* **90** (2014) 035010, [1406.5307].

[174] R. Harlander, M. Kramer and M. Schumacher, *Bottom-quark associated Higgs-boson production: reconciling the four- and five-flavour scheme approach*, 1112.3478.

[175] M. Bonvini, A. S. Papanastasiou and F. J. Tackmann, *Resummation and matching of b-quark mass effects in $b\bar{b}H$ production*, *JHEP* **11** (2015) 196, [1508.03288].

[176] S. Forte, D. Napoletano and M. Ubiali, *Higgs production in bottom-quark fusion in a matched scheme*, *Phys. Lett. B* **751** (2015) 331–337, [1508.01529].

[177] S. Forte, D. Napoletano and M. Ubiali, *Higgs production in bottom-quark fusion: matching beyond leading order*, *Phys. Lett. B* **763** (2016) 190–196, [1607.00389].

[178] C. Duhr, F. Dulat, V. Hirschi and B. Mistlberger, *Higgs production in bottom quark fusion: matching the 4- and 5-flavour schemes to third order in the strong coupling*, *JHEP* **08** (2020) 017, [2004.04752].

[179] F. Krauss and D. Napoletano, *Towards a fully massive five-flavor scheme*, *Phys. Rev. D* **98** (2018) 096002, [1712.06832].

[180] D. Figueroa, S. Honeywell, S. Quackenbush, L. Reina, C. Reuschle and D. Wackeroth, *Electroweak and QCD corrections to Z-boson production with one b jet in a massive five-flavor scheme*, *Phys. Rev. D* **98** (2018) 093002, [1805.01353].

[181] A. Banfi, G. P. Salam and G. Zanderighi, *Infrared safe definition of jet flavor*, *Eur. Phys. J. C* **47** (2006) 113–124, [hep-ph/0601139].

[182] S. Badger, H. B. Hartanto and S. Zoia, *Two-Loop QCD Corrections to $Wb\bar{b}$ Production at Hadron Colliders*, *Phys. Rev. Lett.* **127** (2021) 012001, [2102.02516].

[183] F. Moriello, *Generalised power series expansions for the elliptic planar families of Higgs + jet production at two loops*, *JHEP* **01** (2020) 150, [1907.13234].

[184] J. Kuipers, T. Ueda, J. A. M. Vermaseren and J. Vollinga, *FORM version 4.0*, *Comput. Phys. Commun.* **184** (2013) 1453–1467, [1203.6543].

[185] B. Ruijl, T. Ueda and J. Vermaseren, *FORM version 4.2*, 1707.06453.

[186] G. Cullen, M. Koch-Janusz and T. Reiter, *Spinney: A Form Library for Helicity Spinors*, *Comput. Phys. Commun.* **182** (2011) 2368–2387, [1008.0803].

[187] S. Badger, C. Brønnum-Hansen, D. Chicherin, T. Gehrmann, H. B. Hartanto, J. Henn et al., *Virtual QCD corrections to gluon-initiated diphoton plus jet production at hadron colliders*, 2106.08664.

[188] L. E. K., *Factorization of rational functions of several variables into partial fractions*, *Izvestiya Vysshikh Uchebnykh Zavedenii. Matematika* **47** (1978) .

[189] A. Raichev, *Leinartas's partial fraction decomposition*, *arXiv e-prints* (June, 2012) arXiv:1206.4740, [1206.4740].

[190] S. Abreu, J. Dormans, F. Febres Cordero, H. Ita, B. Page and V. Sotnikov, *Analytic Form of the Planar Two-Loop Five-Parton Scattering Amplitudes in QCD*, *JHEP* **05** (2019) 084, [1904.00945].

[191] J. Boehm, M. Wittmann, Z. Wu, Y. Xu and Y. Zhang, *IBP reduction coefficients made simple*, *JHEP* **12** (2020) 054, [2008.13194].

[192] M. Heller and A. von Manteuffel, *MultivariateApart: Generalized Partial Fractions*, 2101.08283.

[193] S. Badger, C. Brønnum-Hansen, H. B. Hartanto and T. Peraro, *Analytic helicity amplitudes for two-loop five-gluon scattering: the single-minus case*, *JHEP* **01** (2019) 186, [1811.11699].

[194] S. Abreu, J. Dormans, F. Febres Cordero, H. Ita and B. Page, *Analytic Form of Planar Two-Loop Five-Gluon Scattering Amplitudes in QCD*, *Phys. Rev. Lett.* **122** (2019) 082002, [1812.04586].

[195] D. Chicherin, T. Gehrmann, J. Henn, P. Wasser, Y. Zhang and S. Zoia, *Analytic result for a two-loop five-particle amplitude*, *Phys. Rev. Lett.* **122** (2019) 121602, [1812.11057].

[196] D. Chicherin, T. Gehrmann, J. M. Henn, P. Wasser, Y. Zhang and S. Zoia, *The two-loop five-particle amplitude in $\mathcal{N} = 8$ supergravity*, *JHEP* **03** (2019) 115, [1901.05932].

[197] S. Abreu, L. J. Dixon, E. Herrmann, B. Page and M. Zeng, *The two-loop five-point amplitude in $\mathcal{N} = 8$ supergravity*, *JHEP* **03** (2019) 123, [1901.08563].

[198] S. Badger, D. Chicherin, T. Gehrmann, G. Heinrich, J. Henn, T. Peraro et al., *Analytic form of the full two-loop five-gluon all-plus helicity amplitude*, *Phys. Rev. Lett.* **123** (2019) 071601, [1905.03733].

[199] S. Caron-Huot, D. Chicherin, J. Henn, Y. Zhang and S. Zoia, *Multi-Regge Limit of the Two-Loop Five-Point Amplitudes in $\mathcal{N} = 4$ Super Yang-Mills and $\mathcal{N} = 8$ Supergravity*, *JHEP* **10** (2020) 188, [2003.03120].

[200] S. Abreu, B. Page, E. Pascual and V. Sotnikov, *Leading-Color Two-Loop QCD Corrections for Three-Photon Production at Hadron Colliders*, 2010.15834.

[201] H. A. Chawdhry, M. Czakon, A. Mitov and R. Poncelet, *Two-loop leading-color helicity amplitudes for three-photon production at the LHC*, 2012.13553.

[202] D. Chicherin, J. M. Henn and G. Papathanasiou, *Cluster algebras for Feynman integrals*, *Phys. Rev. Lett.* **126** (2021) 091603, [2012.12285].

[203] M. Becchetti, R. Bonciani, V. Del Duca, V. Hirschi, F. Moriello and A. Schweitzer, *Next-to-leading order corrections to light-quark mixed QCD-EW contributions to Higgs boson production*, *Phys. Rev. D* **103** (2021) 054037, [2010.09451].

[204] R. Bonciani, L. Buonocore, M. Grazzini, S. Kallweit, N. Rana, F. Tramontano et al., *Mixed strong−electroweak corrections to the Drell−Yan process*, 2106.11953.

[205] E. Remiddi and J. A. M. Vermaseren, *Harmonic polylogarithms*, *Int. J. Mod. Phys. A* **15** (2000) 725–754, [hep-ph/9905237].

[206] N. Syrrakos, *Pentagon integrals to arbitrary order in the dimensional regulator*, *JHEP* **06** (2021) 037, [2012.10635].

[207] J. Alwall, R. Frederix, S. Frixione, V. Hirschi, F. Maltoni, O. Mattelaer et al., *The automated computation of tree-level and next-to-leading order differential cross sections, and their matching to parton shower simulations*, *JHEP* **07** (2014) 079, [1405.0301].

[208] CMS collaboration, S. Chatrchyan et al., *Measurement of $W\gamma$ and $Z\gamma$ production in pp collisions at $\sqrt{s} = 7$ TeV*, *Phys. Lett. B* **701** (2011) 535–555, [1105.2758].

[209] ATLAS collaboration, G. Aad et al., *Measurement of Wgamma and Zgamma production in proton-proton collisions at $\sqrt{s} = 7$ TeV with the ATLAS Detector*, *JHEP* **09** (2011) 072, [1106.1592].

[210] ATLAS collaboration, G. Aad et al., *Measurement of $W\gamma$ and $Z\gamma$ production cross sections in pp collisions at $\sqrt{s} = 7$ TeV and limits on anomalous triple gauge couplings with the ATLAS detector*, *Phys. Lett. B* **717** (2012) 49–69, [1205.2531].

[211] ATLAS collaboration, G. Aad et al., *Measurements of $W\gamma$ and $Z\gamma$ production in pp collisions at $\sqrt{s}$=7 TeV with the ATLAS detector at the LHC*, *Phys. Rev. D* **87** (2013) 112003, [1302.1283].

[212] CMS collaboration, S. Chatrchyan et al., *Measurement of the $W\gamma$ and $Z\gamma$ Inclusive Cross Sections in pp Collisions at $\sqrt{s} = 7$ TeV and Limits on Anomalous Triple Gauge Boson Couplings*, *Phys. Rev. D* **89** (2014) 092005, [1308.6832].

[213] CMS collaboration, A. M. Sirunyan et al., *Measurement of the $W\gamma$ Production Cross Section in Proton-Proton Collisions at $\sqrt{s}$=13 TeV and Constraints on Effective Field Theory Coefficients*, *Phys. Rev. Lett.* **126** (2021) 252002, [2102.02283].

[214] T. Gehrmann and L. Tancredi, *Two-loop QCD helicity amplitudes for $q\bar{q} \to W^{\pm}\gamma$ and $q\bar{q} \to Z^0\gamma$*, *JHEP* **02** (2012) 004, [1112.1531].

[215] M. Grazzini, S. Kallweit and D. Rathlev, *$W\gamma$ and $Z\gamma$ production at the LHC in NNLO QCD*, *JHEP* **07** (2015) 085, [1504.01330].

[216] J. M. Campbell, G. De Laurentis, R. K. Ellis and S. Seth, *The $pp \to W(\to l\nu) + \gamma$ process at next-to-next-to-leading order*, *JHEP* **07** (2021) 079, [2105.00954].

[217] E. Accomando, A. Denner and C. Meier, *Electroweak corrections to $W\gamma$ and $Z\gamma$ production at the LHC*, *Eur. Phys. J. C* **47** (2006) 125–146, [hep-ph/0509234].

[218] A. Denner, S. Dittmaier, M. Hecht and C. Pasold, *NLO QCD and electroweak corrections to $W + \gamma$ production with leptonic W-boson decays*, *JHEP* **04** (2015) 018, [1412.7421].

[219] M. Grazzini, S. Kallweit, J. M. Lindert, S. Pozzorini and M. Wiesemann, *NNLO QCD + NLO EW with Matrix+OpenLoops: precise predictions for vector-boson pair production*, *JHEP* **02** (2020) 087, [1912.00068].

[220] S. Catani and M. Grazzini, *An NNLO subtraction formalism in hadron collisions and its application to Higgs boson production at the LHC*, *Phys. Rev. Lett.* **98** (2007) 222002, [hep-ph/0703012].

[221] R. Boughezal, C. Focke, W. Giele, X. Liu and F. Petriello, *Higgs boson production in association with a jet at NNLO using jettiness subtraction*, *Phys. Lett. B* **748** (2015) 5–8, [1505.03893].

[222] J. Gaunt, M. Stahlhofen, F. J. Tackmann and J. R. Walsh, *N-jettiness Subtractions for NNLO QCD Calculations*, *JHEP* **09** (2015) 058, [1505.04794].

[223] M. Grazzini, S. Kallweit and M. Wiesemann, *Fully differential NNLO computations with MATRIX*, *Eur. Phys. J. C* **78** (2018) 537, [1711.06631].

[224] R. Boughezal, J. M. Campbell, R. K. Ellis, C. Focke, W. Giele, X. Liu et al., *Color singlet production at NNLO in MCFM*, *Eur. Phys. J. C* **77** (2017) 7, [1605.08011].

[225] T. Cridge, M. A. Lim and R. Nagar, *$W\gamma$ production at NNLO+PS accuracy in GENEVA*, 2105.13214.

[226] CMS collaboration, A. Tumasyan et al., *Measurement of $W^{\pm}\gamma$ differential cross sections in proton-proton collisions at $\sqrt{s}$ = 13 TeV and effective field theory constraints*, 2111.13948.

[227] T. Peraro and L. Tancredi, *Physical projectors for multi-leg helicity amplitudes*, *JHEP* **07** (2019) 114, [1906.03298].

[228] T. Peraro and L. Tancredi, *Tensor decomposition for bosonic and fermionic scattering amplitudes*, *Phys. Rev. D* **103** (2021) 054042, [2012.00820].

[229] L. W. Garland, T. Gehrmann, E. W. N. Glover, A. Koukoutsakis and E. Remiddi, *Two loop QCD helicity amplitudes for $e^+e^- \to$ three jets*, *Nucl. Phys. B* **642** (2002) 227–262, [hep-ph/0206067].

[230] S. Laporta, *High precision calculation of multiloop Feynman integrals by difference equations*, *Int. J. Mod. Phys. A* **15** (2000) 5087–5159, [hep-ph/0102033].

[231] A. Pak, *The Toolbox of modern multi-loop calculations: novel analytic and semi-analytic techniques*, *J. Phys. Conf. Ser.* **368** (2012) 012049, [1111.0868].

[232] D. Bendle, J. Boehm, M. Heymann, R. Ma, M. Rahn, L. Ristau et al., *Two-loop five-point integration-by-parts relations in a usable form*, 2104.06866.

[233] S. Abreu, F. F. Cordero, H. Ita, M. Klinkert, B. Page and V. Sotnikov, *Leading-Color Two-Loop Amplitudes for Four Partons and a W Boson in QCD*, 2110.07541.

[234] W. Decker, G.-M. Greuel, G. Pfister and H. Schönemann, "SINGULAR 4-2-1 — A computer algebra system for polynomial computations." http://www.singular.uni-kl.de, 2021.

[235] H. B. Hartanto, S. Badger, C. Brønnum-Hansen and T. Peraro, *A numerical evaluation of planar two-loop helicity amplitudes for a W-boson plus four partons*, *JHEP* **09** (2019) 119, [1906.11862].

[236] S. Badger, E. Chaubey, H. B. Hartanto and R. Marzucca, *Two-loop leading colour QCD helicity amplitudes for top quark pair production in the gluon fusion channel*, *JHEP* **06** (2021) 163, [2102.13450].

[237] A. Tricoli, M. Schönherr and P. Azzurri, *Vector Bosons and Jets in Proton Collisions*, *Rev. Mod. Phys.* **93** (2021) 025007, [2012.13967].

[238] A. Gehrmann-De Ridder, T. Gehrmann, E. W. N. Glover, A. Huss and D. M. Walker, *Next-to-Next-to-Leading-Order QCD Corrections to the Transverse Momentum Distribution of Weak Gauge Bosons*, *Phys. Rev. Lett.* **120** (2018) 122001, [1712.07543].

[239] R. Boughezal, C. Focke, X. Liu and F. Petriello, *W-boson production in association with a jet at next-to-next-to-leading order in perturbative QCD*, *Phys. Rev. Lett.* **115** (2015) 062002, [1504.02131].

[240] R. Boughezal, X. Liu and F. Petriello, *W-boson plus jet differential distributions at NNLO in QCD*, *Phys. Rev. D* **94** (2016) 113009, [1602.06965].

[241] J. M. Lindert et al., *Precise predictions for V+ jets dark matter backgrounds*, *Eur. Phys. J. C* **77** (2017) 829, [1705.04664].

[242] G. Abbiendi et al., *Measuring the leading hadronic contribution to the muon g-2 via μe scattering*, *Eur. Phys. J. C* **77** (2017) 139, [1609.08987].

[243] G. Abbiendi, *Status of the MUonE experiment*, *Phys. Scripta* **97** (1, 2022) 054007, [2201.13177].

[244] MUonE collaboration, E. Spedicato, *Status of the MUonE experiment*, *PoS* **EPS-HEP2021** (1, 2022) 642.

[245] R. N. Pilato, *The MUonE experiment*, *Nuovo Cim. C* **45** (7, 2022) 67.

[246] C. M. Carloni Calame, M. Passera, L. Trentadue and G. Venanzoni, *A new approach to evaluate the leading hadronic corrections to the muon g-2*, *Phys. Lett. B* **746** (2015) 325–329, [1504.02228].

[247] E. Balzani, S. Laporta and M. Passera, *Hadronic vacuum polarization contributions to the muon g-2 in the space-like region*, *Phys. Lett. B* **834** (2022) 137462, [2112.05704].

[248] Muon g-2 collaboration, B. Abi et al., *Measurement of the Positive Muon Anomalous Magnetic Moment to 0.46 ppm*, *Phys. Rev. Lett.* **126** (2021) 141801, [2104.03281].

[249] T. Aoyama et al., *The anomalous magnetic moment of the muon in the Standard Model*, *Phys. Rept.* **887** (2020) 1–166, [2006.04822].

[250] S. Borsanyi et al., *Leading hadronic contribution to the muon magnetic moment from lattice QCD*, *Nature* **593** (2021) 51–55, [2002.12347].

[251] P. Banerjee et al., *Theory for muon-electron scattering @ 10 ppm: A report of the MUonE theory initiative*, *Eur. Phys. J. C* **80** (2020) 591, [2004.13663].

[252] E. Budassi and C. L. Del Pio, *High precision calculations for the MUonE experiment*, *PoS* **ICHEP2022** (11, 2022) 796.

[253] M. Alacevich, C. M. Carloni Calame, M. Chiesa, G. Montagna, O. Nicrosini and F. Piccinini, *Muon-electron scattering at NLO*, *JHEP* **02** (2019) 155, [1811.06743].

[254] E. Budassi, C. M. Carloni Calame, M. Chiesa, C. L. Del Pio, S. M. Hasan, G. Montagna et al., *NNLO virtual and real leptonic corrections to muon-electron scattering*, *JHEP* **11** (2021) 098, [2109.14606].

[255] M. Fael and M. Passera, *Muon-Electron Scattering at Next-To-Next-To-Leading Order: The Hadronic Corrections*, *Phys. Rev. Lett.* **122** (2019) 192001, [1901.03106].

[256] M. Fael, *Hadronic corrections to μ-e scattering at NNLO with space-like data*, *JHEP* **02** (2019) 027, [1808.08233].

[257] C. M. Carloni Calame, M. Chiesa, S. M. Hasan, G. Montagna, O. Nicrosini and F. Piccinini, *Towards muon-electron scattering at NNLO*, *JHEP* **11** (2020) 028, [2007.01586].

[258] A. Broggio et al., *Muon-electron scattering at NNLO*, *JHEP* **01** (2023) 112, [2212.06481].

[259] Y. Ulrich, "N^{3}LO kick-off workstop/thinkstart." https://conference.ippp.dur.ac.uk/event/1104/, Durham, Aug, 2022.

[260] M. Fael, F. Lange, K. Schönwald and M. Steinhauser, *Massive Vector Form Factors to Three Loops*, *Phys. Rev. Lett.* **128** (2022) 172003, [2202.05276].

[261] M. Fael, F. Lange, K. Schönwald and M. Steinhauser, *Singlet and nonsinglet three-loop massive form factors*, *Phys. Rev. D* **106** (2022) 034029, [2207.00027].

[262] M. Fael, F. Lange, K. Schönwald and M. Steinhauser, *Massive three-loop form factors: Anomaly contribution*, *Phys. Rev. D* **107** (2023) 094017, [2302.00693].

[263] L. W. Garland, T. Gehrmann, E. W. N. Glover, A. Koukoutsakis and E. Remiddi, *The Two loop QCD matrix element for $e^+e^- \to 3$ jets*, *Nucl. Phys. B* **627** (2002) 107–188, [hep-ph/0112081].

[264] "PrecisionSM database." https://precision-sm.github.io/.

[265] G. Abbiendi et al., *Mini-Proceedings of the STRONG2020 Virtual Workshop on "Space-like and Time-like determination of the Hadronic Leading Order contribution to the Muon $g-2$"*, 1, 2022, 2201.12102.

[266] A. A. Penin, *Two-loop photonic corrections to massive Bhabha scattering*, *Nucl. Phys. B* **734** (2006) 185–202, [hep-ph/0508127].

[267] T. Becher and K. Melnikov, *Two-loop QED corrections to Bhabha scattering*, *JHEP* **06** (2007) 084, [0704.3582].

[268] T. Engel, C. Gnendiger, A. Signer and Y. Ulrich, *Small-mass effects in heavy-to-light form factors*, *JHEP* **02** (2019) 118, [1811.06461].

[269] P. Banerjee, T. Engel, N. Schalch, A. Signer and Y. Ulrich, *Bhabha scattering at NNLO with next-to-soft stabilisation*, *Phys. Lett. B* **820** (2021) 136547, [2106.07469].

[270] T. Engel, A. Signer and Y. Ulrich, *Universal structure of radiative QED amplitudes at one loop*, *JHEP* **04** (2022) 097, [2112.07570].

[271] T. Engel, *The LBK theorem to all orders*, 2304.11689.

[272] T. Engel, A. Signer and Y. Ulrich, *A subtraction scheme for massive QED*, *JHEP* **01** (2020) 085, [1909.10244].

[273] T. Gehrmann and E. Remiddi, *Two loop master integrals for $\gamma^* \to 3$ jets: The Planar topologies*, *Nucl. Phys. B* **601** (2001) 248–286, [hep-ph/0008287].

[274] T. Gehrmann and E. Remiddi, *Two loop master integrals for $\gamma^* \to 3$ jets: The Nonplanar topologies*, *Nucl. Phys. B* **601** (2001) 287–317, [hep-ph/0101124].

[275] T. Gehrmann and E. Remiddi, *Analytic continuation of massless two loop four point functions*, *Nucl. Phys. B* **640** (2002) 379–411, [hep-ph/0207020].

[276] T. Gehrmann, P. Jakubčík, C. C. Mella, N. Syrrakos and L. Tancredi, *Two-loop helicity amplitudes for H+jet production to higher orders in the dimensional regulator*, *JHEP* **04** (2023) 016, [2301.10849].

[277] T. Gehrmann, T. Peraro and L. Tancredi, *Two-loop QCD corrections to the $V \to q\bar{q}g$ helicity amplitudes with axial-vector couplings*, *JHEP* **02** (2023) 041, [2211.13596].

[278] T. Gehrmann, P. Jakubčík, C. C. Mella, N. Syrrakos and L. Tancredi, *Two-loop helicity amplitudes for V+jet production including axial vector couplings to higher orders in ϵ*, 2306.10170.

[279] S. Di Vita, P. Mastrolia, U. Schubert and V. Yundin, *Three-loop master integrals for ladder-box diagrams with one massive leg*, *JHEP* **09** (2014) 148, [1408.3107].

[280] D. D. Canko and N. Syrrakos, *Resummation methods for Master Integrals*, *JHEP* **02** (2021) 080, [2010.06947].

[281] D. D. Canko and N. Syrrakos, *Planar three-loop master integrals for $2 \to 2$ processes with one external massive particle*, *JHEP* **04** (2022) 134, [2112.14275].

[282] J. M. Henn, J. Lim and W. J. Torres Bobadilla, *First look at the evaluation of three-loop non-planar Feynman diagrams for Higgs plus jet production*, *JHEP* **05** (2023) 026, [2302.12776].

[283] S. Badger, M. Czakon, H. B. Hartanto, R. Moodie, T. Peraro, R. Poncelet et al., *Isolated photon production in association with a jet pair through next-to-next-to-leading order in QCD*, 2304.06682.

[284] S. Badger, J. Kryś, R. Moodie and S. Zoia, *Ancillary files for "Lepton-pair scattering with an off-shell and an on-shell photon at two loops in massless QED"*, July, 2023. 10.5281/zenodo.8120540.

[285] P. Banerjee, T. Engel, A. Signer and Y. Ulrich, *QED at NNLO with McMule*, *SciPost Phys.* **9** (2020) 027, [2007.01654].

[286] Y. Ulrich, P. Banerjee, A. Coutinho, T. Engel, A. Gurgone, F. Hagelstein et al., *The mcmule manual*, Feb., 2022. 10.5281/zenodo.6046769.

[287] E. Gardi and L. Magnea, *Infrared singularities in QCD amplitudes*, *Nuovo Cim. C* **32N5-6** (2009) 137–157, [0908.3273].

[288] F. V. Tkachov, *A Theorem on Analytical Calculability of Four Loop Renormalization Group Functions*, *Phys. Lett.* **100B** (1981) 65–68.

[289] G. De Laurentis and B. Page, *Ansätze for scattering amplitudes from p-adic numbers and algebraic geometry*, *JHEP* **12** (2022) 140, [2203.04269].

[290] S. Abreu, G. De Laurentis, H. Ita, M. Klinkert, B. Page and V. Sotnikov, *Two-Loop QCD Corrections for Three-Photon Production at Hadron Colliders*, 2305.17056.

[291] X. Liu, *Reconstruction of rational functions made simple*, 2306.12262.

[292] A. Kotikov, *Differential equations method. new technique for massive feynman diagram calculation*, *Physics Letters B* **254** (1991) 158–164.

[293] A. Kotikov, *Differential equation method. the calculation of n-point feynman diagrams*, *Physics Letters B* **267** (1991) 123–127.

[294] J. Henn, B. Mistlberger, V. A. Smirnov and P. Wasser, *Constructing d-log integrands and computing master integrals for three-loop four-particle scattering*, *JHEP* **04** (2020) 167, [2002.09492].

[295] J. M. Henn, K. Melnikov and V. A. Smirnov, *Two-loop planar master integrals for the production of off-shell vector bosons in hadron collisions*, *JHEP* **05** (2014) 090, [1402.7078].

[296] F. Caola, J. M. Henn, K. Melnikov and V. A. Smirnov, *Non-planar master integrals for the production of two off-shell vector bosons in collisions of massless partons*, *JHEP* **09** (2014) 043, [1404.5590].

[297] D. Gaiotto, J. Maldacena, A. Sever and P. Vieira, *Pulling the straps of polygons*, *JHEP* **12** (2011) 011, [1102.0062].

[298] C. W. Bauer, A. Frink and R. Kreckel, *Introduction to the GiNaC framework for symbolic computation within the C++ programming language*, *J. Symb. Comput.* **33** (2002) 1–12, [cs/0004015].

[299] H. R. P. Ferguson and D. H. Bailey, *A Polynomial Time, Numerically Stable Integer Relation Algorithm*, *RNR Technical Report RNR-91-032* (1992) .

[300] D. E. Radford, *A natural ring basis for the shuffle algebra and an application to group schemes*, *Journal of Algebra* **58** (1979) 432–454.

[301] C. Duhr and F. Dulat, *PolyLogTools — polylogs for the masses*, *JHEP* **08** (2019) 135, [1904.07279].

[302] Y. Ulrich, *QED at NNLO and beyond for precision experiments*, *RADCOR 2023 – 16th International Symposium on Radiative Corrections: Applications of Quantum Field Theory to Phenomenology* (2023) .

[303] L. Naterop, A. Signer and Y. Ulrich, *handyG —Rapid numerical evaluation of generalised polylogarithms in Fortran*, *Comput. Phys. Commun.* **253** (2020) 107165, [1909.01656].

[304] D. D. Canko and N. Syrrakos, *Three-loop master integrals for H+jet production at N^{3}LO: Towards the non-planar topologies*, in *16th International Symposium on Radiative Corrections: Applications of Quantum Field Theory to Phenomenology*, 7, 2023, 2307.08432.

[305] J. M. Henn, A. Matijašić and J. Miczajka, *One-loop hexagon integral to higher orders in the dimensional regulator*, *JHEP* **01** (2023) 096, [2210.13505].

[306] J. Henn, T. Peraro, Y. Xu and Y. Zhang, *A first look at the function space for planar two-loop six-particle Feynman integrals*, *JHEP* **03** (2022) 056, [2112.10605].

[307] J. Gluza, K. Kajda and D. A. Kosower, *Towards a Basis for Planar Two-Loop Integrals*, *Phys. Rev. D* **83** (2011) 045012, [1009.0472].

[308] D. Cabarcas and J. Ding, *Linear algebra to compute syzygies and gröbner bases*, in *Proceedings of the 36th International Symposium on Symbolic and Algebraic Computation*, ISSAC '11, (New York, NY, USA), p. 6774, Association for Computing Machinery, 2011, DOI.

[309] R. M. Schabinger, *A New Algorithm For The Generation Of Unitarity-Compatible Integration By Parts Relations*, *JHEP* **01** (2012) 077, [1111.4220].

[310] G. Chen, J. Liu, R. Xie, H. Zhang and Y. Zhou, *Syzygies Probing Scattering Amplitudes*, *JHEP* **09** (2016) 075, [1511.01058].

[311] J. Böhm, A. Georgoudis, K. J. Larsen, M. Schulze and Y. Zhang, *Complete sets of logarithmic vector fields for integration-by-parts identities of Feynman integrals*, *Phys. Rev. D* **98** (2018) 025023, [1712.09737].

[312] J. Bosma, K. J. Larsen and Y. Zhang, *Differential equations for loop integrals without squared propagators*, *PoS* **LL2018** (2018) 064, [1807.01560].

[313] J. Boehm, D. Bendle, W. Decker, A. Georgoudis, F.-J. Pfreundt, M. Rahn et al., *Module Intersection for the Integration-by-Parts Reduction of Multi-Loop Feynman Integrals*, *PoS* **MA2019** (2022) 004, [2010.06895].

[314] Z. Wu, J. Boehm, R. Ma, H. Xu and Y. Zhang, *NeatIBP 1.0, A package generating small-size integration-by-parts relations for Feynman integrals*, 2305.08783.

[315] E. Panzer, *Algorithms for the symbolic integration of hyperlogarithms with applications to Feynman integrals*, *Comput. Phys. Commun.* **188** (2015) 148–166, [1403.3385].

[316] A. B. Goncharov, *Polylogarithms and motivic Galois groups*, in *Motives (Seattle, WA, 1991)*, vol. 55 of *Proc. Sympos. Pure Math.*, pp. 43–96. Amer. Math. Soc., Providence, RI, 1994. DOI.

[317] A. B. Goncharov, M. Spradlin, C. Vergu and A. Volovich, *Classical Polylogarithms for Amplitudes and Wilson Loops*, *Phys. Rev. Lett.* **105** (2010) 151605, [1006.5703].

[318] C. Duhr, H. Gangl and J. R. Rhodes, *From polygons and symbols to polylogarithmic functions*, *JHEP* **10** (2012) 075, [1110.0458].

[319] V. Del Duca, C. Duhr and V. A. Smirnov, *An Analytic Result for the Two-Loop Hexagon Wilson Loop in N = 4 SYM*, *JHEP* **03** (2010) 099, [0911.5332].

[320] V. Del Duca, C. Duhr and V. A. Smirnov, *The Two-Loop Hexagon Wilson Loop in N = 4 SYM*, *JHEP* **05** (2010) 084, [1003.1702].

[321] S. Zoia, *Modern Analytic Methods for Computing Scattering Amplitudes: With Application to Two-Loop Five-Particle Processes*, Ph.D. thesis, Munich U., 2022. 10.1007/978-3-031-01945-6.

[322] O. Steinmann, *Ueber den Zusammenhang zwischen den Wightmanfunktionen und den retardierten Kommutatoren*, doctoral thesis, ETH Zurich, Zürich, 1960. 10.3929/ethz-a-000107369.

[323] O. Steinmann, *Wightman-funktionen und retardierte kommutatoren. ii.*, *Helvetica Physica Acta* **33** (1960) 347–362.

[324] S. Caron-Huot, L. J. Dixon, A. McLeod and M. von Hippel, *Bootstrapping a Five-Loop Amplitude Using Steinmann Relations*, *Phys. Rev. Lett.* **117** (2016) 241601, [1609.00669].

[325] L. J. Dixon, J. Drummond, T. Harrington, A. J. McLeod, G. Papathanasiou and M. Spradlin, *Heptagons from the Steinmann Cluster Bootstrap*, *JHEP* **02** (2017) 137, [1612.08976].

[326] T. Ahmed, M. Mahakhud, P. Mathews, N. Rana and V. Ravindran, *Two-loop QCD corrections to Higgs $\to b + \overline{b} + g$ amplitude*, *JHEP* **08** (2014) 075, [1405.2324].

[327] R. Mondini and C. Williams, *$H \to b\bar{b}j$ at next-to-next-to-leading order accuracy*, *JHEP* **06** (2019) 120, [1904.08961].

[328] S. Catani and M. H. Seymour, *A General algorithm for calculating jet cross-sections in NLO QCD*, *Nucl. Phys. B* **485** (1997) 291–419, [hep-ph/9605323].

[329] M. Sjödahl, *ColorMath - A package for color summed calculations in SU(Nc)*, *Eur. Phys. J. C* **73** (2013) 2310, [1211.2099].

[330] P. Bärnreuther, M. Czakon and P. Fiedler, *Virtual amplitudes and threshold behaviour of hadronic top-quark pair-production cross sections*, *JHEP* **02** (2014) 078, [1312.6279].

[331] R. Bonciani et al., *Two-Loop Four-Fermion Scattering Amplitude in QED*, *Phys. Rev. Lett.* **128** (2022) 022002, [2106.13179].

[332] Y. Wang, L. L. Yang and B. Zhou, *FastGPL: a C++ library for fast evaluation of generalized polylogarithms*, 2112.04122.